

Heat Transfer Analysis in Quenching of Stationary and Moved Hot Metal Plates using Different Arrays of Spray Nozzles

Dissertation

zur Erlangung des akademischen Grades

Doktoringenieur

(Dr.-Ing.)

genehmigt durch die
Fakultät für Verfahrens und Systemtechnik
der Otto-von-Guericke-Universität Magdeburg

von M.Sc. Bilal Mehdi

geboren am 31.12.1990 in Gujrat, Pakistan

Gutachter:

Prof. Dr.-Ing. Eckehard Specht

Institut für Strömungstechnik und Thermodynamik
Otto-von-Guericke-Universität Magdeburg

Prof. Dr.-Ing. Herbert Pfeifer

Institut für Industrieofenbau und Wärmetechnik (IOB)
RWTH Aachen University

Prof. Dr.-Ing. Udo Fritsching

Leibniz-Institut für Werkstofforientierte Technologien (IWT)
Universität Bremen

Eingereicht am: 27.06.2024

Verteidigung der Dissertation am: 31.03.2025

Abstract

The rate at which metals are cooled determines their surface morphology, microstructure, and mechanical properties (hardness, strength). However, controlling this process is challenging and can lead to potential issues such as distortion, cracking, and warping of the material. To address these inhomogeneities and achieve the desired metal properties, the cooling rate or heat transfer must be precisely controlled. In this study, experiments were conducted on a pilot-scale experimental setup to investigate the quenching behavior of metals. A high-speed infrared was employed to measure temperatures on the backside of the plates. A numerical inverse heat conduction 2D model was developed to determine the heat flux and temperature distribution on the quenching side of the metal plate from the measured backside temperatures.

The research focused on both single and arrays of full cone sprays for horizontally moving and stationary plates. The influence of various parameters on heat transfer such as water impingement flux, nozzle pressure, volume flow rate, initial temperature, plate thickness, type of metal, nozzle-to-plate height, nozzle-to-nozzle distance, and plate velocity was studied both experimentally and numerically. These parameters were varied for both top-side and bottom-side cooling. Understanding the influence of these factors on the distribution of heat flux on the plate surface is crucial for achieving homogeneous and uniform cooling, which significantly impacts the quality of quenched metals. The study found that increasing the plate velocity, nozzle height, and nozzle-to-nozzle distance results in a decreased cooling rate and causes non-uniform cooling. The rewetting temperature and departure from nucleate boiling (DNB) temperature increase with greater plate thickness and decreased nozzle-to-plate height. Additionally, rewetting and cooling rates are relatively higher for bottom-side cooling compared to top-side cooling.

Moreover, heat transfer during the cooling of vertically moving metal plates using a field of two flat sprays was studied. In these experiments, vertically moving hot metal plates of different materials and thicknesses were quenched at varying plate speeds and nozzle inclination angles. The temperature distribution along the length of the plate between the middle of two nozzles was measured. Using infrared thermal images, the width of different cooling regions such as pre-cooling, transition boiling, and nucleate

boiling was compared for varying plate velocities. The maximum heat flux, the DNB temperature, and the rewetting temperature were determined for the studied parameters. It was found that the nozzle inclination angle has a minor influence on the cooling. As plate velocity and thickness increase, the maximum heat flux also increases, and the pre-cooling region shortens. This is because the position of the maximum heat flux shifts downstream, closer to the impingement region.

Zusammenfassung

Die Abkühlgeschwindigkeit, mit der Metalle gekühlt werden, bestimmt deren Oberflächenmorphologie, Mikrostruktur und mechanische Eigenschaften (Härte, Festigkeit). Die Kontrolle dieses Prozesses ist jedoch eine Herausforderung und kann zu potenziellen Problemen wie Verformung, Rissbildung und Verzug des Materials führen. Um diese Inhomogenitäten zu verhindern und die gewünschten Metalleigenschaften zu erreichen, muss die Abkühlgeschwindigkeit bzw. der Wärmeübergang genau kontrolliert werden.

Innerhalb dieser Arbeit wurden Experimente an einer pilotmaßstäblichen Versuchsanlage durchgeführt, um das Abschreckverhalten von Metallen zu untersuchen. Dafür wurden die Temperaturen auf der Rückseite der Bleche mit einer Hochgeschwindigkeits-Infrarotkamera gemessen. Ein numerisches inverses Wärmeleitungs-2D-Modell wurde entwickelt, um den Wärmestrom und die Temperaturverteilung auf der Abschreckseite des Metallblechs anhand der gemessenen Temperaturen auf der Rückseite zu bestimmen. Hierbei wurden sowohl einzelne, als auch Düsenfelder von Vollkegeldüsen für horizontale stationäre und bewegte Bleche untersucht. Der Einfluss der Parameter Wasserbeaufschlagdichte, Düsendruck, Volumenstrom, Anfangstemperatur, Blechstärke, Metallart, Düsenhöhe, Düsenabstand und Blechgeschwindigkeit auf den Wärmeübergang wurde experimentell und numerisch untersucht. Der Einfluss dieser Parameter wurde sowohl für eine Besprühung von oben sowie von unten untersucht. Zur Erzielung einer homogenen und gleichmäßigen Abkühlung, die für eine gute Qualität der abgeschreckten Metalle notwendig ist, ist das Verständnis über den Einfluss der einzelnen Parameter entscheidend.

Die Studie ergab, dass eine Erhöhung von Blechgeschwindigkeit, Düsenhöhe und Düsenabstand zu einer verringerten Abkühlgeschwindigkeit und einer vergleichsweise ungleichmäßigen Abkühlung führt. Die Wiederbenetzungstemperatur und die Temperatur beim Verlassen des Blasensiedens (DNB) steigen mit zunehmender Blechdicke und geringerer Düsenhöhe. Darüber hinaus sind die Wiederbenetzungs- und Abkühlraten bei der Kühlung von unten schneller im Vergleich zur Kühlung von oben.

Außerdem wurde der Wärmeübergang während der Abkühlung vertikal bewegter Metallbleche bei Verwendung von zwei Flachstrahldüsen untersucht. In diesen Experimenten wurden vertikal bewegte heiße Metallbleche unterschiedlicher Materialien und Dicken bei variierenden Blechgeschwindigkeiten und Düsenneigungswinkeln abgeschreckt. Die Temperaturverteilung entlang der Länge des Blechs zwischen der Mitte von zwei Düsen wurde gemessen und verglichen. Mit Hilfe von Infrarot-Bildern wurden die Breiten der verschiedenen Kühlzonen, wie Vorabkühlung, Übergangssieden und Blasensieden, bei variierenden Blechgeschwindigkeiten verglichen. Der maximale Wärmestrom, die DNB-Temperatur und die Wiederbenetzungstemperatur wurden für die untersuchten Parameter bestimmt. Es wurde festgestellt, dass der Düsenneigungswinkel einen schwachen Einfluss auf die Abkühlung hat. Mit zunehmender Blechgeschwindigkeit und Blechdicke steigt auch der maximale Wärmestrom und die Vorabkühlzone verkürzt sich. Dies liegt daran, dass die Position des maximalen Wärmestroms stromabwärts in die Nähe des Auftreffbereichs verschoben wird.

Table of Contents

Abstract.....	II
Zusammenfassung.....	IV
Figures	IX
Tables.....	XV
Nomenclature	XVI
Abbreviations	XVIII
1 Motivation and Scope.....	1
2 Theory and Literature Review.....	4
2.1 Basic Principles of Quenching.....	4
2.2 Importance of Heat Transfer Analysis in Metal Processing	6
2.3 Spray Quenching.....	9
2.3.1 Application	9
2.3.1 Spray characteristics	9
2.3.2 Heat Transfer Mechanism and Influencing Parameters	14
3 Experimental Setup	23
3.1.1 Quenching of Horizontal Plates	23
3.1.2 Quenching of Vertical Plates	29
3.2 Experimental Procedure	31
3.3 Measuring Technique	33
3.4 Preliminary Investigations and IR-Validation	36
3.4.1 Measurement of Surface Emissivity	36
3.4.2 Validation of Infrared Camera Measurements.....	37
3.4.3 Measurement of Water Impingement Flux	38
3.4.4 Material Properties.....	40
4 2D Inverse Heat Conduction Method.....	43
5 Quenching of Horizontal Plates.....	52

5.1	Overview	52
5.2	Single Full Cone Nozzle (Stationary).....	52
5.2.1	Cooling from the Top Side of the Plate.....	52
5.2.2	Cooling from the Bottom side of the Plate	76
5.2.3	Comparison of Top and Bottom Side Cooling	81
5.3	Single Full Cone Nozzle (Moving)	88
5.3.1	Cooling from the Top Side of the Plate.....	89
5.3.2	Cooling from the Bottom Side of the Plate	92
5.3.3	Comparison of Top and Bottom Side Cooling	97
5.4	Quenching of Plates in Nozzle Fields (Stationary)	98
5.4.1	Cooling from the Top Side of the Plate.....	98
5.4.2	Cooling from the Bottom Side of the Plate	109
5.4.3	Comparison of Top and Bottom Side Cooling	116
5.5	Quenching of Plates in Nozzle Fields (Moving).....	120
5.5.1	Cooling from the Top Side of the Plate.....	120
5.5.2	Cooling from the Bottom Side of the Plate	124
5.5.3	Comparison of Top and Bottom Side Cooling	131
5.6	Comparison of Single Nozzle and Nozzle Field	133
5.7	Reproducibility of Experiments	136
6	Quenching of Vertical Plates	140
6.1	Overview	140
6.2	Influence of Plate Velocity	141
6.3	Influence of Metal Thickness	146
6.4	Influence of Metal Type	149
6.5	Influence of Nozzle Inclination Angle	151
6.6	Mechanism of Heat Transfer	154
7	Conclusion	160

8	References	165
9	Appendix	169
9.1	Quenching of Horizontal Plates	169
9.2	Quenching of Vertical Plates	177

Figures

Figure 1.1: Basic quenching techniques	1
Figure 2.1: Typical boiling curve with distinct boiling regions (Hu et al., 2017).....	5
Figure 2.2: Temperature variation in a typical heat treatment process (Kaymak, 2007)	6
Figure 2.3: Schematics of continuous cooling transformation diagram for steel (Minamoto et al., 2022)	7
Figure 2.4: Cracks formation during water quenching (R. D. Lopez-Garcia et al., 2022)	8
Figure 2.5: Aluminum alloy AA6082 deformed plates	8
Figure 2.6: Schematics of industrial cooling of moving metal strips (Gradeck et al., 2009)	9
Figure 2.7: Droplet impact pattern of various pressure nozzles	10
Figure 2.8 Water flux distribution of a hydraulic, and pneumatic full cone nozzle (Specht, 2017).....	11
Figure 2.9: Influence of the air pressure on the spray characteristics of pneumatic full cone nozzle (Specht, 2017)	12
Figure 2.10: Spray flux distribution of two flat spray nozzles 40 mm distanced apart from each other at various water pressures.....	13
Figure 2.11: Distribution of the spray flux in a nozzle field (Alam et al., 2008)	14
Figure 2.12: Schematics of heat transfer and propagation of wetting front in spray cooling (Specht, 2017)	15
Figure 2.13: A cooling curve of AA6082 divided into four boiling regions	16
Figure 2.14: Influence of spray on the boiling curve for nickel (Müller and Jeschar, 1983)	17
Figure 2.15: Influence of spray flux on the DNB temperature (Specht, 2017)	17
Figure 2.16: Influence of water temperature on DNB, T_{Le} , and maximum heat flux (Specht, 2017).....	18
Figure 2.17: Influence of water temperature on the heat flux (Kotrbáček et al., 2022)	19
Figure 2.18: Influence of concentrations of $MgSO_4$ for AA6082 cooling (Abdalrahman et al., 2014) ..	19
Figure 3.1: Schematic diagram of the experimental setup for quenching horizontal plates (Top side cooling)	23
Figure 3.2: Schematic diagram of the experimental setup for quenching horizontal plates (Bottom side cooling)	23
Figure 3.3: Schematic representation of impingement of a full cone nozzle.....	25
Figure 3.4: Schematic representation of various nozzle-to-plate and nozzle-to-nozzle distances	27
Figure 3.5: Schematics of inline and staggered nozzle fields	28
Figure 3.6: Inline and staggered configuration of full cone nozzles	28
Figure 3.7: Schematic diagram of the experimental setup for quenching vertical plates	29
Figure 3.8: Schematic representation of two flat sprays	30
Figure 3.9: Measuring and quenching side of a 2 mm AA6082 plate specimen.....	32
Figure 3.10: Thermal image (left) and corresponding cooling curve (right) of a 5 mm nickel plate	34
Figure 3.11: IR images of 5 mm nickel cooled with a single full cone nozzle ($H = 84$ mm)	35

Figure 3.12: Extracted temperature data along the plate width during the cooling process	36
Figure 3.13: Dependence of thermal coating emissivity on temperature adapted from (Fang, 2019) .	37
Figure 3.14: Impingement flux along the two flat sprays axis	38
Figure 3.15: Water impingement flux distribution of single nozzle for various pressures (H = 63 mm) (Hof, 2023)	39
Figure 3.16: Water impingement flux distribution in nozzle fields (H = 63 mm, h = 70 mm) (Hof, 2023)	40
Figure 3.17: Temperature-dependent heat capacity of investigated metals	41
Figure 3.18: Temperature-dependent thermal conductivity of investigated metals	41
Figure 4.1: Algorithm flowchart of the inverse method	46
Figure 4.2: Schematic representation of boundary conditions of the plate	47
Figure 4.3: Model validation along the length of the plate for moving case	48
Figure 4.4: Inverse model validation based on experiment and simulated temperature on the measurement side	49
Figure 4.5: Smoothed heat fluxes against temperatures on the quenched side	50
Figure 4.6: Boiling curve of AA6082 comparing 2D inverse and analytical solution	51
Figure 5.1: Schematics of the full cone nozzle	52
Figure 5.2: Quenching and measuring side cooling curve	53
Figure 5.3: Boiling curve of cooling a 5 mm AA6082 using a full cone nozzle	54
Figure 5.4: Infrared images of cooling of 5 mm nickel with a single full cone nozzle	55
Figure 5.5: Temperature and heat flux profiles of 5 mm nickel along the plate width at various times	56
Figure 5.6: Influence of nozzle height on the cooling curve of 5 mm nickel	57
Figure 5.7: Influence of nozzle height on a boiling curve of 5 mm nickel	58
Figure 5.8: IR images with various nozzle-to-plate distance (AA6082)	59
Figure 5.9: Heat flux of AA6082 along the plate width for various nozzle heights	59
Figure 5.10: Influence of nozzle height on a cooling curve of 10 mm AA6082	60
Figure 5.11: Influence of nozzle height on boiling curve of 10 mm AA6082	61
Figure 5.12: IR images at various times with varying nozzle pressure for nickel	62
Figure 5.13: Influence of nozzle pressure on the temperature and heat flux profiles at a quasi-steady time along the plate width (nickel)	63
Figure 5.14: Influence of nozzle pressure on the cooling curve of nickel at the center of the nozzle ...	64
Figure 5.15: Influence of nozzle pressure on the heat flux of nickel at the center of the nozzle	65
Figure 5.16: Influence of nozzle pressure on the cooling curve of 10 mm AA6082	66
Figure 5.17: Influence of nozzle pressure on the boiling curve of 10 mm AA6082	67
Figure 5.18: Influence of plate thicknesses of AA6082 on cooling curve	68
Figure 5.19: Influence of plate thicknesses of AA6082 on boiling curve	68
Figure 5.20: IR images of cooling of nickel at different start temperatures at 4 s	69

Figure 5.21: Influence of start temperature of nickel on the temperature and heat flux profiles	70
Figure 5.22: Influence of start temperature of nickel on the cooling curve at the center of the nozzle .	71
Figure 5.23: Influence of start temperature of nickel on the boiling curve at the center of the nozzle..	72
Figure 5.24: IR image of nickel and AA6082 plates during cooling at 4 sec	73
Figure 5.25: Influence of metal type on the temperature profile and heat flux during cooling	74
Figure 5.26: Influence of metal type on the cooling curve at the center of the nozzle	75
Figure 5.27: Influence of metal type on the boiling curve at the center of the nozzle	76
Figure 5.28: Schematics of cooling of a plate from the bottom side	76
Figure 5.29: IR images of AA6082 plate with various nozzle-to-plate heights after 4 seconds of cooling	77
Figure 5.30: Influence of nozzle height on temperature and heat flux profiles along the plate width during cooling.....	78
Figure 5.31: Influence of nozzle height on the boiling curve of AA6082	79
Figure 5.32: Influence of nozzle height on temperature and heat flux profiles of nickel during cooling	80
Figure 5.33: Influence of metal thickness of AA6082 on the boiling curve	81
Figure 5.34: Infrared images of top and bottom side cooling (AA6082).....	81
Figure 5.35: Influence of cooling side on temperature and heat flux profiles (AA6082)	82
Figure 5.36: Influence of the cooling side on the boiling curve of AA6082	83
Figure 5.37: Surface heat fluxes of AA6082 for bottom and top side cooling (Nozzle type B)	84
Figure 5.38: Surface heat fluxes of AA6082 for bottom and top side cooling (Nozzle type A)	85
Figure 5.39: Surface heat fluxes of nickel for bottom and top side cooling (Nozzle type B)	87
Figure 5.40: Schematics of impingement of moving plate and Eulerian coordinate z^*	88
Figure 5.41: Temperature profiles of moving AA6082 plate and IR images at various time intervals ..	89
Figure 5.42: IR image of 5 mm moving AA6082 plate at $t = 0$ sec (cooling from the top side).....	90
Figure 5.43: Influence of plate velocity on the cooling of 5 mm AA6082 plate	91
Figure 5.44: Influence of plate velocity on the cooling of 5 mm nickel plate	91
Figure 5.45: Influence of the metal type at a plate velocity of 30 mm/s	92
Figure 5.46: Comparison of temperature profiles and IR images at various plate velocities (AA6082)	93
Figure 5.47: Comparison of Heat fluxes of AA6082 at various plate velocities	94
Figure 5.48: Influence of plate velocity on boiling curve of AA6082.....	95
Figure 5.49: Comparison of temperature profiles and IR images at various plate velocities (nickel) ...	96
Figure 5.50: Comparison of heat fluxes at various plate velocities (nickel)	97
Figure 5.51: Influence of the cooling side on the temperature profile of AA6082 at 30 mm/s plate	97
Figure 5.52: Influence of the cooling side on the temperature profile of nickel at 30 mm/s	98
Figure 5.53: IR images of nickel plate at various nozzle heights in an inline field ($b = 70$ mm).....	99

Figure 5.54: Temperature and heat flux profiles of nickel plate at various heights in inline nozzle field	99
Figure 5.55: IR images of cooling nickel at various nozzle-to-nozzle distances in inline nozzle field.	100
Figure 5.56: Influence of nozzle-to-nozzle distance on temperature and heat flux profiles of nickel in inline field	101
Figure 5.57: IR images of cooling nickel in inline nozzle field with variable nozzle pressure	102
Figure 5.58: Influence of nozzle pressure in inline nozzle field on the temperature and heat flux profiles	102
Figure 5.59: Influence of nozzle pressure in inline nozzle field on the temperature and heat flux profiles	103
Figure 5.60: Influence of start temperature on the heat transfer of nickel in inline nozzle field	104
Figure 5.61: Influence of plate thickness on temperature and heat flux profiles in inline nozzle field	105
Figure 5.62: Influence of volume flow rate on the temperature and heat flux profiles in the inline field	106
Figure 5.63: IR images of cooling of nickel in Inline and Staggered nozzle fields	107
Figure 5.64: Go-Pro image of water impingement of inline and staggered nozzle fields (Hof, 2023).	107
Figure 5.65: Influence of nozzle configuration on the temperature and heat flux profiles	108
Figure 5.66: Influence of nozzle configuration on the cooling curve at the center of the middle nozzle	109
Figure 5.67: IR images of nickel plate at various nozzle heights in an inline field	109
Figure 5.68: Influence of nozzle height on temperature and heat flux profiles in an inline field	110
Figure 5.69: IR images of cooling of nickel at various nozzle to nozzle distance	111
Figure 5.70: Influence of nozzle-to-nozzle distance on temperature and heat flux profiles (inline)	111
Figure 5.71: Cooling curve comparison of center and overlap position in the inline nozzle field.....	112
Figure 5.72: Cooling curve comparison of center and overlap position in the inline nozzle field.....	112
Figure 5.73: Temperature comparison of four positions in between the centers of nozzles and the center position for the inline arrangement	113
Figure 5.74: IR images of cooling of nickel with the variable volume flow rate	114
Figure 5.75: Influence of volume flow rate on temperature and heat flux profiles	114
Figure 5.76: IR images of cooling of nickel in Inline and Staggered nozzle fields	115
Figure 5.77: Influence of nozzle configuration on the temp- and heat flux profiles.....	116
Figure 5.78: IR images of top and bottom side cooling in inline nozzle field	117
Figure 5.79: Influence of the cooling side on the temperature and heat flux profiles.....	118
Figure 5.80: IR images of top and bottom side cooling in inline nozzle field	119
Figure 5.81: Influence of cooling side cooling on the temperature and heat flux profiles	119
Figure 5.82: Schematic of Eulerian coordinate (z^*) in a nozzle field	120
Figure 5.83: IR images captured during cooling moving plates with various velocities in the nozzle field	121

Figure 5.84: Comparison of temperature profiles at various plate velocities in the inline nozzle field	121
Figure 5.85: Influence of nozzle height on the cooling of moving plate using the inline nozzle field ..	122
Figure 5.86: IR images of cooling of nickel and AA6082 moving plates	123
Figure 5.87: Influence of metal type in the inline nozzle field at a plate velocity of 30 mm/s.....	123
Figure 5.88: IR images of variation of plate velocity at two various nozzle-to-nozzle distance	124
Figure 5.89: Influence of plate velocity on the cooling of nickel at $b = 35$ mm, and $b = 70$ mm	125
Figure 5.90: Influence of plate velocity along the width in a nozzle field ($b = 35$ mm).....	126
Figure 5.91: Influence of plate velocity along the width in a nozzle field ($b = 70$ mm).....	126
Figure 5.92: Influence of plate velocity on the heat flux of nickel at $b = 35$ mm, and $b = 70$ mm	127
Figure 5.93: Influence of plate velocity on the boiling curve (nickel, $H = 63$ mm, $b = 35$ mm).....	128
Figure 5.94: Influence of plate velocity on the cooling of AA6082 plate ($H = 63$ mm, $b = 35$ mm)	128
Figure 5.95: Influence of plate velocity along the width in a nozzle field (AA6082, $b = 35$ mm)	129
Figure 5.96: IR images of the influence of cooling of AA6082 at various nozzle heights ($b = 70$ mm).....	129
Figure 5.97: Influence of nozzle height on the cooling of AA6082 metal plates ($b = 70$ mm, $w_p = 30$ mm/s)	130
Figure 5.98: Influence of nozzle configuration on the cooling of AA6082 at a plate velocity of 30 mm/s)	131
Figure 5.99: Top side vs bottom side cooling (AA6082, $H = 63$ mm, $b = 70$ mm, $w_p = 30$ mm/s)	132
Figure 5.100: Top side vs bottom side cooling (nickel, $H = 63$ mm, $b = 70$ mm, $w_p = 30$ mm/s)	132
Figure 5.101: Comparison of single nozzle and inline field ($T_{start} = 500$ °C)	133
Figure 5.102: Comparison of single nozzle and inline field ($T_{start} = 800$ °C)	134
Figure 5.103: Comparison of a single nozzle and inline nozzle field (AA6082)	135
Figure 5.104: Comparison of of moving nickel and AA6082 for single nozzle and inline nozzle field	136
Figure 5.105: Repeatability of experiments single full cone nozzle (AA6082, $H = 63$ mm)	137
Figure 5.106: Repeatability of experiments in an inline nozzle field (AA6082)	138
Figure 5.107: Repeatability of experiments in an inline nozzle field (nickel).....	139
Figure 6.1: Schematics of formation of various boiling regions along the plate length during cooling	140
Figure 6.2: Cooling curves of 2 mm nickel plate with varying plate velocities ($\alpha = 90^\circ$)	141
Figure 6.3: IR images of cooling 2 mm nickel at quasi-stationary time at various plate velocities	142
Figure 6.4: Boiling curves of 2 mm nickel plate with varying plate velocities ($\alpha = 90^\circ$).....	143
Figure 6.5: Cooling curves of AA6082 plate with varying velocities ($\alpha = 90^\circ$).....	143
Figure 6.6: Boiling curves of 2 mm AA6082 plate with varying plate velocities ($\alpha = 90^\circ$)	144
Figure 6.7: Cooling curves of 2 mm microfer plate with varying velocities ($\alpha = 65^\circ$)	145
Figure 6.8: Boiling curves of 2 mm microfer plate with varying plate velocities ($\alpha = 65^\circ$).....	146
Figure 6.9: Cooling curves of AA6082 of 2 mm and 5 mm thick plates ($w_p = 10$ mm/s).....	147
Figure 6.10: Boiling curve of 2 mm and 5 mm AA6082 plate ($w_p = 10$ mm/s)	147

Figure 6.11: Cooling curves of nickel of 2 mm and 5 mm thick plates at 5 mm/s plate velocity	148
Figure 6.12: Boiling curve of 2 mm and 5 mm nickel plate at 5 mm/s plate velocity.....	149
Figure 6.13: Influence of metal type on temperature profile at 15 mm/s plate velocity.....	149
Figure 6.14: Influence of metal type on the boiling curve at 15 mm/s plate velocity.....	150
Figure 6.15: Influence of meta-type on maximum heat flux for varying plate velocities.....	151
Figure 6.16: Influence of nozzle angle during cooling a nickel plate ($w_p = 15$ mm/s).....	152
Figure 6.17: Influence of nozzle angle on boiling curve of nickel plate ($w_p = 15$ mm/s).....	152
Figure 6.18: Influence of nozzle angle on maximum heat flux for varying plate velocities (AA6082) .	153
Figure 6.19: Maximum heat flux of nickel, nicrofer, and AA6082 for various plate velocities ($\alpha = 65^\circ$)	154
Figure 6.20: Maximum heat flux of nickel for various nozzle angles and plate velocities	155
Figure 6.21: Maximum heat flux of AA6082 for various nozzle angles and plate velocities	156
Figure 6.22: Maximum heat flux of nicrofer for various nozzle angles and plate velocities	156
Figure 6.23: IR image with various quenching regions ($s = 5$ mm, AA6082)	157
Figure 9.1: Cooling curve comparison along the radial position of the wetting front.....	169
Figure 9.2: Temperature variation of AA6082 for two different ML positions at 4 s	169
Figure 9.3: Temperature profiles of AA6082 along the plate width for ML2 and ML3.....	170
Figure 9.4: Temperature variation of AA6082 for two different ML positions at 2 s	170
Figure 9.5: Influence of measuring line on the temperature distribution in an inline field	171
Figure 9.6: Cooling curve comparison of the center of the middle nozzle and overlap positions in nozzle field (Staggered, $H = 63$ mm, AA6082, $b = 35$ mm)	171
Figure 9.7: Temperature distribution of AA6082 along the plate width at various nozzle heights	172
Figure 9.8: Comparison of nozzle configuration on the cooling curve at the center of the middle nozzle ($H = 63$ mm, $b = 70$ mm, bottom side cooling)	173
Figure 9.9: Influence of inline and staggered nozzle configuration on the cooling of nickel moving plate ($H = 63$ mm, $b = 70$ mm, $w_p = 30$ mm/s).....	173
Figure 9.10: Temperature profiles along the plate width at three nozzle rows (AA6082, $H = 63$ mm, $b = 35$ mm, $w_p = 30$ mm/s)	174
Figure 9.11: Temperature profiles along the plate width at three nozzle rows (AA6082, $H = 63$ mm, $b = 35$ mm, $w_p = 45$ mm/s)	175
Figure 9.12: Temperature profiles along the plate width at three nozzle rows (nickel, $H = 63$ mm, $b = 70$ mm, $w_p = 30$ mm/s)	176
Figure 9.13: Temperature profiles along the plate width at three nozzle rows (nickel, $H = 63$ mm, $b = 35$ mm, $w_p = 45$ mm/s)	176
Figure 9.14: Boiling curve of Single nozzle vs Inline nozzle filed (5mm, AA6082)	177
Figure 9.15: Cooling curves of 2 mm nickel plate with varying plate velocities ($\alpha = 45^\circ$)	177
Figure 9.16: Boiling curves of 2 mm nickel plate with varying plate velocities ($\alpha = 45^\circ$).....	178
Figure 9.17: Cooling curves of 2 mm nickel plate with varying plate velocities ($\alpha = 65^\circ$)	178

Figure 9.18: Boiling curves of 2 mm nickel plate with varying plate velocities ($\alpha = 65^\circ$)	179
Figure 9.19: Cooling curves of 2 mm nicrofer plate with varying plate velocities ($\alpha = 45^\circ$)	179
Figure 9.20: Boiling curves of 2 mm nicrofer plate with varying plate velocities ($\alpha = 45^\circ$)	180
Figure 9.21: Cooling curves of 2 mm AA6082 plate with varying plate velocities ($\alpha = 65^\circ$)	180
Figure 9.22: Boiling curves of 2 mm AA6082 plate with varying plate velocities ($\alpha = 65^\circ$)	181
Figure 9.23: Boiling curves of 2 mm AA6082 plate with varying plate velocities ($\alpha = 45^\circ$)	181
Figure 9.24: Boiling curves of 2 mm AA6082 plate with varying nozzle angle ($w_p = 15$ mm/s)	182
Figure 9.25: Cooling curves of 5 mm nicrofer plate with varying plate velocities	182
Figure 9.26: Cooling curves of 5 mm nickel plate with varying plate velocities	183
Figure 9.27: Maximum heat flux against the local position z^* with varying plate velocities (nickel, nicrofer, $s = 5$ mm)	183
Figure 9.28: Influence of nozzle angle on maximum heat flux for varying plate velocities (nickel) ..	184
Figure 9.29: Influence of nozzle angle on maximum heat flux for varying plate velocities (nickel)	184
Figure 9.30: Maximum heat flux of AA6082 for various plate velocities and plate thicknesses	185
Figure 9.31: Maximum heat flux of nickel for various plate velocities and plate thicknesses	185

Tables

Table 1: Specific characteristics of the infrared camera	25
Table 2: Parameter variations for quenching of horizontal plates	26
Table 3: Parameter variations for quenching of vertical plates	31
Table 4: Material properties of various investigated metals at mean temperature	42
Table 5: Variation of the volume flow rate of two nozzles with varying nozzle pressure	62
Table 6: Width of various cooling regions for nickel at various plate velocities ($\alpha = 90^\circ$, $s = 2$ mm) ..	158
Table 7: Width of various cooling regions for nicrofer at various plate velocities ($\alpha = 65^\circ$, $s = 2$ mm)	158
Table 8: Width of various cooling regions for AA6082 at various plate velocities ($\alpha = 90^\circ$, $s = 2$ mm)	159

Nomenclature

<i>Latin Symbol</i>	Meaning	Unit
A	Area	m ²
b	Nozzle to nozzle distance	mm
B	Flat spray impacting length	mm
b_s	Flat spray width	mm
c_p	Heat capacity	kJ/kg·K
d	Diameter	mm
H	Nozzle to plate height	mm
k	Iteration number	-
L	Length of plate	mm
M	Total number of measurements	-
\dot{m}_s	Spray flux	kg/m ² ·s
N	Nozzle	-
p	Nozzle pressure	bar
p^k	Direction of descent	-
\dot{q}	Heat flux	MW/m ²
\dot{q}^0	Initial heat flux guess	MW/m ²
$\dot{q}_{max.}$	Maximum heat flux	MW/m ²
R	Radius	m
s	Plate thickness	mm
S	Objective function	-
t	Time	s
T	Temperature	°C
T_{DNB}	Departure from nucleate boiling temperature	°C

t_f	Final time	s
T_{le}	Leidenfrost temperature	°C
T_m	Calculated temperature	°C
T_{sat}	Saturation temperature	°C
T_{start}	Start temperature	°C
T_w	Water temperature	°C
T_0	Initial temperature	°C
T_{rw}	Rewetting temperature	°C
\dot{V}	Volume flow rate	m ³ /s
w	Velocity of spray particles	m/s
w_p	Plate velocity	m/s
Y_m	Measured temperature	°C
z	Langrangian coordinate	mm
z^*	Eulerian coordinate	mm

<i>Greek Symbol</i>	Meaning	Unit
α	Nozzle inclination angle	°
β^k	Search step size	-
γ	Conjugate coefficient	-
Γ_{ms}	Measuring side boundary condition	-
Γ_{qs}	Quenching side boundary condition	-
Δp	Pressure drop	bar
ΔT	Temperature difference	°C
ε	Emissivity	-
σ	Standard deviation	°C
λ	Thermal conductivity	W/m·K
ρ	Density	kg/m ³

Ω	Domain	-
τ	Stopping criteria	-

Abbreviations

DNB	Departure nucleate boiling
IR	Infrared
ONB	Onset nucleate boiling
CHF	Critical heat flux
ML	Measuring line
2D	Two dimensional
ASCII	American Standard Code for Information Interchange
IHCP	Inverse heat conduction problem
3D	Three dimensional
CGM	Conjugate gradient method

1 Motivation and Scope

Quenching or ultrafast cooling is commonly exercised in the metallurgy industry. The advanced high-strength metallic components have found several applications in the automobile, aerospace, and construction industry. In the manufacturing process of metals, quenching is an essential heat treatment process, in which material is rapidly cooled from high temperature to low temperature to achieve precise material properties. During the quenching process, the metal workpieces are cooled at high temperatures, up to 900 °C to 1200 °C for steel alloys and from 500 °C to 600 °C for aluminum alloys. Achieving desired material properties necessitates controlled cooling of the metals. This cooling process involves either immersing the hot metals in a cooler liquid or cooling them with jets or sprays as shown in Figure 1.1.

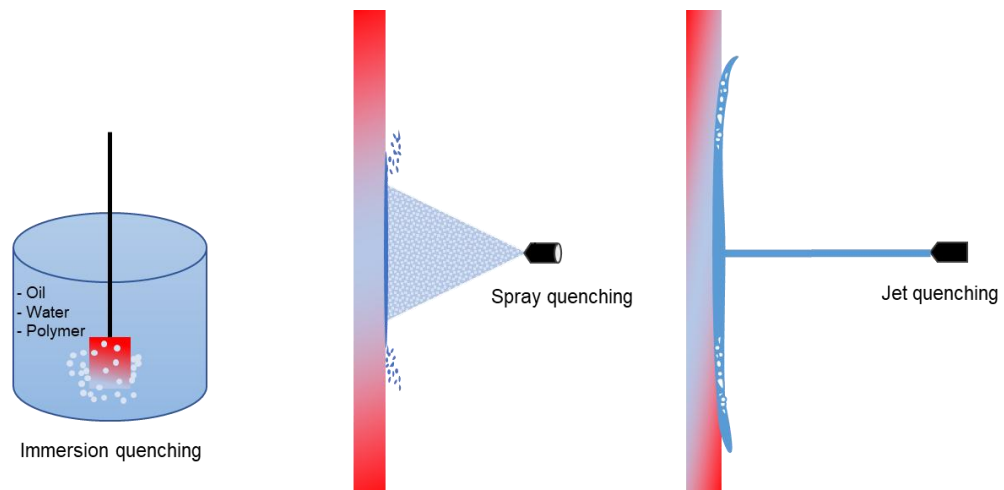


Figure 1.1: Basic quenching techniques

During rapid cooling, the temperatures drop by several hundred degrees within seconds causing the boiling of water. Generally, four boiling regions can be observed during the cooling process. In the beginning, due to extreme vapor formations, a vapor layer forms on the surface which acts as an insulating layer restricting the direct contact and the heat transfer between the hot surface and cooling medium, this mode of heat transfer is known as film boiling. As the metal cools down to Leidenfrost temperature or rewetting temperature, the partial contact between the hot metal and cooling medium is established, resulting in increasing heat transfer until the maximum heat flux is achieved known as the transition boiling region. The surface temperature at which maximum heat flux is obtained is called DNB temperature (Departure Nucleate

Boiling). After this point, an intensive bubble formation can be observed following the nucleate boiling region, in which the heat flux decreases again until the saturation temperature of the coolant is reached, followed by single-phase forced convection. Each one of these boiling regions is characterized by different heat transfer mechanisms.

The cooling rate, at which the metals are cooled, determines the surface morphology, microstructure, and mechanical properties (hardness, strength) of the metals. However, it is a very challenging process and can lead to the potential distortion, cracking, and warping of material. To address these inhomogeneities, and to meet the aforementioned metal properties, the cooling rate or heat transfer must be controlled accordingly. Industrial setups are often designed based on empirical data, as the temperatures of the metal plates are not measurable, and the heat fluxes are unknown. Moreover, it is not possible to vary parameters, such as nozzle arrangement, and configuration, during operation. Particularly relevant during the cooling of horizontally guided strips in continuous heat treatment plants, such as those found in the aluminum industry. The water is applied to the metal surface using spray nozzles. To cover the entire width of the strip, the nozzles are arranged in nozzle fields. The resulting heat transfer on the surface is primarily a function of the nozzles used and the arrangement of the nozzles in the nozzle field. Additionally, the nozzle pressure and the distance between the nozzle and the surface influence the heat transfer on it. Poor nozzle field configuration can lead to thermal stress, resulting in defects, deformations, and cracks in metal sheets. These issues lead to downtime and the need for re-melting the materials, both of which are costly and energy-intensive.

The literature predominantly focuses on the quenching of steel, given the steel industry's significant global presence. In contrast, the quenching of materials like aluminum, nickel, and nicrofer has been less studied. Additionally, research has primarily concentrated on single nozzles rather than nozzle fields. Therefore, this study is dedicated to investigating the quenching process of aluminum alloy, nickel, and nicrofer. Initially, single nozzles (full cone nozzles) were studied on horizontal stationary and moving plates. Subsequently, nozzle fields were examined under both, stationary and moving conditions. Additionally, two flat spray nozzles on the cooling of vertical moving plates were investigated.

For this work, a pilot-scale experimental setup was developed to study the quenching behavior. Given the challenges and limitations of measuring surface temperatures with thermocouples, a high-speed infrared camera was employed to measure the temperatures on the backside of the plates. A numerical inverse 2D model was developed to calculate the heat flux and temperature distribution on the quenching side of the metal plate from the measured backside temperatures. The backside of the plates was black-coated before they were heated to a start temperature (500° to 800 °C) in an electrically heated experimental furnace. Subsequently, the plates were transferred to a quenching chamber using a rail system, where various nozzle configurations and operational parameters can be adjusted.

The insights gained from this study enhance the fundamental understanding of the thermal processes during quenching and provide valuable information for the design and optimization of industrial nozzle fields.

2 Theory and Literature Review

2.1 Basic Principles of Quenching

Quenching refers to the rapid cooling of high-temperature metallic components resulting from their sudden contact with a lower-temperature liquid. Since the metal temperature is significantly higher than the boiling temperature of the liquid at atmospheric conditions, boiling heat transfer occurs. Before discussing the quenching process, a quick insight into the boiling process is necessary.

Heat is transmitted from a solid (wall) to a saturated or superheated liquid in contact with its surface during the two-phase process of boiling. The Heat transfer starts with phase change, which results in vapor bubble formation. These vapor bubbles grow and depart the wall continuously. (Schweizer, 2010) proposes several explanations for why heat transport is improved during boiling compared to single-phase forced convection:

- A thin liquid microlayer is formed on the wall at the bubble foot, which greatly increases the heat transfer rate.
- The motion of vapor bubbles causes enhancement of the single-phase convection due to liquid agitation near the surface.
- At each bubble cycle, the thermal resistance is lowered due to the renewal of the thermal boundary layer.

How the heat flux varies against the surface temperature is represented by the boiling curve. Figure 2.1 shows the typical pool boiling curve commonly known as Nukiyama's curve named after Nukiyama (1934) who first constructed it for pool boiling of water.

the quenching process follows the route $D \rightarrow C \rightarrow B \rightarrow A$. Four boiling regions formed during quenching in the Nukiyama's curve are described:

Film boiling: this boiling region appears during the quenching process when the surface temperature is higher than the Leidenfrost temperature (D-C). Above this temperature a stable vapor layer forms on the heated surface, which prevents direct contact between the surface and the liquid. The heat conduction through the vapor film dominates in the film boiling region. The end of this region is referred to as the Leidenfrost point also known as the rewetting point indicated by C.

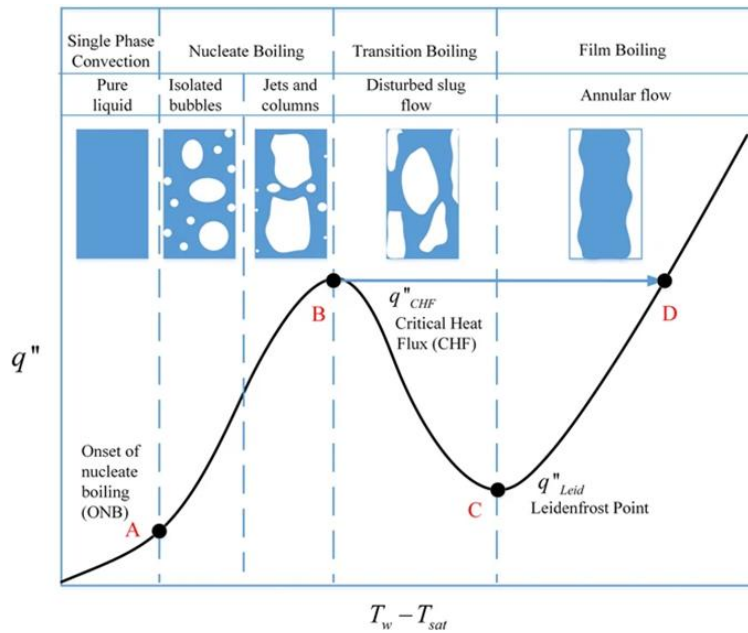


Figure 2.1: Typical boiling curve with distinct boiling regions (Hu et al., 2017)

Transition boiling: it is characterized by an intermediate region between film boiling and nucleate boiling region from point C to B. The establishment of partial contact between liquid and surface increases heat transfer by decreasing the surface temperature. At the end of this region, the heat flux reaches its maximum value, known as maximum or critical heat flux. The temperature at the end of this region or at which maximum heat flux is obtained is called departure nucleate boiling temperature (T_{DNB}).

Nucleate boiling: In this two-phase boiling region, the bubbles nucleate, grow, and depart from the heated wall. The end of this boiling region is defined by the onset of nucleate boiling (ONB).

Single-phase convection: This region starts when the wall superheat is low, due to low superheat, any possible vapor bubble if generated would immediately condense in the subcooled liquid around it.

Pool boiling is a natural convection-based boiling process, whereas, during jet impingement quenching, the liquid is forced to flow over the heated surface. Although the representative features of the boiling curve still resemble those of Nukiyama's curve for pool boiling, the heat flux in the case of forced convection boiling is a function of the local liquid velocity and subcooling in all regimes. When examining the boiling

process, it is important to take into account the hydrodynamics of the impact of the jet on heat transfer.

2.2 Importance of Heat Transfer Analysis in Metal Processing

Heat treatment is a process involving controlled heating and cooling to alter the crystalline structure of metals and metal alloys. Depending on the material and specific treatment process, heat treatment can offer various benefits, such as enhanced hardness, increased temperature resistance, greater ductility, and improved material strength. Heat treatment is a proven technique for altering the properties of metal by controlling the rate of diffusion within its microstructure. This means that the same alloy can develop different microstructures depending on the cooling rates applied. Common heat-treating methods include annealing, hardening, quenching, and stress relieving, each with its distinct process to achieve specific results. Figure 2.2 shows the variation of temperature in a heat treatment process.

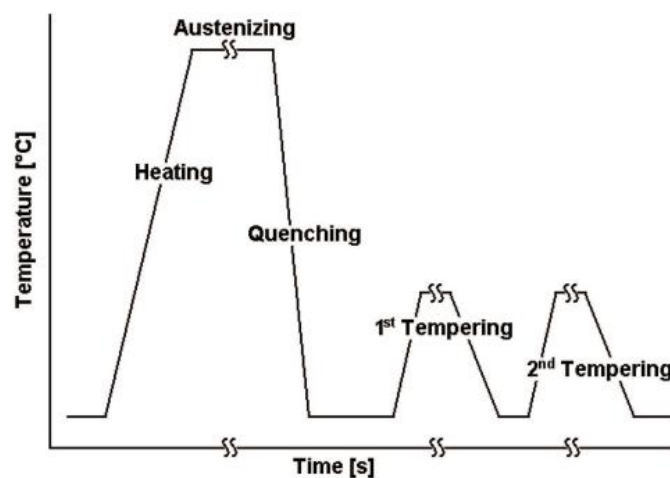


Figure 2.2: Temperature variation in a typical heat treatment process (Kaymak, 2007)

Quenching is a heat treatment method that involves rapid cooling of metal to achieve specific physical or mechanical properties. Although oil is commonly used as the cooling medium, quenching can also be done using air, water, or brine, depending on the material and desired qualities. Similar to other heat-treating processes, the metal is heated to a temperature below its melting point, where the crystalline structure becomes fluid. It is then held at this temperature for a specific duration, based on the

desired properties, before being quenched in one of the aforementioned media to rapidly lower its temperature and establish the required internal structure. Depending on the cooling rate, various microstructures form within the metal. The various types of crystalline microstructures of steel are shown in Figure 2.3.

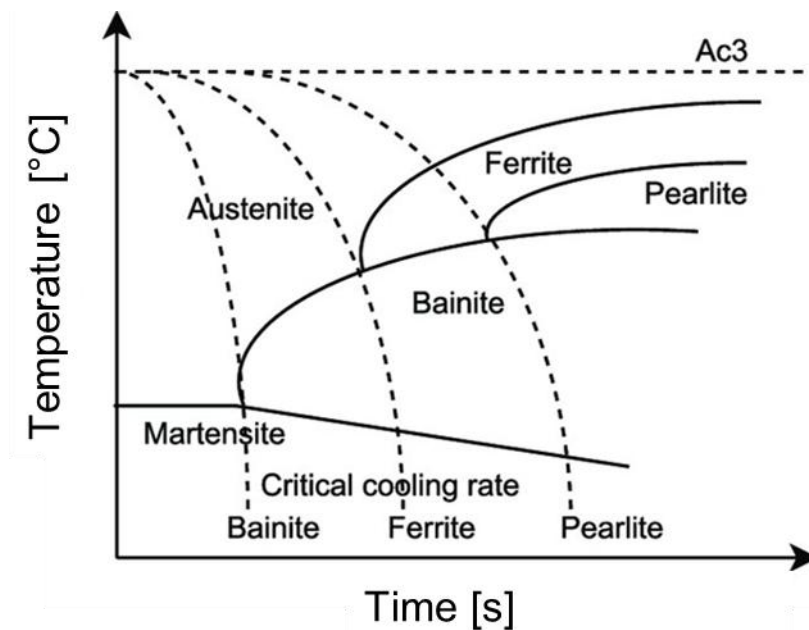


Figure 2.3: Schematics of continuous cooling transformation diagram for steel (Minamoto et al., 2022)

Austenite: Austenite forms when iron is heated during metalworking. It is a tough, yet formable microstructure, making it excellent for welding. Austenitic steel has various applications, but it is often further processed to create martensitic steel.

Martensite: Martensite forms through the rapid cooling of heated metal. While martensitic steel is very hard, it is also quite brittle. Post-quenching treatment helps restore some ductility and relieve internal stresses.

Ferrite: Ferrite is a soft, thermodynamically stable microstructure that forms before transforming into austenite. It is primarily found in low-carbon steel.

Cementite: Cementite is a thermodynamically unstable microstructure containing iron and carbon. Its rigid structure results in a very hard, yet brittle, metal.

Pearlite: Slow cooling produces a pearlite microstructure, composed of alternating layers of ferrite and cementite. This structure is strong, lightweight, and has high wear resistance.

Bainite: Bainite is a hard, brittle microstructure formed when steel is cooled faster than the rate needed to produce pearlite but slower than the rate required for martensite.

During the process of quenching, deformation may arise as a result of thermal stresses and phase changes occurring within the material. The occurrence of quench cracking in aluminum alloy samples is closely related to the maximum temperature difference within the samples during quenching. The deformation observed in the quenching process is mainly attributed to the subsequent factors:

Thermal stresses: Rapid cooling of a material leads to differential cooling rates between the outer surface and the inner core, causing thermal gradients and internal stresses. When these stresses surpass the material's yield strength, plastic deformation may ensue, resulting in warping, distortion, or cracking (Samuel and Prabhu, 2022) as shown in Figure 2.4, and Figure 2.5.

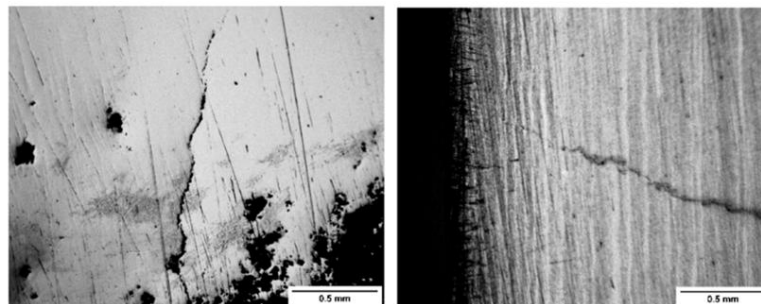


Figure 2.4: Cracks formation during water quenching (R. D. Lopez-Garcia et al., 2022)



Figure 2.5: Aluminum alloy AA6082 deformed plates

Phase transformations: Various steels and alloys undergo phase alterations while cooling, such as the shift from austenite to martensite in steels. These transformations

involve volume fluctuations that can generate internal stresses and deformation if they exceed the material's yield strength (Krauss, 2015).

2.3 Spray Quenching

2.3.1 Application

Over the years, spray quenching has been widely utilized in many industrial applications like metallurgy, nuclear power plants, aerospace, and microelectronic engineering. Water spray cooling is most commonly used in secondary cooling in the continuous casting of metals e.g. steel industry. The array of sprays impinges on the strand of hot solidifying metal in the second cooling stage after exiting the mold. Spray quenching offers many advantages over other quenching methods, such as relatively uniform cooling, a wide adjustable cooling rate range by varying flow rates, enhanced heat transfer, and the capability to cool large surface areas. In the field of metal heat treatment, a horizontal strip is preferred to be cooled with an array of sprays, as it offers relatively homogeneous cooling along the strip. Figure 2.6 represents the scheme of the industrial cooling system at the end of the rolling process.

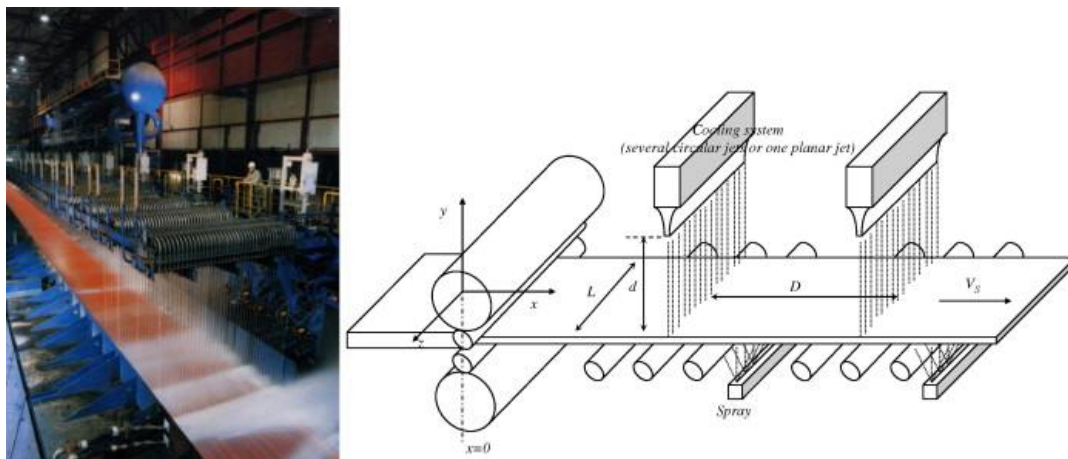


Figure 2.6: Schematics of industrial cooling of moving metal strips (Gradeck et al., 2009)

2.3.1 Spray characteristics

Generally, two types of sprays are employed in the industry: air assist using atomizer nozzles and hydraulic nozzles. Pressure spray nozzles also named one fluid nozzle

are preferred for spray cooling. The momentum of liquid alone (water) is used to break up liquid into tiny droplets to produce a spray. According to the droplet distribution manner across the surface, the pressure nozzles are further categorized into full cone, hollow cone, and flat spray, see Figure 2.7

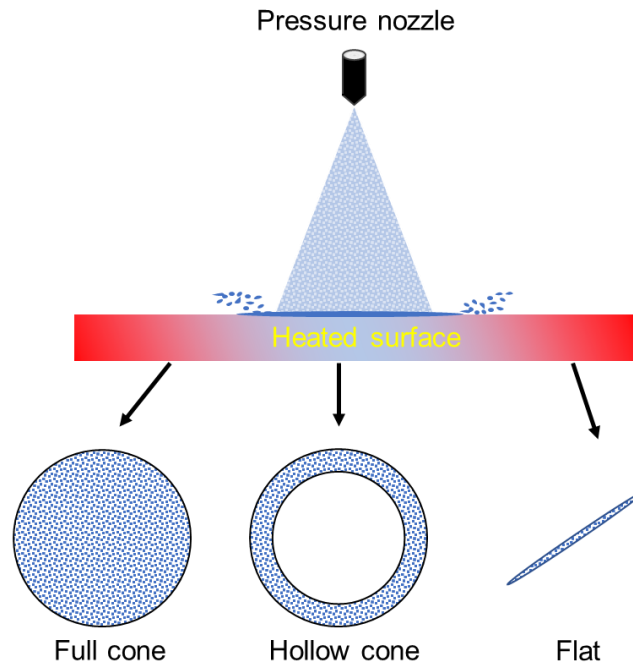


Figure 2.7: Droplet impact pattern of various pressure nozzles

A full cone nozzle covers the entire circular impact area and distributes the droplets in the form of a circle. A hollow cone nozzle concentrates in the periphery region of the impact circle, which forms uniform droplets in a ring form. In contrast, flat sprays produce rectangular to oval-shaped wetting fronts.

For hydraulic pressure nozzles, the exit velocity of the spray is strongly influenced by water pressure in the nozzle.

$$\Delta p = w^2 \cdot \frac{\rho}{2} \quad (2-1)$$

Whereas, the volume flow depends on the nozzle diameter (d)

$$\dot{V} = \frac{\pi}{4} d^2 \cdot w = \frac{\pi}{4} d^2 \cdot \sqrt{\frac{2 \cdot \Delta p}{\rho}} \quad (2-2)$$

To produce fine droplets, small diameters are required. The relatively small outlet orifices in hydraulic nozzles are prone to blockages and wear. Additionally, hydraulic nozzles have a smaller adjustment range, approximately 1:4, compared to pneumatic nozzles. Figure 2.8 illustrates the water flux distribution impinging on the wall of a special nozzle at three different mass flows. The water flux, or spray flux, represents the amount of water that strikes the surface per unit area and time. The figure shows that the distribution for this nozzle is symmetric only at a mass flow of 20 l/h. When the mass flow increases to 25 and 30 l/h, the spray flux also increases, resulting in a nonuniform local distribution, which negatively impacts local heat transfer (Specht, 2017).

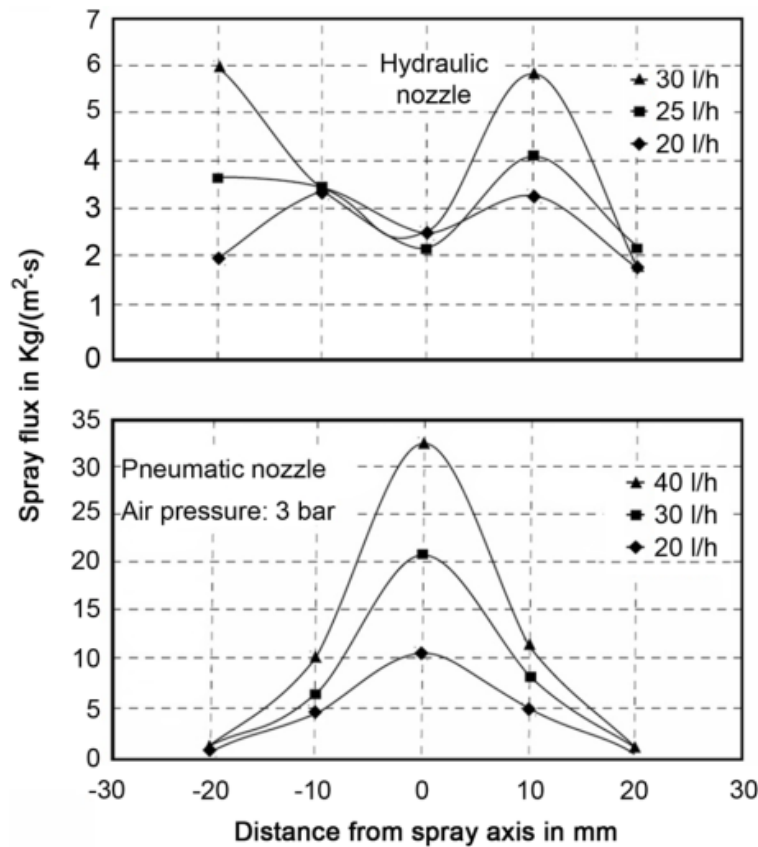


Figure 2.8 Water flux distribution of a hydraulic, and pneumatic full cone nozzle (Specht, 2017)

Using water as the sole flow medium in hydraulic nozzles eliminates the need for compressors to generate compressed air, resulting in significant cost savings.

Additionally, the installation of fewer pipelines further reduces both investment and maintenance costs. Moreover, hydraulic nozzles are less expensive than pneumatic nozzles due to their simpler design. In pneumatic nozzles, both water and air flow through the outlet orifice, with the volume flow of air being significantly higher than that of water. Consequently, the outlet orifice must be considerably larger compared to hydraulic nozzles. The water's volume flow is influenced not only by its own pressure but also by the air pressure.

Figure 2.9 illustrates the local distribution of the average droplet diameter (Sauter mean diameter) and droplet velocity at different air pressures with a constant water flow for a pneumatic nozzle.

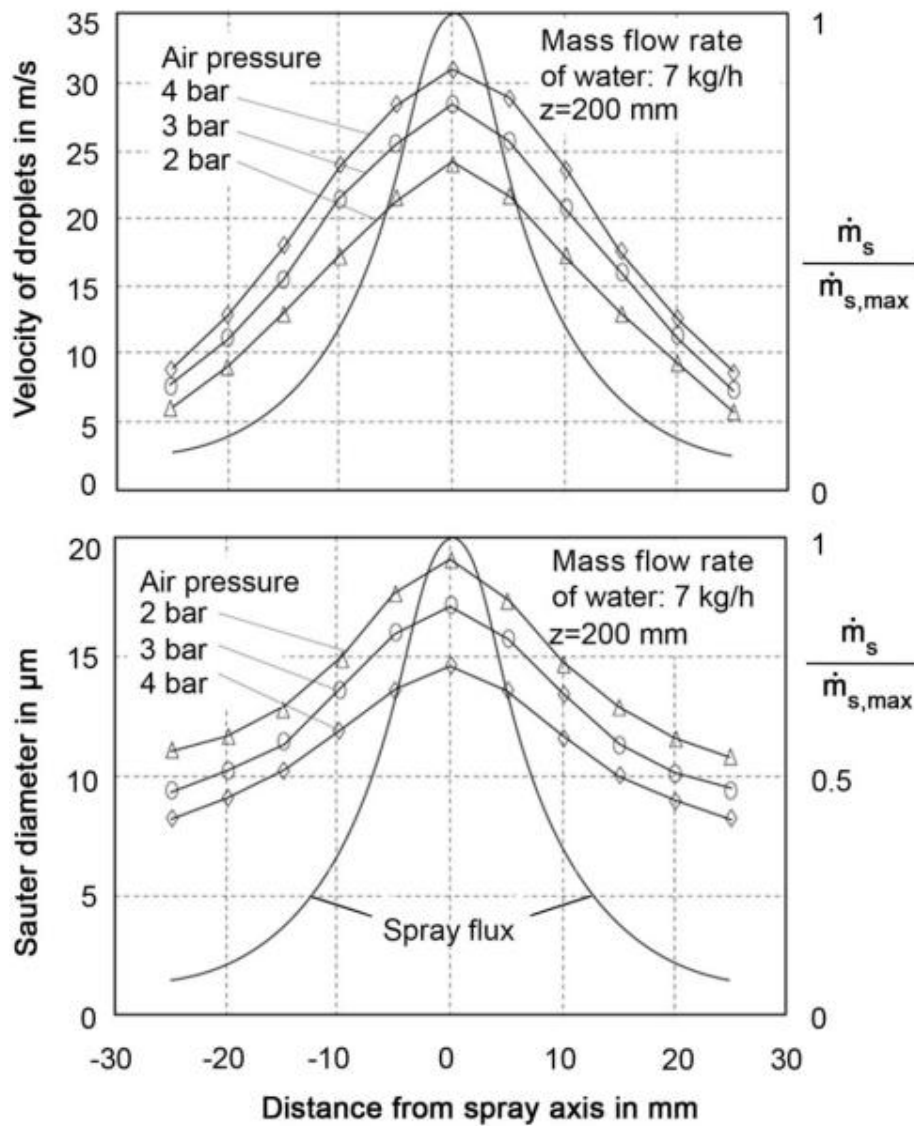


Figure 2.9: Influence of the air pressure on the spray characteristics of pneumatic full cone nozzle (Specht, 2017)

As the spray angle remains unchanged, the distribution of the spray flux, normalized to the maximum value on the axis, is consistent across all air pressures. The droplet velocity is highest along the spray axis and gradually decreases toward the edge, with the central-to-edge velocity ratio being approximately 5:1. Similarly, the droplet diameter is largest on the spray axis and diminishes toward the edge, although the differences are relatively minor. Increasing the air pressure results in smaller droplet sizes.

Figure 2.10 shows the spray flux variation of two flat sprays 40 mm apart from each other.

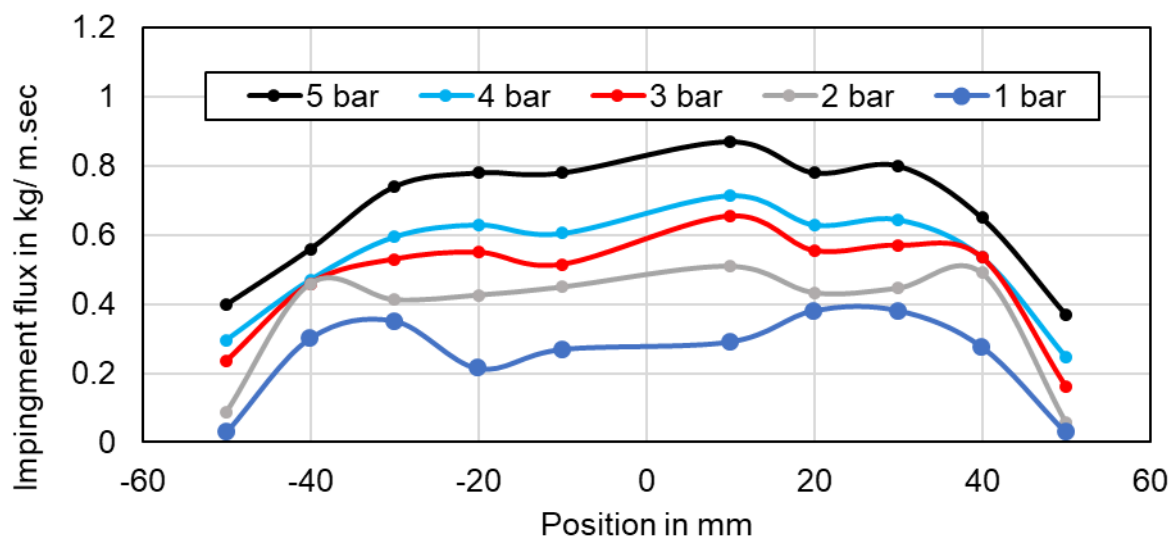


Figure 2.10: Spray flux distribution of two flat spray nozzles 40 mm distanced apart from each other at various water pressures

An increase in water pressure raises the spray impingement flux and the homogeneity of spray flux across the spray axis improves as well.

Figure 2.11 shows the distribution of impingement flux in a spray nozzle field of three pneumatic flat spray nozzles.

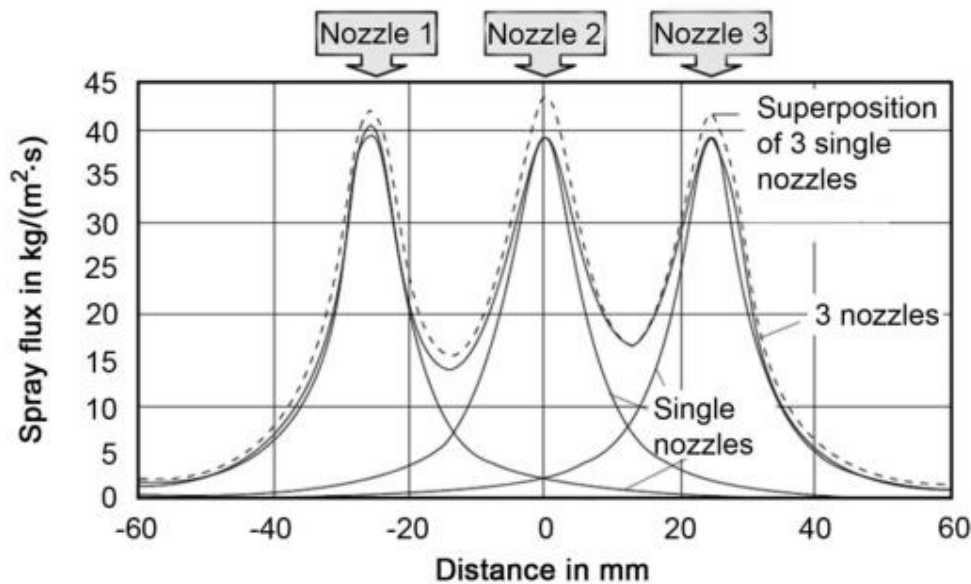


Figure 2.11: Distribution of the spray flux in a nozzle field (Alam et al., 2008)

Three nozzles are arranged in a line with a distance of 35 mm between them. The impingement flux is more uniform along the spray axis compared to a single nozzle, which improves uniform cooling and avoids variation in large thermal gradients and cooling rates.

2.3.2 Heat Transfer Mechanism and Influencing Parameters

During contact, heat is conducted from the hot surface to the water. When the water at the contact point reaches 100 °C, vapor is formed, causing the droplet to be ejected from the surface. Due to the brief contact duration, the surface appears dry to the eye. Heat transfer is higher, when more droplets impinge on the surface. If the surface temperature drops below the Leidenfrost temperature, the droplets remain adherent. As the water flux is highest along the jet axis, surface wetting begins there and then progresses radially.

Figure 2.12 illustrates the advancing wetting front when a metal disc is sprayed with water, the central area is quenched below the boiling temperature first. The water adhering to the surface flows radially.

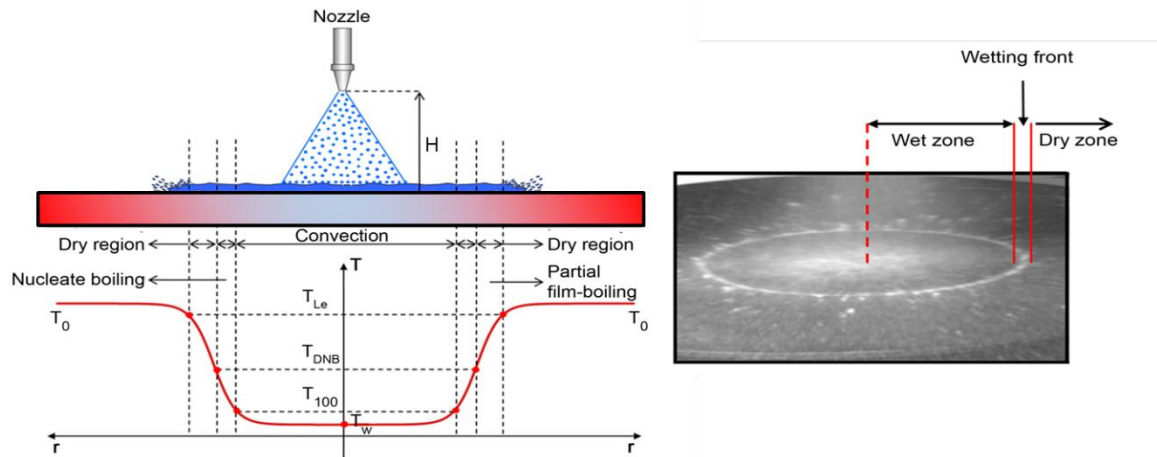


Figure 2.12: Schematics of heat transfer and propagation of wetting front in spray cooling (Specht, 2017)

At the radius, where the surface reaches the boiling temperature, vapor bubbles form. This vapor formation continues until the Leidenfrost temperature is reached, at which point the water is splashed away, forming droplets on the surface, leaving the adjacent area dry. The range of nucleate and film boiling is relatively small, as shown in the figure. This advancing wetting front moves radially with decreasing velocity. Higher heat transfer rates result in a faster moving wetting front.

Figure 2.13 shows the temperature history during the cooling of the aluminum alloy plate with a single full cone nozzle.

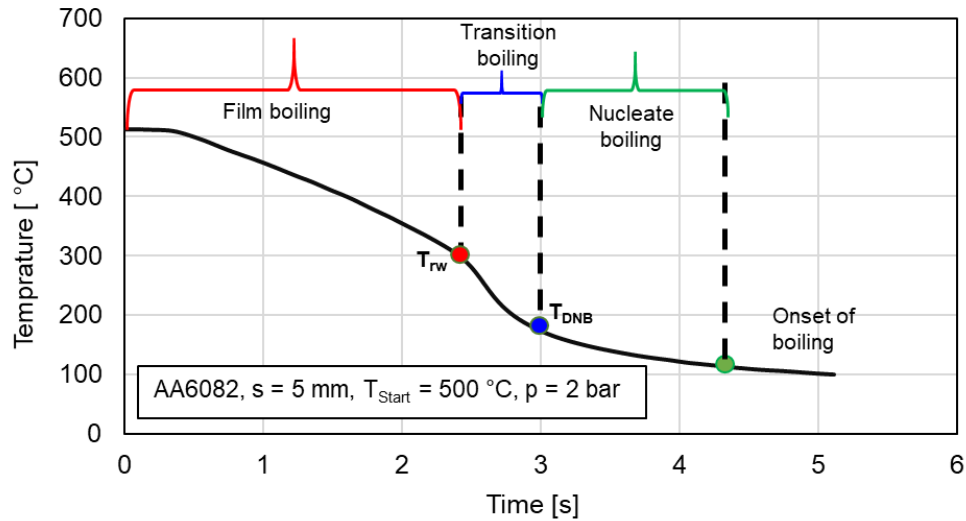


Figure 2.13: A cooling curve of AA6082 divided into four boiling regions

Initially, the temperature decreases at a very slow rate due to the low heat transfer rate characteristic of film boiling. As the liquid makes contact with the hot surface and the process transitions through the stages of transition boiling and nucleate boiling, a significant temperature drop occurs due to the intense heat extraction rate. During single-phase convection, the cooling effect is reduced, as boiling is not involved.

Beyond the spray flux, multiple factors play pivotal roles in shaping the heat transfer dynamics. This includes the temperature and quality of the quenching medium, start temperature and type of metal, nozzle to surface distance, nozzle type, and the thickness of metal. Interestingly, the size of the droplets exhibits minimal impact on the heat transfer efficiency, while the velocity of the droplets demonstrates a relatively modest influence. The subsequent sections delve into a comprehensive examination of these varied influencing variables.

Influence of Spray Flux

The heat transfer in spray quenching is primarily influenced by the spray flux, which refers to the amount of water droplets impacting the surface per unit area and time.

Figure 2.14 presents the boiling diagram for nickel, highlighting the spray flux as a key parameter.

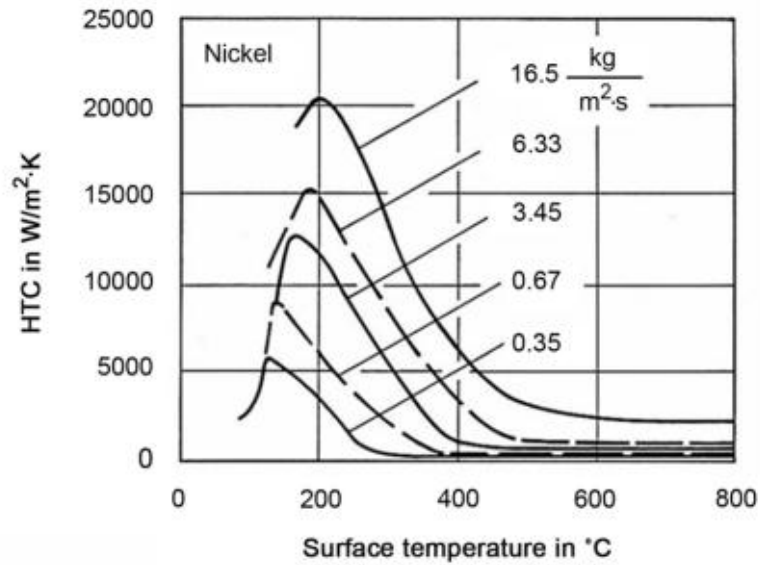


Figure 2.14: Influence of spray on the boiling curve for nickel (Müller and Jeschar, 1983)

The diagram reveals that an increase in spray flux not only enhances the heat transfer coefficient but also shifts the Leidenfrost temperature and the temperature corresponding to the maximum heat flux to higher values.

Figure 2.15 shows the DNB temperature for various metals with varying spray flux.

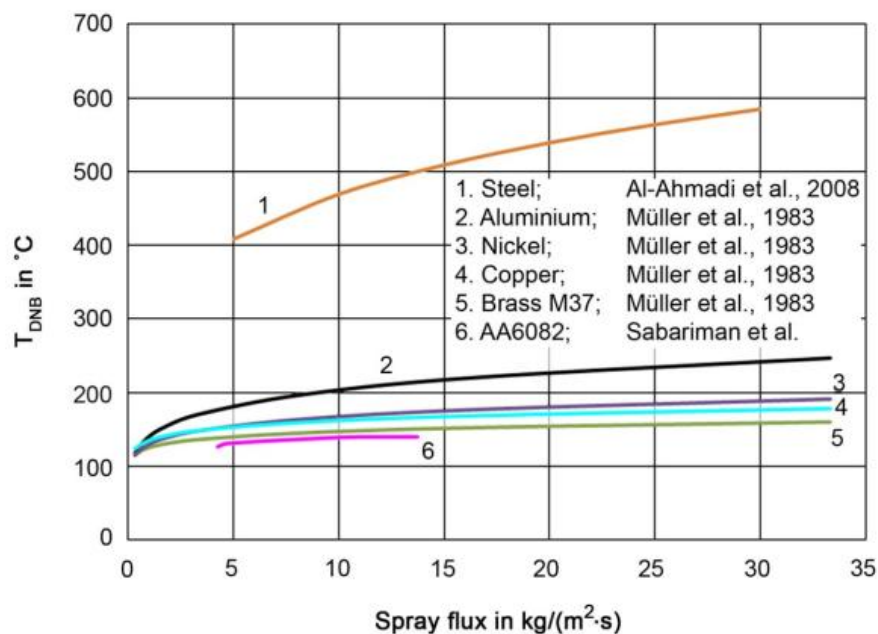


Figure 2.15: Influence of spray flux on the DNB temperature (Specht, 2017)

As the spray flux increases, the DNB temperature shifts to higher temperatures for all metals.

Influence of Water Temperature

The temperature of the cooling water varies seasonally in the industry. The heat flux transferred from the cooled surface is directly correlated with the temperature differential between the cooled surface and the cooling water. Additionally, the thermophysical properties of water depend on temperature viscosity, and surface tension particularly decreases as water temperature increases and influences the heat transfer on the metal surface.

Figure 2.16 shows the impact of the water temperature on the DNB temperature, rewetting temperature, and the maximum heat flux.

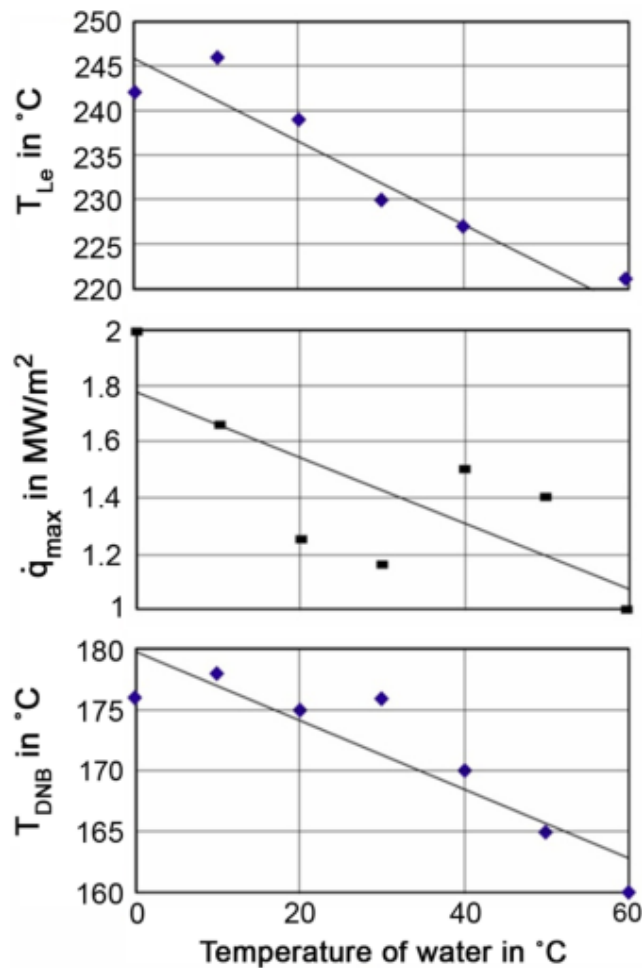


Figure 2.16: Influence of water temperature on DNB, T_{Le} , and maximum heat flux (Specht, 2017)

It can be seen that all values decrease approximately linearly with increasing water temperature.

The influence of water temperature on the heat flux is shown in Figure 2.17.

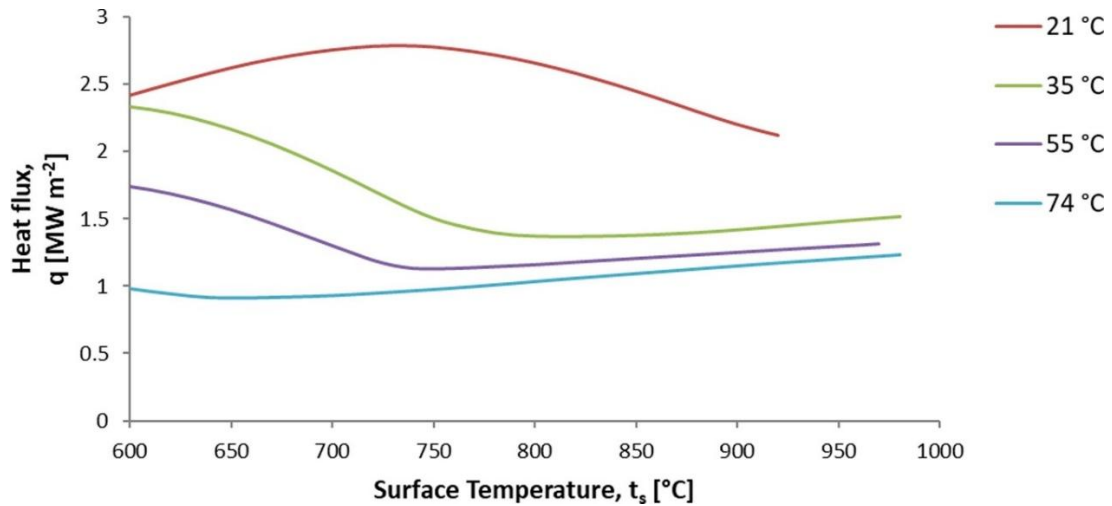


Figure 2.17: Influence of water temperature on the heat flux (Kotrbaček et al., 2022)

The heat flux decreases with increasing water temperature.

Influence of Water Quality

The presence of salts in water influences the heat treatment process. The presence of salts leads to an earlier collapse of vapor film as a result elevated Leidenfrost temperatures can be obtained. Figure 2.18 shows the effect of various salt concentrations on the boiling curve of aluminum alloy (AA6082).

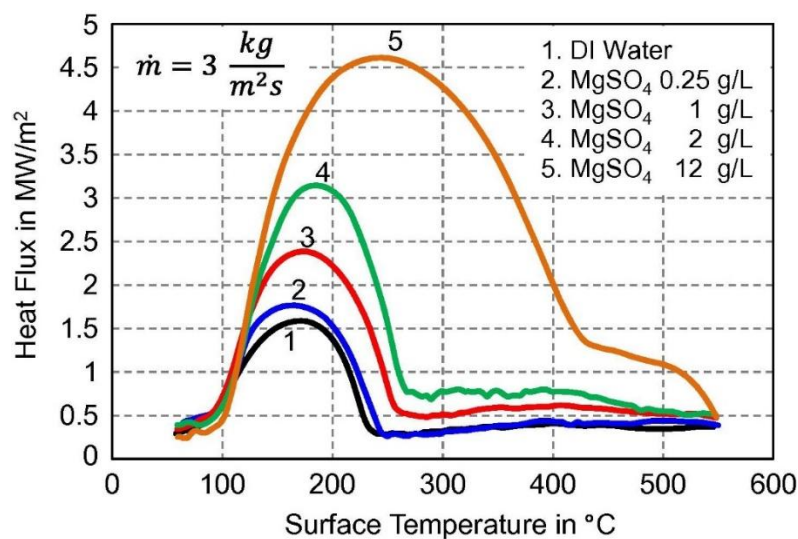


Figure 2.18: Influence of concentrations of MgSO_4 for AA6082 cooling (Abdallah et al., 2014)

It can be seen that higher salt concentrations shorten the film boiling. As a result Leidenfrost temperature as well as maximum heat flux increases (Abdallah et al., 2014).

Additional Parameters

In addition to the aforementioned spray parameters, various other factors exert an influence on the heat transfer phenomenon in the course of the cooling process. Among these factors are the distance between the nozzle and the surface, the type of spray nozzle employed, the nature of the metal, the thickness of the metal, the initial temperature, the angle of inclination of the nozzle, the velocity of the plate, and so forth (Aamir et al., 2014). Many studies have been focusing on some of these parameters. (Cebo-Rudnicka et al., 2016) investigated the impact of spray cooling parameters on the heat transfer coefficient for brass. It was determined in the research, that the heat transfer on the cooled surface is influenced by the water pressure, while the heat transfer coefficient decreases as the nozzle-to-surface distance increases. A phenomenon where the film boiling region is prolonged due to a rise in initial temperature was noted. (Stark et al., 2011) determined, that heat transfer coefficients are proportional to water impingement density. (Freund et al., 2007) investigated heat transfer coefficients for single and four nozzle arrays using IR thermography. (Yang et al., 2012) studied the effect of spray angle on the spray cooling of extruded aluminum alloy numerically. The results showed, that increasing the angle enhances surface temperature uniformity and cooling efficiency. (Nayak et al., 2018) Investigated the influence of air-water pressure, water flow rate, nozzle-to-surface distance, and impingement density on the cooling of stationary steel plates experimentally.

At the Otto von Guericke University Magdeburg, practical experience in the cooling of metals has been investigated since 2011, focusing on the influential variables affecting cooling processes using various nozzle configurations and molds. Initial studies involved experiments with smaller nickel samples, progressing towards larger metal samples of different thicknesses and materials. (Umair Alam, 2011) conducted a study focusing on spray and mold interactions during quenching using nickel and aluminum alloy. Two types of sprays were utilized: pneumatic spray (water, air) and hydraulic spray (water). The study highlighted the significance of the spray impingement flux in altering heat transfer rates in both types of sprays. Additionally, salts were introduced

into deionized water to explore the impact of salinity on heat transfer with the spray nozzles, revealing that salt additives enhance heat transfer in film, transition, and nucleate boiling. Furthermore, molds were employed for quenching the hot plate, utilizing two types with different numbers and diameters of orifices. The investigation continued with (Abdallah, 2012) studying the influence of salinity using hydraulic spray nozzles. Their results showed that heat flux, DNB temperature, and rewetting temperature increased linearly with salt concentration. The surface roughness was also examined using samples with varying roughness values, indicating that higher roughness levels decrease the cooling rate. Moreover, an optimal water jet velocity range was identified for quenching hot surfaces using molds. (Sabariman, 2015) proposed a theoretical model for predicting the heat flux during film boiling when a spray nozzle is utilized. Incorporating factors such as droplet size, velocity, spray flux, surface and water temperatures, and salinity level. The model's accuracy was validated through comparisons with experimental results from different sources, demonstrating its ability to capture the influence of these factors during film boiling. Investigations on quenching with molds were also conducted with stationary and moving mold. (Kulkarni, 2019) further investigated the effect of various parameters such as water quality and temperature, jet velocity and angle, metal thickness, casting speed, initial temperature, and kind of metal on the cooling of moving plates using mold. It has been observed that heat transfer in the free-falling zone is more influenced by variations in parameters compared to the impingement zone. (Fang, 2019) investigated the cooling of metals using jet, flat spray, and full cone nozzle. Additionally, nozzle fields consisting of full jet nozzles are employed with varying parameters in a stationary case.

A full-cone nozzle has been experimentally investigated in the past at Otto von Guericke University Magdeburg and many studies discussed the heat transfer of a single full-cone nozzle. The influence of various parameters, like metal thickness, nozzle pressure, surface roughness, etc. on the cooling of vertical plates was gained practically. However, the cooling mechanism of stationary and moving horizontal plates using a single full cone nozzle and a field of full cone nozzles has not been studied so far. Additionally, there are few studies available on flat spray quenching with moving plates. This study focuses on the cooling of stationary and moving metals using single and array configurations of full cone nozzles. It examines the influence of various

parameters, including metal type, metal thickness, initial temperature, volume flow rate, nozzle-to-plate distance, nozzle-to-nozzle distance, nozzle inclination angle, and plate velocity on the cooling process.

3 Experimental Setup

3.1.1 Quenching of Horizontal Plates

The experimental setup for quenching of horizontal plates using full cone nozzles from top and bottom side cooling is shown in Figure 3.1 and Figure 3.2.

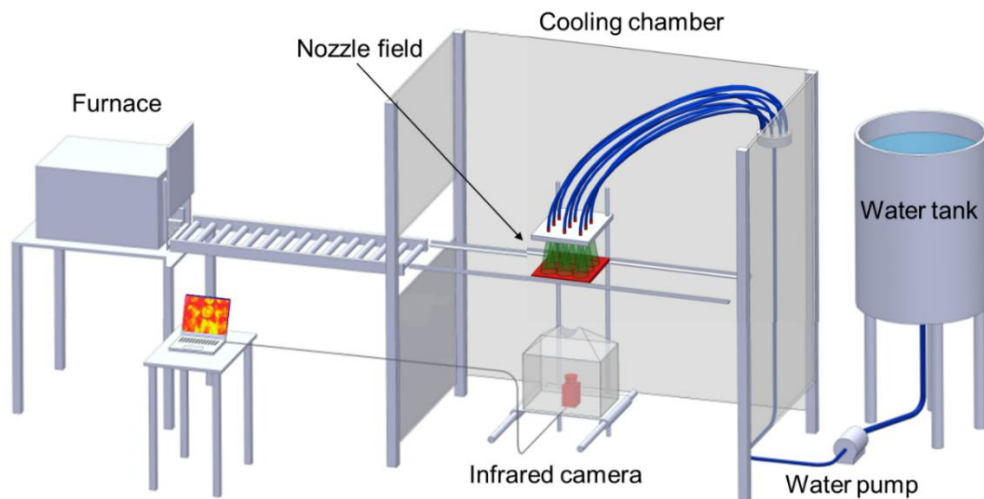


Figure 3.1: Schematic diagram of the experimental setup for quenching horizontal plates (Top side cooling)

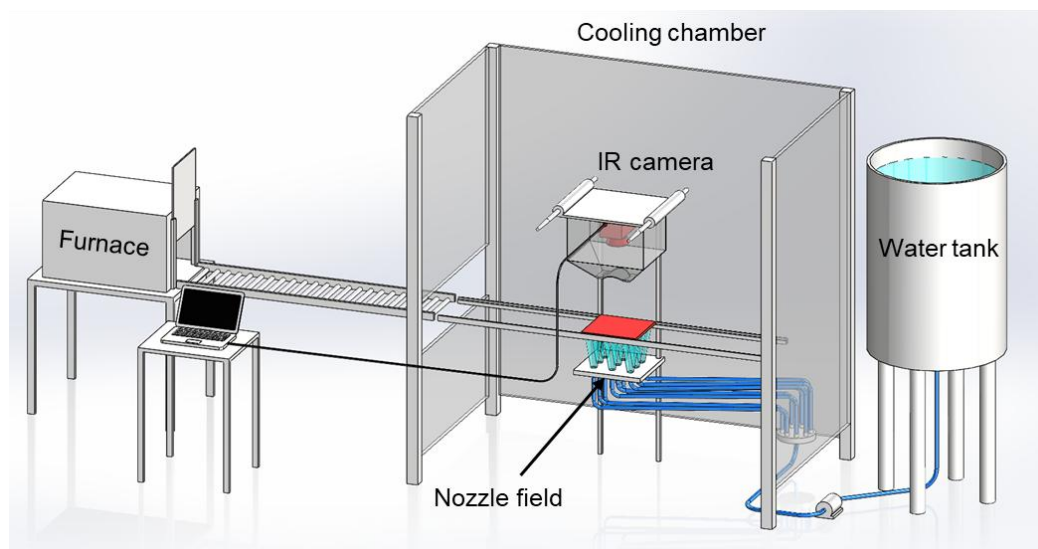


Figure 3.2: Schematic diagram of the experimental setup for quenching horizontal plates (Bottom side cooling)

The major components of the setup are an electric heated laboratory furnace, a cooling chamber, and an infrared camera. The electric furnace offers robust heating with a power rating of 10 KW. Engineered for optimal performance, it operates at a recommended nominal voltage of 400 V within a frequency range of 50-60 Hz. Designed for a current of 32 A, the furnace incorporates 14 strategically positioned spiral heating coils embedded in ceramic plates, 8 on the bottom surface and 6 on the top. Metal samples undergo heating through radiation heat transfer within the furnace. Enhancing its thermal efficiency, an additional layer of calcium silicate plates reinforces the furnace, renowned for their stability, reduced thermal conductivity, and easy replacement, effectively minimizing heat loss through the walls. To facilitate the experimental process, a ceramic plate holder frame is located inside the furnace, allowing for the convenient manual placement and removal of metal plates. The furnace is equipped with an adjustable thermocouple for precise temperature measurement. External regulation is achievable through its connection to a controlling unit, complemented by a mounted touchscreen display. It is capable of heating plates up to 1200 °C with an automated front door, which provides access to a foldable conveyor belt.

The cooling chamber consists of aluminum frames and transparent PVC sheets. It protects the other components from water droplets and vapors. Positioned adjacent to the left exterior corner of the quenching chamber, a folded conveyor belt seamlessly connects the furnace to the chamber. This purposeful conveyor belt serves as a guiding mechanism for hot metal samples, facilitating their smooth transition into the chamber for the quenching process. Inside the cooling chamber, on the top side is an adjustable nozzle holder, where investigated nozzles can be easily mounted for experiments.

The experimental setup involves positioning an infrared camera on the ground directly beneath the hot plate, aligning its focus with precision. To safeguard the camera from potential interference caused by splash water, it is securely housed within a protective chamber located at the bottom of the apparatus. This precaution ensures the uninterrupted functionality of the infrared camera during the experimental procedures.

As an infrared camera, "ImagelR® 8800", designed by "InfraTec GmbH" was used. With this high-speed advanced camera, the cooling process of heated plates can be

accurately measured, ranging from 850 °C to below 100 °C in a single pass. The measured data is stored in a computer connected to the infrared camera.

The specific characteristics of the infrared camera are listed below in Table 1.

Table 1: Specific characteristics of the infrared camera

Infrared camera ImageIR® 8800	
Detector resolution (IR pixel)	640 x 512
Measuring range	100 – 850 °C
Measuring accuracy	± 1 °C or $\pm 1\%$
Focus	Manual / Automatic
Frame size	200 per sec
Water-resistant	IP54
Detector cooling	Sterling cooler

Quenching of horizontal plates is performed using a full cone nozzle and a field of full cone nozzles. Two Lechler full cone nozzles with a spray angle of 45° are employed for experiments, named nozzle type A (490.403), and B (490.523).

A full cone nozzle covers the entire circular impact area and distributes the droplets in the form of a circle, as shown in Figure 3.3

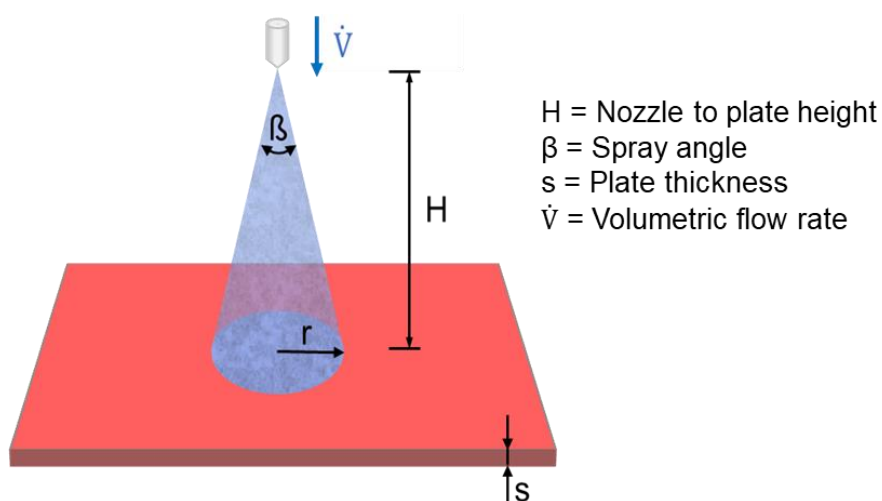


Figure 3.3: Schematic representation of impingement of a full cone nozzle

The quenching experiments have been conducted and the influence of process parameters like metal thickness, metal type, nozzle pressure, start temperature, and nozzle height is investigated. Table 2 shows the list of parameters which are varied during this study.

Table 2: Parameter variations for quenching of horizontal plates

Parameter	
Nozzle type	Single full cone / Nozzle field
Nozzle configuration	Inline / Staggered
Nozzle to nozzle distance b	35 / 70 mm
Nozzle position	Top side / Bottom side
Nozzle height H	63 / 84 / 127 mm
Nozzle pressure p	2 / 3 / 6 / 9 bar
Plate thickness s	2 / 5 / 8 / 10 mm
Start temperature T_{start}	500 / 700 / 800 °C
Plate velocity w_p	0 / 30 / 45 / 60 / 75 / 85 / 110 mm/s
Metal type	Aluminum alloy (AA6082) / Nickel

The table above illustrates the variation of the parameters during experiments conducted with full cone nozzles. Notably, the adjustment of parameters such as nozzle-to-plate height (H) and nozzle-to-nozzle distance (h) influences the interaction of circular wetting fronts generated by the sprays in a nozzle field.

Figure 3.4 shows the schematics of the nozzle field consisting of nine full cone nozzles at various nozzle-to-plate heights at nozzle-to-nozzle distances of 35 mm and 70 mm.

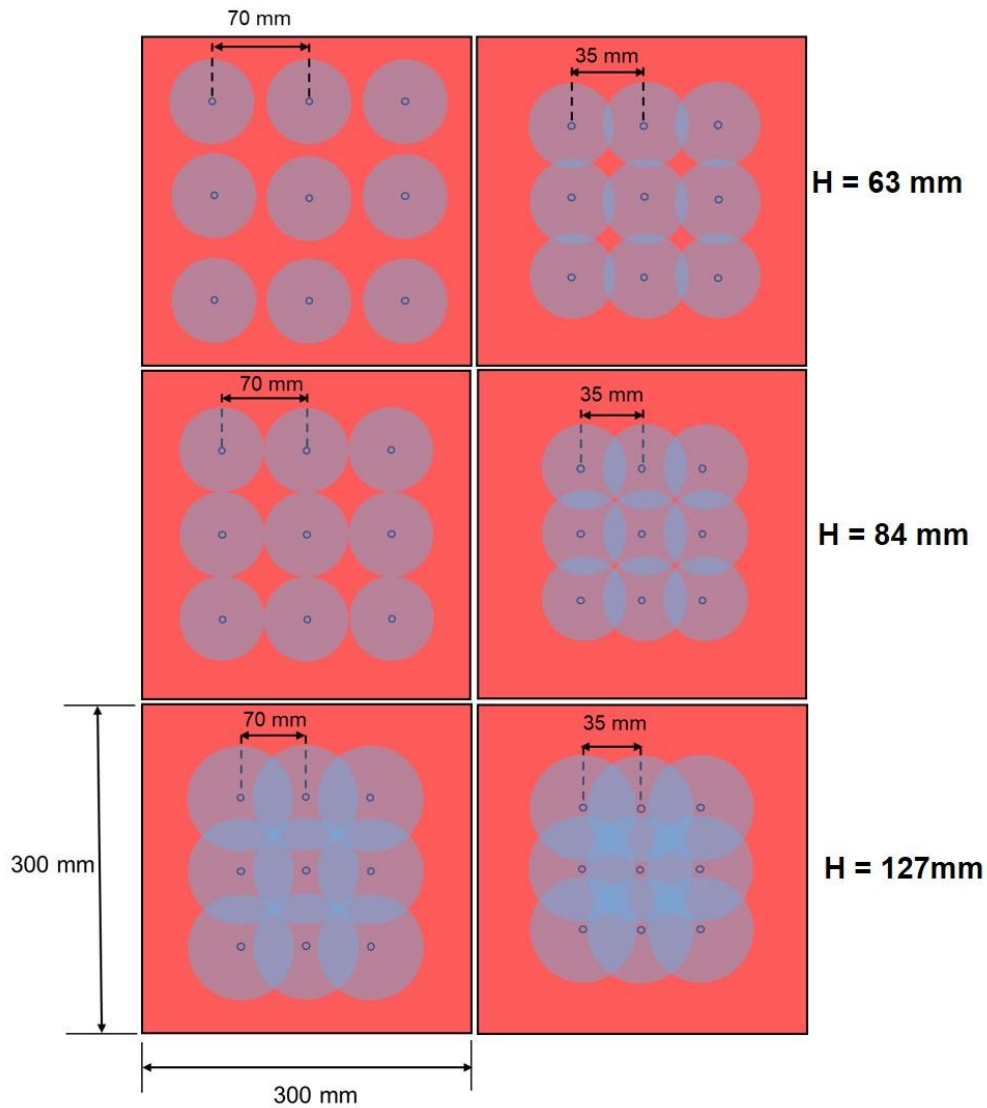


Figure 3.4: Schematic representation of various nozzle-to-plate and nozzle-to-nozzle distances

As the nozzle-to-plate height increases, the circular impact areas expand. Specifically, when the nozzle-to-plate height is $H = 63$ mm and the nozzle-to-nozzle distance is $b = 35$ mm, the nozzles overlap, creating an interaction between the sprays. Conversely, at $b = 70$ mm, the sprays do not interact, indicating a separation between the circular wetting fronts. Certainly, at $H = 84$ mm and $b = 70$ mm, the spray circles touch each other. Conversely, at $b = 35$ mm, where the nozzles are closer to each other, a strong overlapping occurs. These variations in nozzle-to-plate and nozzle-to-nozzle distances result in different levels of interaction among spray circles. This interaction and overlapping significantly impact the flow dynamics and turbulence of water on the surface of the plate. The changes in distance parameters contribute to

altering the behavior of the water sprays and their effects on the target surface during the experimental process.

Figure 3.5 illustrates the schematics of an inline field consisting of nine nozzles and a staggered field with seven nozzles. Figure 3.6 shows the nozzle configurations with full cone nozzles employed in experiments.

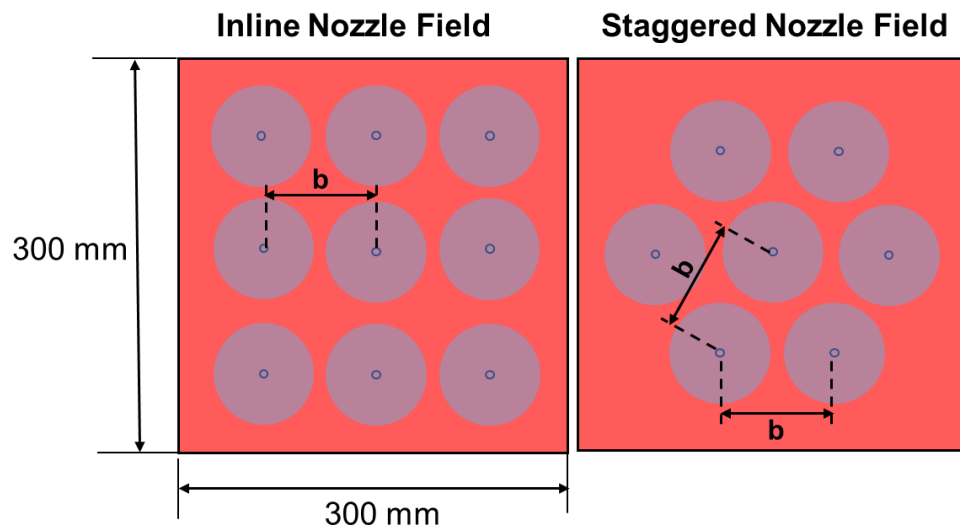


Figure 3.5: Schematics of inline and staggered nozzle fields

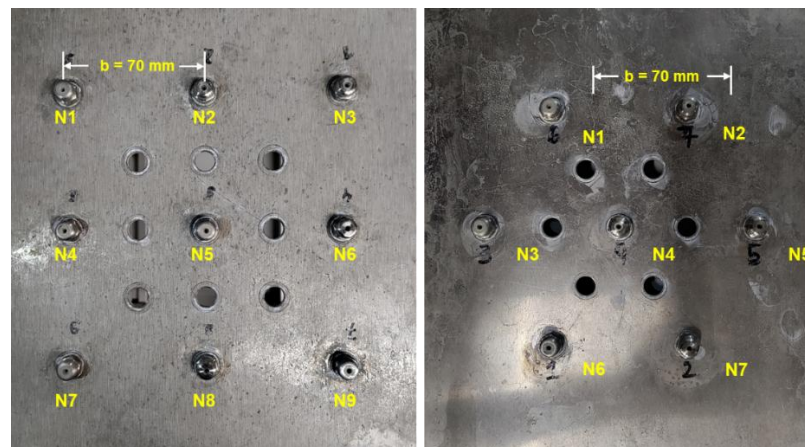


Figure 3.6: Inline and staggered configuration of full cone nozzles

3.1.2 Quenching of Vertical Plates

Figure 3.7 illustrates the experimental setup, in which hot, vertically moving metal plates are quenched from high temperatures by two flat sprays.

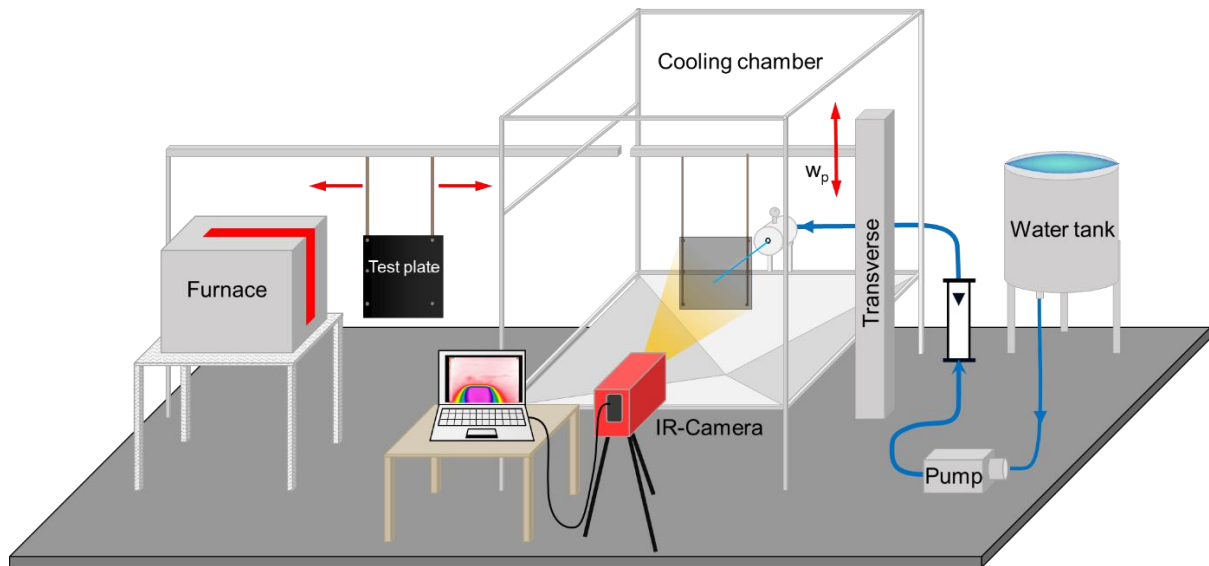


Figure 3.7: Schematic diagram of the experimental setup for quenching vertical plates

As the previously described setup, it can also be divided into three main components; an electric furnace electrically heated laboratory furnace, a cooling chamber, and an infrared camera. To heat the metal plates to the desired start temperature an electrically heated laboratory furnace with a heat intensity of 1 kW is used. The heating is done by 10 heating coils that are installed in the ceramic fiber boards. The furnace is insulated with low thermal conductivity calcium silicate plates, to minimize heat losses. Within the electric furnace, two internal temperature sensors are strategically placed to precisely measure the actual temperature. A display is mounted on the outside of the furnace, which provides real-time temperature feedback and can be used for setting the target temperature. The furnace reaches the desired temperature within approximately two hours.

A similar cooling chamber used for the horizontal cooling out of aluminum struts and transparent PVC sheets is used. The PVC sheets protect the sensitive measuring component of the infrared camera from the splashing water and the produced vapors during the quenching process. The nozzle head is mounted inside the cooling

chamber, whose height is easily adjustable. Different nozzle types and nozzle fields can be installed using the nozzle head or holder.

Adjacent to the cooling chamber, a traverse system is strategically positioned. The traverse is equipped with a guide rail, enabling the controlled vertical movement of heated plates. The metal sheets are effectively cooled by water-carrying nozzles, ensuring precise and efficient quenching processes. The same infrared camera “ImageIR® 8800” designed by “InfraTec GmbH” is used to measure temperatures in the quenching process of vertical plates as in the investigation of horizontal plates.

For the experimental investigation of vertical plates, a spray field of two flat sprays 35 mm apart from each other is used. The flat spray is characterized by the spray angle (β), spray width (b_s), and impacting length (B), which forms a rectangular-shaped liquid film on the moving hot plate of the thickness (s) with velocity (w_p) as shown in Figure 3.8.

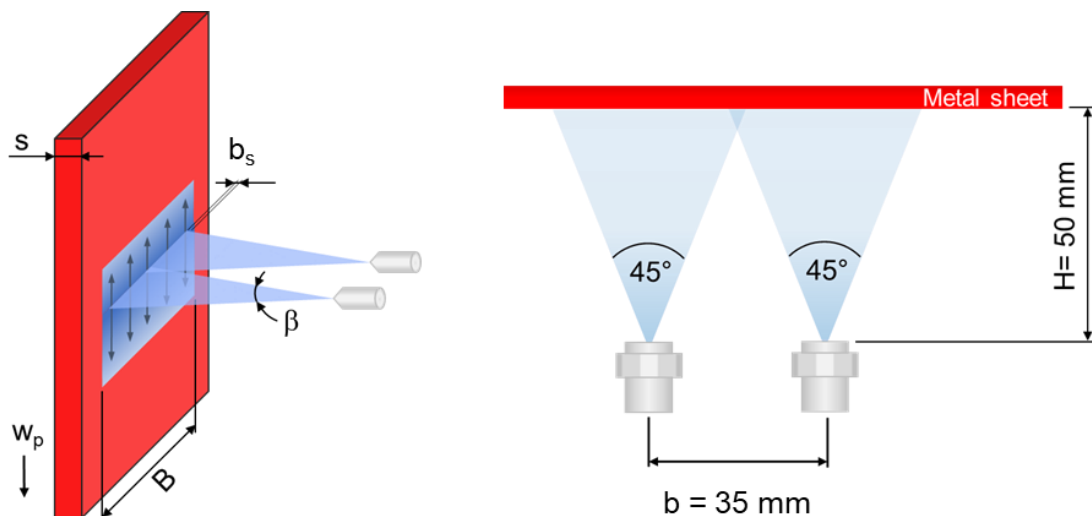


Figure 3.8: Schematic representation of two flat sprays

Magdeburg tap water with a temperature of 22 °C is used for the experiments.

Table 3 depicts the varied parameters for this study.

Table 3: Parameter variations for quenching of vertical plates

Parameter	
Nozzle type	Flat spray (Lechler, 632.403)
Nozzle pressure p	2 bar
Nozzle inclination angle α	45 / 65 / 90 °
Plate thickness s	2 / 5 mm
Start temperature T_{start}	500 / 800 °C
Plate velocity w_p	5 / 10 / 15 mm/s
Metal type	Aluminum alloy (AA6082) / Nickel / Nicrofer

3.2 Experimental Procedure

The metal samples of various thicknesses and dimensions are repeatedly used during the experiments. For each experiment, the plates are straightened with the help of a straightening machine. Afterward, the plates are cleaned with acetone to obtain a dust and deposited salt-free surface. As the temperatures of quenched plates are measured using an infrared camera, it is necessary to coat one side of the metal plates, facing the camera (Measuring side) with a black paint of known emissivity. For coating, a matt black thermal paint “Ulfalux” is used. After a drying phase of 24 hours, the metal plates are ready for experiments. Figure 3.9 shows the quenching and the measuring sides of the prepared metal plates for an experiment. The measured emissivity and its high-temperature stability can be found in chapter 3.4.1.

The standardized procedure for each experiment remained consistent during the study. The procedure was started by activating the furnace and configuring the desired temperature. The set temperature on the kiln is adjusted always to 50 °C higher than the desired start temperature. This temperature difference is essential to accommodate the heat losses during the plate transportation from the furnace to the cooling chamber. Subsequently, the lab computer was initiated, and the infrared camera was positioned. The infrared camera was connected to the lab computer through “IRBIS3 Professional” software, where the emissivity of the black coating, measuring range, and ambient temperature were defined. Before heating the metal

plate, it was moved into the cooling chamber, to set the focus of the infrared camera on it, to obtain thermal images with higher accuracy.

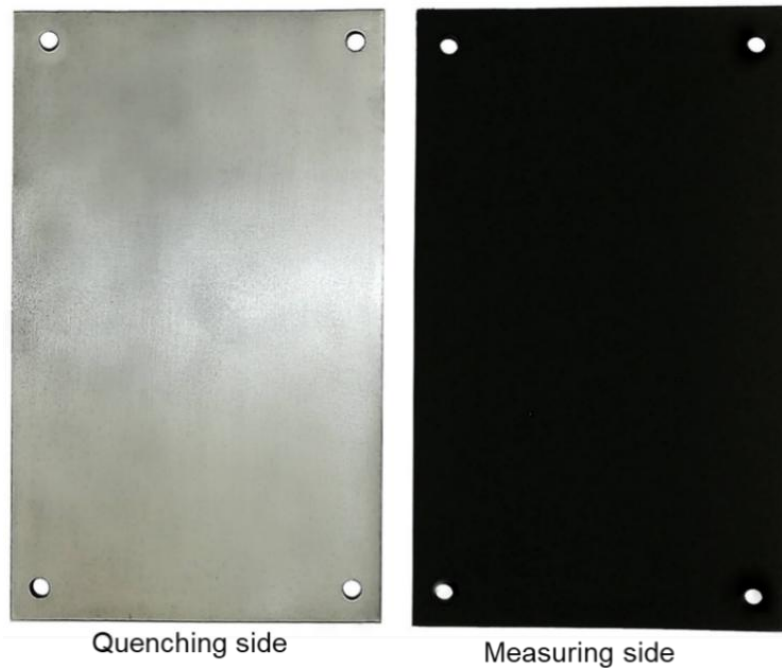


Figure 3.9: Measuring and quenching side of a 2 mm AA6082 plate specimen

Once the furnace reached the desired temperature, the material sample was introduced into it. Meanwhile, to initiate the cooling system, the water tank was filled, and the pump was activated. Ensuring proper functionality, water was supplied to the nozzles for a preliminary test, and the nozzle pressure was finely tuned by adjusting the pump speed.

Approximately 15 minutes later, the heated metal plate was carefully guided into the cooling chamber, where it was positioned in front of the nozzle head. A protective plate was maintained between the nozzles and the heated material sample to ensure controlled cooling. The actual temperature of the metal plate was carefully monitored on the measuring computer. The protective sheet was removed quickly as the measuring computer showed the desired start temperature of the metal plate and the metal plate was quenched under controlled conditions. Simultaneously, the temperature data of the quenched plate was measured and recorded with the help of the high-speed infrared camera and measuring computer.

For moving plates, the same approach and procedure is applied, in which the removal of the protective sheet and movement of the plate was carried out at the same time. The velocity of the moving plate can be adjusted accurately. For horizontal plates, apart from the cooling of the top side of the plate, experiments were conducted in which metal plates were quenched from the bottom side by measuring from the top side respectively.

3.3 Measuring Technique

As mentioned above, an infrared camera is used to capture the temporal and spatial thermal data of metal plates during the cooling process. The infrared camera has many advantages over thermocouples, which are conventional means of temperature measurements. Measuring the surface temperatures on the quenching surface is quite challenging due to boiling phenomena. Thermocouples limit the spatial resolution because they can not be physically installed as close as possible to the quenched surface. Additionally, thermocouples may disturb the fluid dynamics on the surface or can not withstand harsh conditions during the heat and cooling process. The measured data from the camera was preliminarily analyzed using the "IRBIS® 3 professional" software. The thermal data is captured frame by frame in a thermal video. To initiate the analysis, the IRB files from the camera are imported into the software. By utilizing the expanding option, the entire video is expanded into individual frames.

Further, the data is filtered by identifying the start temperature and the first water contact on the thermal image. Throughout the experiment, a rectangular region is consistently delineated within the frames to denote the average temperature within that specific area. This rectangular region serves as a reference for the exact starting temperature (505 °C, 705 °C, or 805 °C) and is maintained consistent across all experiments. From the expanded frames of the recording, the frame where the anticipated starting temperature is observed is identified and selected as the initial frame of the recording. Subsequently, all frames above this selected frame are erased.

Afterward, the measuring line is drawn on the thermal video to extract the data throughout the experiment. The extracted data includes temperatures along the measuring line for the entire cooling time. Since the measuring line consists of individual pixel points, the pixel resolution can be utilized to estimate the precise

position in millimeters. This allows for accurate spatial referencing and analysis of the temperature data.

A thermal image of a 5 mm thick nickel plate is illustrated in Figure 3.10.

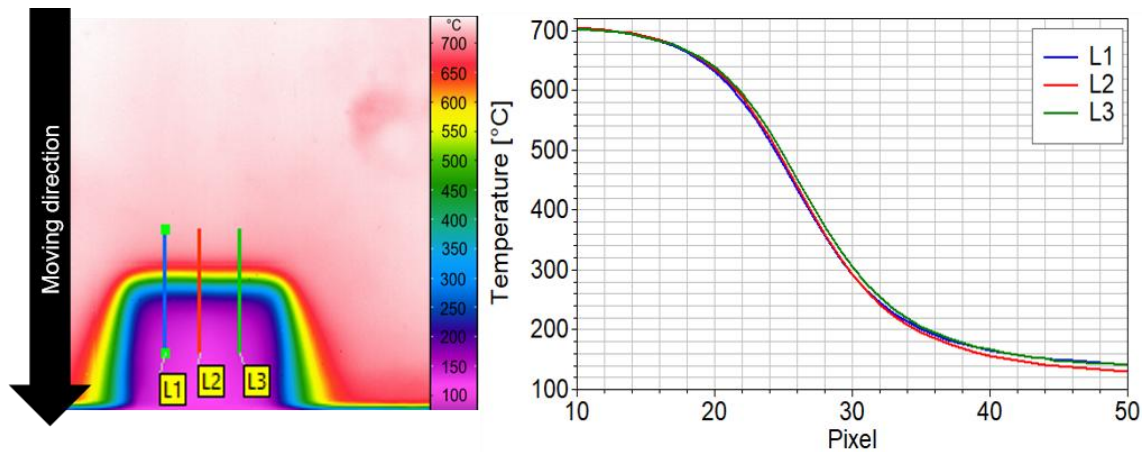


Figure 3.10: Thermal image (left) and corresponding cooling curve (right) of a 5 mm nickel plate

The plate is moved with a velocity of 5 mm/s and cooled with flat sprays. Its corresponding profile at the time instant, 10 s can be seen. For the extraction of temperatures during the cooling process, measuring lines L1, L2, and L3 are drawn. On the top side of the sheet, a high temperature near the start temperature of 800 °C is present, decreasing sharply as the wetting front or wetted region advances. Temperature profiles along these measuring lines exhibit a uniform and homogeneous cooling pattern, with all three profiles demonstrating similarity due to the propagation of the rectangular wetting front. For further analysis in the case of flat sprays, the measuring line is consistently drawn for all experiments in the middle of two interacting nozzles. This location corresponds to the maximum spray flux and, consequently, the highest heat flux.

Figure 3.11 shows IR images of a 5 mm nickel plate at various times during the cooling process.

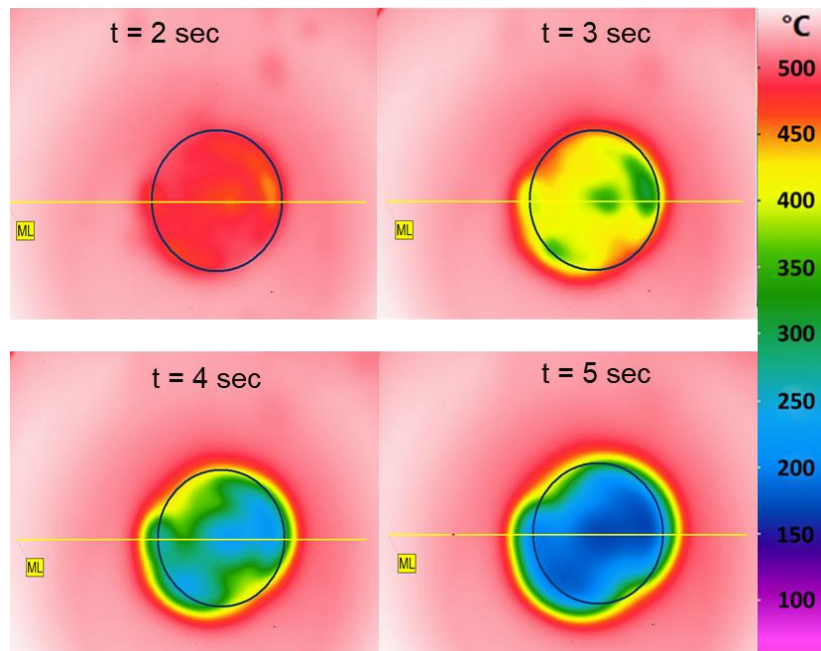


Figure 3.11: IR images of 5 mm nickel cooled with a single full cone nozzle ($H = 84$ mm)

A measuring line ML (yellow) is drawn on the center of the nozzle. IR images depict that nonuniform cooling happens at the start due to uneven water impingement flux of a nozzle, which will be shown in Figure 3.15. Once the cooling surpasses the film boiling region and reaches the rewetting temperature, a relatively uniform wetting front starts spreading in the form of a circle.

The temperature data of the cooling process as shown in the above figures in the form of thermal images is exported in the form of ASCII files. The ASCII files are comprised of all temperatures of pixels along the measuring line for each second during the whole cooling process. Further, these ASCII files are used in MatLab to obtain the temperature profiles along the position or width of the metal plate at all times.

Figure 3.12 shows the temperature profiles for quenching a 5 mm nickel plate.

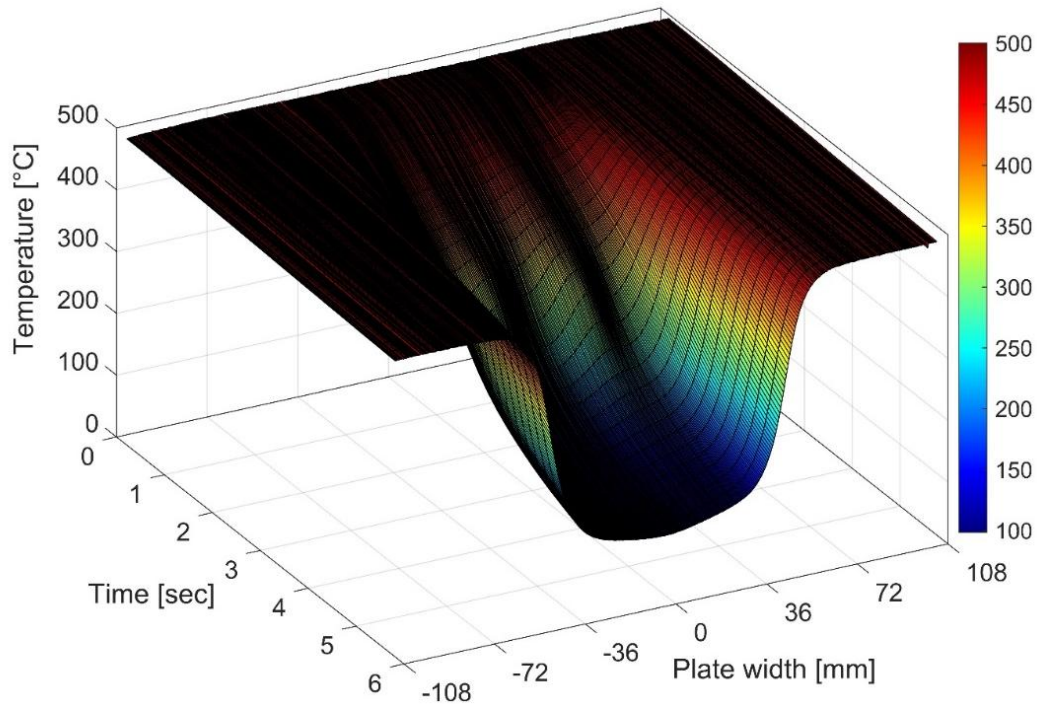


Figure 3.12: Extracted temperature data along the plate width during the cooling process

The center of the nozzle is indicated by 0 mm. In the time frame of 6 seconds, the metal plate cools from 500 °C to 100 °C. Further, extracted temporal and spatial temperatures are utilized in the inverse heat conduction model to obtain heat fluxes.

3.4 Preliminary Investigations and IR-Validation

3.4.1 Measurement of Surface Emissivity

In general, surface emissivity (ϵ) is characterized as the ratio of thermal radiation emitted by a real object to that of a black body at the same temperature. The black body serves as an ideal body, which absorbs irrespective of frequency all incident electromagnetic radiation. The emissivity of such a theoretical body is defined as 1. As this experimental work involves infrared thermography, precise knowledge, and determination of the surface emissivity of the used “Ulfalux” coating is necessary.

Incorrect emissivity values would significantly influence measurements, leading to distortion and inaccuracies. Therefore, the stability and the value of the emissivity

should be known as a function of surface temperature. To determine the emissivity of the black coating, experiments were conducted. The details of these experiments can be found in (Fang, 2019). Figure 3.13 shows the emissivity in dependence of the surface temperature.

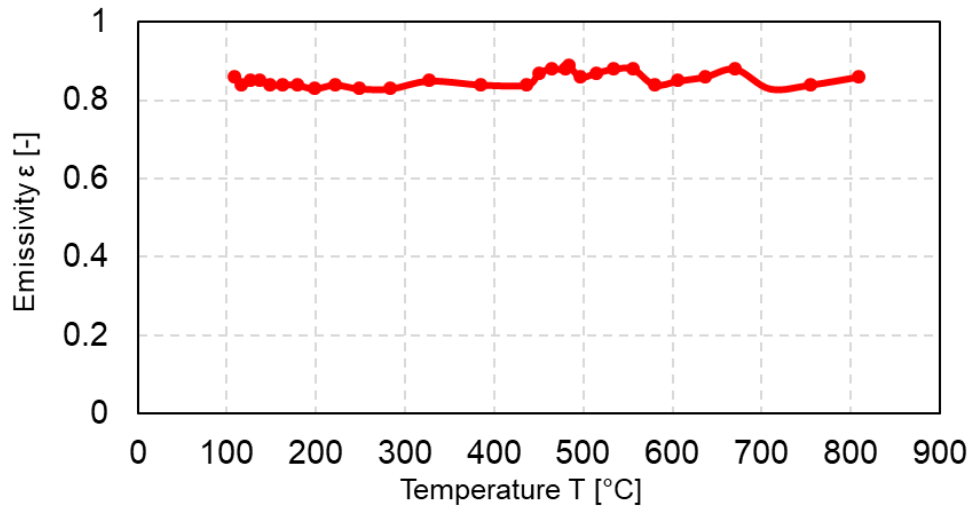


Figure 3.13: Dependence of thermal coating emissivity on temperature adapted from (Fang, 2019)

It is observed that, within the high-temperature range, fluctuations are relatively more pronounced compared to the low-temperature range for this particular infrared camera. Overall, the emissivity values are stable in the temperature range of experiments. Hence, a constant average value of emissivity of 0.85 was used for the measurement of surface temperatures during the cooling process.

3.4.2 Validation of Infrared Camera Measurements

A validation experiment was conducted to validate the IR camera measurements. In this experiment, a thermocouple was positioned 1 mm below the surface of a 10 mm stainless steel plate, and temperature profiles were compared with surface temperature recordings from the IR camera. With the sheet temperature held constant, the deviation between both measurements was within ± 1 K. During the plate cooling in ambient air, starting at 850 °C, a temperature difference of 11 K was observed between the thermocouple and IR camera measurements due to the depth of the thermocouple.

3.4.3 Measurement of Water Impingement Flux

For flat sprays, the volume flow rate serves as a key characteristic parameter. The total water volume flow rate is 2 L/min and it is directed onto a surface with a width of 80 mm. An essential factor influencing flat sprays is the impingement flux, including its local distribution. This factor is measured using a patternator, a device constructed and designed within the university. Figure 3.14 illustrates the schematics of the patternator and the impingement flux profile for two flat sprays at a constant pressure of 2 bar.

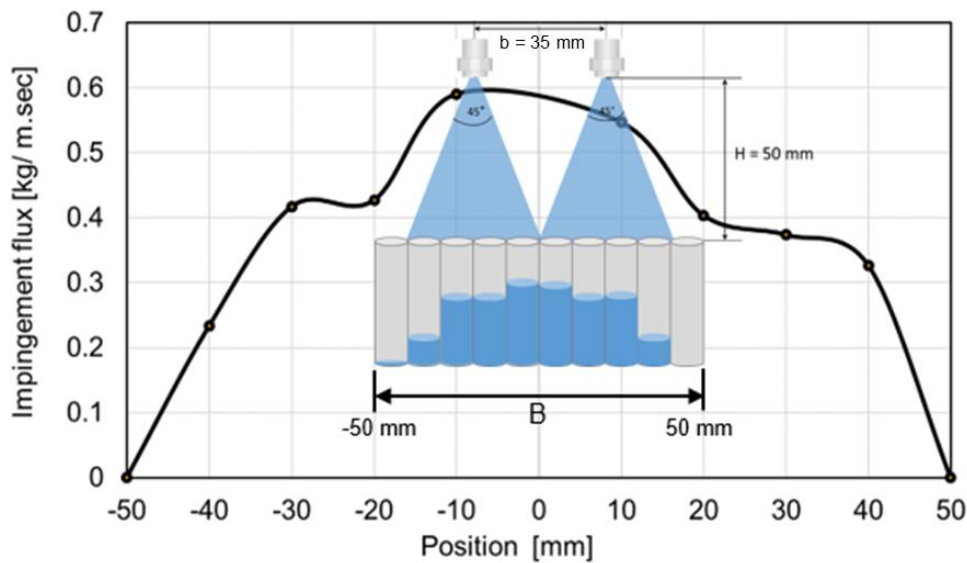


Figure 3.14: Impingement flux along the two flat sprays axis

The setup comprises nozzles mounted 35 mm apart from each other, facing downward, and positioned on a stand that can precisely move in all three dimensions with millimeter accuracy. Beneath the nozzles, a board features 10 mm small cylindrical tubes arranged in a linear array, each of 10 mm diameter, and connected to small water collecting bottles. The highest spray flux is achieved at the midpoint between the two sprays, owing to their superposition. Notably, within the range of -10 to 10 mm, the impingement flux attains its maximum and remains relatively stable. Consequently, during the processing of experimental data, the measuring line is strategically drawn along the center of the two sprays to ensure accurate representation.

The impingement flux is the main factor influencing the heat transfer of full cone spray nozzles, which is why the local distribution of the impingement flux has to be examined in more detail. For this purpose, experiments were conducted at the Institute for

Industrial Furnaces and Heat Engineering at RWTH University Aachen. A patternator with approximately 1330 measuring points has been employed to determine the impingement flux of individual nozzles and nozzle fields. More details about the experimental setup and the measuring method can be found in (Hof, 2023). For consistency, the tests in Aachen utilized identical spray nozzles and boundary conditions as those in the Magdeburg test series, ensuring a meaningful correlation of results.

Figure 3.15 shows the water impingement flux distribution of a single full cone nozzle (Nozzle type A) at a nozzle height of 63 mm for various nozzle pressures.

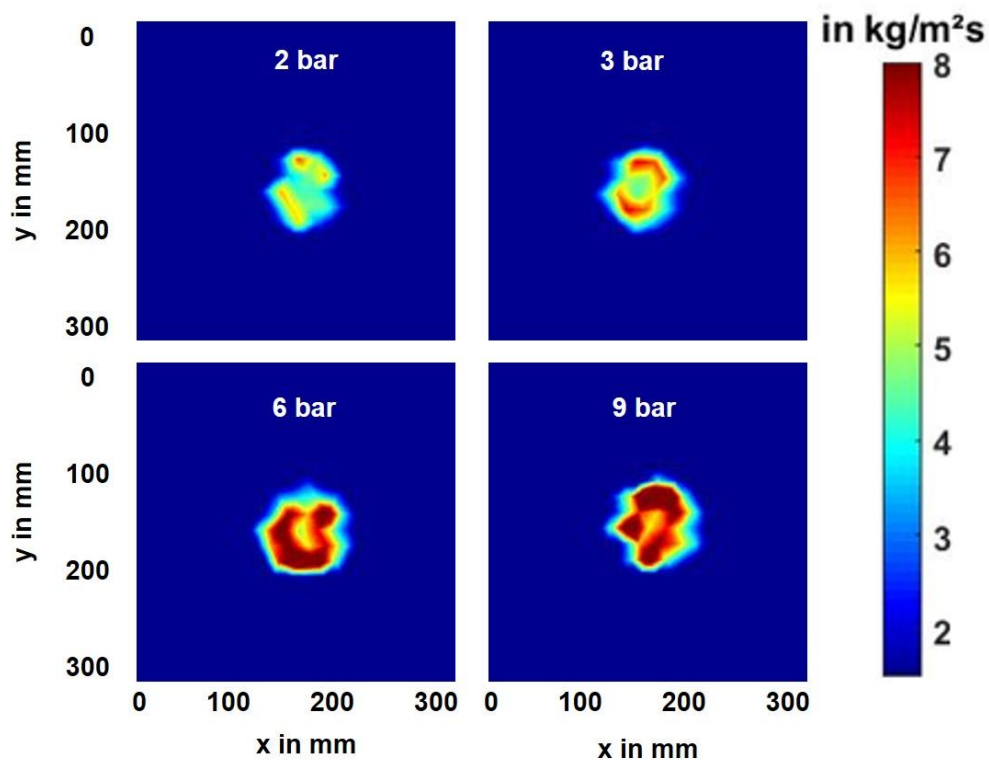


Figure 3.15: Water impingement flux distribution of single nozzle for various pressures ($H = 63$ mm) (Hof, 2023)

It is evident, that irrespective of the nozzle pressures applied, a full cone nozzle, recognized for its uniform distribution of water droplets, exhibits an uneven impingement flux distribution across the impact surface. The highest flux is concentrated in the peripheral region of the circular wetting front. Moreover, the impingement water flux demonstrates an increase with the escalation of nozzle pressure.

Figure 3.16 shows the impingement flux distribution in inline and staggered fields at a nozzle height of 63 mm, pressure 2 bar, and where the nozzle-to-nozzle distance is 70 mm.

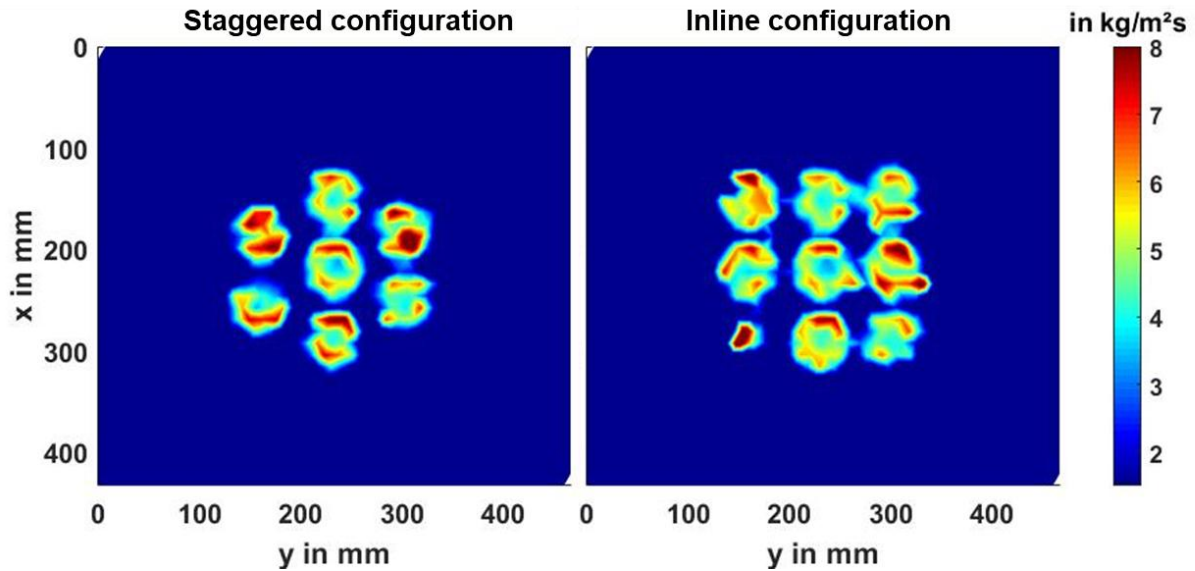


Figure 3.16: Water impingement flux distribution in nozzle fields ($H = 63$ mm, $h = 70$ mm) (Hof, 2023)

The generally observed maximum values fall within a similar range, typically reaching up to $8 \text{ kg/m}^2\text{s}$. However, differences exist in the impact characteristics among individual nozzles, likely attributed to variations in the flow conditions in front of each nozzle or potential soiling. These deviations are also observable in the infrared images captured during the cooling process.

3.4.4 Material Properties

The material properties of investigated metals are required for the heat analysis and calculation of the heat fluxes. For that purpose, these properties were measured in the laboratory and shown against the temperature in Figure 3.17, and Figure 3.18.

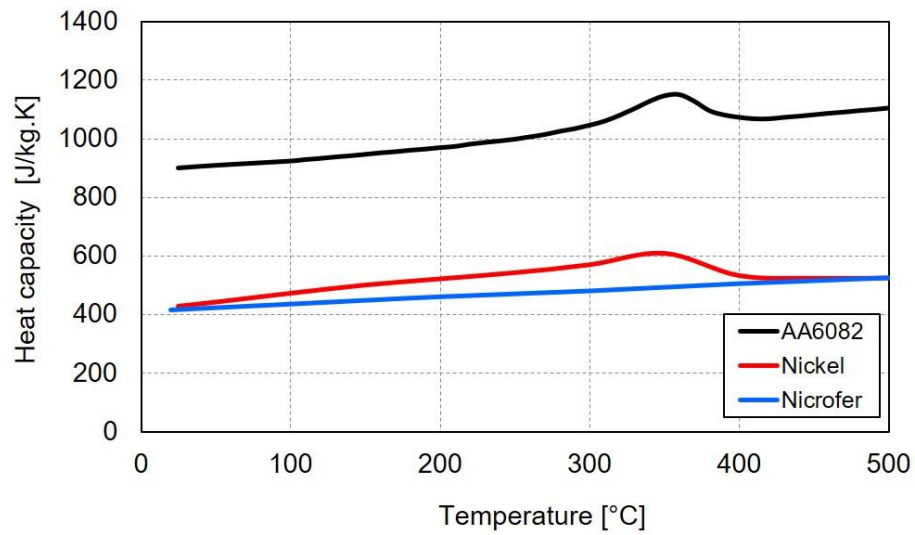


Figure 3.17: Temperature-dependent heat capacity of investigated metals

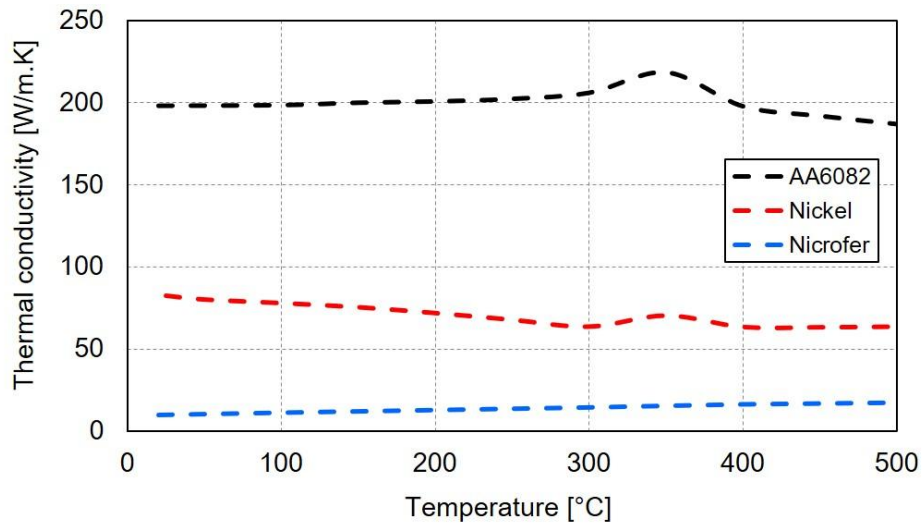


Figure 3.18: Temperature-dependent thermal conductivity of investigated metals

As the variation of material properties is minor against the temperature, the material properties at the mean temperature are used in heat transfer calculations.

Table 4 depicts the thermal properties of nickel, nicrofer, and aluminum alloy, which are employed for experimental investigations.

Table 4: Material properties of various investigated metals at mean temperature

Property	Nickel	Nicrofer	AA6082
Density (kg/m ³)	8908	8400	2700
Thermal conductivity (W/m·K)	70	20	200
Specific heat capacity (J/kg·K)	510	500	1000

4 2D Inverse Heat Conduction Method

It is not feasible to measure the temperature distribution directly on the quenched surface using either contact or non-contact techniques, as the water turbulence and presence of vapors due to boiling further complicate the measurement and increase the error. Therefore, temperatures are measured either below or on the opposite side of the plate. Using thermocouples, temperatures are recorded at a certain distance from the quenched side, and these measurements are utilized to evaluate heat transfer. In contrast, to contact temperature measurements, infrared thermography is employed to record thermal images on the backside of the quenched side with high spatial and temporal resolution. For thicker metal plates, a temperature difference between the quenched side and the measured side can be observed. The temperatures of the quenched surface are necessary for the heat transfer analysis. As a result, these temperatures are determined using the surface temperatures that were recorded on the backside of the plate, an inverse method of heat conduction was used for this computation. Due to its unique applications, inverse modeling has gained a lot of interest recently. Many researchers have developed various inverse models to calculate the heat flux or heat transfer coefficient. (Huang and Wang, 1999) present a three-dimensional inverse heat conduction problem, where the transient surface heat flux is estimated using the conjugate gradient method. (Groß et al., 2005) consider a 3D inverse heat conduction problem (IHCP) in a falling film experiment. The IHCP is solved using the conjugate gradient method. They employed the step theta method for time discretization and piecewise linear finite elements on a tetrahedral grid for space discretization. The resulting sparse system is solved using the Krylov subspace method. (J. Beck et al., 1996) compare several inverse methods using experimental data, including function specification with various function approximations, Tikhonov regularization, iterative regularization, and specified functions over a time region using Green's function. While the comparison of measured and computed temperatures was not discussed, the comparison of surface heat fluxes was reported. The heat flux comparison shows a clear agreement with other inverse techniques.

A one-dimensional heat conduction formulation based on a sequential function specification method has been developed by (Wang et al., 2016) to estimate the heat flux during jet impingement on a high-temperature plate surface. (Nallathambi and

Specht, 2009) used the two-dimensional finite element method to estimate the heat flux during the metal quenching process using an array of jets. (Malinowski et al., 2018) developed an inverse method to determine three-dimensional heat flux and heat transfer coefficient distributions in space and time over a metal surface cooled by water. (Heung-Kyu Kim and Soo-Ik Oh, 2001) present a solution method for a non-linear 3D inverse problem using the sequential gradient method with a cubic spline function.

In the present study, the inverse heat transfer problem is solved using a conjugate gradient method with an adjoint problem; more details about this method can be found in (Orlande and Özisik, 2021).

The method minimizes the objective function, which is given by :

$$S [\dot{q}(y, t)] = \sum_{t=0}^{t_f} \sum_{m=1}^M (T_m(t) - Y_m(t))^2 \quad (4-1)$$

The objective function involves the squared difference between the measured temperature $Y_m(t)$ with the help of the infrared camera and the calculated temperatures $T_m(t)$ estimated with the direct problem by using the estimated heat flux $\dot{q}(y, t)$ on the quench side, t_f represents the final time, and M is the total number of measurement points on the quench surface (number of pixels).

The CGM (conjugate gradient method) is an iterative method that converges to a minimum of the objective function. At each iteration the estimated heat flux $\dot{q}(y, t)$ is computed using,

$$\dot{q}^{k+1}(y, t) = \dot{q}^k(y, t) - \beta^k P^k(y, t), \quad (4-2)$$

where β^k is the search step size, P^k the direction of descent and k the iteration number.

The direction of descent is a linear combination of the gradient direction with the previous iteration's direction of descent, which is given below in equation (4-3)

$$P^k(y, t) = S^k(y, t) + \gamma^k P^{k-1}(y, t) \quad (4-3)$$

The conjugate coefficient γ can be calculated using equation (4-4) as done by (Orlande and Özisik, 2021)

$$\gamma^k = \frac{\sum_{t=0}^{t_f} \sum_{m=1}^M (S^k)^2}{\sum_{t=0}^{t_f} \sum_{m=1}^M (S^{k-1})^2} \quad (4-4)$$

The stopping criterion is given by

$$\tau = M\sigma^2 t_f, \quad (4-5)$$

$$\sigma = T_m(t) - Y_m(t), \quad (4-6)$$

where σ is the standard deviation of the temperature measurements and is assumed to be constant. To perform the iterative process, first, the step size β and the gradient of descent $S^k(y, t)$ are computed by solving the sensitivity and adjoint problems (Orlande and Özisik, 2021). As stated by (Orlande and Özisik, 2021) these problems can be transformed into a simple Fourier law problem by specifying boundary and initial conditions. These problems are solved numerically using the finite difference method. For further details of these problems, the reader is referred to (Huang and Wang, 1999), (Alifanov, 1994), and (Woodbury, 2002).

To solve the partial differential equation, a transient two-dimensional finite difference method was implemented. Initially, the unknown heat fluxes were approximated as zero. For the adjoint problem, the gradient of the objective function was initialized before the start of the iteration. Experimental temperatures were used to determine the optimal search direction for estimating the unknown heat flux through an iterative process.

Figure 4.1 shows, a simplified flowchart of the used inverse heat conduction method.

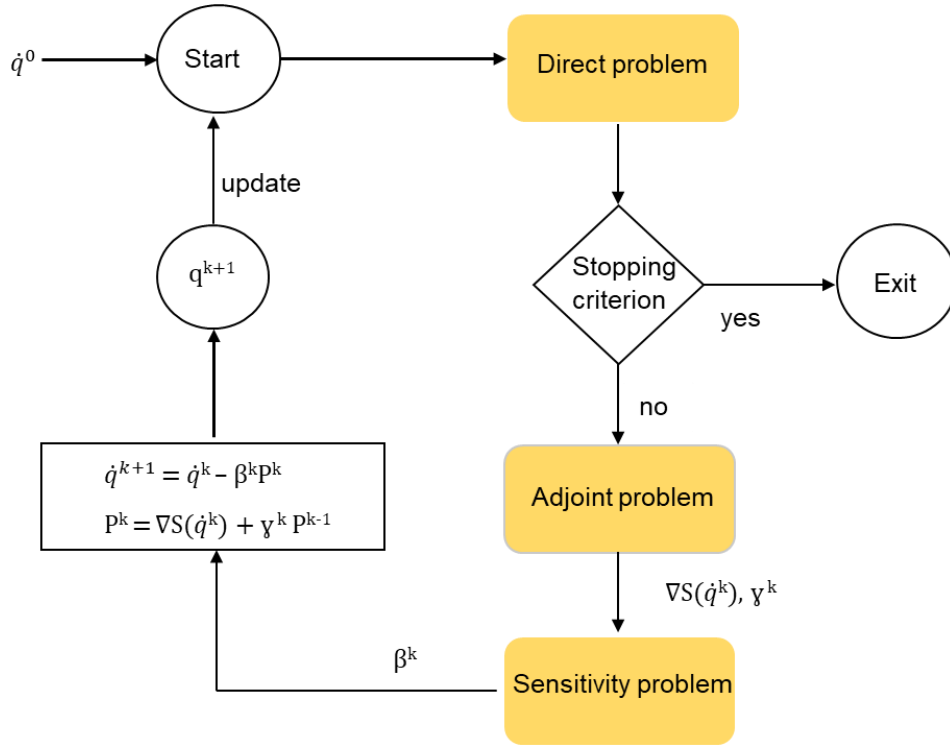


Figure 4.1: Algorithm flowchart of the inverse method

Step 1: Solving the direct problem $(T(x, y, t))$ using the initial guess of the boundary condition $\dot{q}^0(y, t)$.

Step 2: Checking the stopping criterion given by equation (4-5). Continuing if not satisfied.

Step 3: Computing the gradient direction $S^k(y, t)$ from the adjoint problem and then the conjugate coefficient γ^k from equation (4-4).

Step 4: Compute the direction of descent P^k using equation (4-3).

Step 5: Computing the new search step size β^k solving the sensitivity problem.

Step 6: Computing the new estimation for \dot{q}^{k+1} and return to step 1.

To evaluate the heat flux, the iterative method described above is applied to the 2D structure, as shown in Figure 4.2.

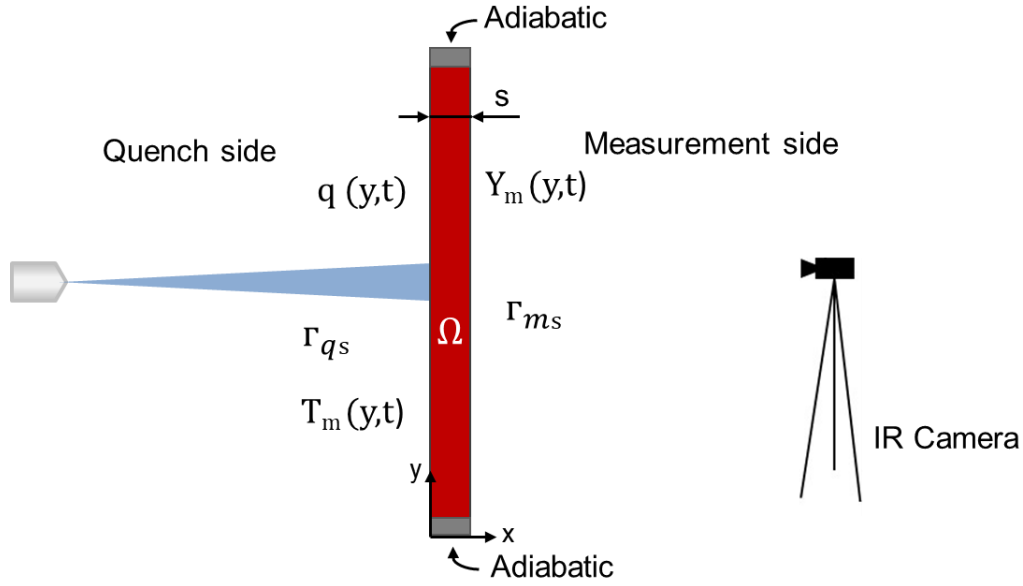


Figure 4.2: Schematic representation of boundary conditions of the plate

The two-dimensional heat equation is calculated numerically along the plate length (y) and thickness (x) of the plate. The heat conduction equation in the cartesian coordinate system (x,y) is:

$$\rho c_p \frac{\partial T}{\partial t} = \lambda \left[\frac{\partial^2 T}{\partial x^2} + \frac{\partial^2 T}{\partial y^2} \right] \quad \text{in } \Omega, t > 0 \quad (4-7)$$

$$\frac{\partial T}{\partial t} = \alpha \left[\frac{\partial^2 T}{\partial x^2} + \frac{\partial^2 T}{\partial y^2} \right] \quad \text{in } \Omega, t > 0 \quad (4-8)$$

$$T(y, 0) = T_0 \quad \text{in } \Omega, t = 0 \quad (4-9)$$

$$\lambda \frac{\partial T}{\partial y} = q(y, t) \quad \text{On } \Gamma_{qs} \quad (4-10)$$

For a domain, the initial temperature equals T_0 , when $t > 0$ all the boundary conditions are assumed insulated except the quenching side which is subjected to $q(y,t)$. For the

inverse problem, the boundary heat flux $q(y,t)$ and $T_m(y, t)$ on the quench side are regarded as unknown. The measured spatial and temporal temperature $Y_m(y, t)$ along the y-axis from the measurement side is used to numerically solve the problem in the y and x directions to obtain the heat flux along the y-axis on the quenching side. The transient inverse heat conduction method is solved using the central finite difference method in Matlab.

The mathematical model of the moving boundary is complex to solve both, analytically and numerically. To simplify this modeling, the movement of the plate can be reduced to a stationary (fixed plate) condition. The plate position can be tracked at each time step using $x = L \cdot w_p \cdot t$ with this method, the surface temperature can be recorded at each time interval. Thus, by tracking the plate position continuously, the movement of the plate is effectively rendered stationary. Hence the plate velocity becomes zero and the Euler equation becomes:

$$\frac{DT}{Dt} = \frac{\partial T}{\partial t} \quad (4-11)$$

Figure 4.3 shows the measured and simulated measured temperatures on the measurement side for start time to end time. It can be seen that measured and simulated temperatures are approximately the same at all times.

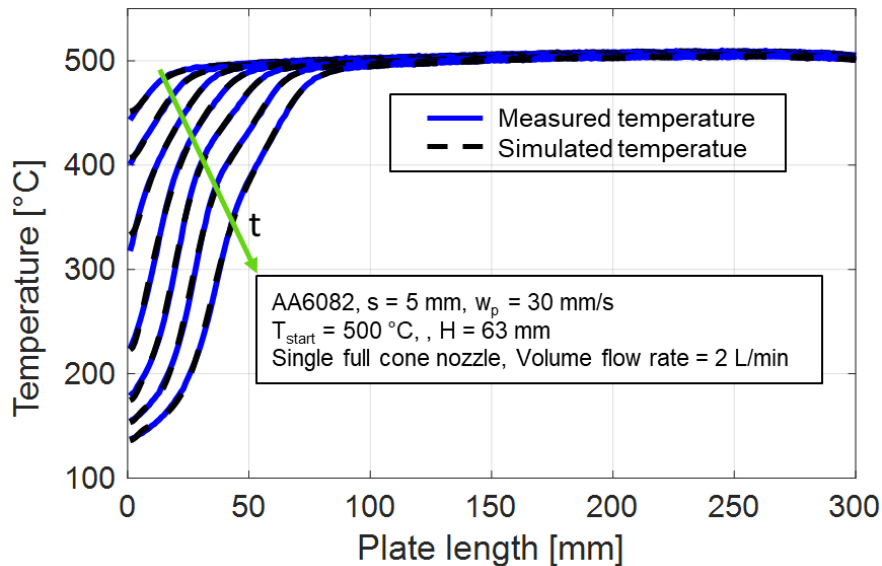


Figure 4.3: Model validation along the length of the plate for moving case

Figure 4.4 shows the validation of the developed two-dimensional inverse heat conduction method.

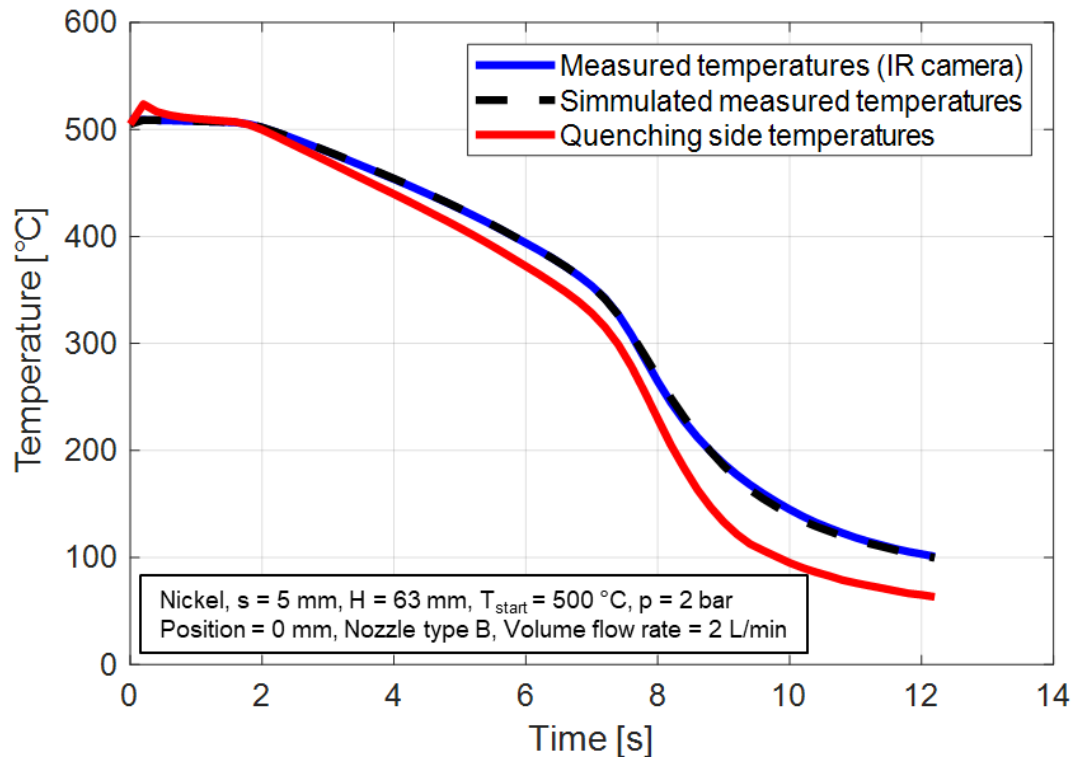


Figure 4.4: Inverse model validation based on experiment and simulated temperature on the measurement side

The temperature evolution of a 5 mm nickel plate, initially heated to 500 °C and subsequently cooled by a single full cone nozzle, is graphically depicted against cooling time. The blue curve represents the experimentally measured temperatures on the measuring side, captured using an infrared camera, while the dotted black curve illustrates the simulated temperatures on the same measuring side. These simulated temperatures are derived numerically through the application of an inverse model. A minor difference between the experimental and simulated temperatures proves the validation of the inverse model. Furthermore, the temperatures on the quenching side of the plate, obtained through the inverse model, are illustrated by the red curve. Notably, the temperatures on the quenching side exhibit a more rapid decline compared to the measuring side, showcasing an approximate 50 K temperature difference for a 5 mm thick nickel plate between the two sides.

The surface heat flux as a function of the quenched surface temperature, also known as the boiling curve, approximated through the inverse heat transfer method is plotted in Figure 4.5 for a 2 mm nickel plate as an example.

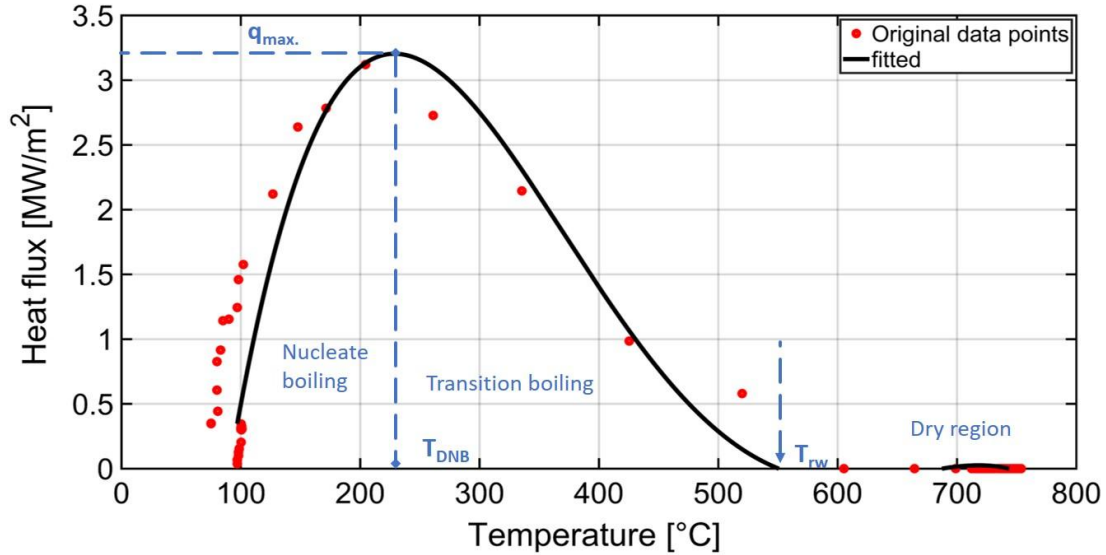


Figure 4.5: Smoothed heat fluxes against temperatures on the quenched side

The red colored points show the original data points obtained from the inverse solution. As the inverse heat transfer methods give very unstable fluctuating results, they require fine smoothing and fitting of results. The black curve shows the best fitting of the original solution, the data points are fitted using the polynomial function of order 4. This technique is employed so that the effect of various parameters on the heat flux can be better understood. The curve is divided into three regimes: dry region, transition boiling region, and nucleate boiling region. The cooling starts when the rewetting temperature T_{rw} of 560 °C is reached and heat flux starts rising. The transition boiling region is in a range from 560 °C to 220 °C. The maximum value of 3.3 MW/m² of heat flux occurs at T_{DNB} of 220 °C. Nucleate boiling follows the transition boiling, in which the evaporation rate and the heat flux decrease due to the low surface temperature and small bubble nuclei formation on the surface.

Figure 4.6 illustrates the comparison of boiling curves of the 5 mm aluminum alloy plate obtained from the developed 2D inverse heat conduction model, and using the analytical equations with the same parameters.

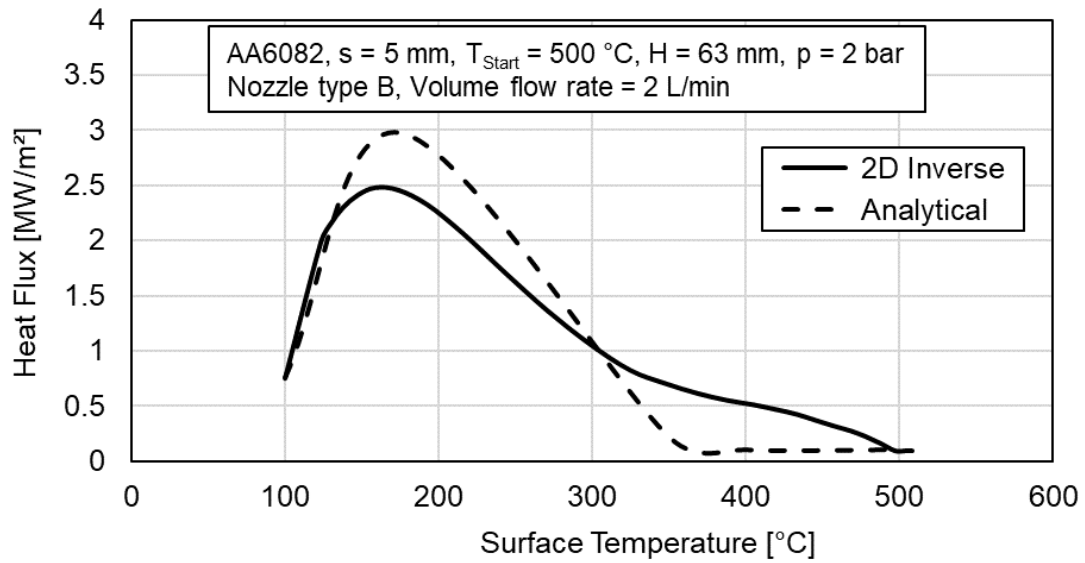


Figure 4.6: Boiling curve of AA6082 comparing 2D inverse and analytical solution

The plate was heated to a start temperature of 500 °C and then cooled with a single full cone nozzle (type B) with a nozzle pressure of 2 bar.

Comparing the two curves, it can be seen that the 2D inverse model aligns well with the analytical boiling curve under the same parameters. Both curves peak at a temperature of around 170 °C and the maximum heat flux is approximately 3 MW/m² for analytical and 2.5 MW/m² for the inverse model.

The analytical boiling curve is calculated using the equations reported by (Hof, 2023). Whereas, 2D inverse modeling, is a type of numerical method used to estimate parameters or states of a system based on observed data.

5 Quenching of Horizontal Plates

5.1 Overview

This chapter presents the results of experiments involving a single full-cone nozzle and a field of full cone sprays. The experiments were conducted for both, stationary and moving plates, with cooling from the top and bottom sides. The parameters such as the thickness of metal, volumetric flow rate, nozzle height, nozzle configurations, and nozzle to nozzle spacing, etc. are varied. The influence of the above-mentioned parameters on the cooling rate, uniform temperature distribution, and resulting heat fluxes are presented.

Before delving into the heat transfer analysis within full cone nozzle fields, it is essential to initially explore how a single full cone nozzle behaves and influences heat transfer by varying different parameters. The investigation focuses on a single full cone nozzle, examining the effects of changing parameters, specifically for top-side and bottom-side cooling. This preliminary study lays the groundwork for a comprehensive understanding of the nozzle impact on heat transfer dynamics before extending the analysis to multiple nozzles in a field.

5.2 Single Full Cone Nozzle (Stationary)

5.2.1 Cooling from the Top Side of the Plate

The metal thickness, nozzle pressure, volumetric flow rate, and nozzle height from the surface of the plate varied from 63 mm to 127 mm as shown in Figure 5.1.

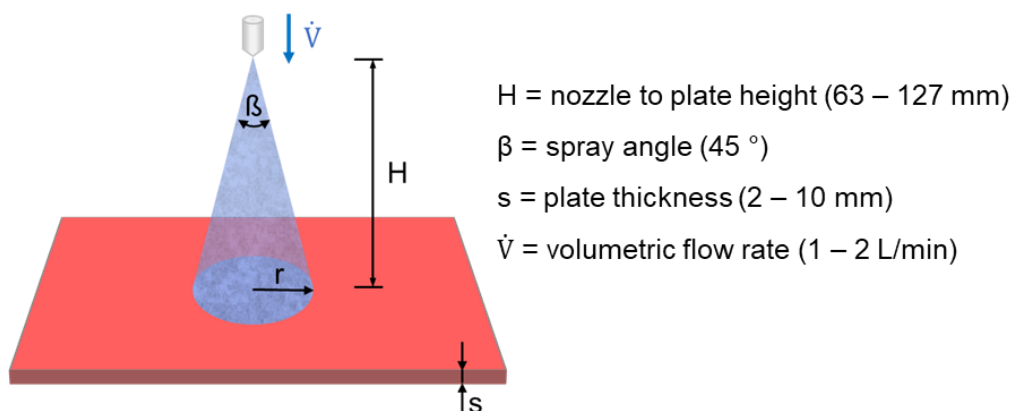


Figure 5.1: Schematics of the full cone nozzle

The quenching experiments were carried out employing Lechler full cone nozzles (490.403, 490.523) with a spray angle of 45°. The volume flow rates utilized were 1 and 2 L/min, maintaining a constant nozzle pressure of 2 bar.

Figure 5.2 shows the measured temperatures (camera side) at the center of the full cone nozzle and the numerically inverse calculated temperatures (quenching side) along the time.

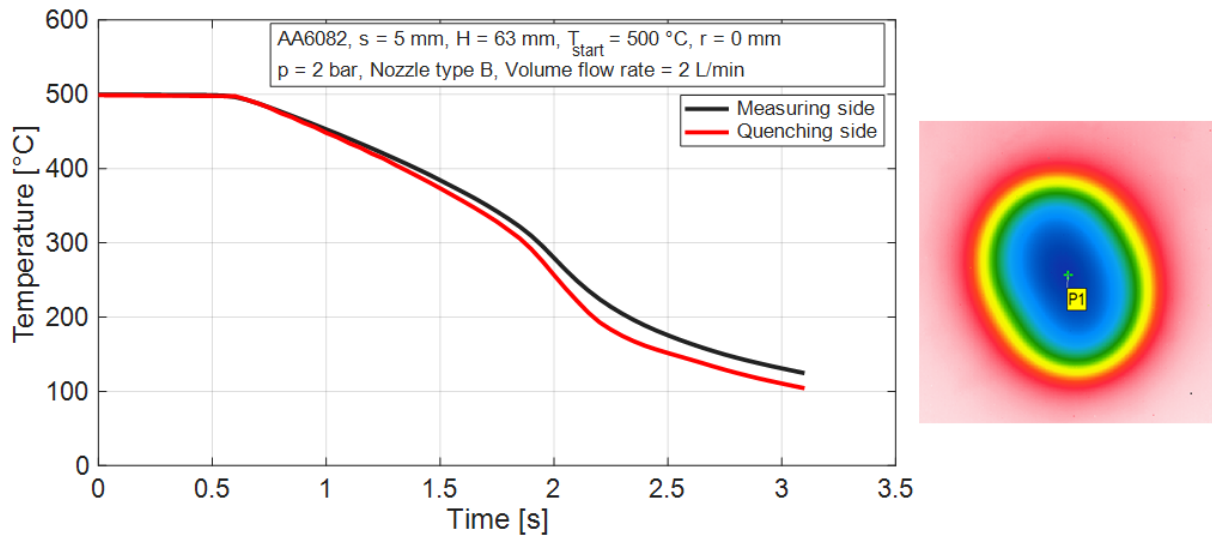


Figure 5.2: Quenching and measuring side cooling curve

Despite the high thermal conductivity of aluminum alloy, there is a temperature difference between the quenching and measuring sides during the cooling process. Different boiling regions can also be distinguished.

In the initial 0.5 to 1.5 seconds, film boiling is observed, wherein temperatures gradually decrease until reaching the Leidenfrost temperature, at approximately 300 °C. Following the Leidenfrost temperature, a notable decline in the cooling curve signifies the transition boiling region. It is evident from the above cooling curve, that the temperatures on the measuring and quenching sides differ more significantly during the nucleate boiling period. The maximum temperature difference observed is 30 K. In the following figures, the quenching side temperatures will be shown.

Figure 5.3 illustrates the heat flux on the quenched surface of a 5 mm thick aluminum alloy plate, representing the boiling curve.

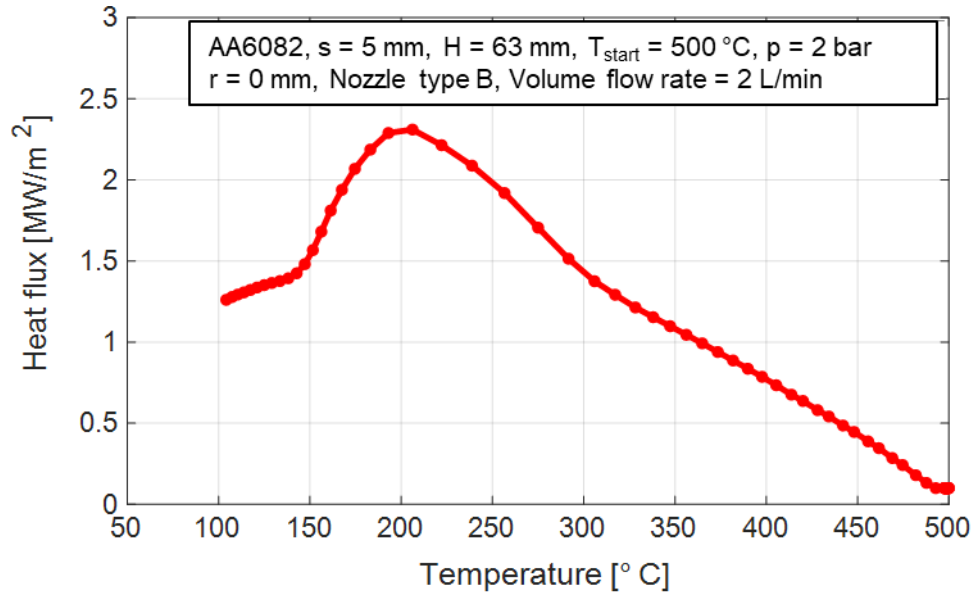


Figure 5.3: Boiling curve of cooling a 5 mm AA6082 using a full cone nozzle

As the plate initiates its cooling process from the start temperature of $500\text{ }^{\circ}\text{C}$, the heat flux exhibits a gradual increase. It reaches its peak at a DNB temperature of approximately $200\text{ }^{\circ}\text{C}$. Subsequently, after attaining the DNB temperature, the heat flux undergoes a decrease, indicating the transition to the convection region. The alteration in gradient observed at $310\text{ }^{\circ}\text{C}$, signifies the Leidenfrost temperature.

The quenching of nickel plates with a thickness of 5 mm is investigated. The parameters like nozzle to plate height, nozzle pressure, and start temperature are varied during the experiments. Figure 5.4 provides a visual and qualitative representation of the cooling of the nickel plate at a nozzle height of 63 mm over a time ranging from 1 to 3.5 seconds.

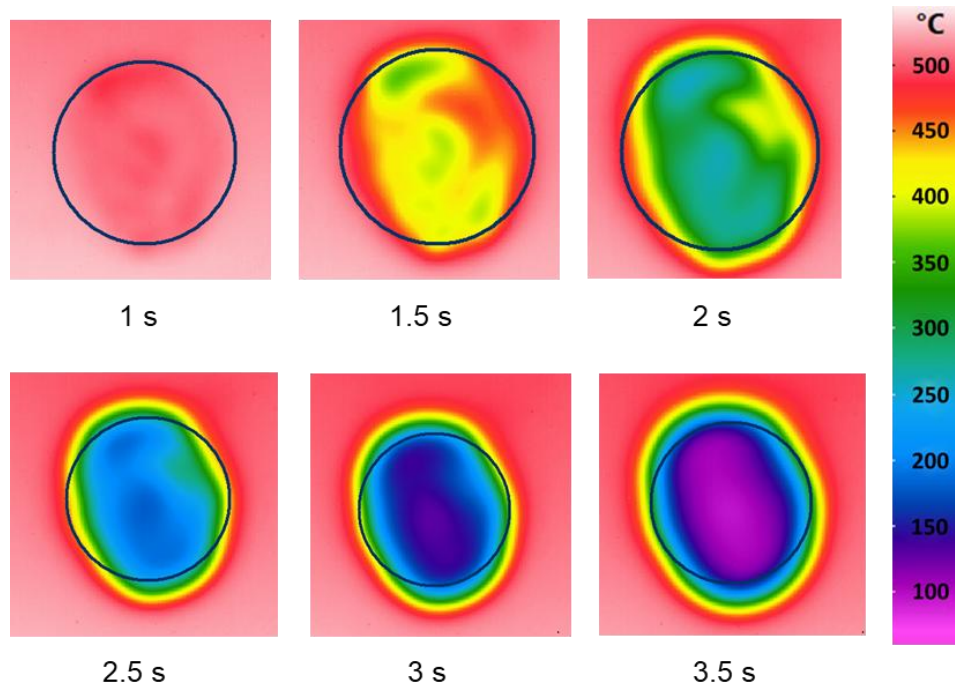


Figure 5.4: Infrared images of cooling of 5 mm nickel with a single full cone nozzle

The IR images depict the non-homogeneous cooling process observed from 1 to 2.5 seconds, preceding the initiation of the fully wetting front propagation. This non-uniform cooling behavior is due to variations in the spray impingement flux across the impact area, as stated in section 3.4.3 in detail. For this reason, temperature profiles are presented along the width of the plate at specific time intervals, as well as at the center of the nozzle, spanning the entire duration of the cooling process.

Figure 5.5 shows the temperature and heat flux profiles along the plate width corresponding to IR images from 1 to 4 seconds.

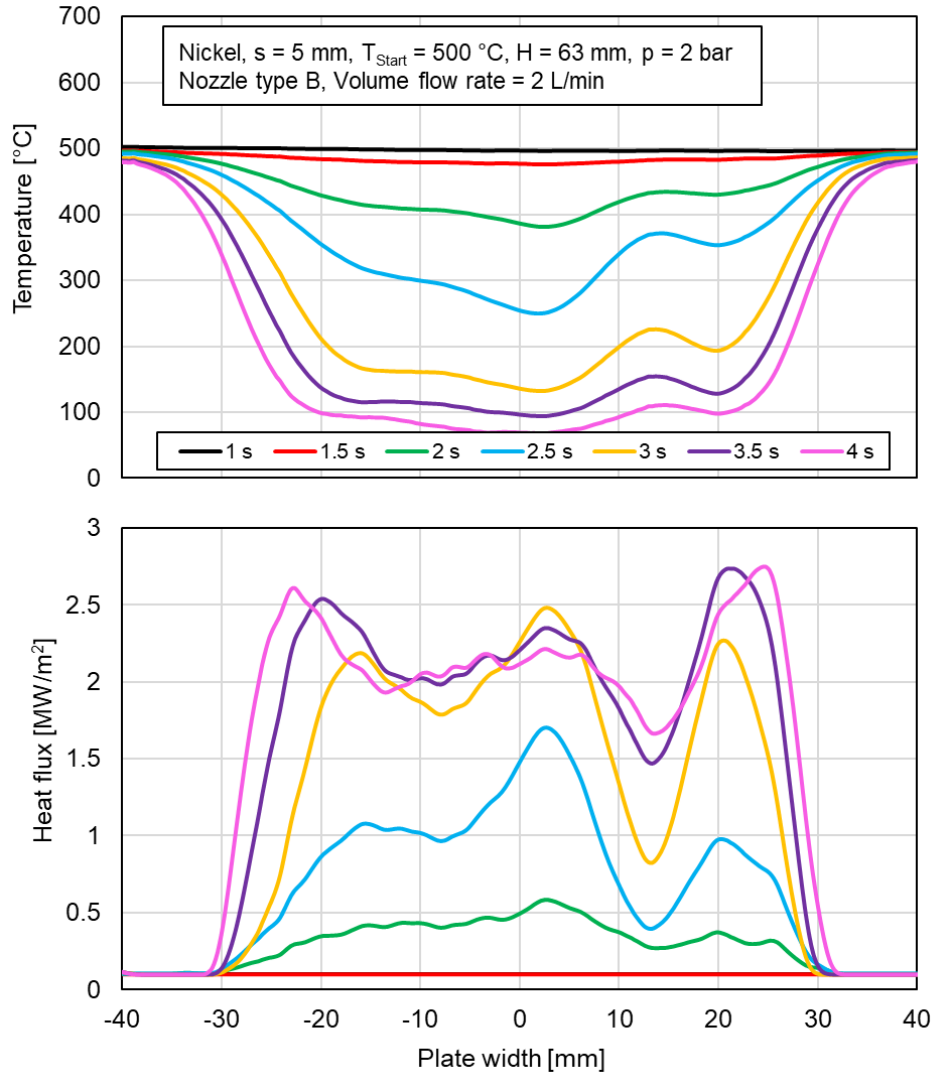


Figure 5.5: Temperature and heat flux profiles of 5 mm nickel along the plate width at various times

The cooling process initiates from an initial temperature of 500 °C, with a constant nozzle volume flow rate of 2 L/min maintained throughout. The temperature profiles presented correspond to the measuring line (ML), which intersects the center of the circle. The nozzle center is denoted as position 0 mm. Across the cooled area, all temperature profiles exhibit fluctuating trends, as observed in the IR images, see Figure 5.4.

The heat flux demonstrates an increasing trend with time as the plate undergoes cooling, with a significant increase from 2.5 to 3.5 seconds. This phenomenon is attributed to the presence of distinct boiling regions on the plate surface. Initially, film boiling prevails until the rewetting temperature is attained at 2.5 seconds.

Subsequently, upon reaching the rewetting temperature, the heat flux experiences a substantial rise. Notably, the maximum heat flux is approximately 2.5 MW/m^2 around positions $+20 \text{ mm}$ and -20 mm , at 3.5 seconds.

Influence of Nozzle Height

Figure 5.6 shows the cooling curves of a 5 mm thick nickel plate for various nozzle-to-plate heights 127 mm, 84 mm, and 63 mm.

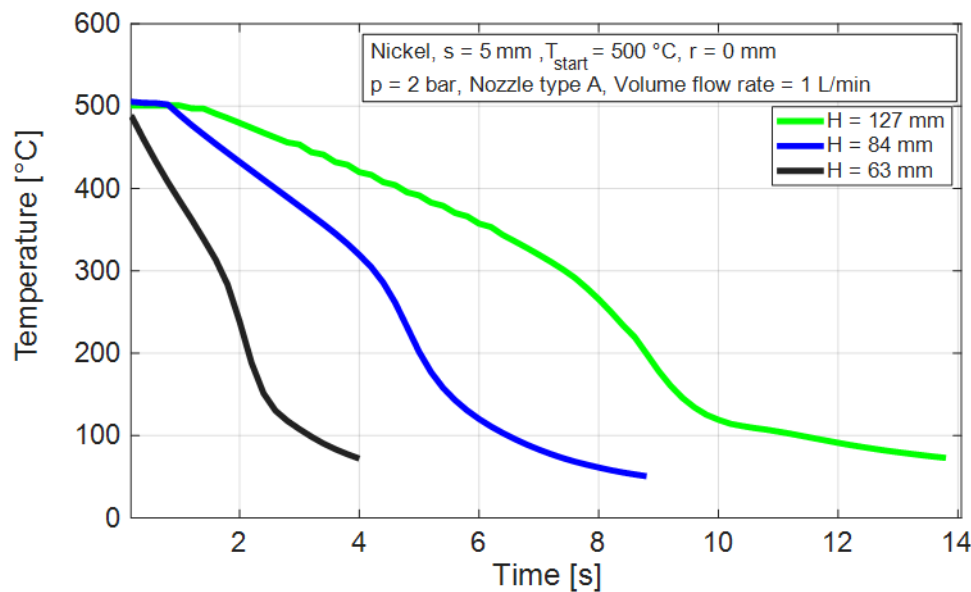


Figure 5.6: Influence of nozzle height on the cooling curve of 5 mm nickel

The increase of the nozzle height from 63 mm to 127 mm correlates with an increase in cooling time from 4 to 14 seconds. This increase in cooling duration is directly linked to variations in the spray flux. As the nozzle height increases, there is a reduction in spray flux, leading to a decrease in both, the cooling rate and the intensity of cooling. For all nozzle heights considered, two distinct cooling regions are observable. The first cooling region spans from 500 °C to approximately 300 °C, during which the plate gradually cools. Subsequently, the second cooling region extends from 300 °C to below 100 °C. Furthermore, with an increase in nozzle height, the duration of the film boiling phase expands until the Leidenfrost temperature is attained. Specifically, the duration of the film boiling phase is less than 2 seconds for a nozzle height of 63 mm, whereas it extends to approximately 7 seconds for a nozzle height of 127 mm.

The Influence of the nozzle height on the boiling curve is shown in Figure 5.7

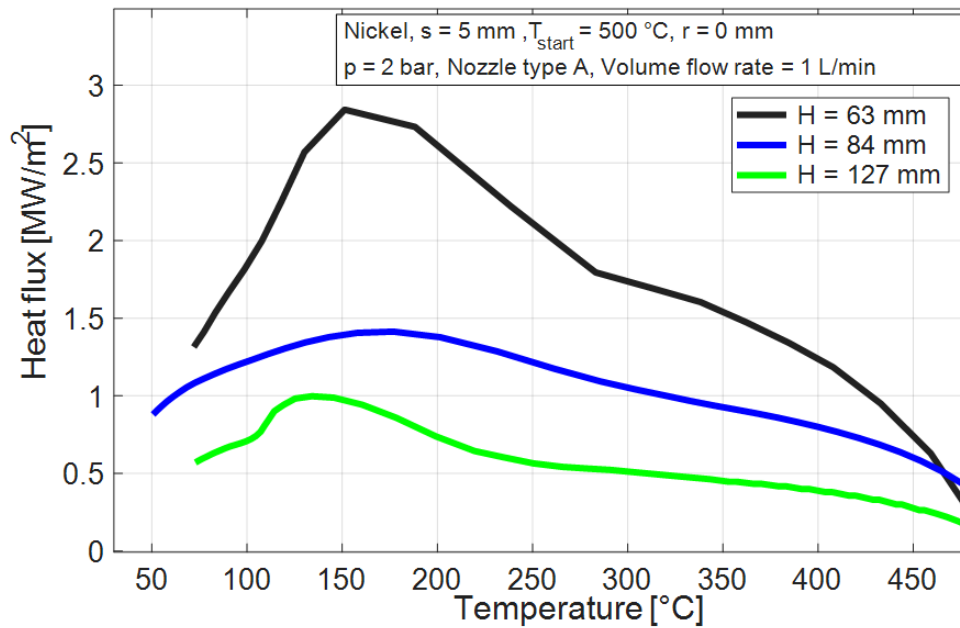


Figure 5.7: Influence of nozzle height on a boiling curve of 5 mm nickel

At all nozzle heights, the heat flux exhibits a gradual increase from 500 °C to approximately 300 °C , reaching the Leidenfrost temperature. Subsequently, the heat flux experiences a relatively sharp rise, peaking at the DNB temperature. Notably, the maximum heat flux increases from 1 to 2.8 MW/m^2 as the nozzle height decreases from 127 to 63 mm . This increase is primarily attributed to the rise in spray flux associated with a reduction in nozzle height. The DNB temperature is observed to fall within the range of 150 °C to 180 °C and demonstrates a slight decrease with decreasing nozzle-to-plate distance. Increasing the nozzle to plate height results in an enlargement of the cooled area. This is visually presented through IR images in Figure 5.8 at various nozzle heights of 63 , 75 , 84 , and 127 mm .

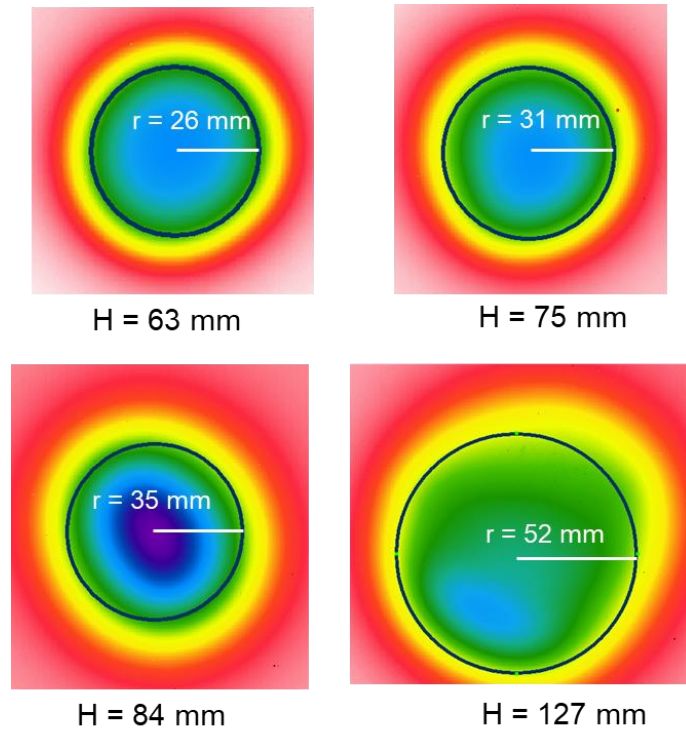


Figure 5.8: IR images with various nozzle-to-plate distance (AA6082)

Figure 5.9 illustrates the heat flux distribution across the width of the plate after a cooling time of 6 seconds, considering the four nozzle heights.

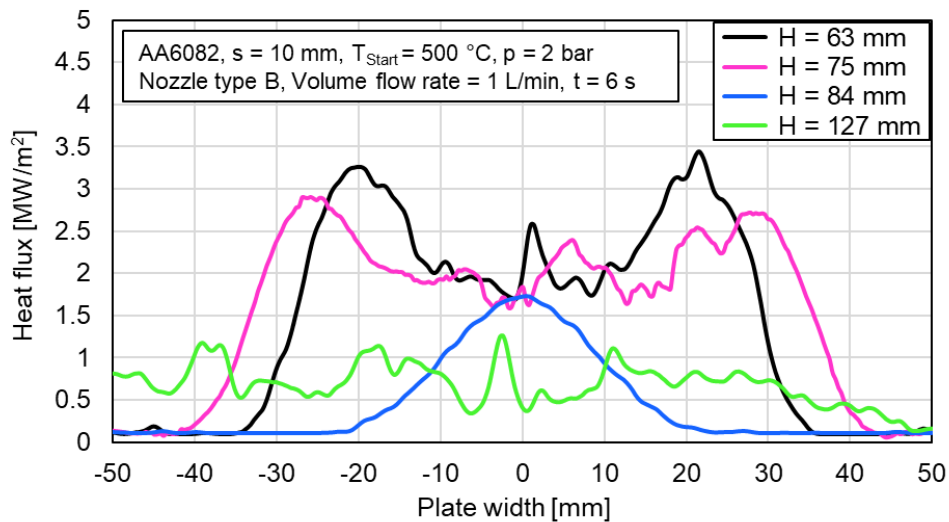


Figure 5.9: Heat flux of AA6082 along the plate width for various nozzle heights

The reference point 0 mm corresponds to the center of the nozzle. Notably, heat transfer is non-uniform along the plate width. The highest heat flux is observed at a

nozzle height of 63 mm, followed by 75 mm and 84 mm. For the smaller heights of 63 and 75 mm, a peak is observed at the radius of approximately ± 20 mm. At this location, the water flux reaches its highest values for the employed full cone nozzle, as depicted in Figure 3.15. In contrast, the heat flux remains relatively consistent at a nozzle height of 127 mm.

Figure 5.10 depicts temperature profiles of a 10 mm thick aluminum alloy plate with varying nozzle-to-plate distance.

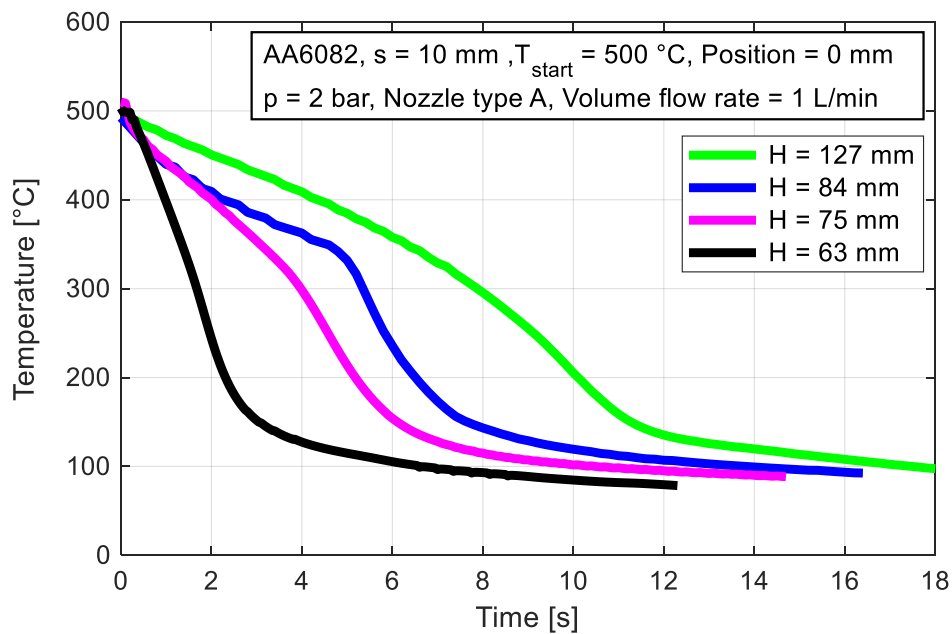


Figure 5.10: Influence of nozzle height on a cooling curve of 10 mm AA6082

The temperature profiles presented in Figure 5.10 reveal that the cooling time, from an initial temperature of 500 °C to 100 °C, extends from 7 to 18 seconds with an increase in nozzle height. This variation occurs while maintaining a constant nozzle volume flow rate of 1 L/min. It can also be observed that the length of the film boiling period in which the plate cools down gradually until the Leidenfrost temperature is also higher for 84, and 127 mm nozzle-to-plate distances. At a nozzle height of 63 mm, the vapor film collapses immediately, leading to a shortened film boiling region and a higher thermal gradient compared to a 127 mm nozzle height, where the overall cooling time is dominated by film boiling. The rate of heat transfer on the surface of the plate with a full cone spray is significantly influenced by the spray flux. An increase in the nozzle-

to-plate distance leads to a decrease in spray flux, consequently resulting in a slower heat transfer rate. Specifically, the heat flux is larger for a nozzle-to-plate distance of 63 mm compared to 127 mm. The maximum heat flux increases from 1.3 MW/m² to 3 MW/m² with a decreasing nozzle height, as illustrated in boiling curves in Figure 5.11.

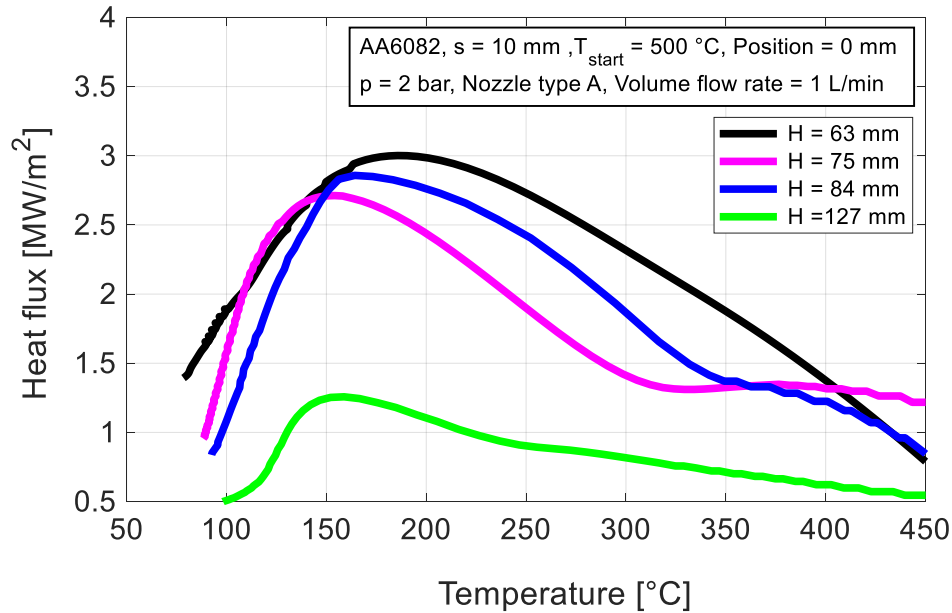


Figure 5.11: Influence of nozzle height on boiling curve of 10 mm AA6082

There is a slight increase in DNB temperature with decreasing nozzle height. For example, at $H = 127$ mm, the DNB temperature is 150 °C, while for $H = 63$ mm, it is approximately 190 °C.

Influence of Nozzle Pressure

The nozzle pressure is varied from 2 to 9 bar by keeping the other parameters constant which results in a change in the volume flow rate of the two investigated nozzles as shown in Table 5.

Table 5: Variation of the volume flow rate of two nozzles with varying nozzle pressure

Nozzle pressure [bar]	Volume flow rate	
	490.403 (A) [L/min]	490.523 (B) [L/min]
2	1	2
3	1.2	2.4
6	1.6	3.1
9	1.8	3.6

The IR images of the cooling of a 5 mm nickel plate with varying pressure of nozzle type A are shown in Figure 5.12.

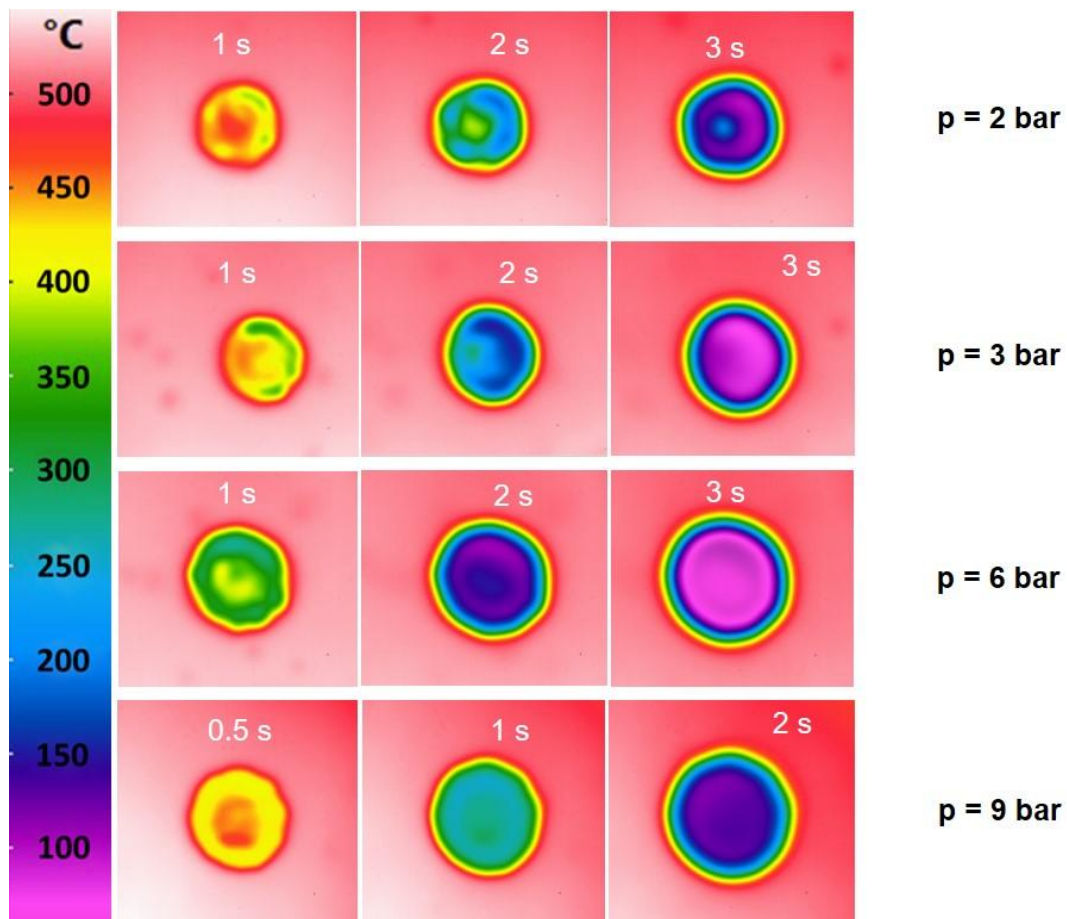


Figure 5.12: IR images at various times with varying nozzle pressure for nickel

The thermal images depict three different time intervals for various nozzle pressures. At the start of cooling for all pressure nozzles, the temperature begins to decrease in

a ring-like pattern, and rewetting initiates across the circumferential area of the impacting circle. As time progresses, the wetting front propagates, and the hollow ring shape gradually dissipates. With increasing pressure, the spray flux increases, resulting in decreased inhomogeneities and a fully developed wetting front forming in a shorter duration, compared to lower pressures.

Figure 5.13 shows the temperature and corresponding heat flux profiles with variable nozzle pressure at a time of 3 seconds. The reference point 0 mm corresponds to the center of the nozzle. With an increase in nozzle pressure, the temperature at the center of the nozzle decreases, leading to an increase in the uniformity of cooling.

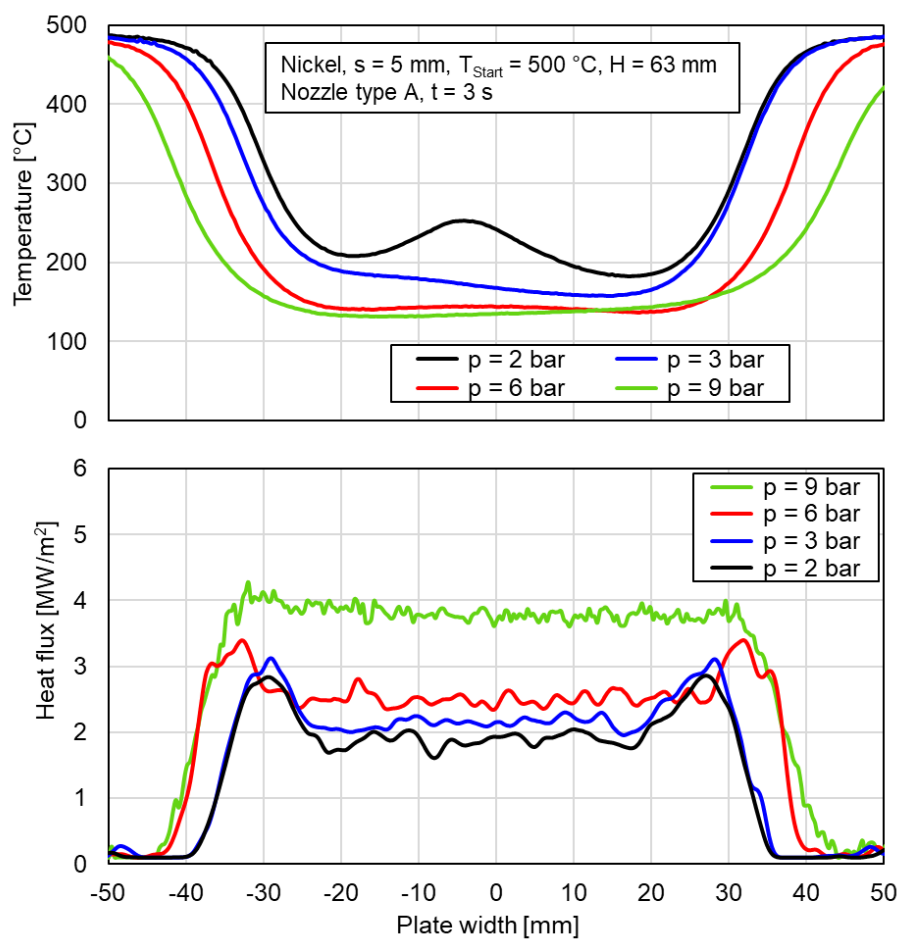


Figure 5.13: Influence of nozzle pressure on the temperature and heat flux profiles at a quasi-steady time along the plate width (nickel)

For instance, at a nozzle pressure of 2 bar, a temperature peak is observed within the range of -10 mm to 0 mm, with temperatures exceeding 200 °C. This peak in the temperature profile results from non-uniform cooling and is also evident in the IR image

at 3 seconds in Figure 5.12. In contrast, at a higher nozzle pressure of 9 bar, the temperature distribution becomes more uniform and remains around 150 °C.

Similarly, the heat flux profiles exhibit a corresponding trend. By increasing the nozzle pressure from 2 to 9 bar, the heat flux rises from increases from 2 to 4 MW/m² within the impact circle. The fluctuations in heat flux diminish with a rise in nozzle pressure. Figure 5.14 shows the cooling curves of varying nozzle pressures at the center of the nozzle.

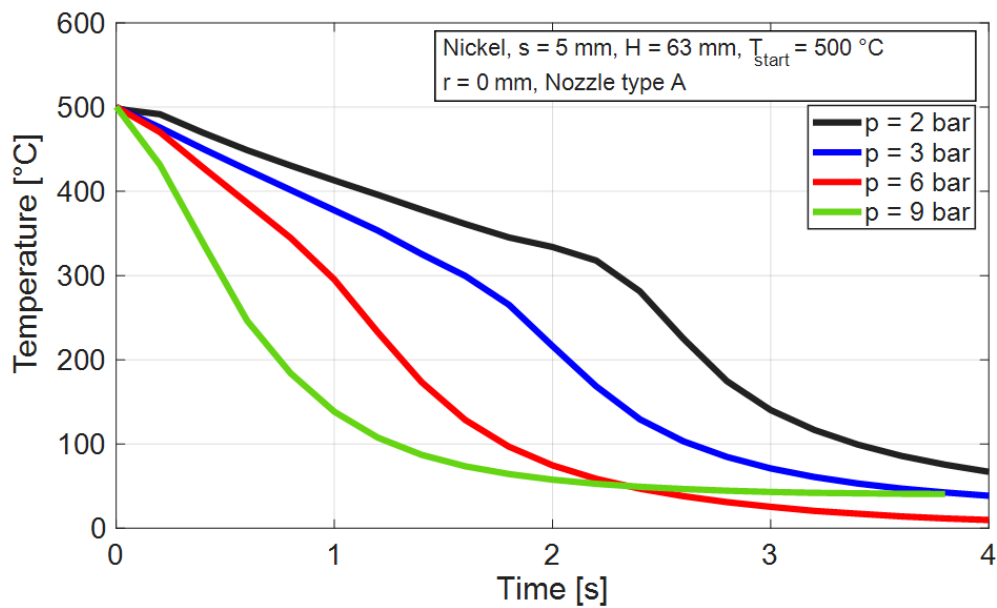


Figure 5.14: Influence of nozzle pressure on the cooling curve of nickel at the center of the nozzle

It is evident, that increasing the nozzle pressure results in a reduction of the cooling time from 4 to 2 seconds. Conversely, decreasing the pressure prolongs the film boiling region and slows down the cooling process. Additionally, the Leidenfrost temperature increases with an increase in nozzle pressure. Figure 5.15 illustrates the heat fluxes corresponding to the aforementioned cooling curve profiles at the center of the nozzle.

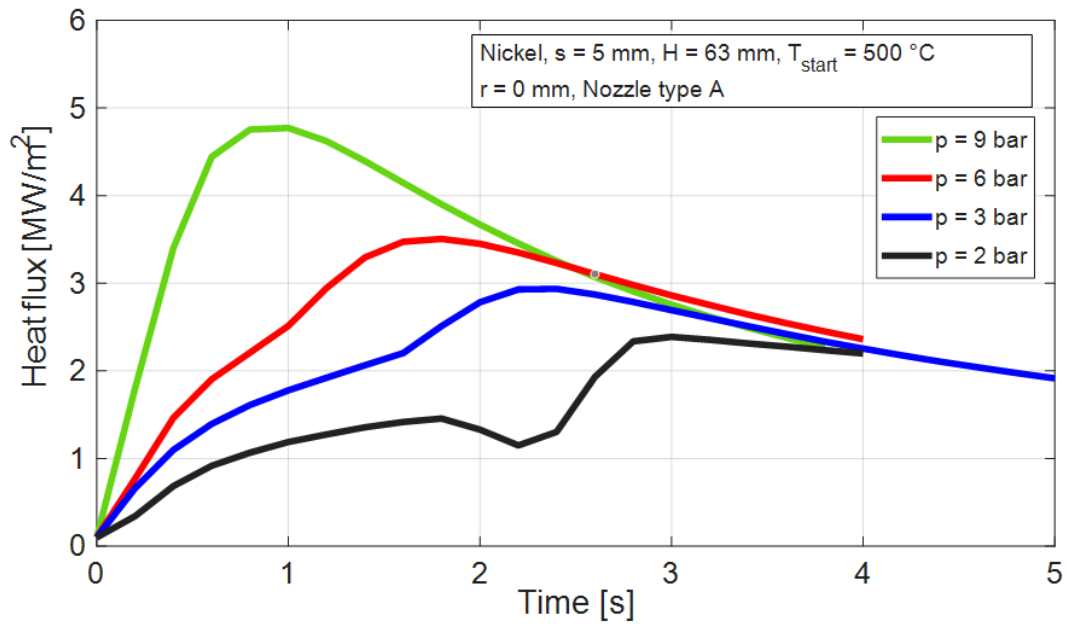


Figure 5.15: Influence of nozzle pressure on the heat flux of nickel at the center of the nozzle

The maximum heat flux demonstrates an increase with an increase in nozzle pressure. Notably, the heat flux ascends rapidly to its peak value at 9 bar nozzle pressure, whereas for 6 bar, it reaches the maximum after 1.5 seconds, for 3 bar after 2.5 seconds, and for 2 bar after 3 seconds.

The temperature profiles of the 10 mm thick aluminum alloy plate with varying pressure of nozzle A are shown in Figure 5.16.

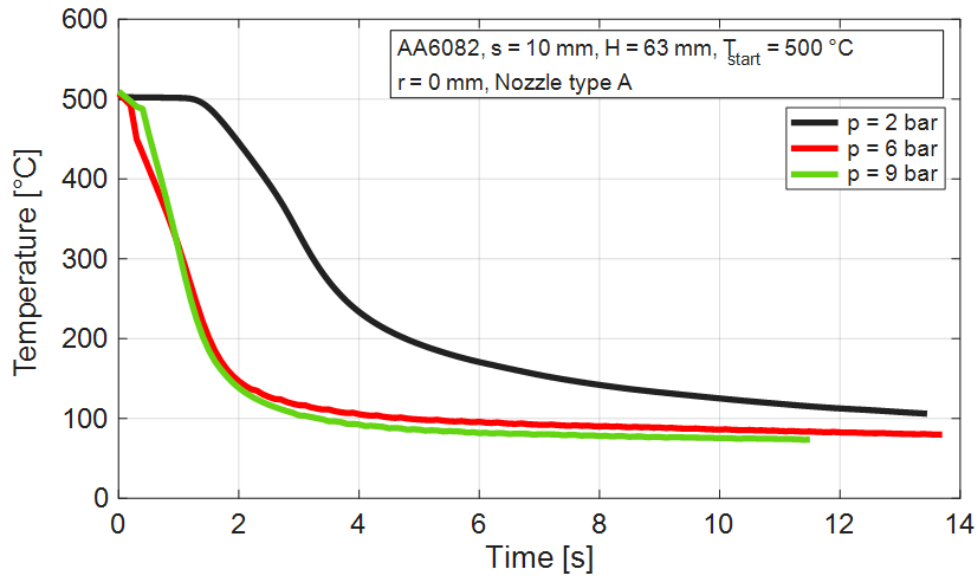


Figure 5.16: Influence of nozzle pressure on the cooling curve of 10 mm AA6082

It is evident, that increasing the pressure from 2 to 6 bar substantially enhances the cooling efficiency, leading to an immediate rewetting of the surface with an accelerated cooling rate. However, from 6 to 9 bar, there is no significant additional influence observed. The temperature gradient is more pronounced for 6 and 9 bar compared to 2 bar. In terms of time, the cooling duration drops significantly, reducing from 13 to just 3 seconds with higher pressures. Additionally, higher pressures facilitate a faster spreading of the wetting front.

The corresponding heat fluxes at the center of nozzle positions are presented at the above-varied nozzle pressures in Figure 5.17.

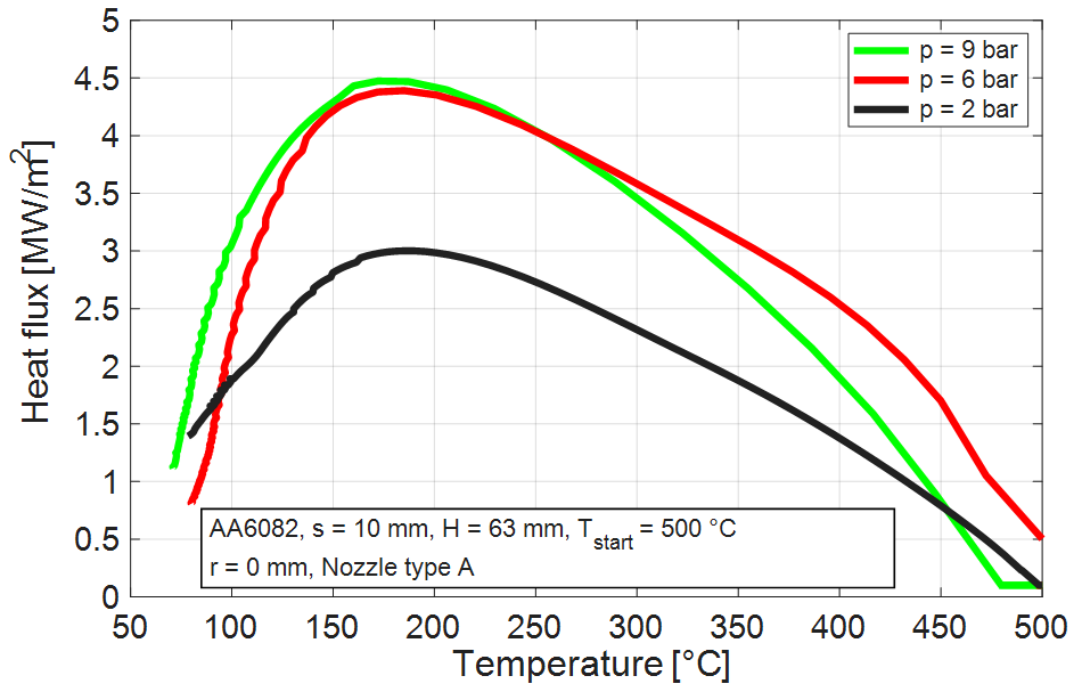


Figure 5.17: Influence of nozzle pressure on the boiling curve of 10 mm AA6082

The heat flux in all regions, including the maximum heat flux, exhibits an upward trend with increasing pressure. Notably, there is minimal variation in heat flux between the 6 and 9 bar pressure levels, closely aligning with the cooling curves depicted in Figure 5.16. Importantly, the DNB temperature remains consistently at 190 °C, even with the increase in pressure.

Influence of Plate Thickness (AA6082)

The comparison of aluminum alloy metal plate thicknesses is conducted at a nozzle height of 84 mm, maintaining a constant volume flow rate of 2 L/min. Figure 5.18 illustrates the impact of varying plate thicknesses on the temperature profiles of the aluminum alloy.

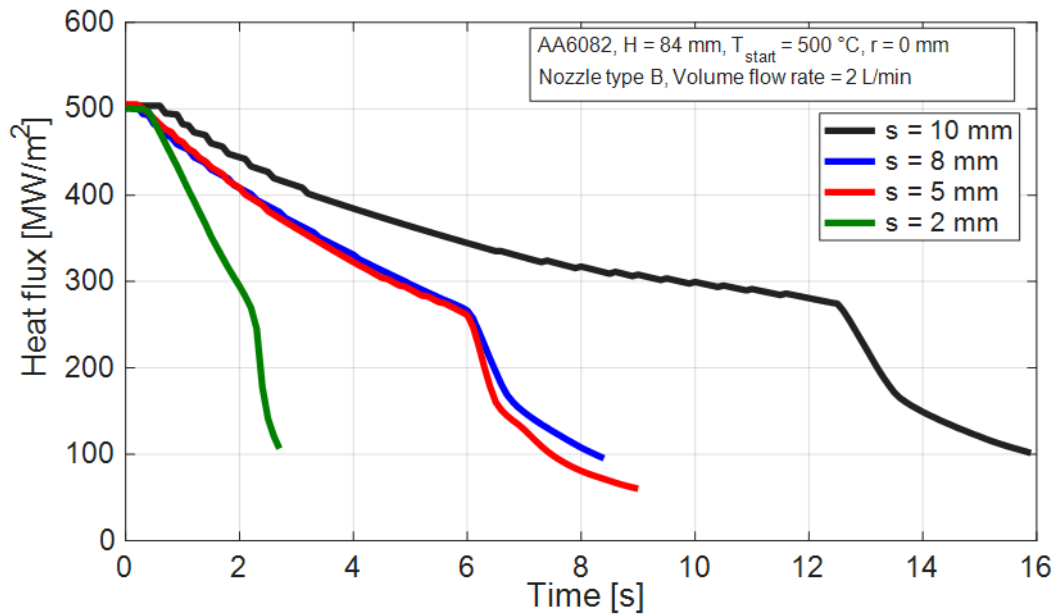


Figure 5.18: Influence of plate thicknesses of AA6082 on cooling curve

The increase in plate thickness from 2 to 10 mm results in a prolonged cooling time. It is noteworthy that there is a distinct temperature difference between the 2 and 5 mm plates, while there is a minimal change between the 5 and 8 mm plates. The cooling process can be divided into two stages: initially, all curves exhibit a slower cooling rate, followed by a rapid temperature drop characterized by a steeper gradient.

These two cooling phases are also evident in the boiling curves presented in Figure 5.19.

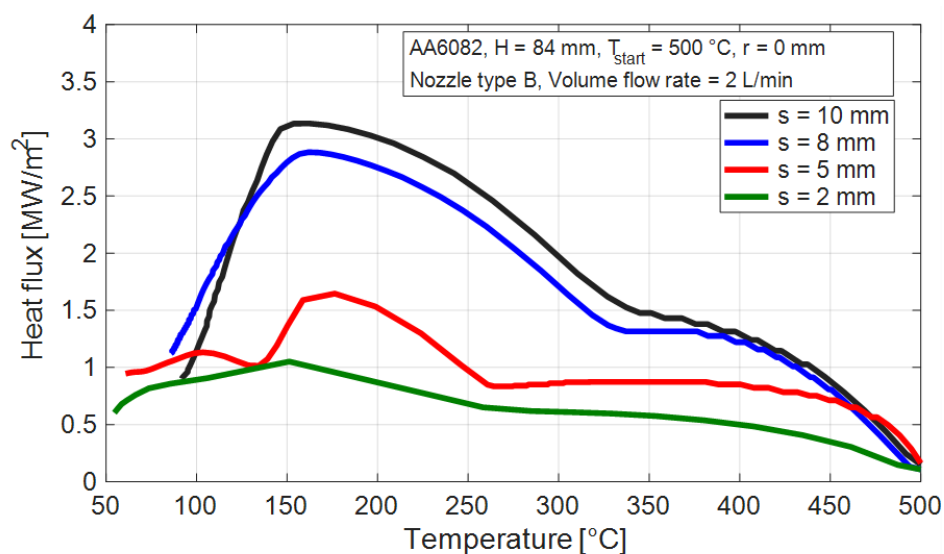


Figure 5.19: Influence of plate thicknesses of AA6082 on boiling curve

The Leidenfrost temperature is observed to be between 280 °C and 320 °C, and it shows an increase with the rise in plate thicknesses. As the thickness of the plate increases from 2 to 10 mm, there is a noticeable increase in the maximum heat flux, reaching its peak at 2.36 MW/m² with the 10 mm thickness. Furthermore, both the DNB temperature and the rewetting temperature exhibit a consistent upward trend with increasing plate thickness. This trend aligns with the findings presented in (Fang, 2019).

Influence of Start Temperature (Nickel)

The start temperature of a 5 mm thick nickel plate is varied between 500 °C and 800 °C to study its effect on heat transfer. Figure 5.20 depicts IR images of the nickel plate at a 4-second cooling period at different start temperatures.

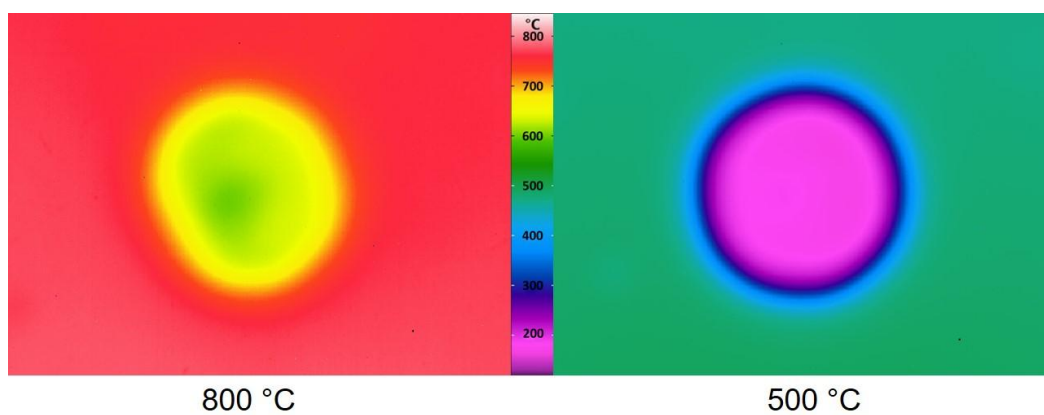


Figure 5.20: IR images of cooling of nickel at different start temperatures at 4 s

After 4 seconds, the plate initially heated to 500 °C is observed to be in the nucleate boiling, whereas the plate starting at 800 °C temperature still exhibits film boiling.

Figure 5.21 illustrates the temperature and corresponding heat flux profiles of nickel plate with varying start temperatures at 4 seconds.

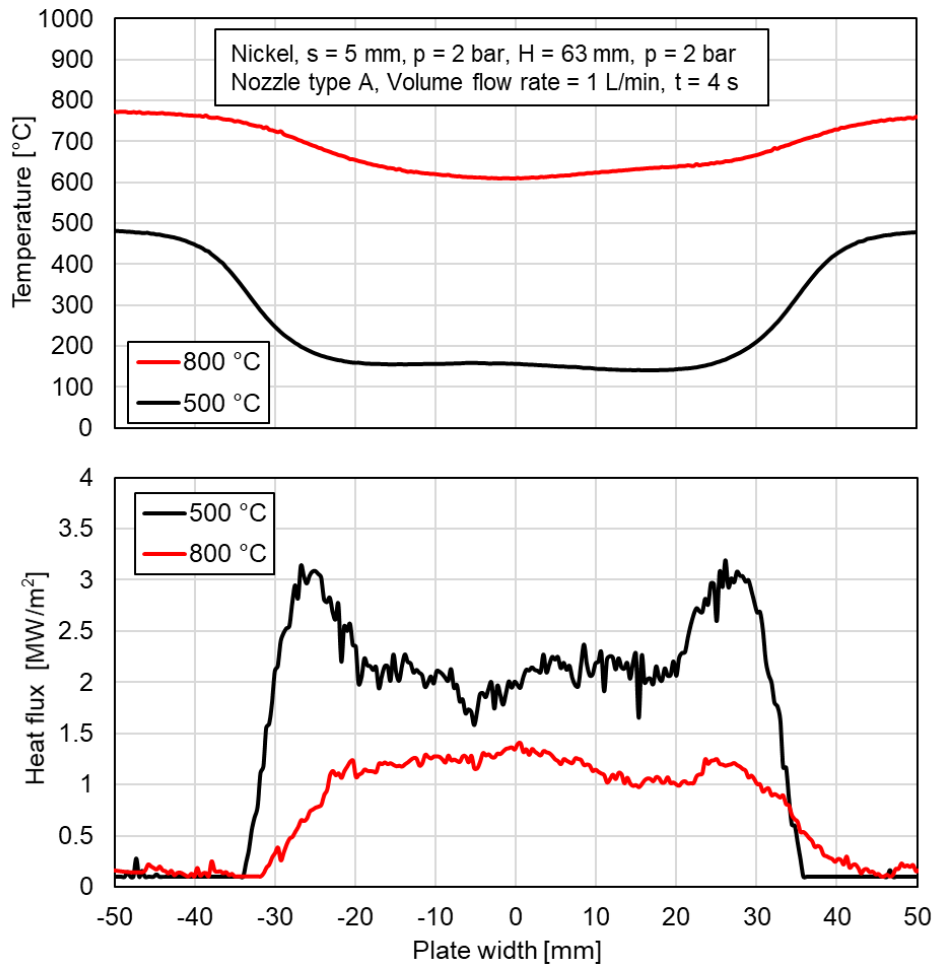


Figure 5.21: Influence of start temperature of nickel on the temperature and heat flux profiles

Throughout the period from 0 to the endpoint, depending on the heat transfer and temperatures, the plate undergoes periods of film boiling, transition boiling, and nucleate boiling. At the 4-second mark, it is evident that the red curve (representing a start temperature of 800 °C) remains within the film boiling region, cooling from 800 °C to 600 °C. In contrast, the black curve indicates the plate in the nucleate boiling region, with temperatures decreasing to 150 °C. Furthermore, it's notable that the temperature gradient is higher for the plate starting at 500 °C compared to 800 °C.

The maximum heat flux is higher for the nickel plate starting at 500 °C compared to 800 °C. Specifically, for the plate starting at 500 °C, two heat flux peaks of 3 MW/m² are observed at -25 mm and +25 mm positions, while in the center of the nozzle, the heat flux fluctuates around 2 MW/m². In contrast, due to film boiling, the heat flux for the plate starting at 800 °C ranges between 1 to 1.4 MW/m², reflecting a lower overall heat transfer rate compared to the plate starting at 500 °C.

The heat transfer varies with time and position on the surface of the plate during the cooling process.

Figure 5.22 shows the decrease in temperature along the cooling time at the center of the nozzle with varying start temperatures.

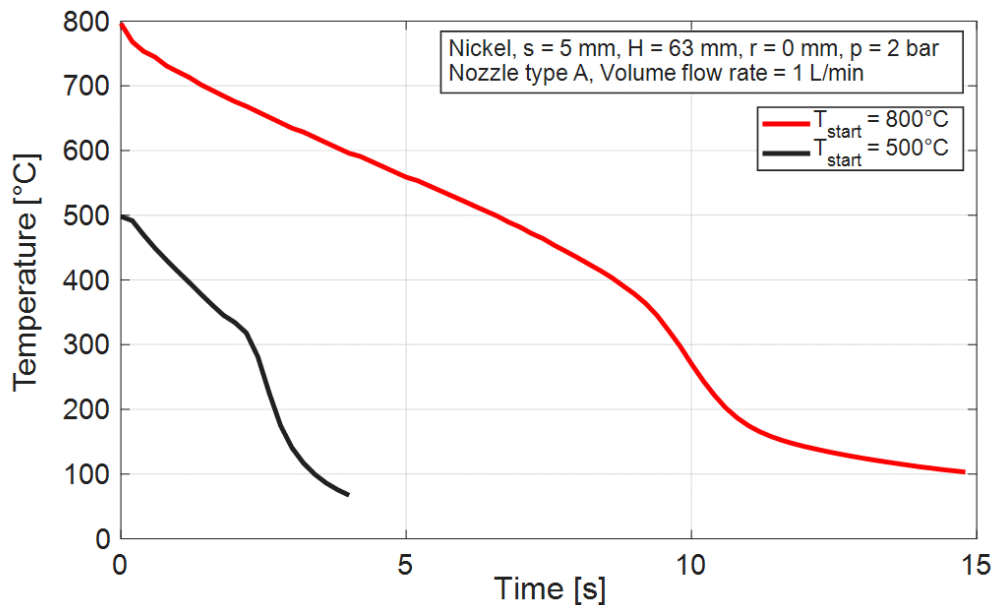


Figure 5.22: Influence of start temperature of nickel on the cooling curve at the center of the nozzle

The plate with a starting temperature of 800°C exhibits a relatively slower cooling rate compared to the one starting at 500°C . The cooling curves can be divided into two distinct sections: initially, the plate cools gradually until reaching a temperature of around 300°C , followed by a sudden drop in temperature. This abrupt temperature decrease is attributed to the transition from partial film boiling to transition boiling, eventually reaching the Leidenfrost temperature of approximately 300°C .

Figure 5.23 shows the boiling curves of the nickel plate with varying start temperatures at the center of the nozzle. It is observed that the maximum heat flux, reaching 2.7 MW/m^2 is for the plate starting at 500°C compared to 800°C . Furthermore, the DNB temperature, as well as the Leidenfrost temperature, show a slight increase with an increase in start temperature.

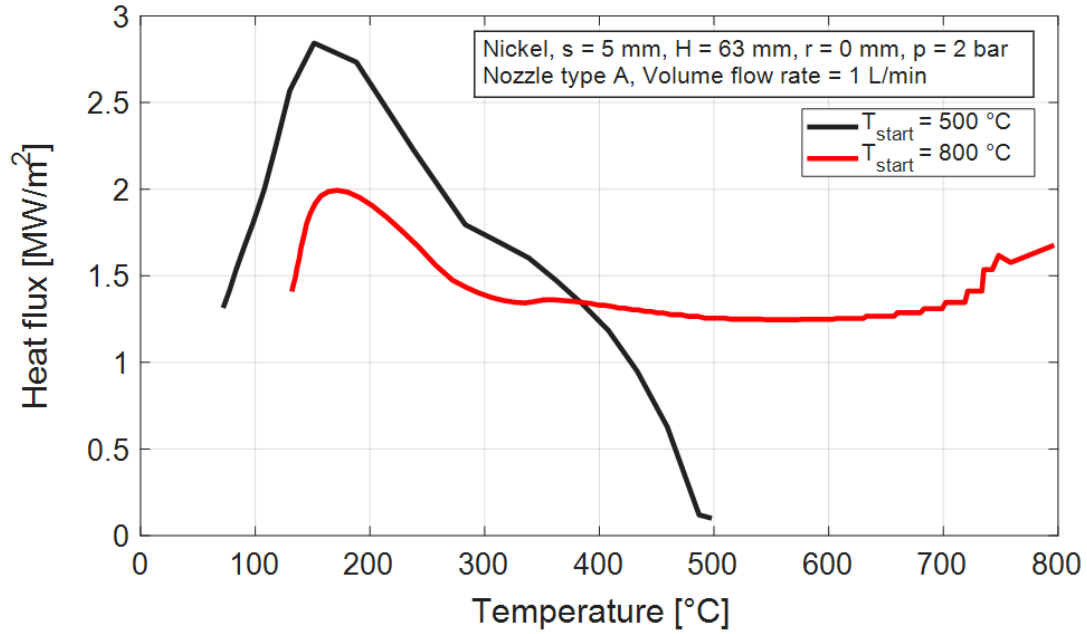


Figure 5.23: Influence of start temperature of nickel on the boiling curve at the center of the nozzle

Influence of Metal Type

Various metals possess distinct material properties that significantly influence the cooling and heat transfer processes. To quantify the impact of these material properties, plates made of nickel and aluminum alloy are subjected to cooling experiments. The experimental conditions maintain a constant height between the nozzle and plate ($H = 63$ mm), a consistent start temperature ($T_{\text{start}} = 500$ °C), plate thickness ($s = 5$ mm), and nozzle pressure ($p = 2$ bar). The specific material properties of these metals are outlined in section 3.4.4, Table 4.

Figure 5.24 presents the IR images captured during the cooling process of 5 mm thick nickel and aluminum alloy after 4 seconds of cooling.

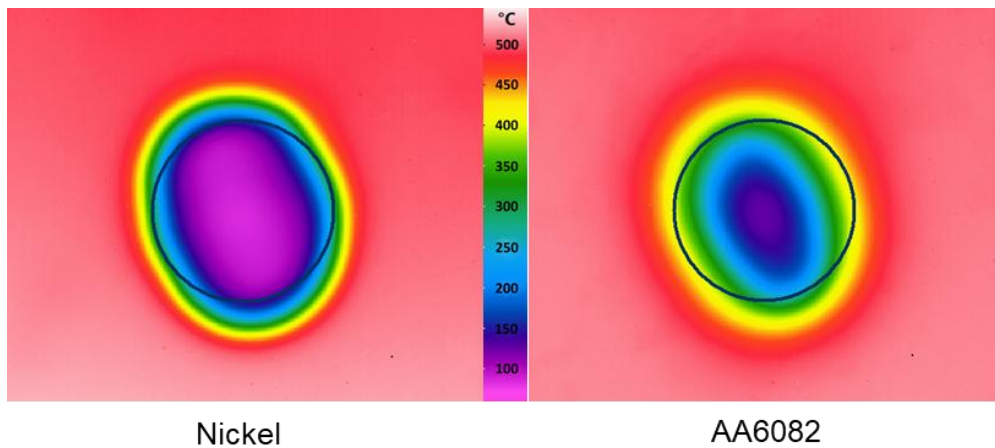


Figure 5.24: IR image of nickel and AA6082 plates during cooling at 4 sec

In the images, the round-shaped impact area of the spray is depicted in black, while the development of the wetting front on the surface of the metals is observed. Due to the higher thermal conductivity of the aluminum alloy plate, a higher radial heat conduction occurs at the impingement point, leading to a delay in the wetting and the subsequent development of the wetting front. Consequently, at 4 seconds, wetting initiates in the center of the nozzle impact area and gradually spreads outward.

In contrast, the wetting front on the nickel plate is already fully developed by the 4-second mark, covering a larger area compared to the aluminum alloy plate. This difference in wetting behavior between the two metals is attributed to their distinct material properties, particularly thermal conductivity, which affects the heat transfer dynamics during the cooling process.

The temperature and heat flux profiles of both metals at 4 seconds are illustrated in Figure 5.25.

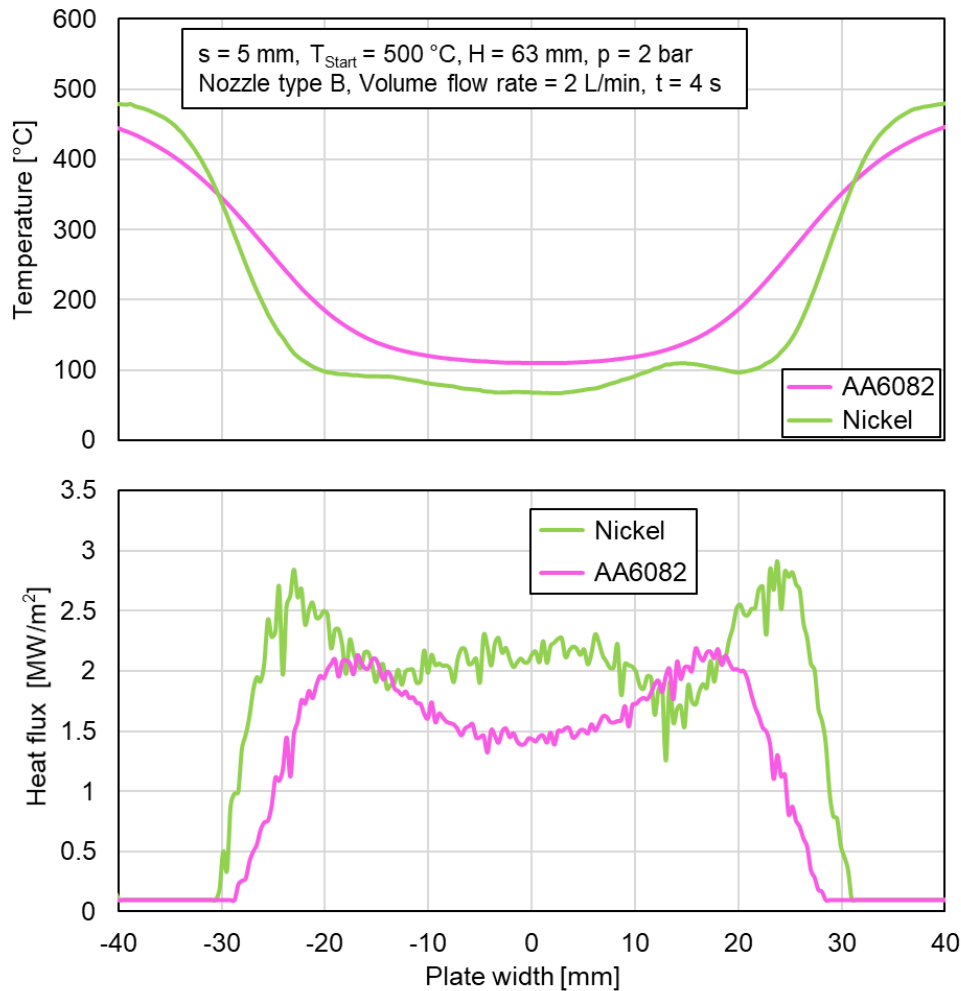


Figure 5.25: Influence of metal type on the temperature profile and heat flux during cooling

It is evident, that the thermal gradient, representing the rate at which the temperature decreases from the start temperature, is higher for the nickel plate compared to aluminum alloy. Furthermore, outside the impacting area, the temperature is notably higher for nickel, with temperatures decreasing approximately from 490 °C to 100 °C. In contrast, for the aluminum alloy plate, the higher radial conduction results in a temperature decrease from 450 °C to 100 °C. This disparity in temperature profiles highlights the differences in heat transfer behavior between nickel and aluminum alloy, with nickel exhibiting a more rapid temperature decrease and maintaining higher temperatures outside the impacting area. Due to the higher thermal gradient experienced by nickel, its heat flux is also higher compared to aluminum alloy. Inside the impact area, an average heat flux of 2 MW/m² for nickel is measured, while for aluminum alloy, it is slightly lower at 1.5 MW/m².

As the wetting front spreads beyond the impact area, different boiling regions develop on the surface of the plate, resulting in variations in heat flux. These variations culminate in maximum heat flux values occurring at the DNB temperature. Specifically, nickel exhibits two peaks of 2.8 MW/m^2 at positions $+25 \text{ mm}$ and -25 mm , while aluminum alloy reaches a maximum heat flux of approximately 2.1 MW/m^2 at positions $+18 \text{ mm}$ and -18 mm .

Figure 5.26 shows the decrease in temperature along the cooling time at the center of the nozzle for nickel and aluminum alloy plates.

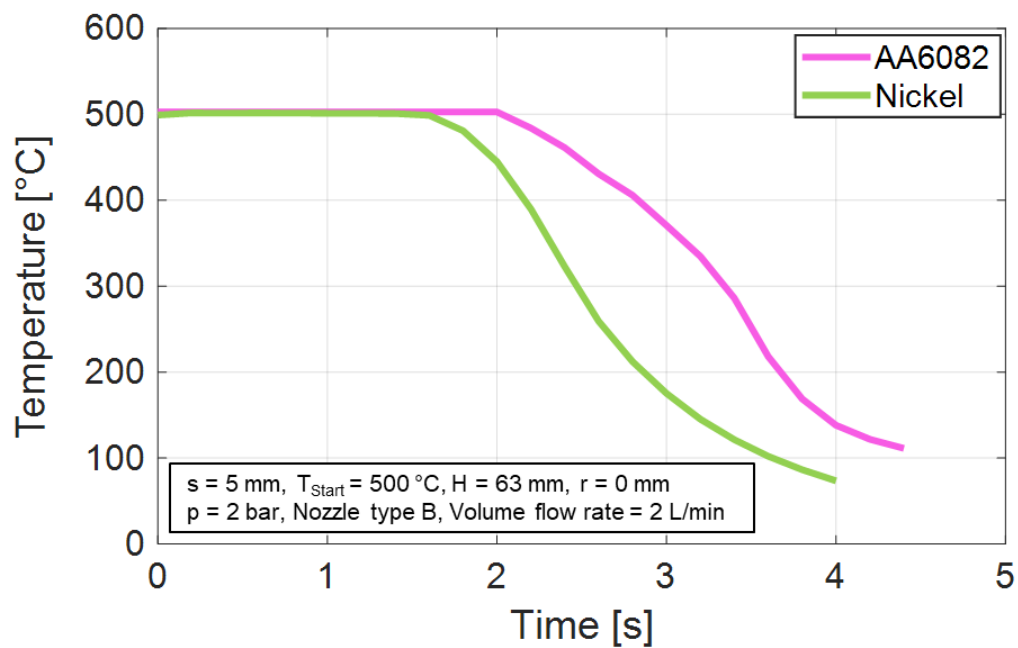


Figure 5.26: Influence of metal type on the cooling curve at the center of the nozzle

In Figure 5.27, the boiling curves for nickel and aluminum alloy are depicted.

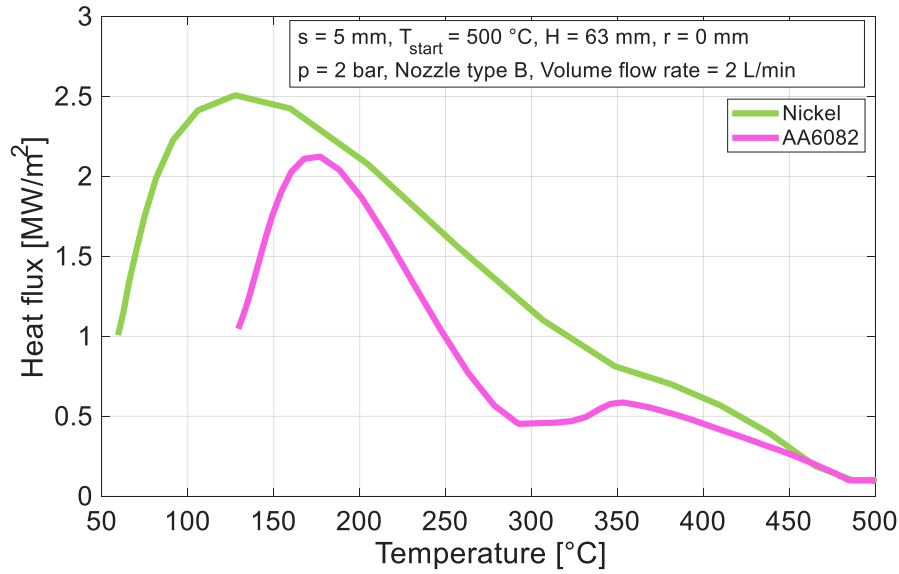


Figure 5.27: Influence of metal type on the boiling curve at the center of the nozzle

Consistent with the observed temperature and heat flux profiles as shown in Figure 5.25, it is evident, that the maximum heat flux for nickel surpasses that of aluminum alloy. Additionally, the rewetting temperature for nickel is approximately 350 °C, while for aluminum alloy, it occurs at around 300 °C. The DNB temperature for aluminum alloy is slightly higher compared to the nickel plate.

5.2.2 Cooling from the Bottom side of the Plate

In the following section, the cooling of plates is presented in which the plates are cooled using a full cone nozzle mounted at the bottom of the plate see, Figure 5.28.

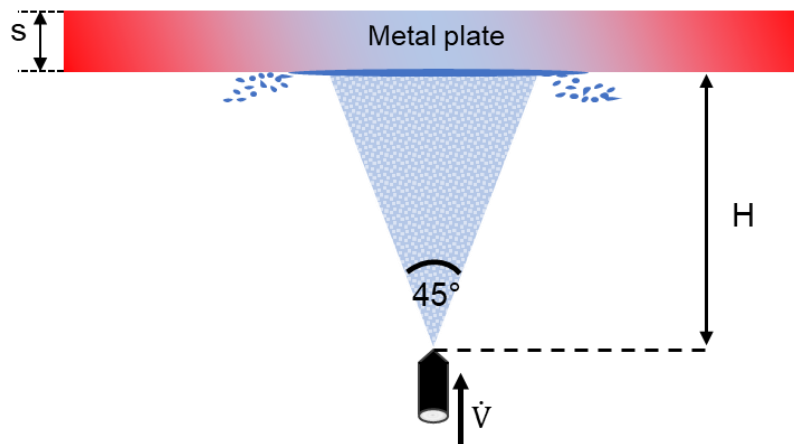


Figure 5.28: Schematics of cooling of a plate from the bottom side

The parameters like nozzle-to-plate distance, plate thickness, metal type, and the volume flow rate of the nozzle are varied. The temperature profiles and the heat fluxes on the surface of the plate are compared for different parameters with cooling from the top side presented above. By changing the orientation of the spray from an upward to a downward direction, the flow mechanism on the surface of the plate influences the heat transfer.

Influence of Nozzle Height

Figure 5.29 illustrates the infrared images capturing the cooling process of 5 mm aluminum alloy plates with varying heights between the nozzle and plate. As the nozzle height increases, the diameter of the impinging nozzle circle expands, leading to a reduction in the spray impingement flux.

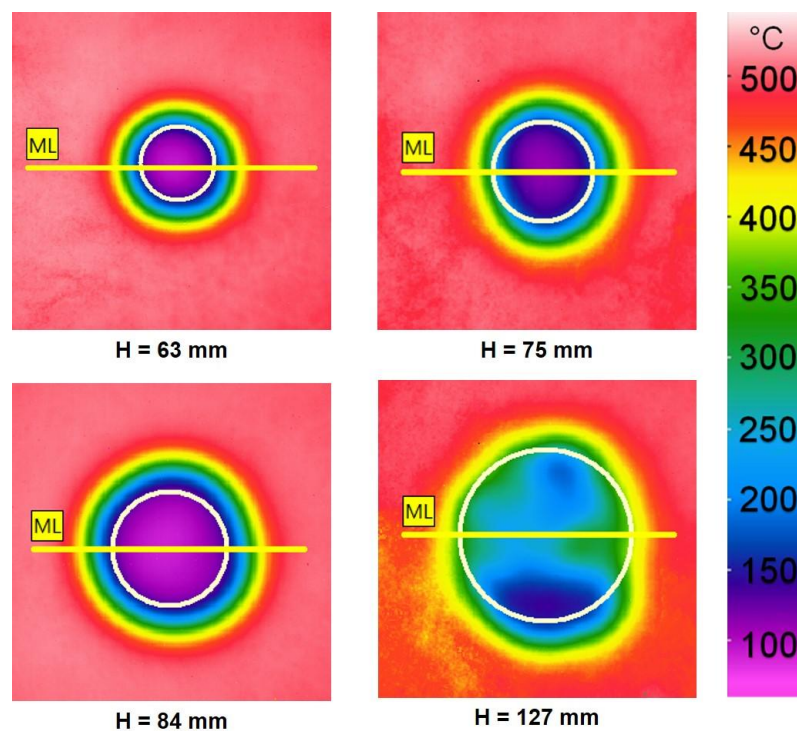


Figure 5.29: IR images of AA6082 plate with various nozzle-to-plate heights after 4 seconds of cooling

The trend observed during cooling from the bottom side mirrors that for cooling from the top side, increasing nozzle height causes similar effects on the cooling process. However, at higher nozzle heights, specifically for $H = 127$ mm, non-uniform and non-

homogeneous cooling patterns become apparent, indicating variations in heat transfer across the plate surface.

Figure 5.30 shows the corresponding infrared images of the temperatures and heat fluxes along the plate width.

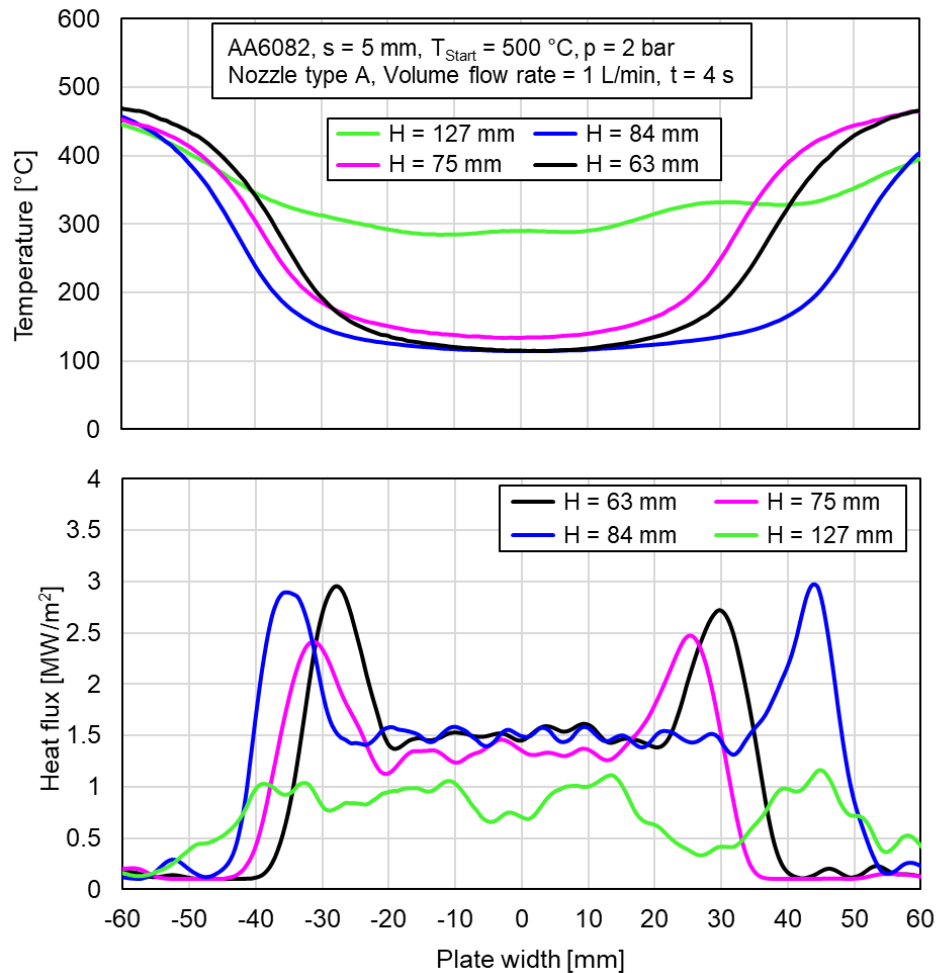


Figure 5.30: Influence of nozzle height on temperature and heat flux profiles along the plate width during cooling

The boiling curves at various nozzle heights are illustrated in Figure 5.31. There is no significant change in rewetting and DNB temperatures compared to nozzle height variation from the top-side cooling.

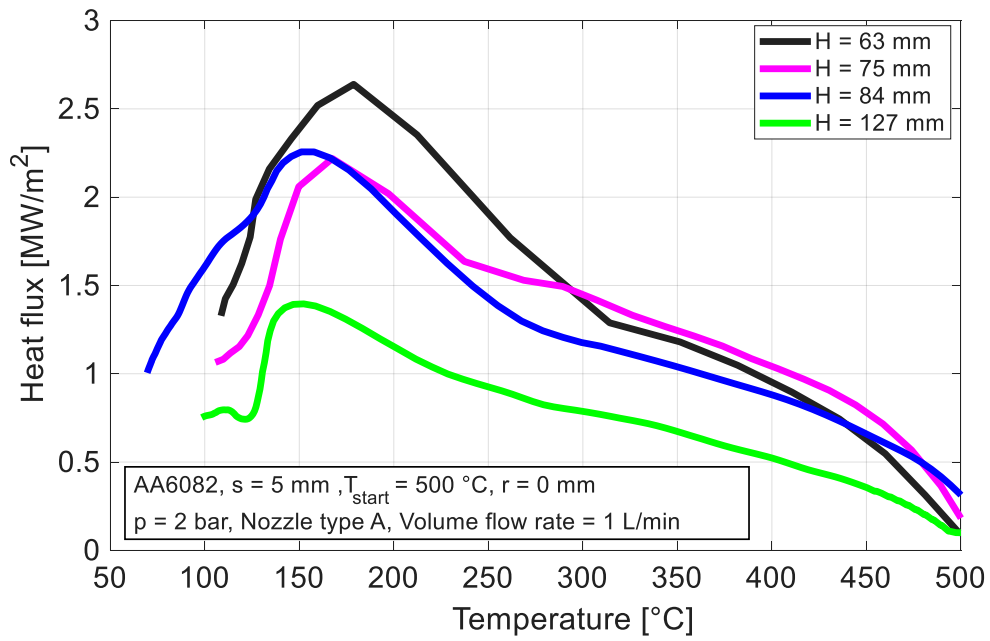


Figure 5.31: Influence of nozzle height on the boiling curve of AA6082

Figure 5.32 shows the temperature and heat flux along the plate width at various nozzle heights for 5 mm nickel.

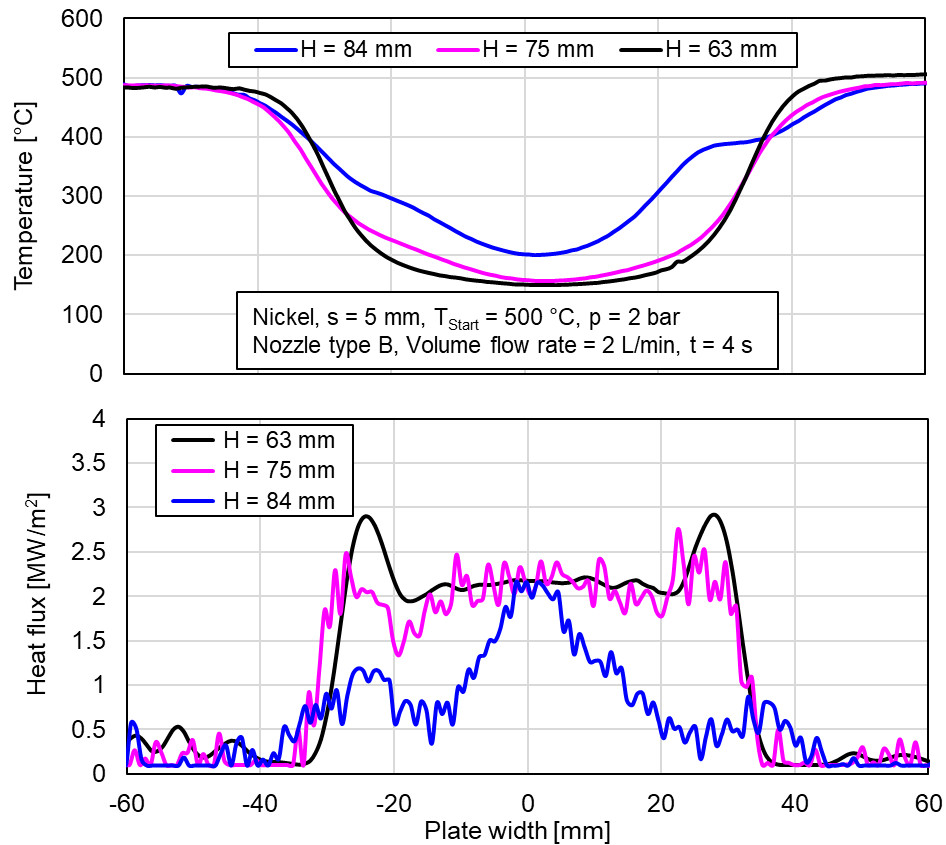


Figure 5.32: Influence of nozzle height on temperature and heat flux profiles of nickel during cooling

Influence of Plate Thickness (AA6082)

In Figure 5.33, the boiling curve for the cooling of aluminum alloy plates with thicknesses of 5 and 10 mm is illustrated. Bottom-side cooling exhibits a similar trend as top-side cooling, with the maximum heat flux increasing for thicker plates. The heat flux gradually rises for both plate thicknesses until approximately 300 °C, after which it sharply increases, reaching its peak value at a temperature of 150 °C.

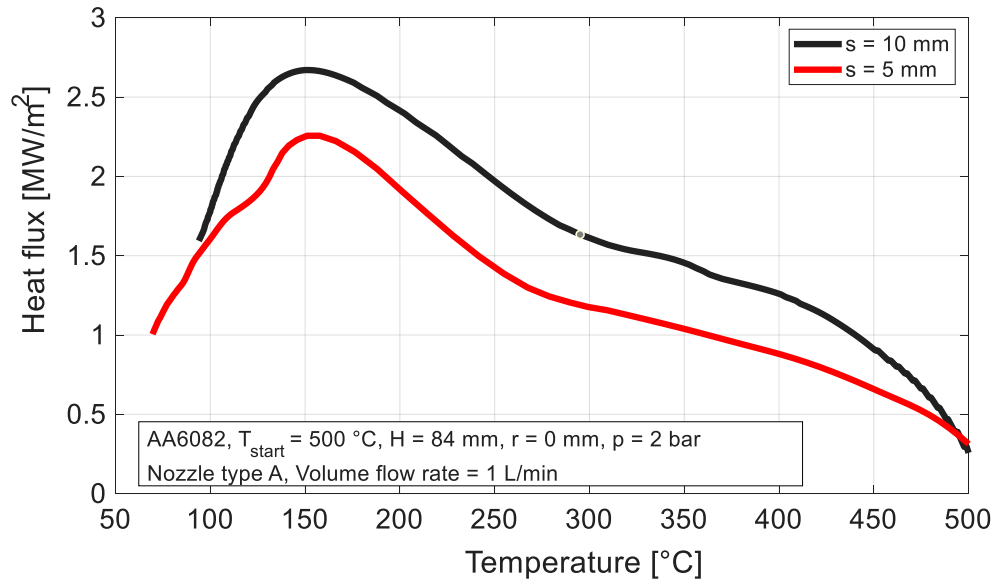


Figure 5.33: Influence of metal thickness of AA6082 on the boiling curve

The DNB temperature remains consistent at 150 °C, as observed during cooling from the top side.

5.2.3 Comparison of Top and Bottom Side Cooling

Figure 5.34 shows the IR images of the top side and bottom side cooling of 5 mm aluminum alloy at a constant nozzle height.

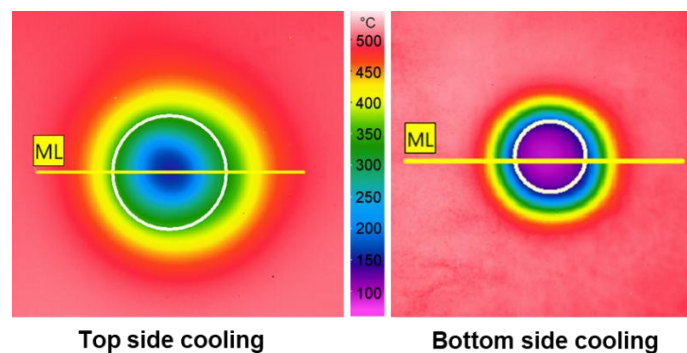


Figure 5.34: Infrared images of top and bottom side cooling (AA6082)

Notably, at the 4-second mark, the formation and propagation of the wetting front are observed to occur more rapidly during bottom-side cooling. Furthermore, at 4 seconds

the temperature inside the impacting area for top-side cooling is higher, compared to the bottom-side cooling.

The temperature and heat flux profiles corresponding to the infrared images mentioned above are presented in Figure 5.35.

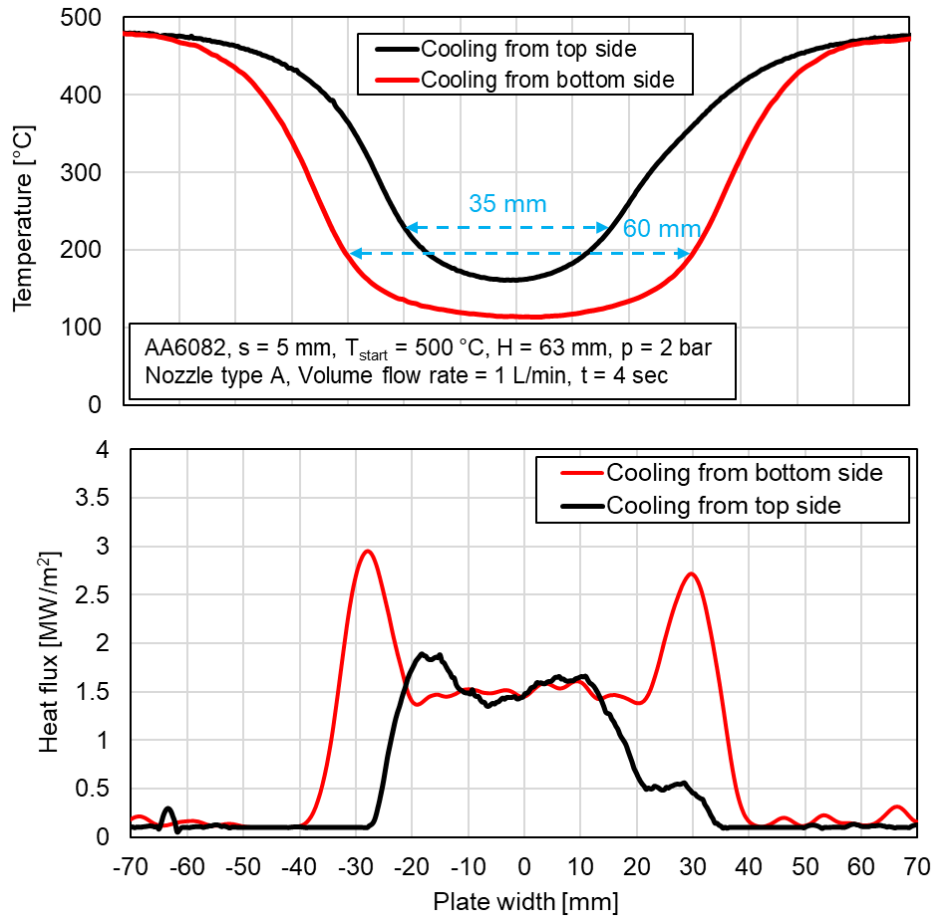


Figure 5.35: Influence of cooling side on temperature and heat flux profiles (AA6082)

The width of the wetting front is larger during bottom-side cooling, consistent with observations from the IR images. Specifically, the width of the wetting front for bottom-side cooling is approximately 60 mm, whereas it measures around 35 mm for top-side cooling. The maximum heat flux in the nucleate boiling region is higher for bottom-side cooling.

Figure 5.36 depicts a comparison of the boiling curves for bottom-side and top-side cooling at two nozzle heights; 63 and 127 mm.

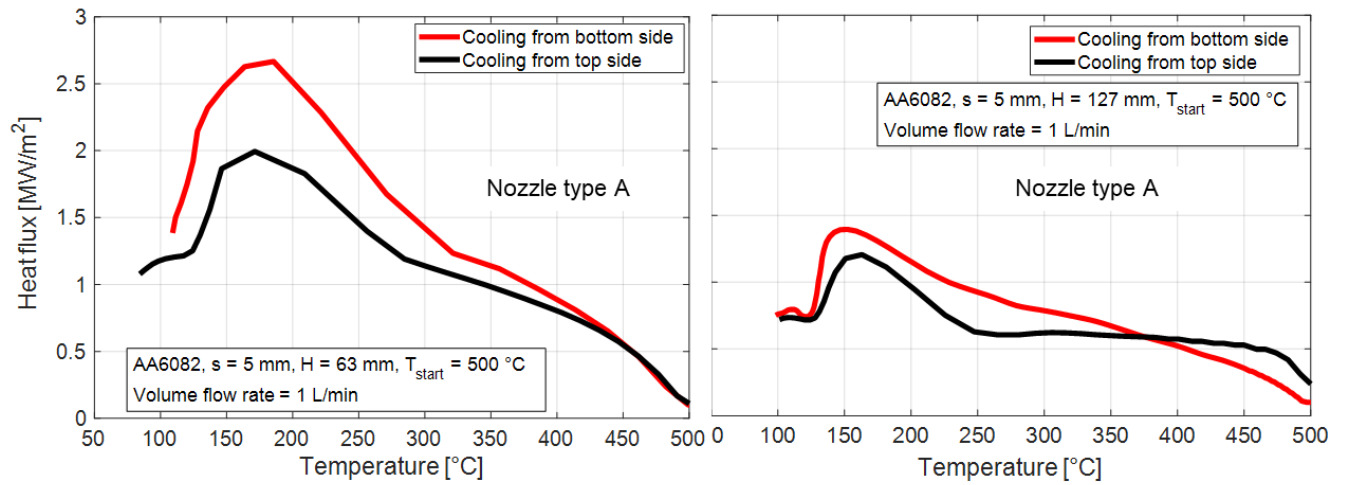


Figure 5.36: Influence of the cooling side on the boiling curve of AA6082

Remarkably, at both observed nozzle heights, the maximum heat flux is higher for bottom-side cooling, while the DNB temperature remains relatively constant. Furthermore, the rewetting temperature for top-side cooling is observed to be approximately 40 °C lower compared to bottom-side cooling.

Figure 5.37 and Figure 5.38 illustrate a 3D comparison between the top-side and bottom-side cooling of aluminum alloy plates at a nozzle height of 63 mm for nozzle B and nozzle A, respectively.

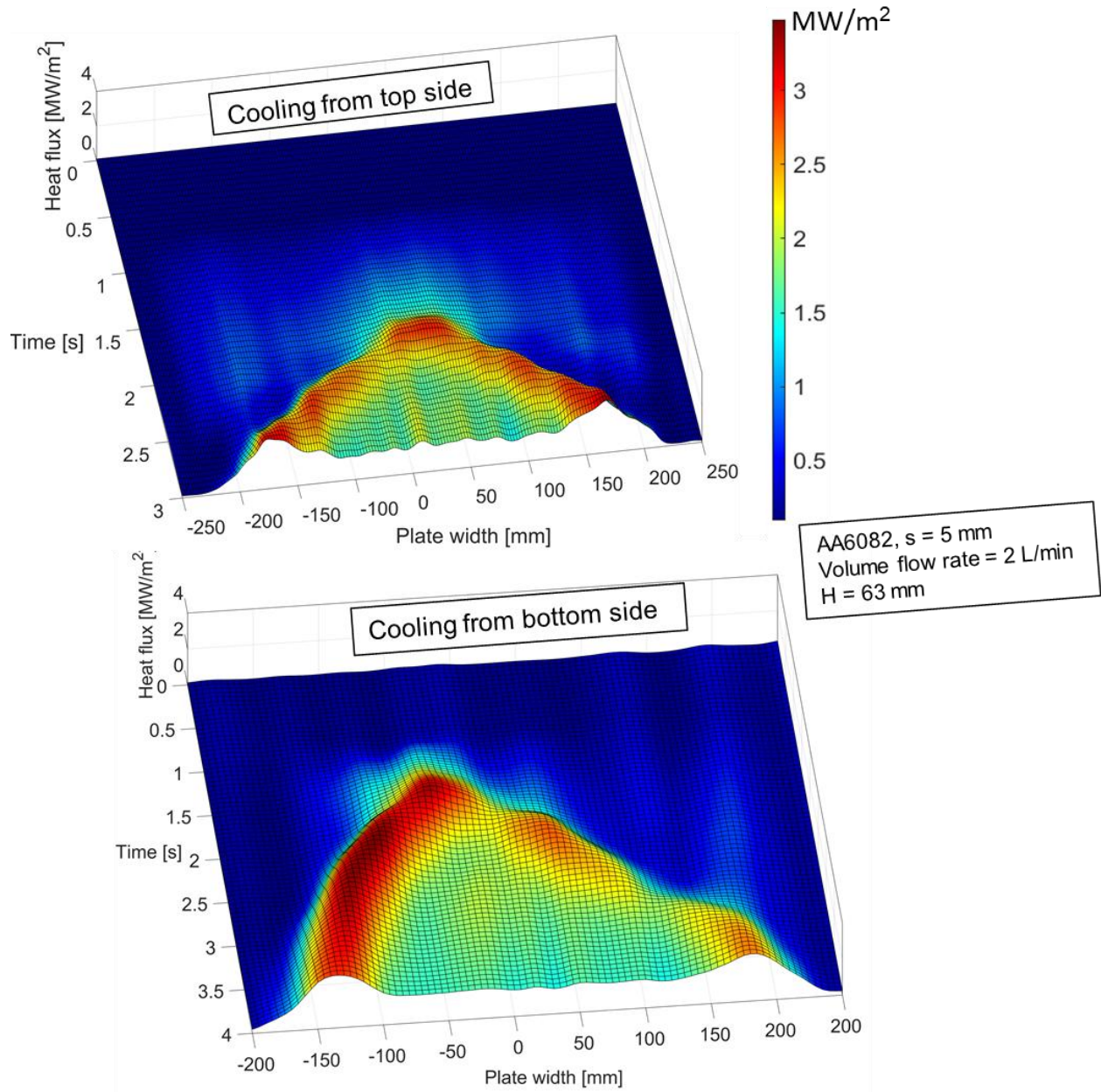


Figure 5.37: Surface heat fluxes of AA6082 for bottom and top side cooling (Nozzle type B)

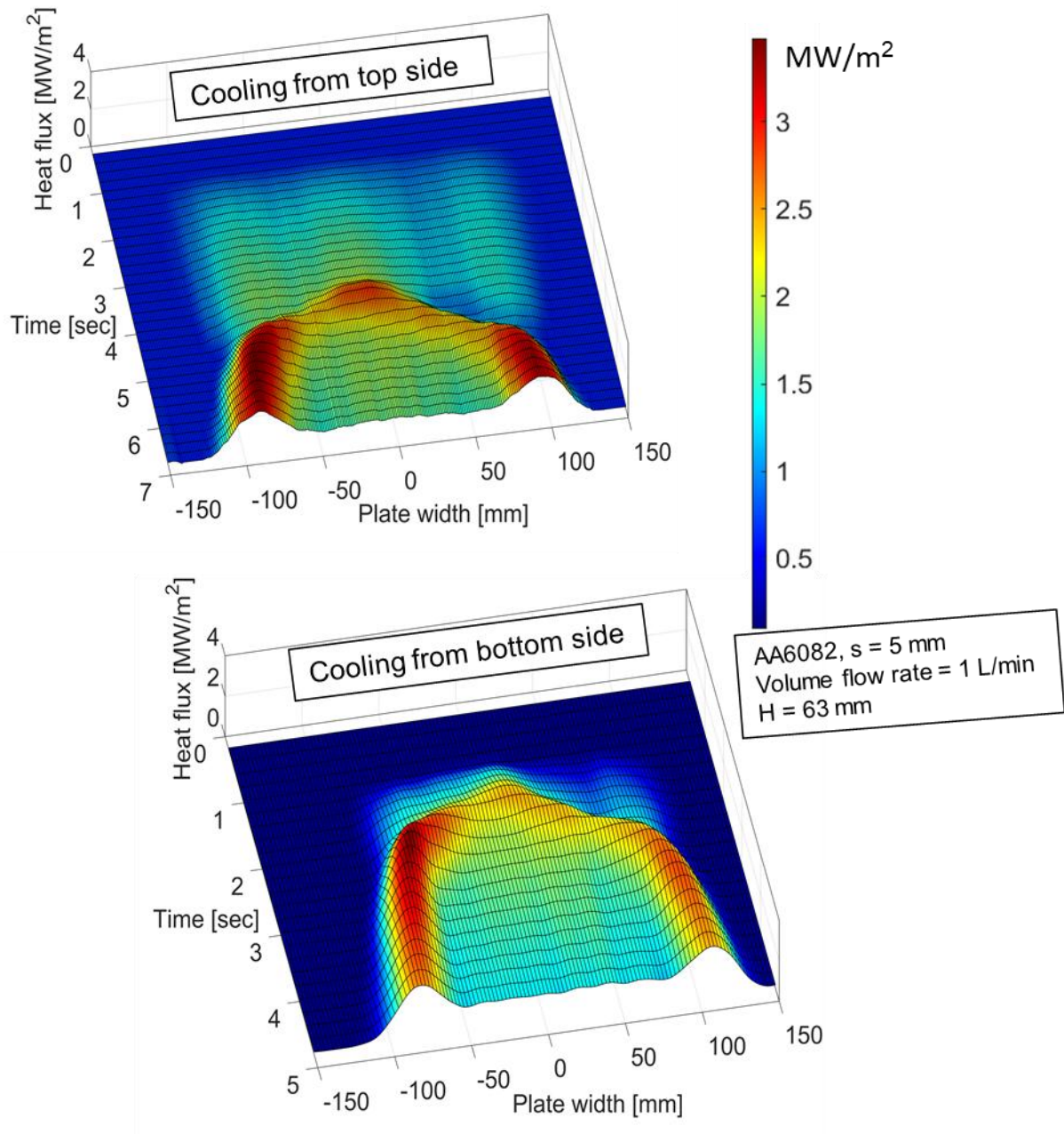


Figure 5.38: Surface heat fluxes of AA6082 for bottom and top side cooling (Nozzle type A)

The surf plot illustrates the heat flux distribution along the plate width at various time intervals, revealing several observations: Rewetting is comparatively faster for bottom-side cooling, whereas the partial film boiling region, where the plate cools slower with minimum heat flux, is longer in case of top-side cooling. Following rewetting, the maximum heat flux is observed in the vicinity of the nozzle center. As the wetting front propagates, the heat flux remains relatively constant near the center of the nozzle. As the wetting front propagates outwards, various boiling regions occur on the surface of

the plate, reaching maximum heat fluxes in the nucleate boiling region. The presence of two heat flux peaks in the positive and negative plate widths indicates nucleate boiling regions.

Figure 5.39 shows a similar heat flux surf plot for cooling a nickel plate. Nickel exhibits a trend similar to that of aluminum alloy plates. Moreover, bottom-side cooling demonstrates comparatively uniform heat transfer with minimal heat flux fluctuations along the plate width.

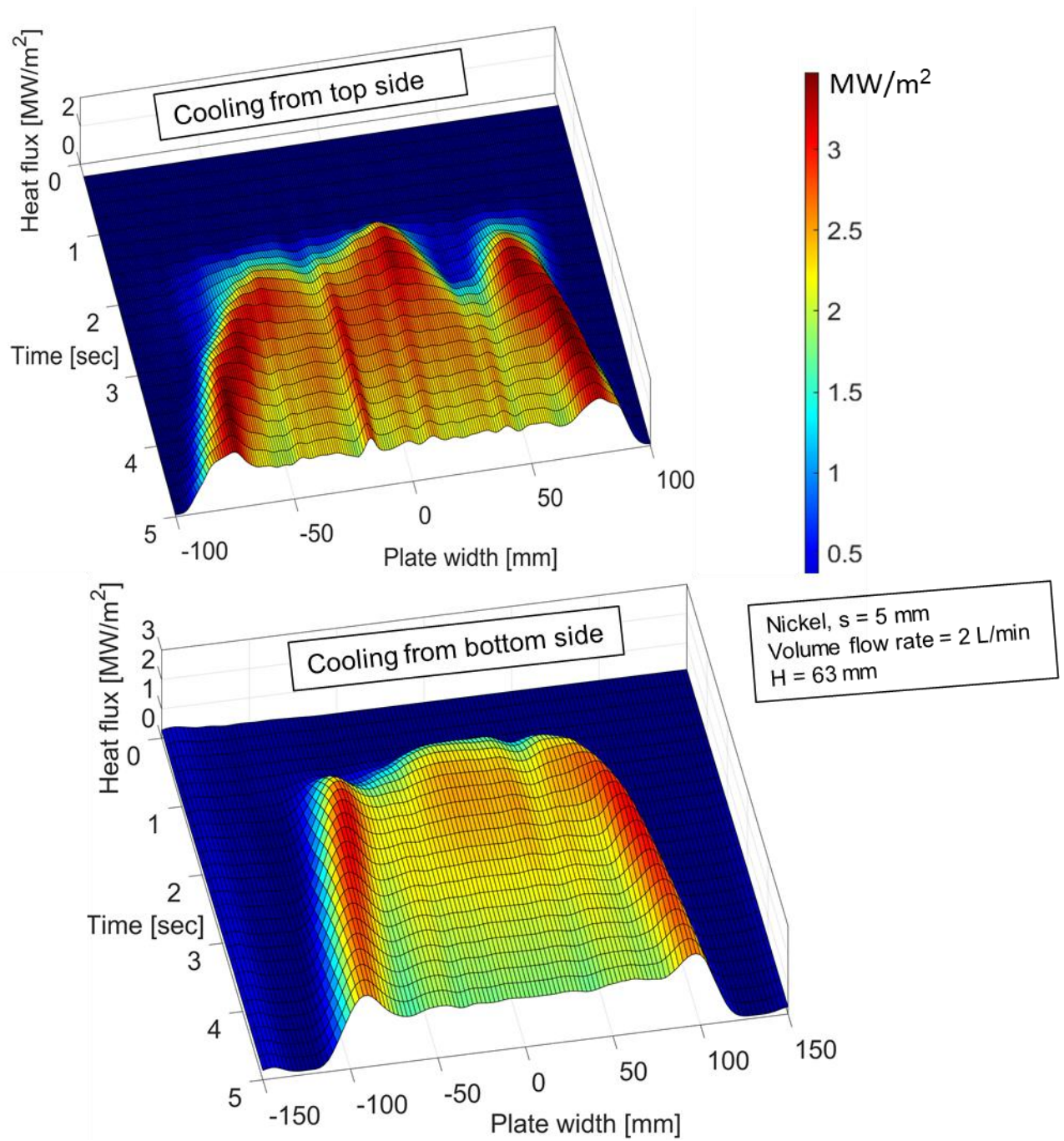


Figure 5.39: Surface heat fluxes of nickel for bottom and top side cooling (Nozzle type B)

5.3 Single Full Cone Nozzle (Moving)

Heat transfer mechanism in cooling of moving horizontal plates is investigated for some chosen parameters from the stationary case. The moving plates of aluminum alloy and nickel are quenched using a single full cone nozzle and nozzle fields. The plate velocity (w_p) varies from 30 to 60 mm/s. The cooling starts with the impingement of the full cone nozzle on the right edge of the plate, as the plate starts moving from left to right with a constant velocity under controlled conditions. The Eulerian coordinate system is defined to track the temperature profiles relative to a fixed point in space. In this context, the coordinate z^* is oriented in the direction of the plate's movement, with $z^* = 0$ marking the center of the nozzle impingement point. As time progresses, the plate moves while the spatial position of the nozzle impingement point remains fixed at $z^* = 0$, see Figure 5.40.

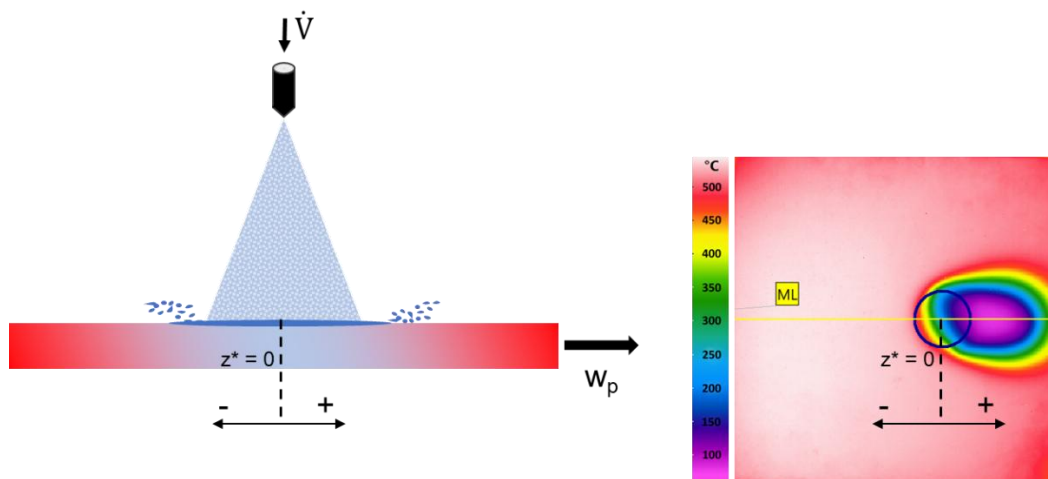


Figure 5.40: Schematics of impingement of moving plate and Eulerian coordinate z^*

The nozzle center is indicated with $z^* = 0$ as spray impinges on the plate. The upstream and downstream plate regions are indicated respectively $-z^*$ and $+z^*$.

The resulting temperature profiles are plotted against the Eulerian coordinate z^* . Figure 5.41 depicts the temperature profiles and corresponding IR images during the cooling of the aluminum alloy plate as it moves with $w_p = 5$ mm/s plate velocity.

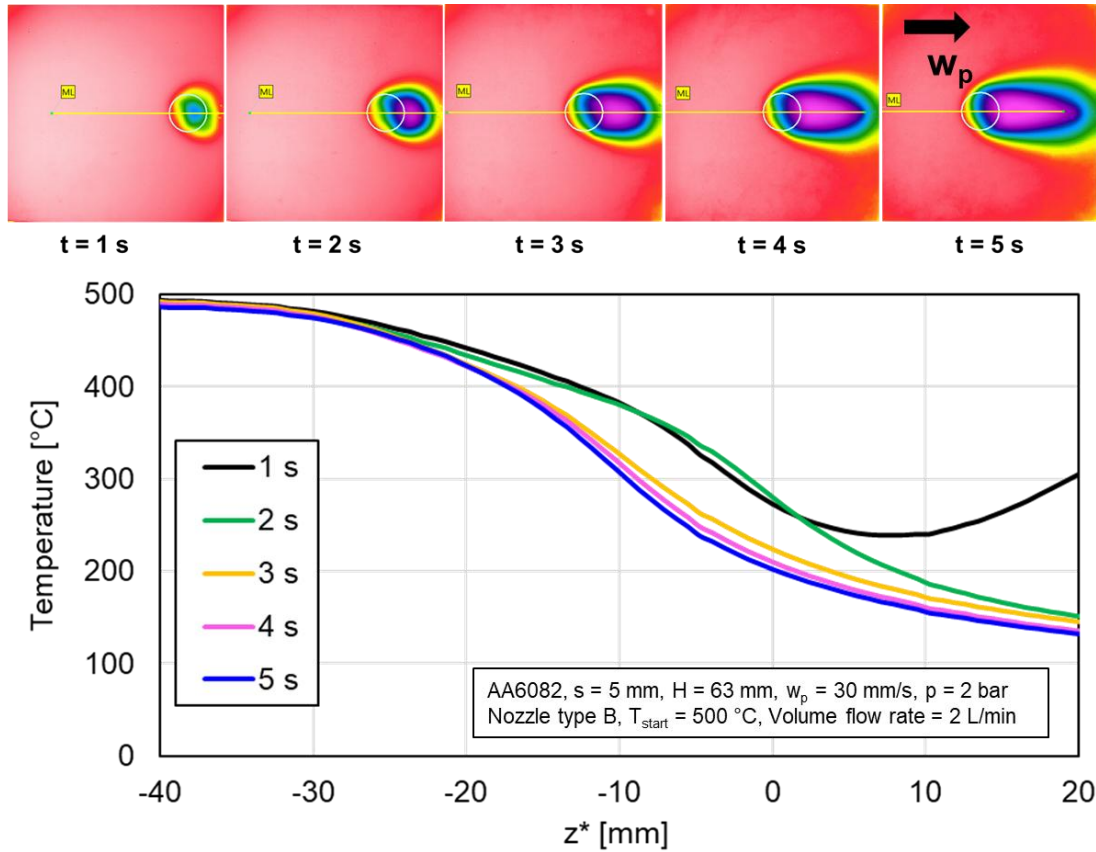


Figure 5.41: Temperature profiles of moving AA6082 plate and IR images at various time intervals

As the plate moves from left to right, initial impingement occurs at 1 second, resulting in a temperature drop from 500 °C to 250 °C. Subsequently, as the plate continues its movement, the temperature in the impingement region or at the center of the nozzle ($z^* = 0\text{ mm}$) decreases further to 200 °C. Notably, after a time interval of 3 seconds, the plate reaches an Eulerian steady state, characterized by temperature curves and gradients that become more uniform and consistent.

5.3.1 Cooling from the Top Side of the Plate

Nickel and aluminum alloy plates, each with a thickness of 5 mm, are subjected to cooling experiments involving moving plates from the top side. The velocity of the plate is primarily varied while maintaining a constant nozzle-to-plate height of $H = 63\text{ mm}$. The design of the experimental setup for top-side cooling in moving experiments presents limitations in capturing comprehensive temperature data throughout the entire cooling process.

Due to these constraints, temperature measurements are restricted to the initial 20 mm of the plate, as depicted in the infrared image below in Figure 5.42.

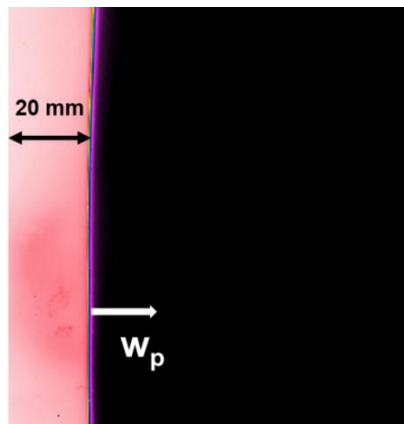


Figure 5.42: IR image of 5 mm moving AA6082 plate at $t = 0$ sec (cooling from the top side)

Consequently, conducting heat flux calculations becomes impractical, as the inverse heat conduction model necessitates temperature data for the entire plate at all times.

Influence of Plate Velocity

When comparing cooling curves for different plate velocities, the temperatures are plotted at the same plate movement distance of 120 mm. For this reason, the cooling time differs.

Figure 5.43 depicts the temperature profiles of 5 mm thick aluminum alloy plates, cooled with a plate velocity of 30 and 45 mm/s.

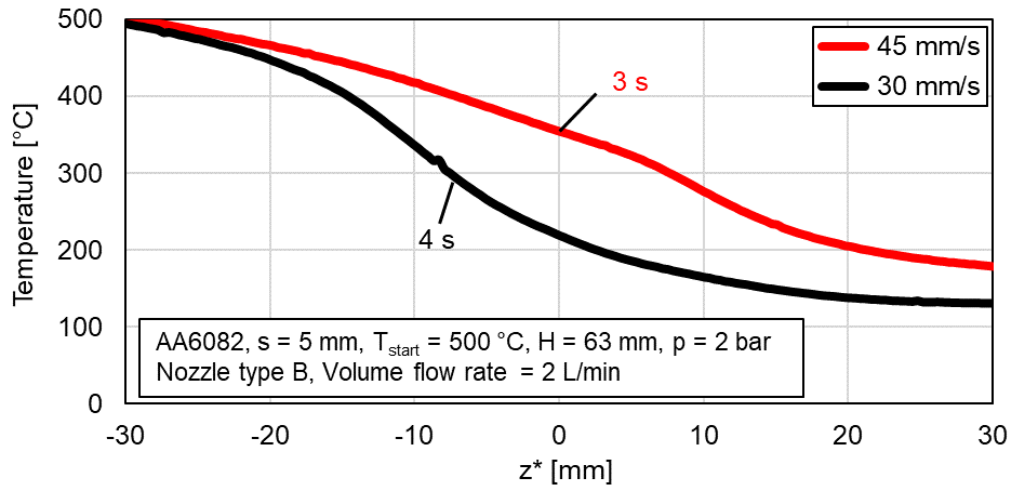


Figure 5.43: Influence of plate velocity on the cooling of 5 mm AA6082 plate

The plate experiences uniform cooling from 500 °C at both plate velocities. In the figure, the negative x-axis represents the upstream region, while the positive x-axis represents the downstream region. $z^* = 0$ mm indicates the center of the nozzle impact circle. The observed decrease in temperature before the 0 mm mark is attributed to a combination of axial heat conduction and the impingement of the 26 mm diameter spray circle. Notably, the temperature at the center of the circle or in the vicinity of the nozzle region increases, as the plate velocity increases.

The temperature profiles of the moving 5 mm nickel plate at various plate velocities are shown in Figure 5.44.

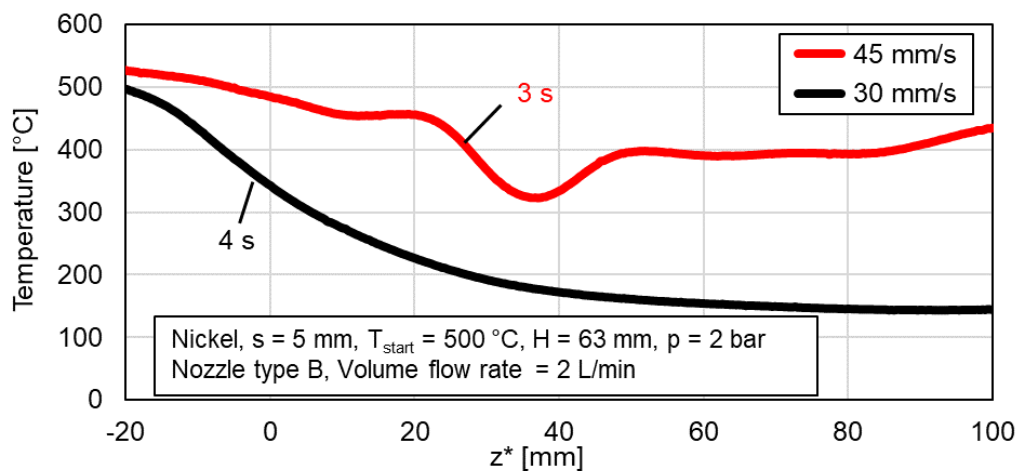


Figure 5.44: Influence of plate velocity on the cooling of 5 mm nickel plate

With an increase in plate velocity for nickel from 30 to 45 mm/s, non-uniform cooling is evident. The plate cools only from 500 °C to 400 °C and experiences film boiling, whereas the slowly moving plate cools uniformly to below 200 °C.

Influence of Metal Type

Figure 5.45 shows the comparison of nickel and aluminum alloy, moving with a constant plate velocity of 30 mm/s.

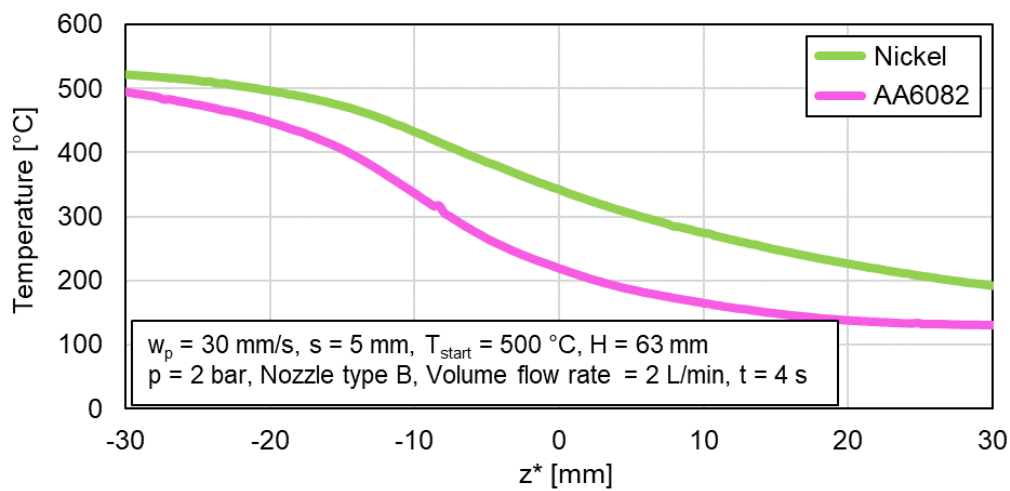


Figure 5.45: Influence of the metal type at a plate velocity of 30 mm/s

The pre-cooling effect in the upstream region is more pronounced in the case of aluminum alloy compared to nickel. Additionally, the temperature at the center of the nozzle measures 210 °C for aluminum alloy and 350 °C for nickel.

5.3.2 Cooling from the Bottom Side of the Plate

In the cooling process from the bottom side, similar parameters are utilized as in the cooling process from the top side of the plate. Additionally, the heat flux profiles of the moving plate are presented, as it was possible to measure temperatures across the entire plate during bottom-side cooling.

Influence of Plate Velocity

Figure 5.46 illustrates the IR images and the corresponding temperature profiles of the aluminum alloy plate with varying plate velocities at 90 mm plate movement.

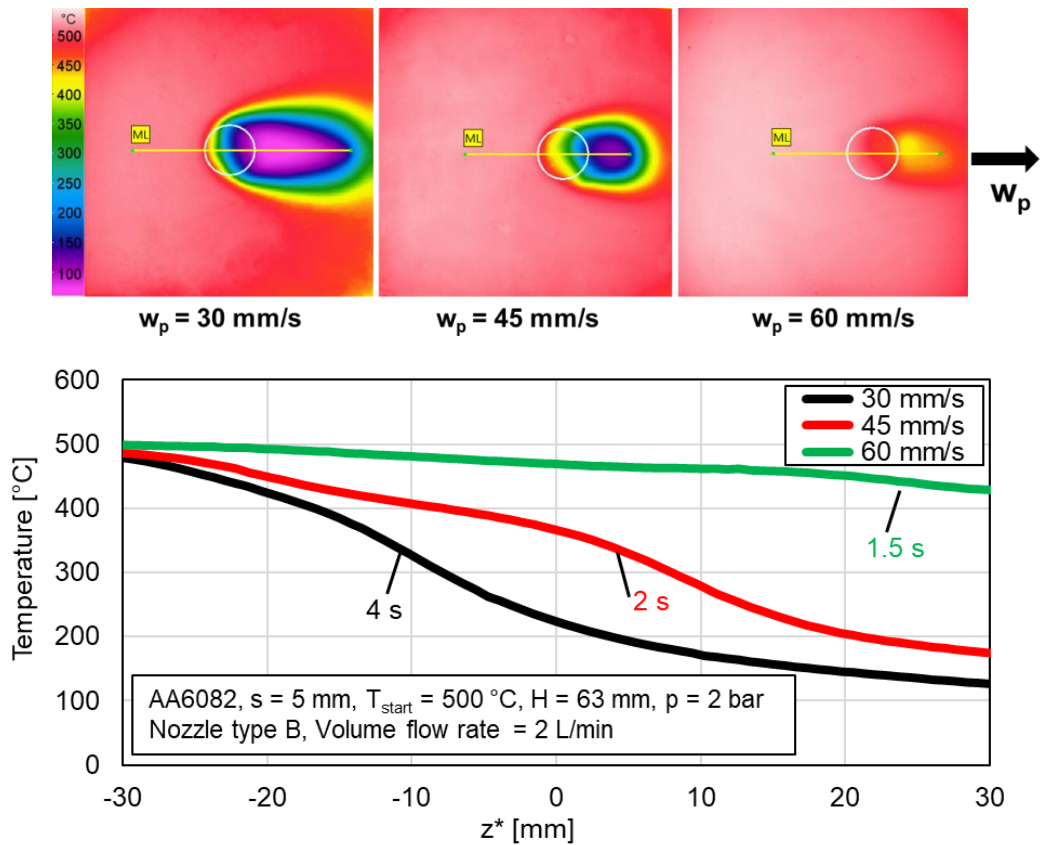


Figure 5.46: Comparison of temperature profiles and IR images at various plate velocities (AA6082)

As the plate velocity increases, both, axial heat conduction and the rate of cooling decrease. Concurrently, the temperature in the vicinity of the nozzle impact area rises from 210 °C to 580 °C, with an increase in plate velocity from 30 to 60 mm/s.

Figure 5.47 shows the heat flux profiles at various plate velocities.

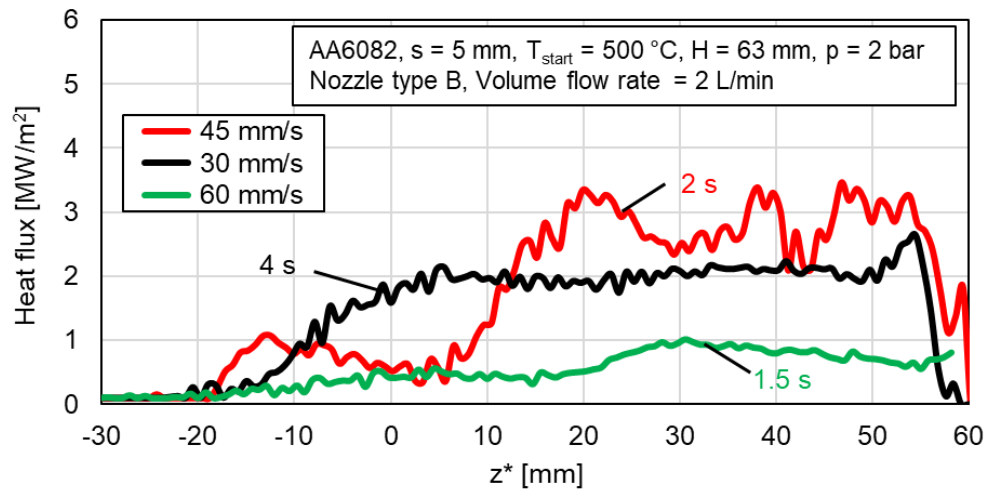


Figure 5.47: Comparison of Heat fluxes of AA6082 at various plate velocities

Heat fluxes are minimal in the upstream region ($-z^*$ region), due to the presence of dry and film-boiling regions. The heat flux gradually increases as the nozzle impingement or wetting front progresses, peaking at 2 MW/m^2 for 30 mm/s and 3.2 MW/m^2 for 45 mm/s plate velocity, respectively. Subsequently, the heat flux remains constant in the downstream region (wet region). However, at a plate velocity of 60 mm/s , the plate experiences film boiling, as notable in the temperature profile and IR image. Consequently, the heat flux is minimized for this higher plate velocity.

Figure 5.48 shows boiling curves for 5 mm aluminum alloy at various plate velocities.

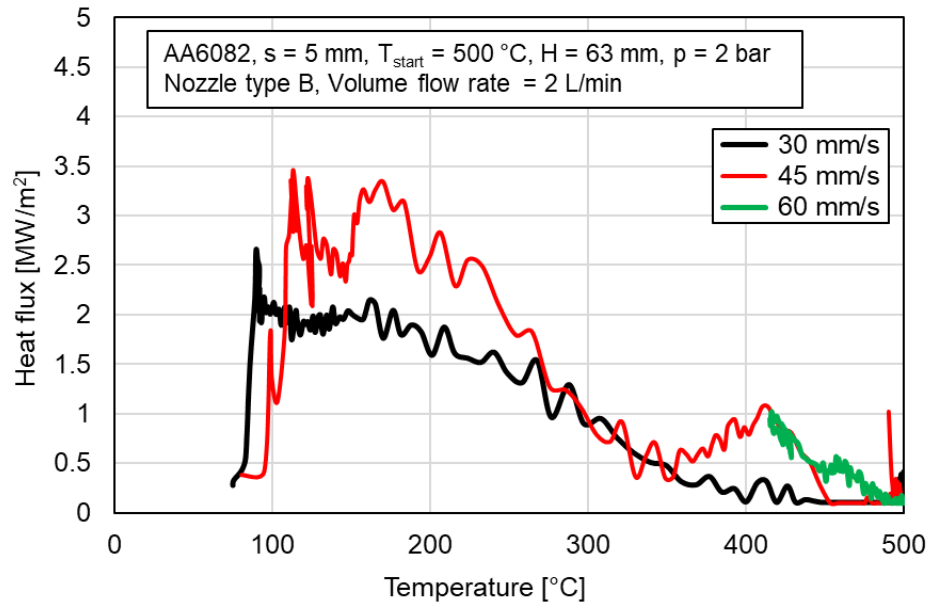


Figure 5.48: Influence of plate velocity on boiling curve of AA6082

The maximum heat flux is higher for a velocity of 45 mm/s, whereas the plate velocity of 60 mm/s is in the film boiling zone with a minimum heat flux.

Figure 5.49 shows the temperature profiles and IR images for nickel at various plate velocities.

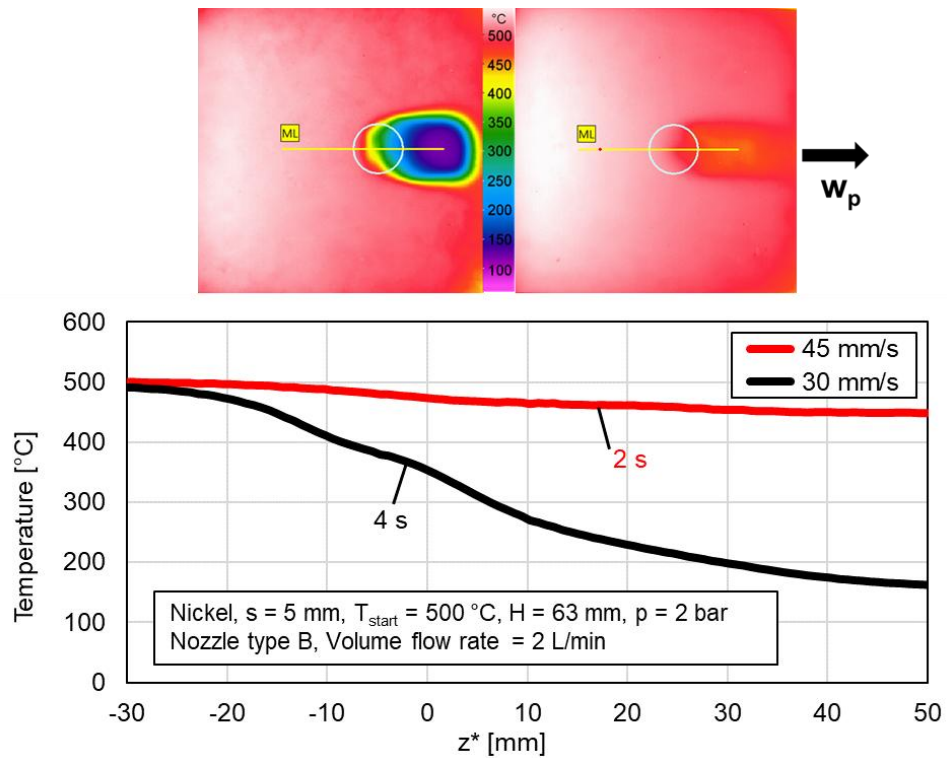


Figure 5.49: Comparison of temperature profiles and IR images at various plate velocities (nickel)

At lower plate velocities, nickel undergoes a decrease in temperature from 500 °C to 130 °C, with a temperature of 350 °C at $z^* = 0$ mm. However, at higher velocities, nickel experiences film boiling at 45 mm/s. In contrast, aluminum alloy experiences film boiling at 60 mm/s.

Figure 5.50 shows the heat flux profiles along the plate length at various plate velocities for nickel.

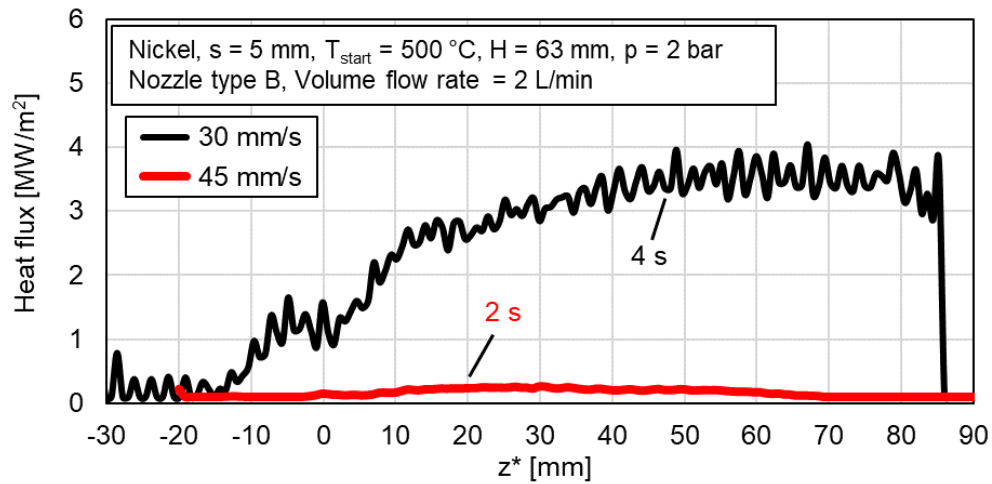


Figure 5.50: Comparison of heat fluxes at various plate velocities (nickel)

The average heat flux in the downstream region is around 3.5 MW/m^2 at a plate velocity of 30 mm/s , whereas at 45 mm/s plate is at a higher temperature in a film boiling region.

5.3.3 Comparison of Top and Bottom Side Cooling

Figure 5.51 and Figure 5.52 compare the top-side and bottom-side cooling and show the influence of the cooling side on the temperature profiles at 30 mm/s respectively for aluminum alloy and nickel.

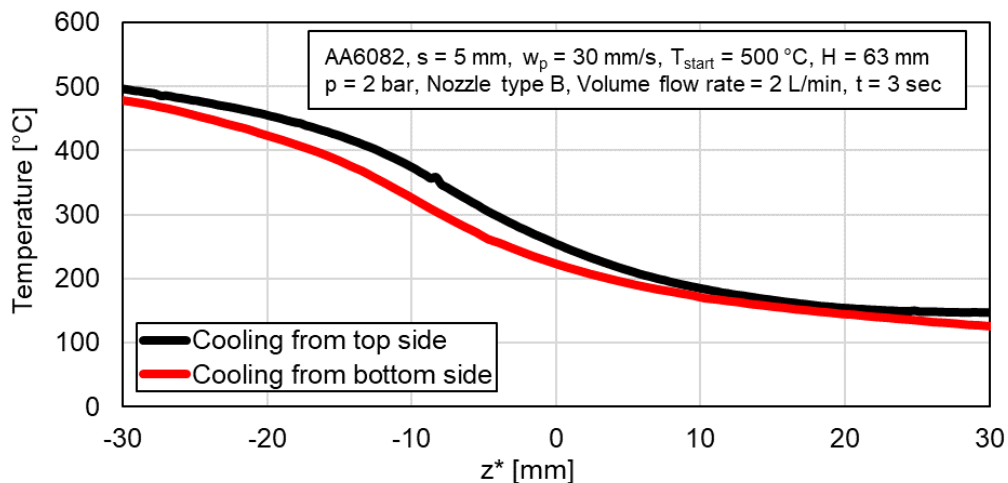


Figure 5.51: Influence of the cooling side on the temperature profile of AA6082 at 30 mm/s plate

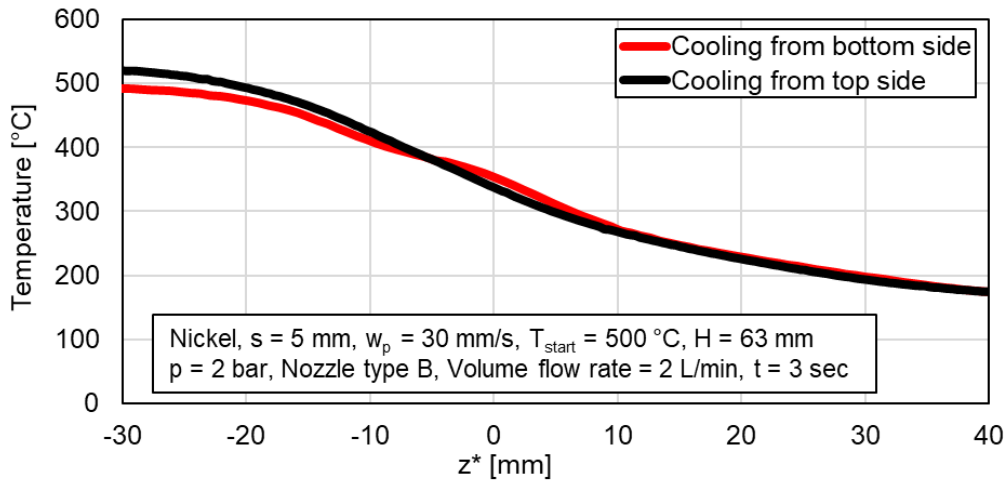


Figure 5.52: Influence of the cooling side on the temperature profile of nickel at 30 mm/s

When comparing the influence of the cooling side on the temperature gradients, for both metals, only a minor effect is visible. However, the temperature at $z^* = 0$ mm for bottom-side cooling is relatively lower for aluminum alloy. In contrast, for nickel plates at 30mm/s, no significant influence of the cooling side on the plate cooling is observed.

5.4 Quenching of Plates in Nozzle Fields (Stationary)

The quenching process of stationary plates is examined within a setup comprising 9 full cone spray nozzles arranged in an inline configuration and 7 nozzles arranged in a staggered configuration. This section delves into the impact of several parameters on heat transfer, including nozzle height (H), nozzle-to-nozzle distance (b), nozzle pressure (p), start temperature (T_{start}), volume flow rate, and the metal thickness (s). Further, the cooling from the top side and bottom side are compared for selected parameters. Additionally, a comparison is made between the heat transfer during cooling observed from the top and bottom sides for specific parameters.

5.4.1 Cooling from the Top Side of the Plate

Influence of Nozzle to Plate Height

Figure 5.53 shows the IR images during cooling at 4 seconds for various nozzle heights at a constant nozzle-to-nozzle distance of 70 mm in an inline nozzle configuration. An increase in nozzle height from 63 mm results in the interaction and overlapping of impacting spray circles as well as a decrease in water impingement flux (Hof, 2023).

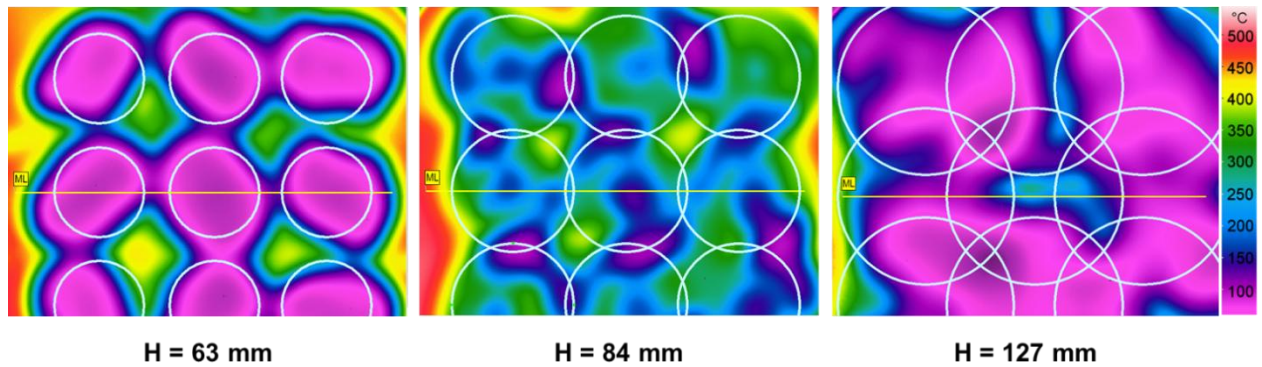


Figure 5.53: IR images of nickel plate at various nozzle heights in an inline field ($b = 70$ mm)

The interaction of wetting fronts from adjacent nozzles leads to the stagnation of water at the center of the middle nozzle, particularly noticeable at a nozzle height of 127 mm. The resultant temperature profiles and heat fluxes at these three nozzle heights are depicted below in Figure 5.54.

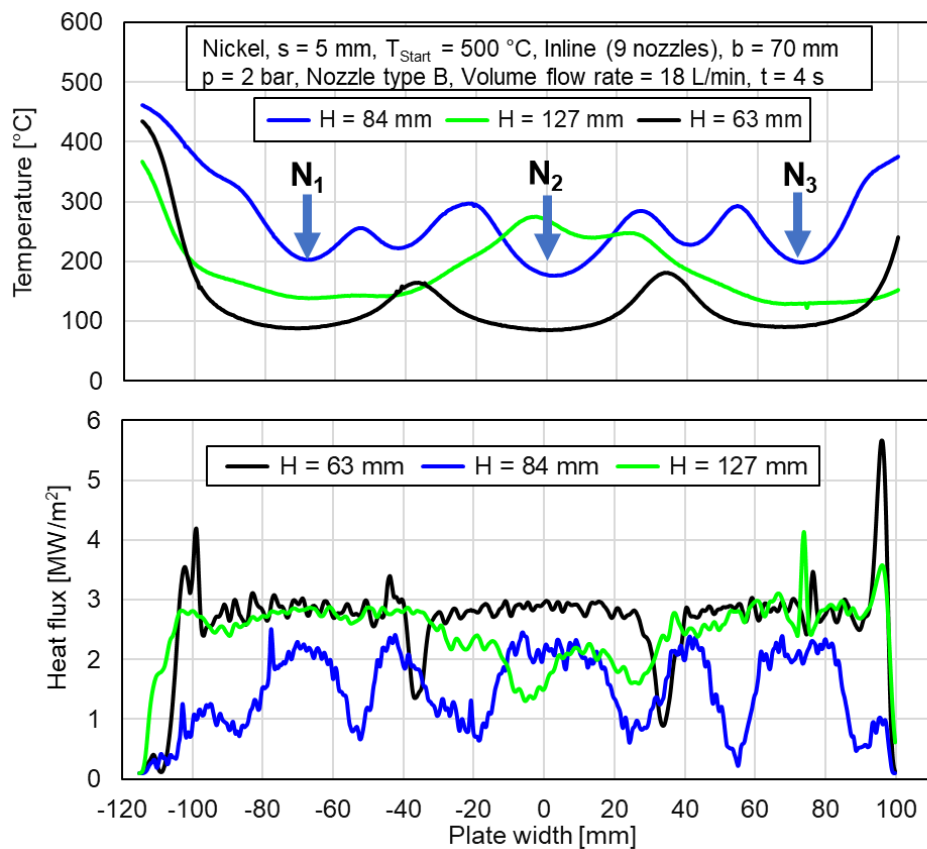


Figure 5.54: Temperature and heat flux profiles of nickel plate at various heights in inline nozzle field

N_1 , N_2 , and N_3 denote the three middle nozzles within the nozzle field. The 0 mm on the x-axis shows the center of the middle nozzle (N_2). At a nozzle height of 63 mm, the plate cools to 100 °C, exhibiting two temperature peaks of 180 °C at positions -40 mm and 40 mm. These peaks emerge within the region between two nozzles. Increasing the nozzle height to 84 mm introduces turbulences on the plate surface due to nozzle interaction. These water turbulences lead to fluctuations and inhomogeneous temperature and heat flux distribution along the plate width. Moreover, with the increase in nozzle height, the temperature at the center of the middle nozzle increases from 100 °C to 280 °C, and the heat flux decreases from 3 to 1.5 MW/m².

Influence of Nozzle to Nozzle Distance

Figure 5.55 shows the IR images of the cooling of the nickel plate with the variable nozzle-to-nozzle distance at the nozzle height of 63 mm.

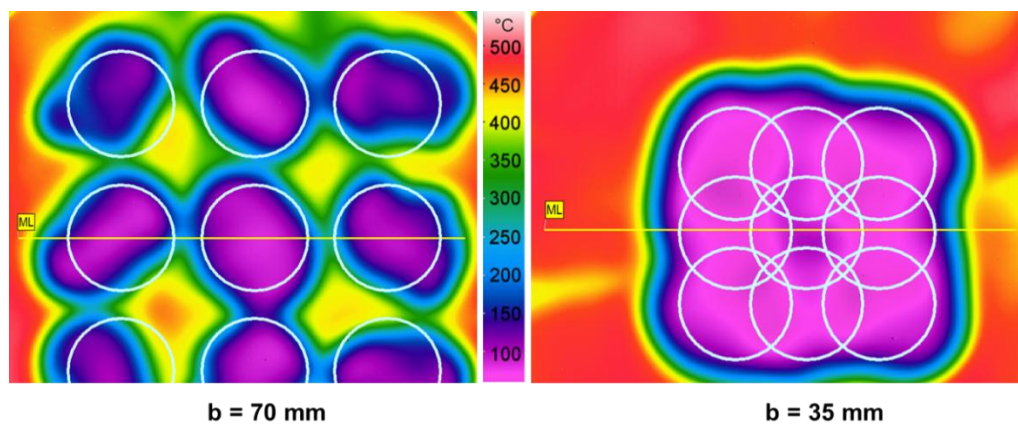


Figure 5.55: IR images of cooling nickel at various nozzle-to-nozzle distances in inline nozzle field

At a nozzle-to-nozzle distance of 70 mm, hot spots are observed between four nozzles, with temperatures ranging from 400 °C to 450 °C. In contrast, at a nozzle distance of 35 mm, the temperatures within the cooled area exhibit more uniformity.

Figure 5.56 depicts the temperature and heat flux profiles corresponding to the aforementioned varied nozzle-to-nozzle distances.

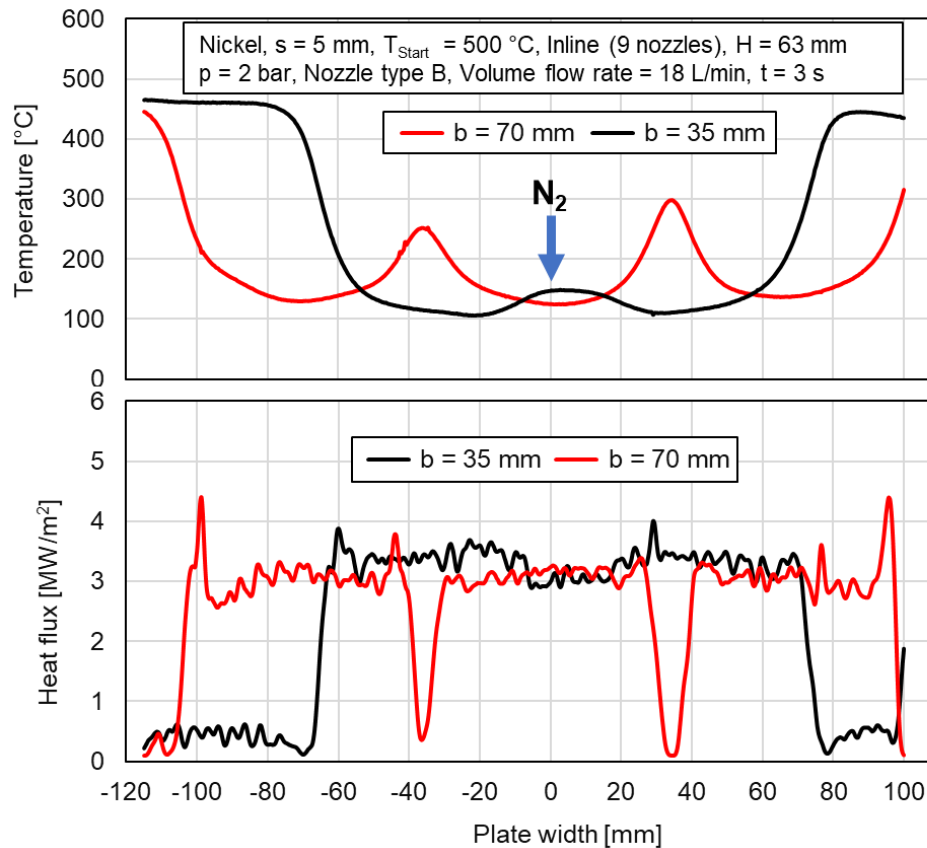


Figure 5.56: Influence of nozzle-to-nozzle distance on temperature and heat flux profiles of nickel in inline field

At higher nozzle-to-nozzle distances, temperature peaks emerge between two nozzles, leading to a decrease in the heat flux. Conversely, reducing the nozzle-to-nozzle distance results in a more uniform temperature decrease along the plate width. The average heat flux remains around 3 MW/m².

Influence of Nozzle Pressure

The nozzle pressure is varied for the cooling process of the nickel plate within the inline nozzle field at $H = 63$ mm, and $b = 35$ mm. Figure 5.57 shows the captured IR images.

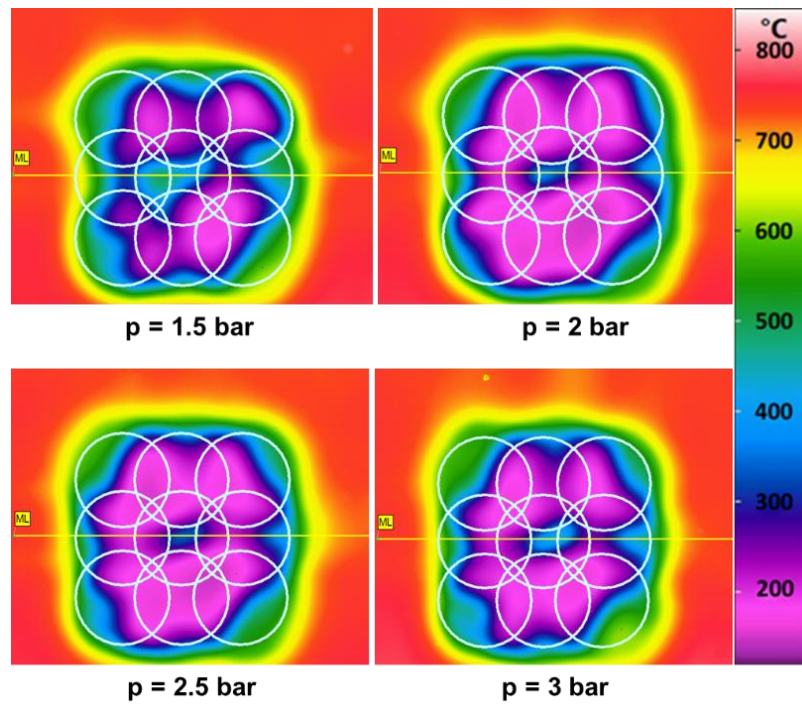


Figure 5.57: IR images of cooling nickel in inline nozzle field with variable nozzle pressure

($H = 63 \text{ mm}$, $b = 35 \text{ mm}$)

Figure 5.58 illustrates temperature and heat fluxes after 5 seconds of cooling for pressure variations from 1.5 to 3 bar.

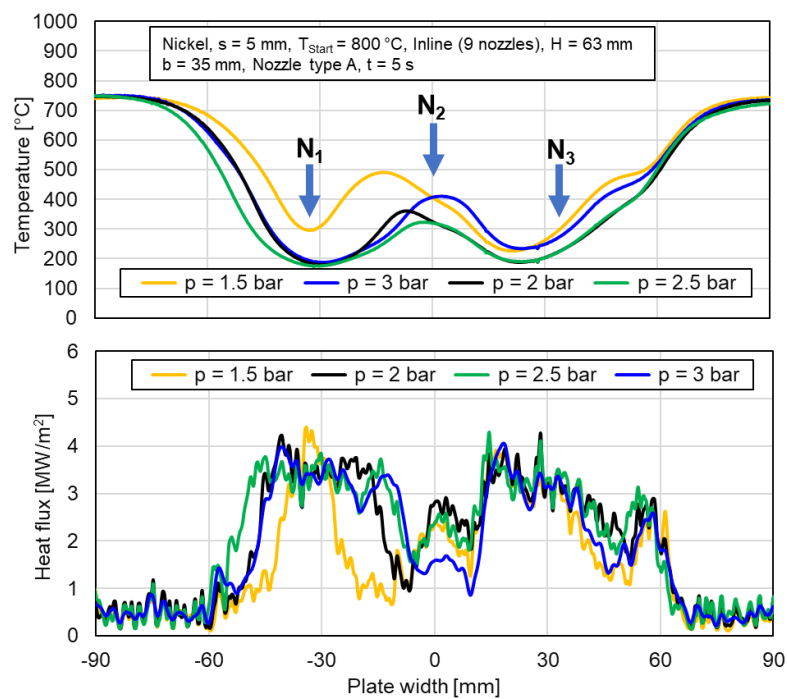


Figure 5.58: Influence of nozzle pressure in inline nozzle field on the temperature and heat flux profiles

The strong overlapping of wetting fronts from the nozzles results in water stagnation at the plate center, where the temperature is relatively higher. Water stagnates below the middle nozzle and cannot be drained away so that no fresh water reaches the surface of the plate and the plate cools down more slowly in this zone. However, the size of this zone and its temperature decrease with the increase in nozzle pressure. There is no significant change in heat flux with pressure and fluctuates between 1 and 4 MW/m².

Figure 5.59 shows the influence of the nozzle pressure for 10 mm aluminum alloy on the temperature and heat flux profiles.

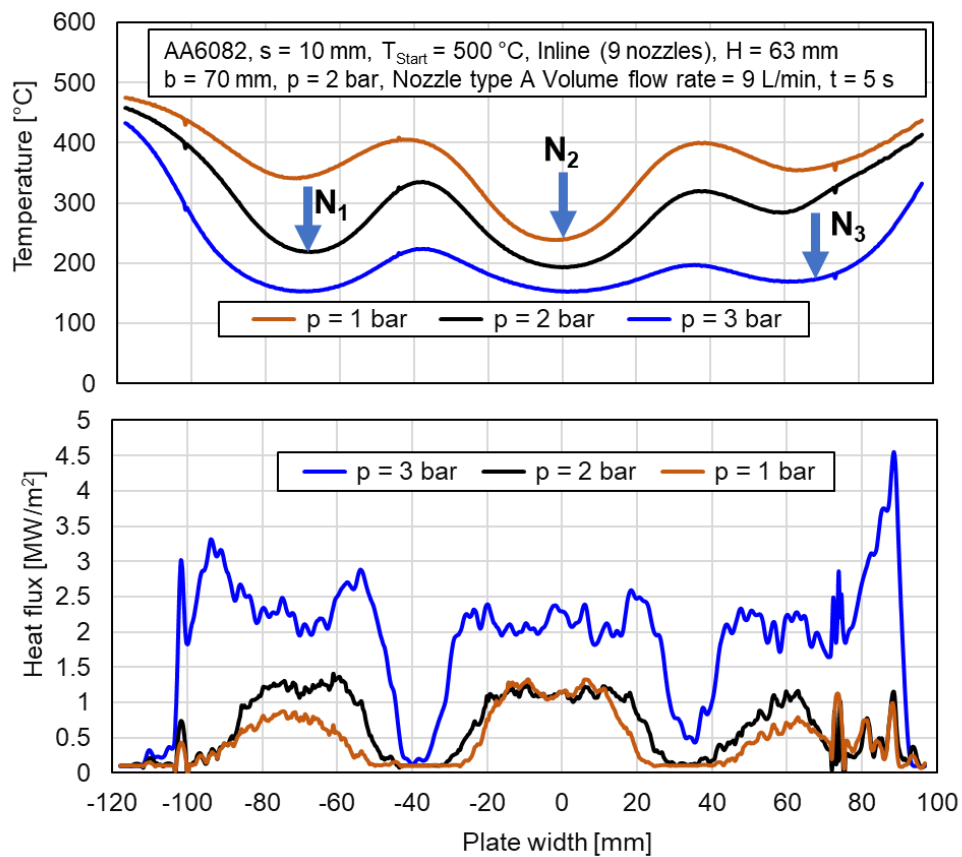


Figure 5.59: Influence of nozzle pressure in inline nozzle field on the temperature and heat flux profiles

The rise in pressure leads to a reduction in temperature fluctuations, causing the temperature between nozzles to decrease from 400 °C to 200 °C. Additionally, the heat flux near the nozzles measures 1.5 MW/m² for nozzle pressures of 1 and 2 bar, whereas it increases to 2.5 MW/m² for a pressure of 3 bar.

Influence of Start Temperature

A 5 mm thick nickel metal plate was heated to three different initial temperatures; 500 °C, 700 °C, and 800 °C. In Figure 5.60, the temperature and heat flux distribution across the plate width after 4 seconds of cooling is illustrated for these three initial temperatures.

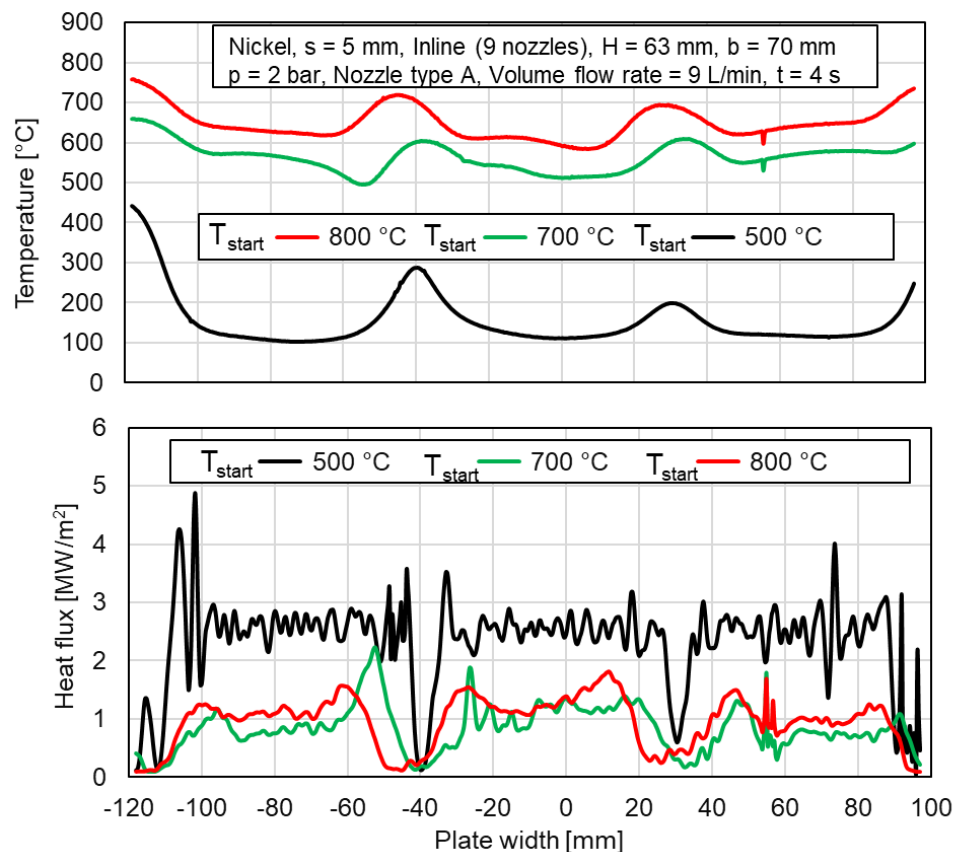


Figure 5.60: Influence of start temperature on the heat transfer of nickel in inline nozzle field

At this point, the temperature at 0 mm (center of the middle nozzle) measures approximately 100 °C for an initial temperature of 500 °C, while it rises to 500 °C and 600 °C for initial temperatures of 700 °C and 800 °C, respectively. For all three initial temperatures, two peaks at identical positions are evident, indicating the region between the two nozzles. The heat flux exhibits significant variation with the initial temperature as, after 4 seconds, the 500 °C initial temperature corresponds to the nucleate boiling region, while the 700 °C and 800 °C initial temperatures lie within the transition region.

Influence of Metal Thickness

Similar to the investigation of a single full cone nozzle, the metal thickness variation is investigated in the nozzle field. Figure 5.61 shows the temperature and heat flux profiles for 2 to 10 mm thick aluminum alloy plates at 4 seconds of cooling.

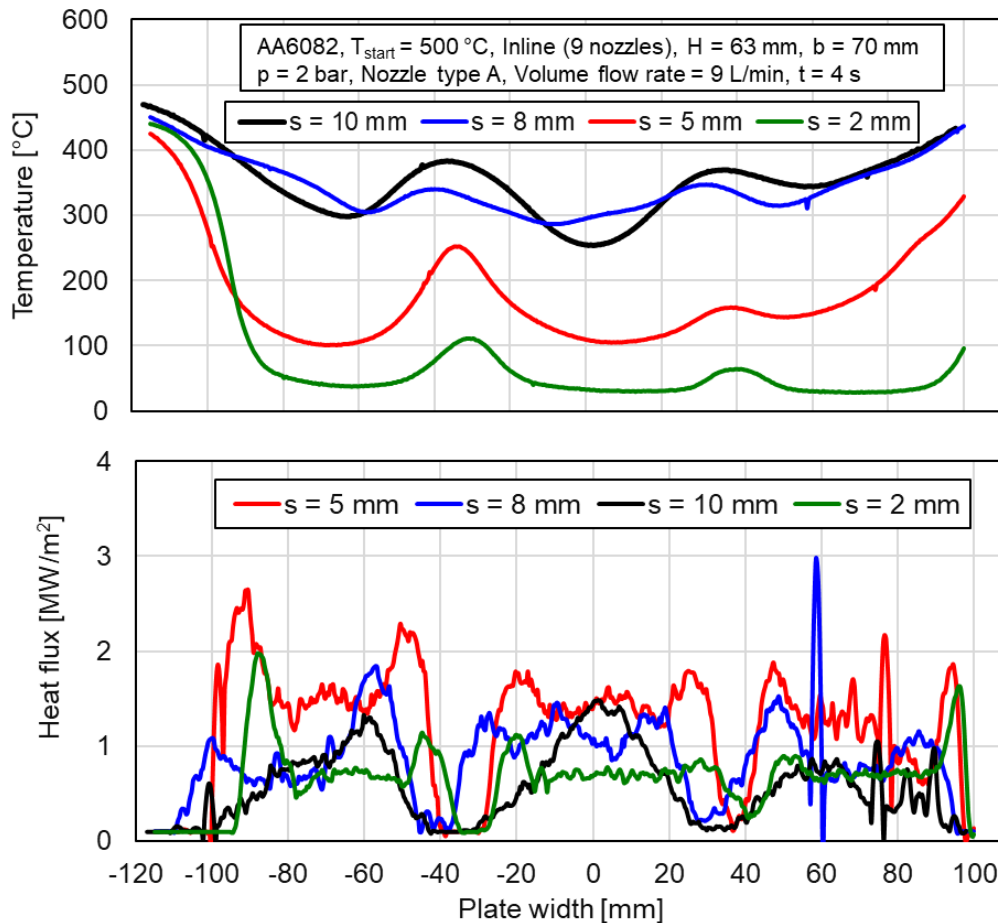


Figure 5.61: Influence of plate thickness on temperature and heat flux profiles in inline nozzle field

The 2 and 5 mm thick plates are cooled to 100 $^{\circ}\text{C}$, while thicker plates of 8, and 10 mm, are cooled to 280 $^{\circ}\text{C}$. Notably, even for the 2 mm plate, small temperature peaks between nozzles are observed, and these temperature fluctuations increase with an increase in plate thickness.

Influence of Volume Flow Rate

Figure 5.62 illustrates the temperature and heat flux profiles for different volume flow rates within an inline nozzle field with a nozzle-to-nozzle distance of 70 mm.

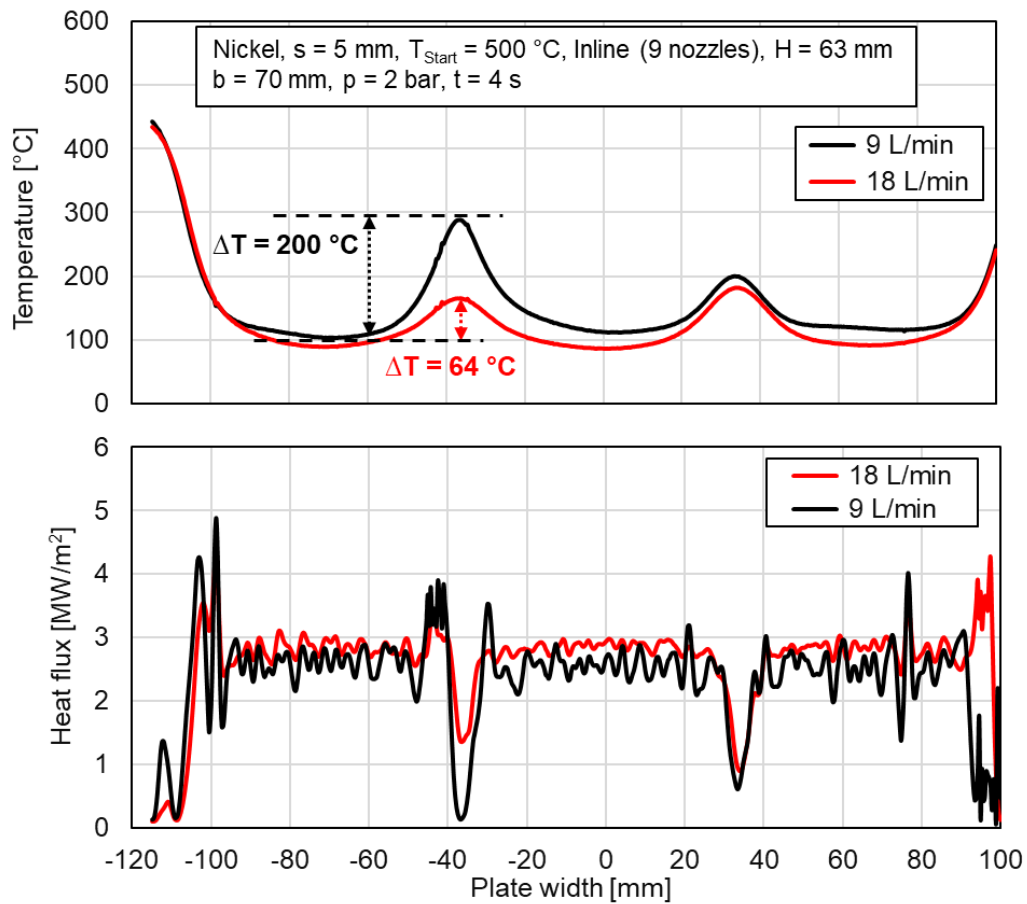


Figure 5.62: Influence of volume flow rate on the temperature and heat flux profiles in the inline field

As the volume flow rate increases from 9 to 18 L/min, the temperature difference between the nozzles at the -60 mm position decreases from 200 °C to 64 °C. However, there is no significant increase in heat flux with the increase in flow rate.

Influence of Nozzle Configuration

The IR images of the investigated inline and staggered nozzle fields are shown in Figure 5.63.

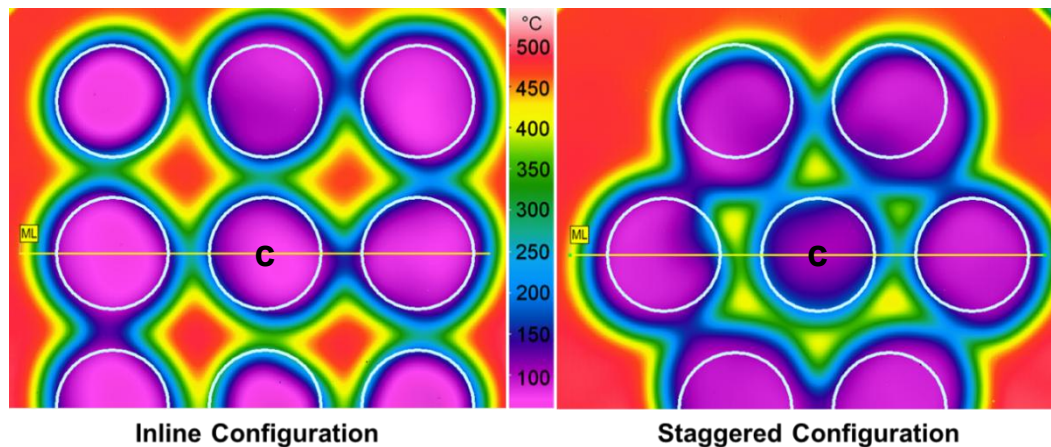


Figure 5.63: IR images of cooling of nickel in Inline and Staggered nozzle fields

Comparing the region in between the nozzles for the staggered arrangement reaches lower temperatures, compared to inline, therefore a more uniform cooling can be achieved.

Figure 5.64 shows the quenching side visuals of inline and staggered arrangements. The regions between the nozzle are occupied with water stagnation, which results in hot spots as shown in Figure 5.63.

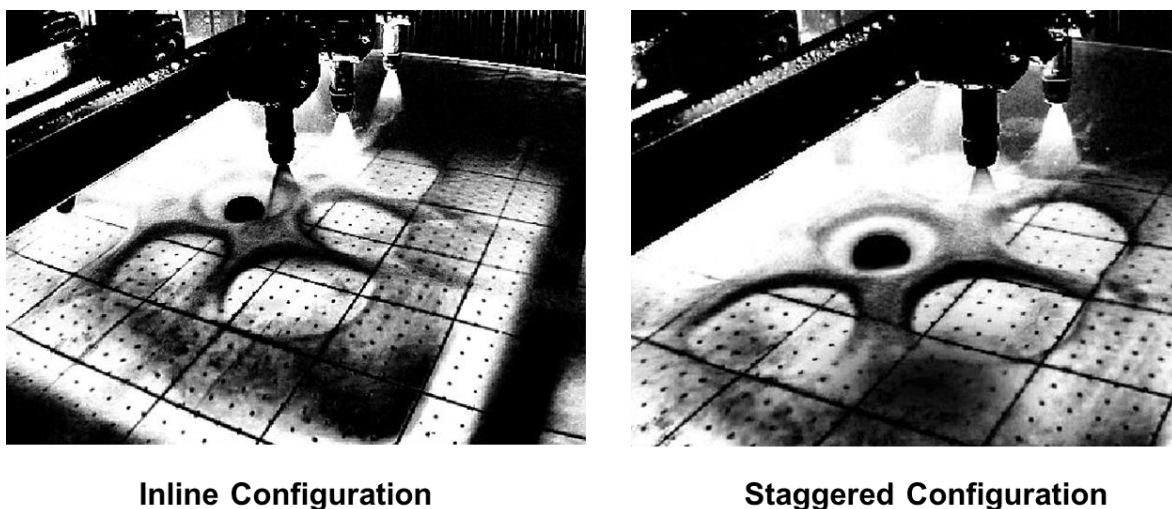


Figure 5.64: Go-Pro image of water impingement of inline and staggered nozzle fields (Hof, 2023)

The temperatures and heat fluxes along the plate width, measured along line ML, are depicted in Figure 5.65.

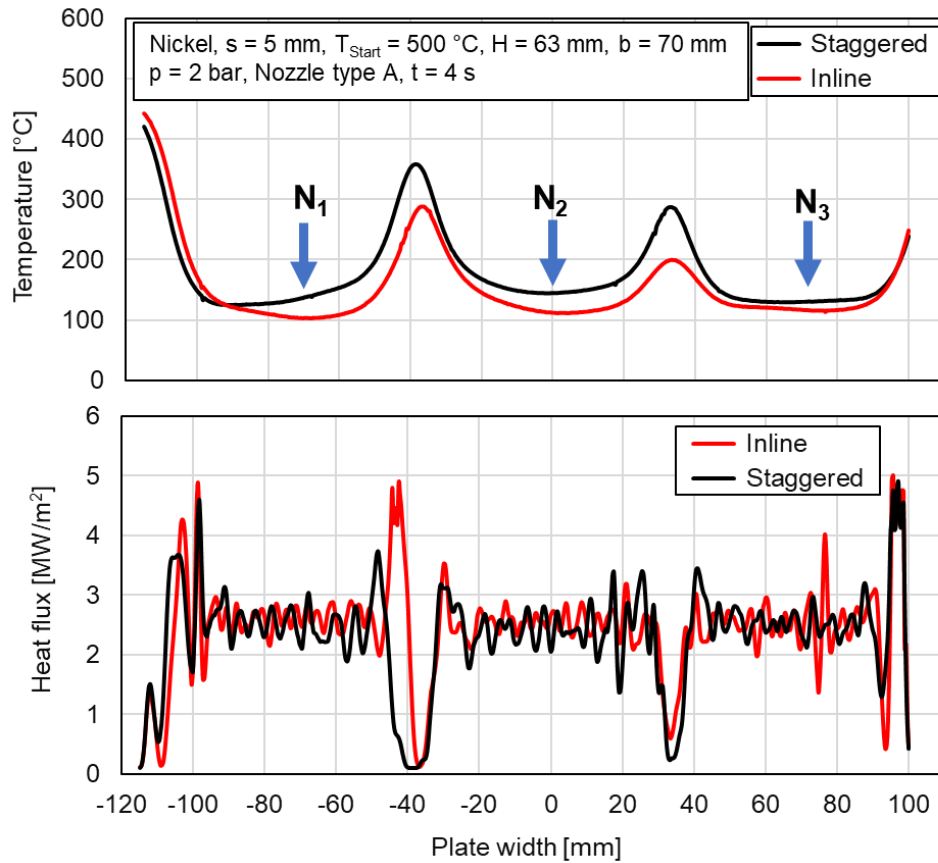


Figure 5.65: Influence of nozzle configuration on the temperature and heat flux profiles

Notably, there is a temperature difference of approximately $100 \text{ }^{\circ}\text{C}$ between the peaks for the inline and staggered arrangements between nozzles N_1 and N_2 , as well as N_2 and N_3 . However, the average heat flux along the plate width remains approximately $2.5 \text{ MW}/\text{m}^2$.

Additionally, temperature analysis is conducted at the center point C, and cooling curves are compared for both arrangements in Figure 5.66.

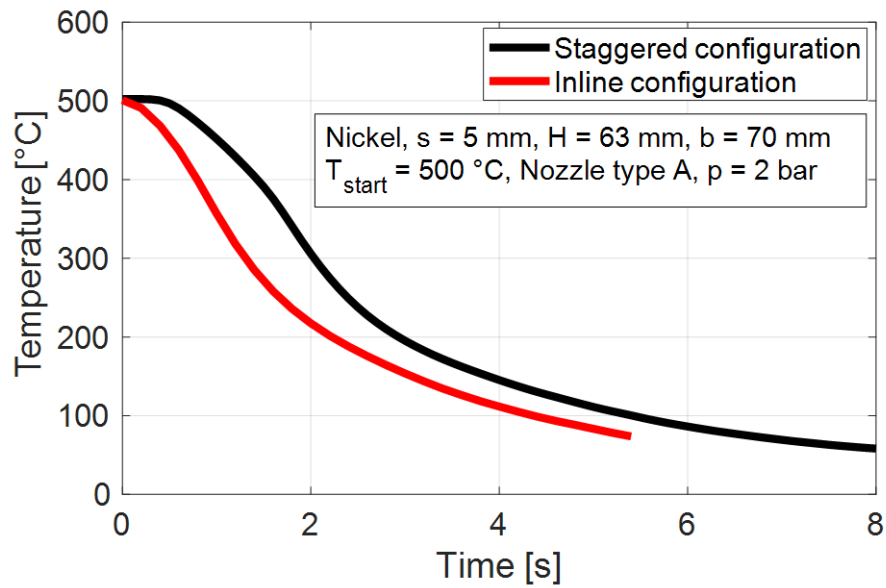


Figure 5.66: Influence of nozzle configuration on the cooling curve at the center of the middle nozzle

It is observed that the temperature for the staggered arrangement at the center point C decreases at a slower rate compared to the inline arrangement.

5.4.2 Cooling from the Bottom Side of the Plate

Influence of Nozzle to Plate Height

IR images captured after 5 seconds of cooling of a nickel plate with variable nozzle height in the inline nozzle filed at $b = 70$ mm are shown in Figure 5.67. The nozzle heights are purposely chosen to avoid interaction and overlapping of impacting sprays.

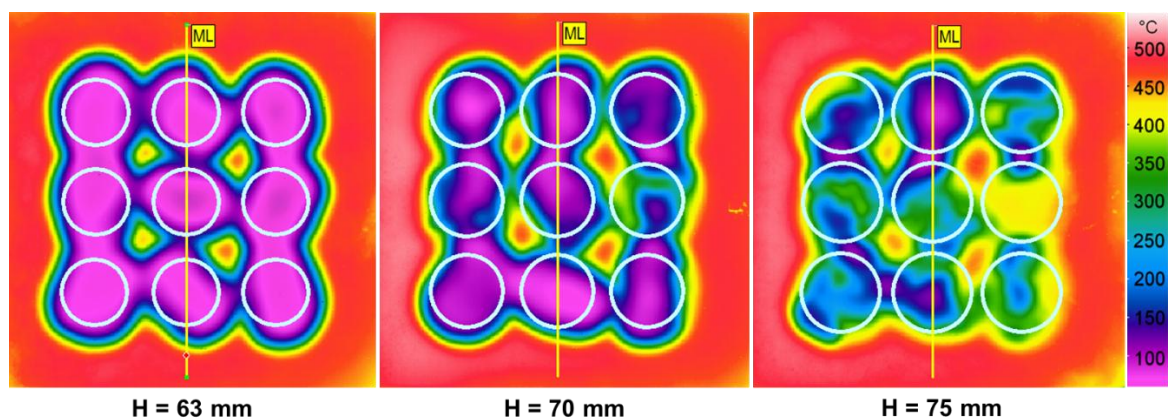


Figure 5.67: IR images of nickel plate at various nozzle heights in an inline field

At nozzle heights of 63 and 70 mm, a more uniform cooling is observed, compared to the uneven and inhomogeneous cooling at 75 mm. As the nozzle height increases from 63 to 75 mm, the temperature between the nozzles increases.

Figure 5.68 shows the temperature and heat flux distribution corresponding to the aforementioned IR images at 5 seconds.

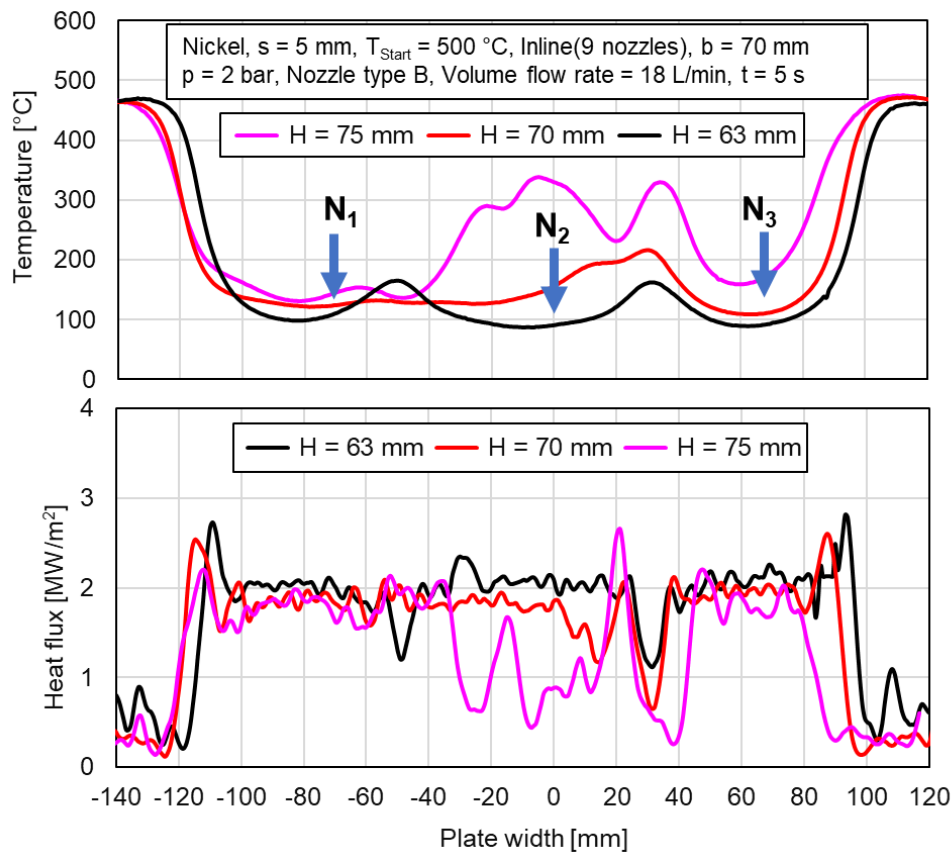


Figure 5.68: Influence of nozzle height on temperature and heat flux profiles in an inline field

With an increase in nozzle height, the temperature at position 0 mm rises from 100 °C to 330 °C. Consequently, due to this temperature increase at the middle position, the heat flux decreases.

Influence of Nozzle to Nozzle Distance

Nozzle-to-nozzle distance is varied from 35 to 70 mm at the constant nozzle height of 63 mm in the inline nozzle arrangement for bottom-side cooling similar to top-side cooling. The captured IR images and corresponding temperatures and heat transfer analysis are shown respectively in Figure 5.69, and Figure 5.70. At a higher nozzle

distance of $b = 70$ mm, a slower and non-uniform cooling is observed, compared to a 35 mm nozzle distance.

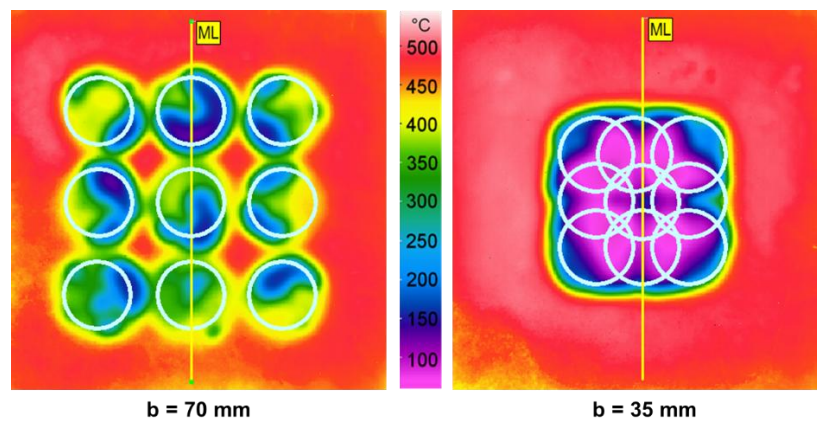


Figure 5.69: IR images of cooling of nickel at various nozzle to nozzle distance

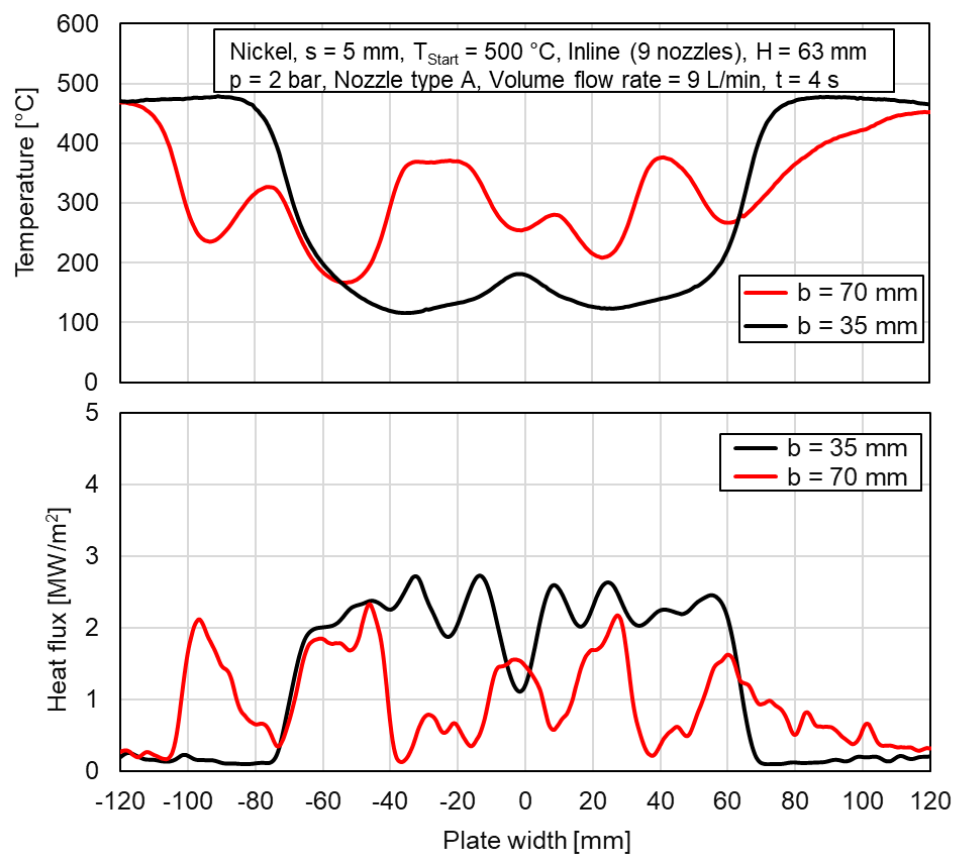


Figure 5.70: Influence of nozzle-to-nozzle distance on temperature and heat flux profiles (inline)

Cooling curves at the center position and the overlap positions are compared in Figure 5.71 for the aluminum alloy plate in the inline nozzle arrangement.

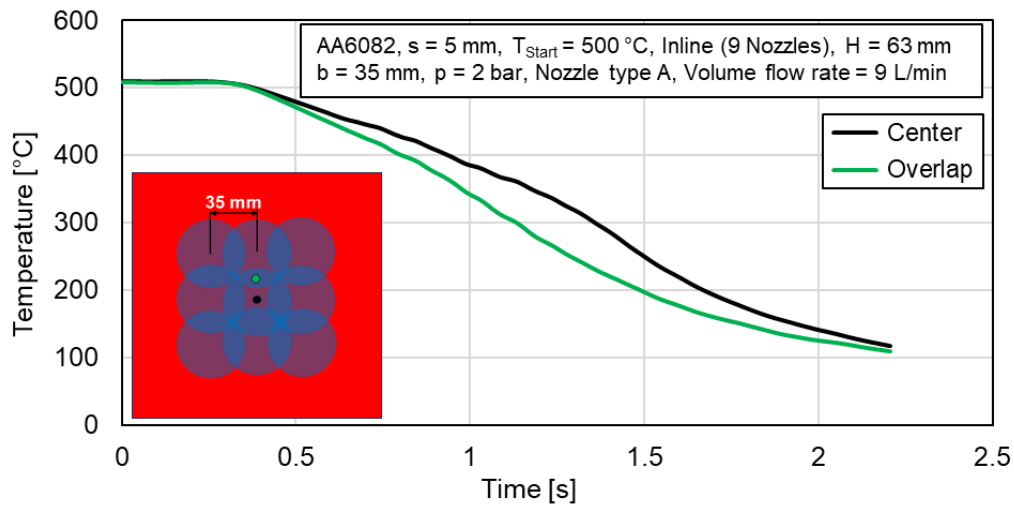


Figure 5.71: Cooling curve comparison of center and overlap position in the inline nozzle field

The cooling at the overlap position is faster than the center of the middle nozzle, which is also evident in the IR images due to the stagnation of water. Water stagnates below the middle nozzle and cannot be drained away so that no fresh water reaches the surface of the plate and the plate cools down more poorly in this zone.

Similarly, the temperature at the center and overlap position are compared at a nozzle height of 84 mm and a nozzle to nozzle distance of 70 mm, where the nozzle-impinging outer circles interact or touch each other as shown in Figure 5.72.

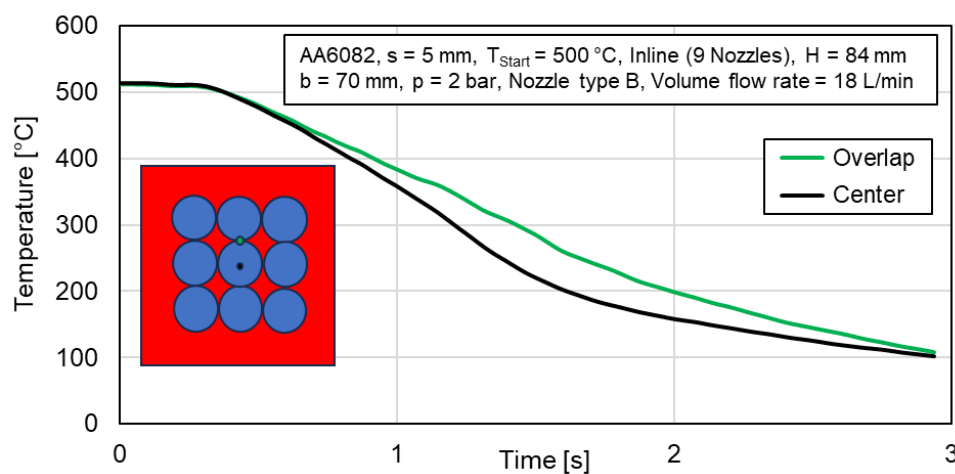


Figure 5.72: Cooling curve comparison of center and overlap position in the inline nozzle field

For further analysis, temperatures at four positions between the nozzles are compared with the center of the nozzle as depicted in Figure 5.73.

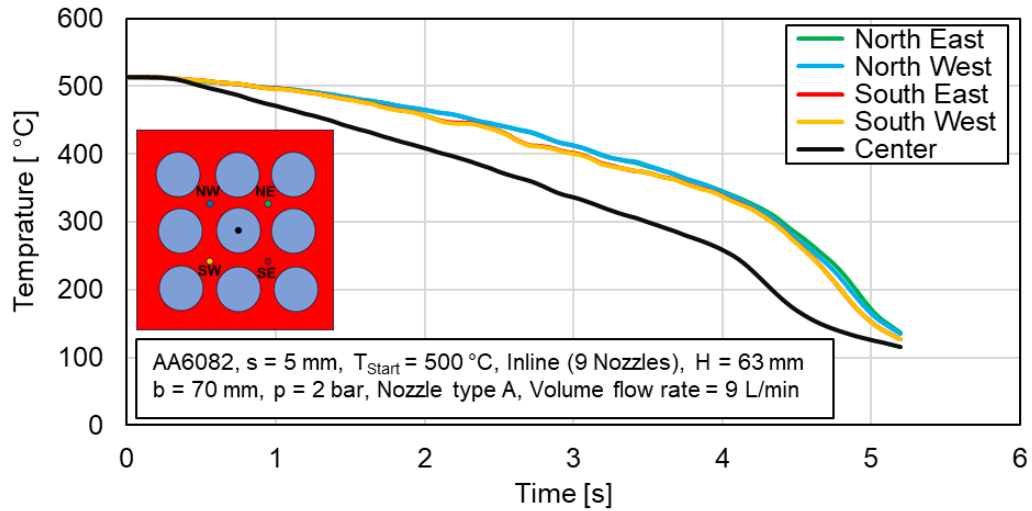


Figure 5.73: Temperature comparison of four positions in between the centers of nozzles and the center position for the inline arrangement

It is observed that the temperature decreases more rapidly at the center of the nozzle compared to the other four positions. However, the temperature profile for the four positions remains similar and follows the same trend.

Influence of Volume Flow Rate

The variation of the volume flow rate in the inline nozzle arrangement for the nickel plate is illustrated in Figure 5.74, and Figure 5.75.

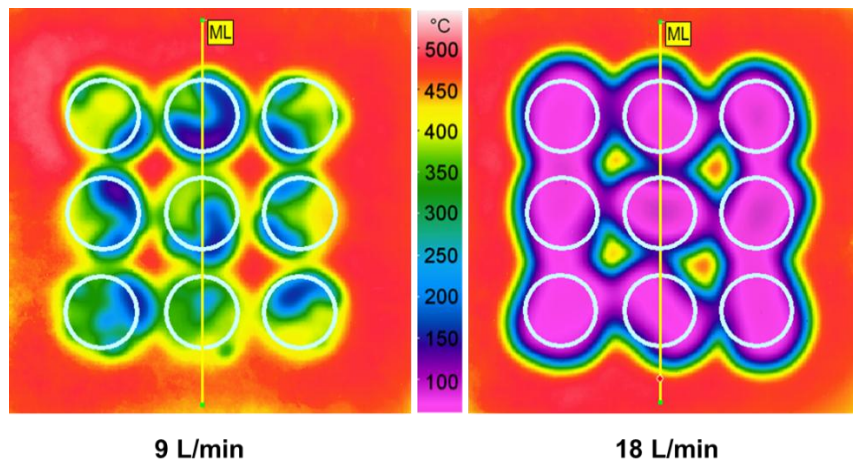


Figure 5.74: IR images of cooling of nickel with the variable volume flow rate

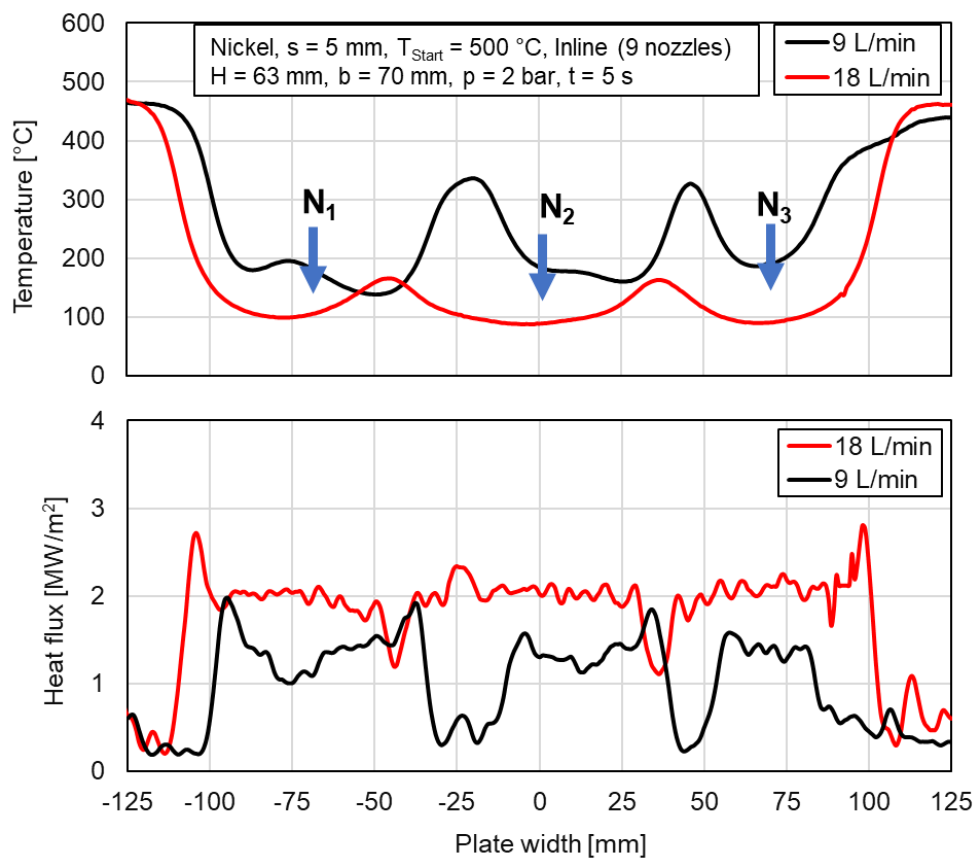


Figure 5.75: Influence of volume flow rate on temperature and heat flux profiles

An increase in flow rate promotes uniform cooling over the plate surface, attributed to the rise in impingement flux. Temperature peaks between the two nozzles are notably higher for 9 L/min, reaching slightly above 300 °C, compared to around 150 °C for

18 L/min. Non-uniform temperature distribution leads to thermal stresses in the plate during cooling, which can compromise product quality causing deformation and cracks.

Influence of Nozzle Configuration

Inline and staggered nozzle arrangements are examined from the bottom side of the plate. Figure 5.76 shows thermal images captured during the cooling of the nickel plate at 4 seconds.

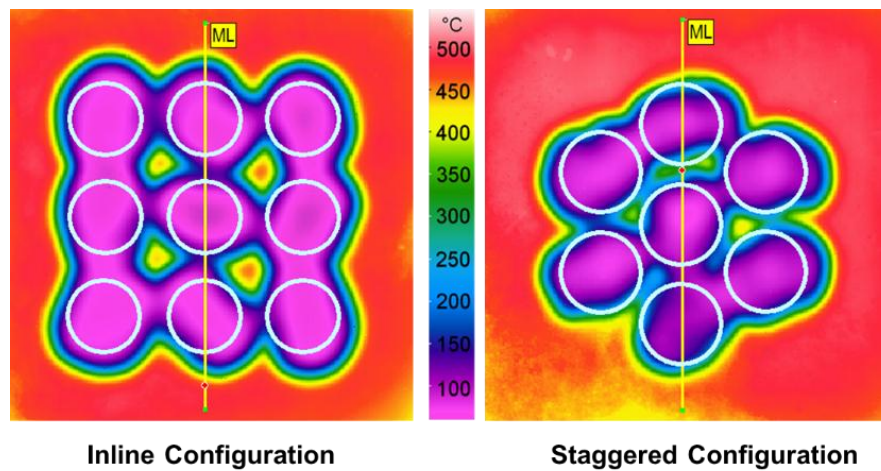


Figure 5.76: IR images of cooling of nickel in Inline and Staggered nozzle fields

Additionally, temperature and heat flux profiles along the plate width on the measuring lines for both arrangements are presented in Figure 5.77.

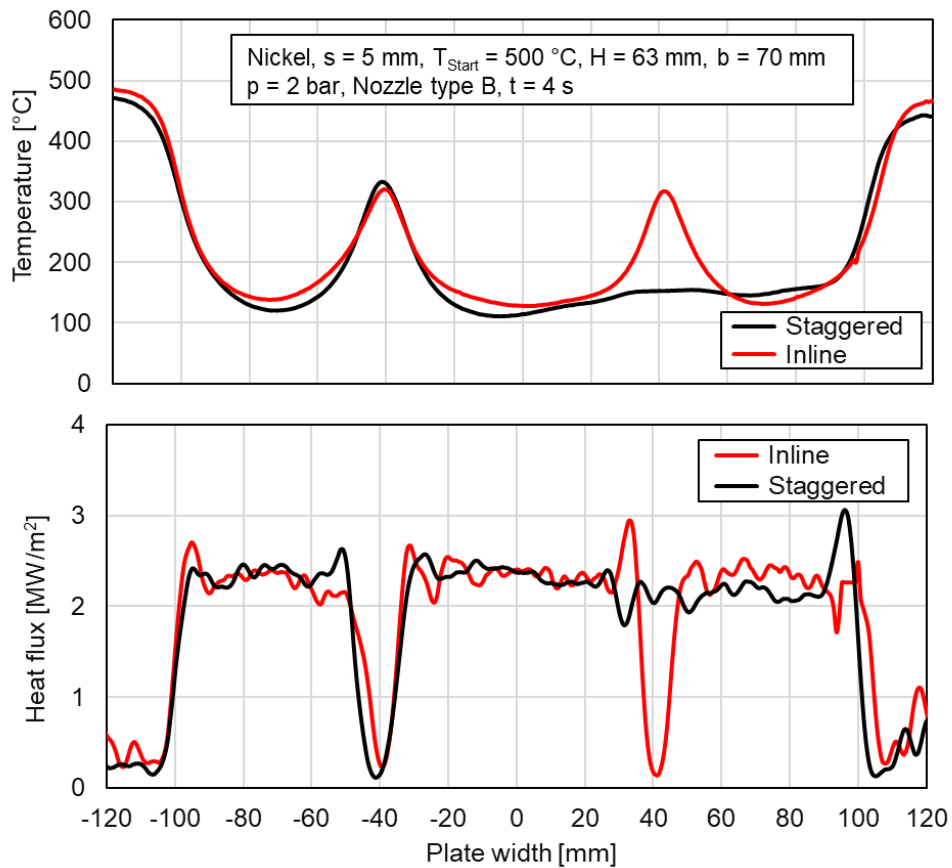


Figure 5.77: Influence of nozzle configuration on the temp- and heat flux profiles

It is noted that there is no significant influence of nozzle arrangement on temperature and heat flux profiles. When considering the measuring line, the IR image of the staggered arrangement exhibits relatively overall homogeneous cooling over the plate surface, whereas for the inline configuration, small hot spots are visible between four nozzles.

5.4.3 Comparison of Top and Bottom Side Cooling

In this section, the comparison of top-side and bottom-side cooling using a nozzle field is presented. Figure 5.78 shows the IR images for bottom and top-side cooling at the nozzle height, $H = 63$ mm, and the nozzle-to-nozzle distance of 35 mm.

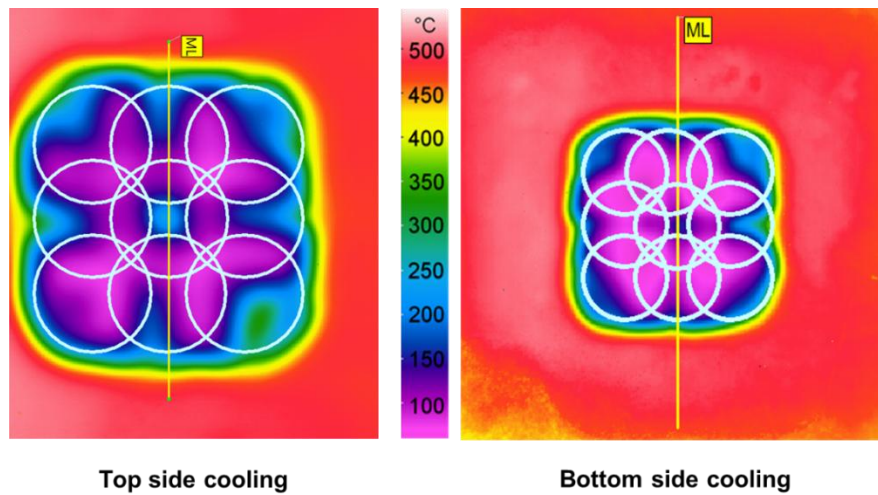


Figure 5.78: IR images of top and bottom side cooling in inline nozzle field

The nozzle circles were the same size in reality, in the case of the top side cooling IR camera was positioned closer to the plate, which restricted the capturing of the full IR image of the plate as for the bottom side cooling.

For both side cooling, temperatures at the overlapping positions are approximately 100 °C. The temperature and heat flux profiles along the plate width after 4 seconds correspond to the IR images depicted below in Figure 5.79.

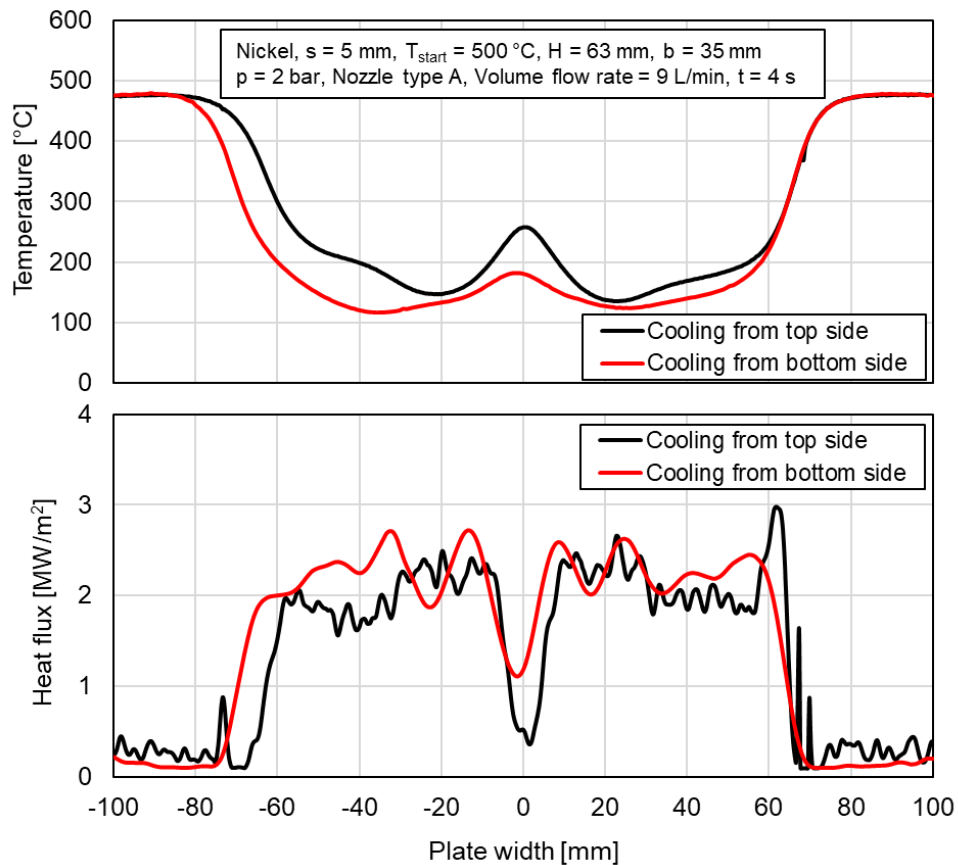


Figure 5.79: Influence of the cooling side on the temperature and heat flux profiles

It is observed, that the cooling from the bottom is slightly faster, compared to top-side cooling. Additionally, at the 0 mm position, the temperature is 80 °C lower than the top side cooling. This is attributed to the smaller water stagnation zone formation due to the overlapping of nozzle circles.

Similarly, both sides are compared for the inline nozzle arrangement without overlapping at $H = 63$ mm, and $b = 70$ mm for nickel plate below in Figure 5.80, and Figure 5.81.

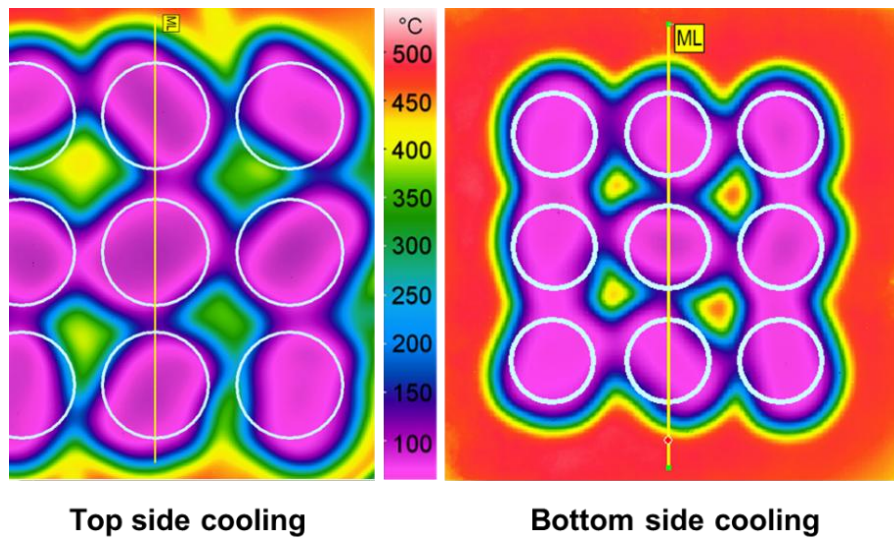


Figure 5.80: IR images of top and bottom side cooling in inline nozzle field

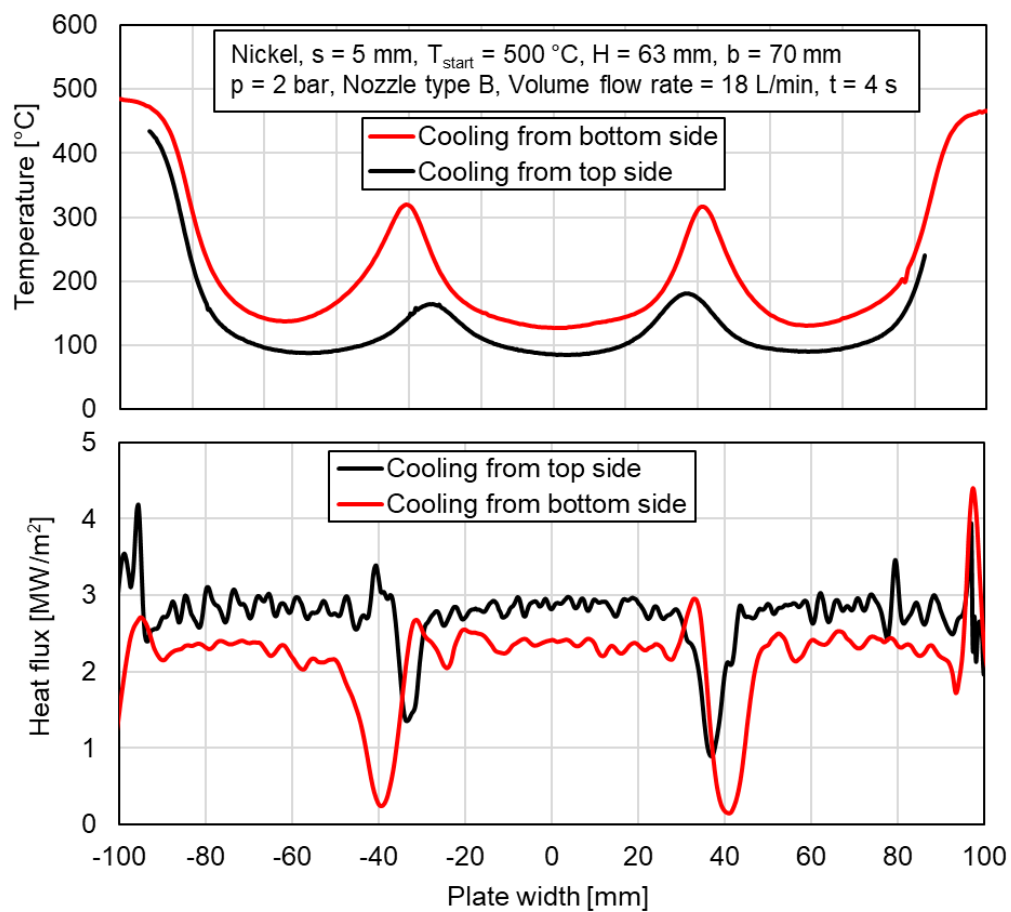


Figure 5.81: Influence of cooling side cooling on the temperature and heat flux profiles

5.5 Quenching of Plates in Nozzle Fields (Moving)

Nickel and aluminum alloy moving plates with a thickness of 5 mm are cooled using a nozzle field from the top side and bottom side. The heat transfer during the cooling of moving plates is analyzed and the influence of plate velocity, nozzle height, nozzle configuration, and metal type is investigated. The temperature profiles are presented along the Eulerian coordinate z^* . The nozzle center of the first row of a nozzle field is indicated as 0 mm along with upstream ($-z^*$) and downstream regions ($+z^*$), as shown in Figure 5.82.

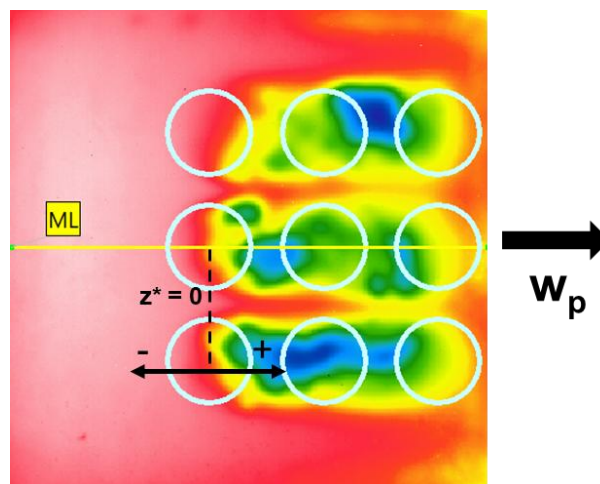


Figure 5.82: Schematic of Eulerian coordinate (z^*) in a nozzle field

5.5.1 Cooling from the Top Side of the Plate

Influence of Plate Velocity

Figure 5.83 shows thermal images of moving nickel plates at various plate velocities. The images are depicted as the plate with all velocities that have moved 150 mm distance.

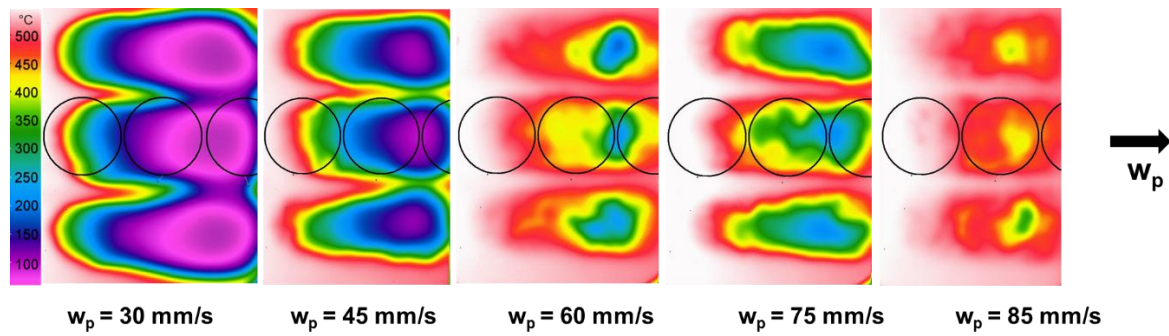


Figure 5.83: IR images captured during cooling moving plates with various velocities in the nozzle field

As the velocity increases, inhomogeneities and non-uniformities during the cooling process rise. Figure 5.84 illustrates the corresponding temperature profiles for the investigated velocities.

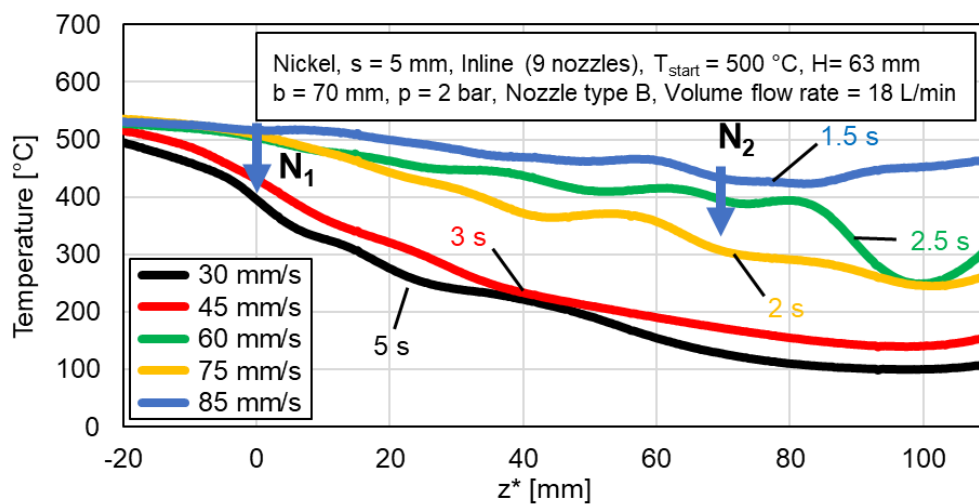


Figure 5.84: Comparison of temperature profiles at various plate velocities in the inline nozzle field

The rate of cooling decreases for higher plate velocities and temperatures in the vicinity of the first nozzle increase.

Influence of Nozzle to Plate Height

The impact of nozzle height on the cooling of the aluminum alloy moving plate with a velocity of 30 mm/s is depicted in Figure 5.85.

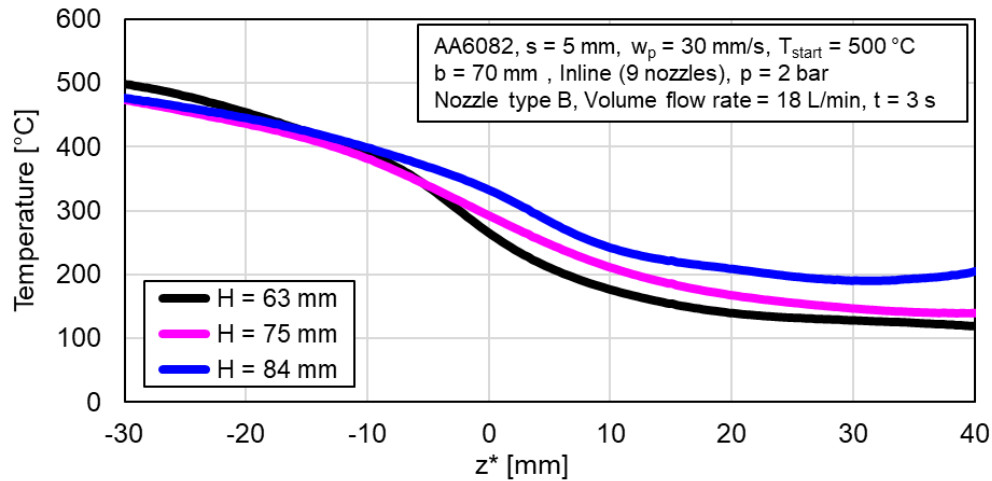


Figure 5.85: Influence of nozzle height on the cooling of moving plate using the inline nozzle field

Three nozzle heights are examined with a constant nozzle-to-nozzle distance of 70 mm. Increasing the nozzle height results in lower impingement flux and larger impinging circles, as observed by (Hof, 2023). The variation in nozzle height results in the interaction of nozzle circles, see Figure 3.4, and Figure 5.96. The temperature profiles exhibit a similar trend with varying nozzle height, although the temperature at position $z^* = 0$ mm increases from 250 °C to 330 °C as the nozzle height increases.

Influence of Metal Type

Figure 5.86 shows the cooling of nickel, and aluminum alloy plates moving with a constant velocity of 30 mm/s in the inline nozzle field.

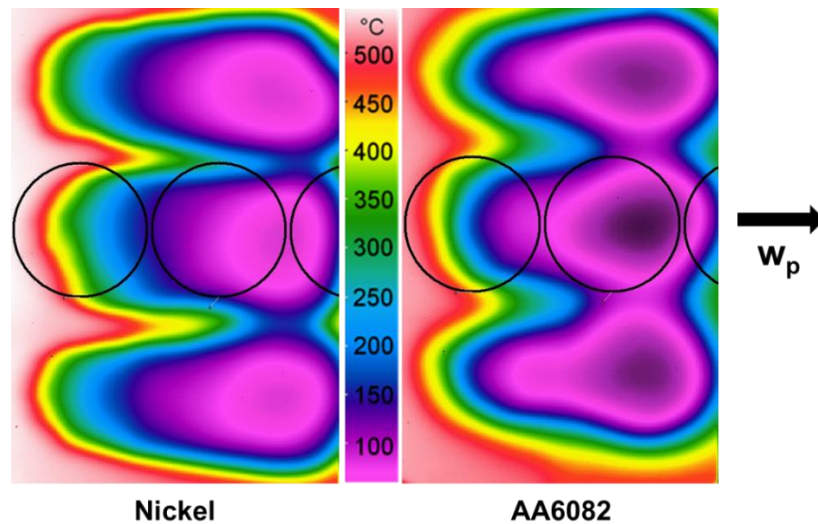


Figure 5.86: IR images of cooling of nickel and AA6082 moving plates

The temperature profiles for both metals after 4 seconds of cooling are illustrated in Figure 5.87.

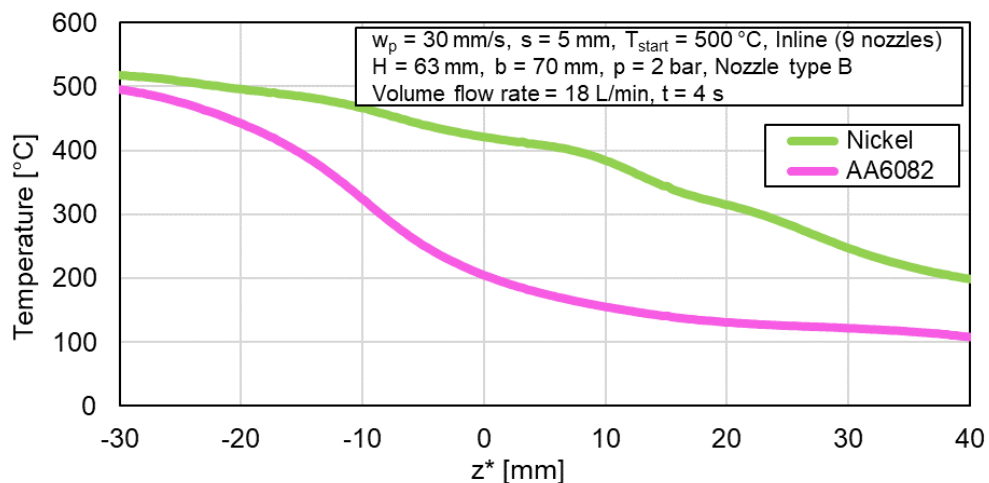


Figure 5.87: Influence of metal type in the inline nozzle field at a plate velocity of 30 mm/s

The aluminum alloy plate exhibits a faster cooling rate with a steeper gradient compared to the nickel plate. The pre-cooling effect in the upstream region is more pronounced in the cooling of aluminum alloy, resulting in the temperature at the center of the first nozzle being approximately 160 °C lower, compared to nickel. Additionally, the movement of the wetting front in the upstream region for aluminum alloy is faster.

5.5.2 Cooling from the Bottom Side of the Plate

Influence of Plate Velocity

In the investigation of bottom-side cooling, the velocity of moving plates undergoes variation for both, nickel and aluminum alloy. This study investigates how plate velocity influences cooling under two nozzle configurations: one with a tight nozzle-to-nozzle distance exhibiting strong overlapping, and another with $b = 70$ mm, where there is no overlap between nozzles.

Figure 5.88 shows thermal images during the cooling process of moving plates, showcasing different velocities and nozzle-to-nozzle distances for nickel at a specific height.

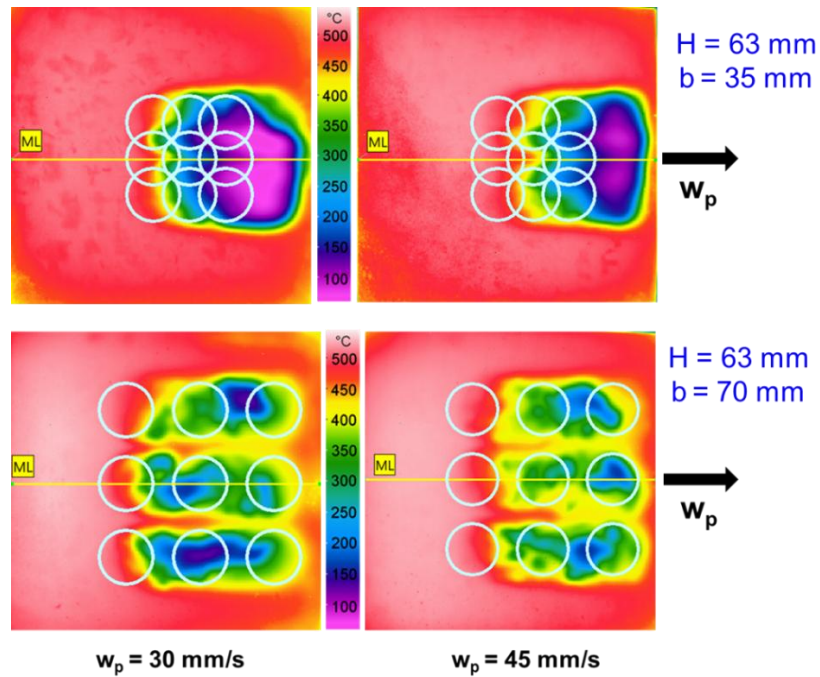


Figure 5.88: IR images of variation of plate velocity at two various nozzle-to-nozzle distance

Figure 5.89 illustrates the temperature profiles corresponding to thermal images at a plate movement of 180 mm.

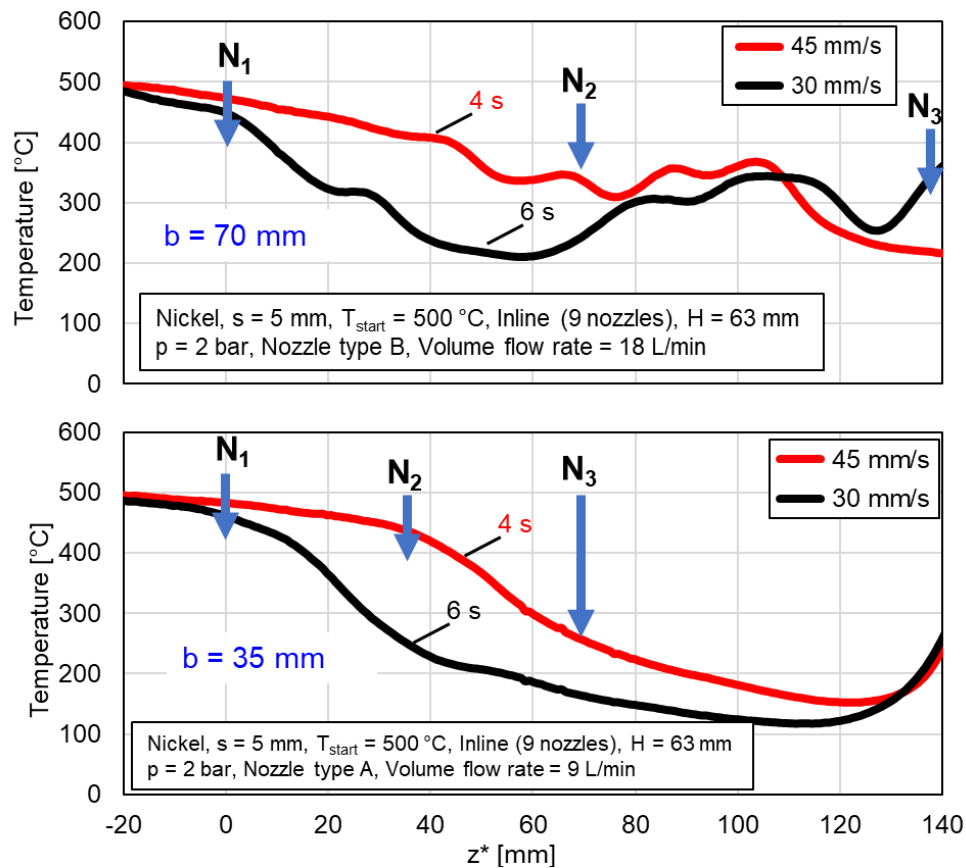


Figure 5.89: Influence of plate velocity on the cooling of nickel at $b = 35$ mm, and $b = 70$ mm

The nozzle configuration with a tight nozzle-to-nozzle distance demonstrates uniform and homogeneous cooling at plate velocities of 30 and 45 mm/s. In contrast, non-uniform cooling and temperature fluctuations are observed at $b = 70$ mm with no overlapping. There is no significant change in temperature at the 0 mm position for both configurations.

Figure 5.90, and Figure 5.91 show the velocity comparison at the center nozzle row along the width of a nozzle field.

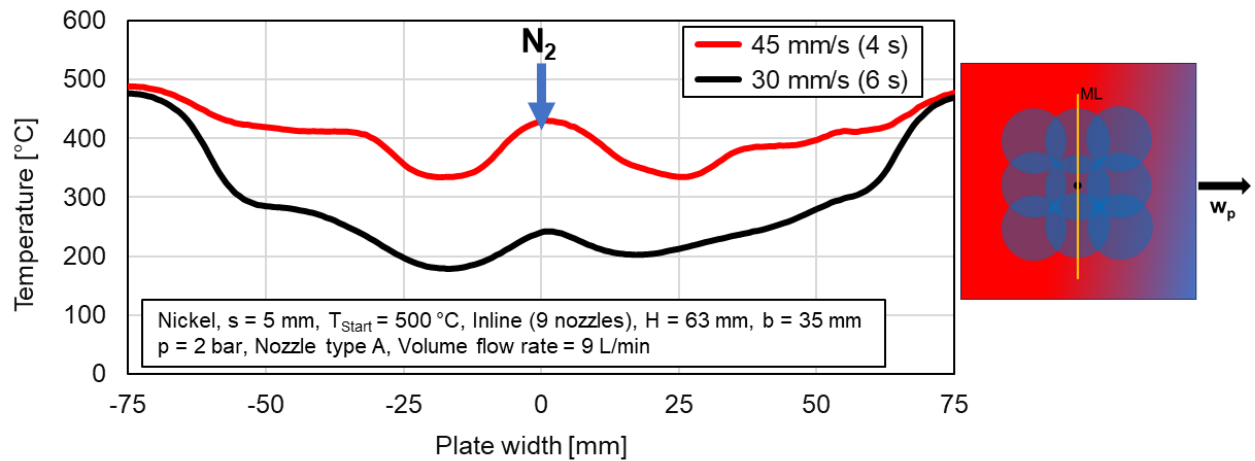


Figure 5.90: Influence of plate velocity along the width in a nozzle field ($b = 35$ mm)

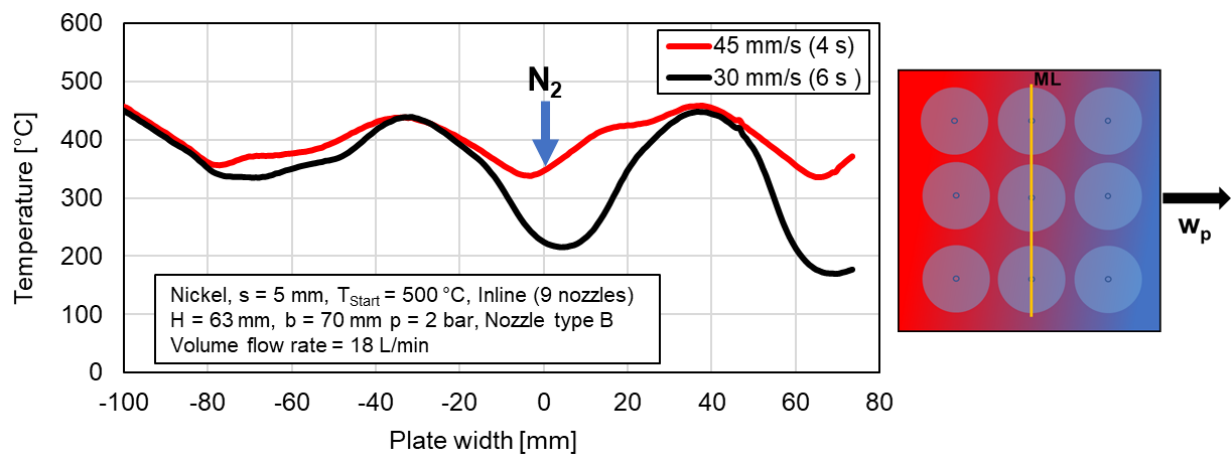


Figure 5.91: Influence of plate velocity along the width in a nozzle field ($b = 70$ mm)

Measuring line along the plate width at the constant plate movement of 180 mm shows, that there is a small peak in temperature profile at the center of the middle nozzle in case of 35 mm nozzle distance. This peak appears because of water stagnation in the vicinity of the middle nozzle. In contrast, at a higher nozzle distance of 70 mm, two peaks appear in between the nozzle.

Figure 5.92 depicts the heat fluxes for both configurations at various plate velocities.

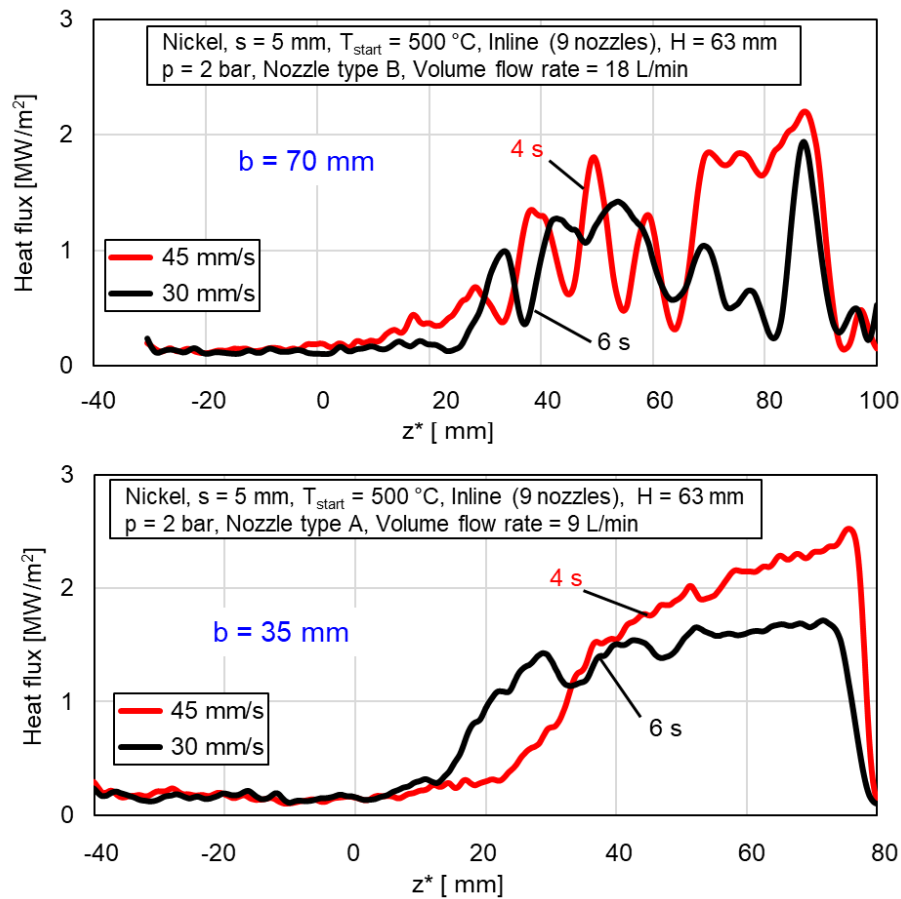


Figure 5.92: Influence of plate velocity on the heat flux of nickel at $b = 35$ mm, and $b = 70$ mm

The heat flux increases with an increase in plate velocity for both nozzle configurations. However, the maximum heat flux reaches around 2.5 MW/m^2 at 45 mm/s for $b = 35 \text{ mm}$, whereas for $b = 70 \text{ mm}$, it peaks at 2.1 MW/m^2 at a plate velocity of 45 mm/s . The heat fluxes reach zero again because the first impingement point is 10 mm away from the right edge of the plate.

Boiling curves of the nickel metal plate at both plate velocities are shown in Figure 5.93.

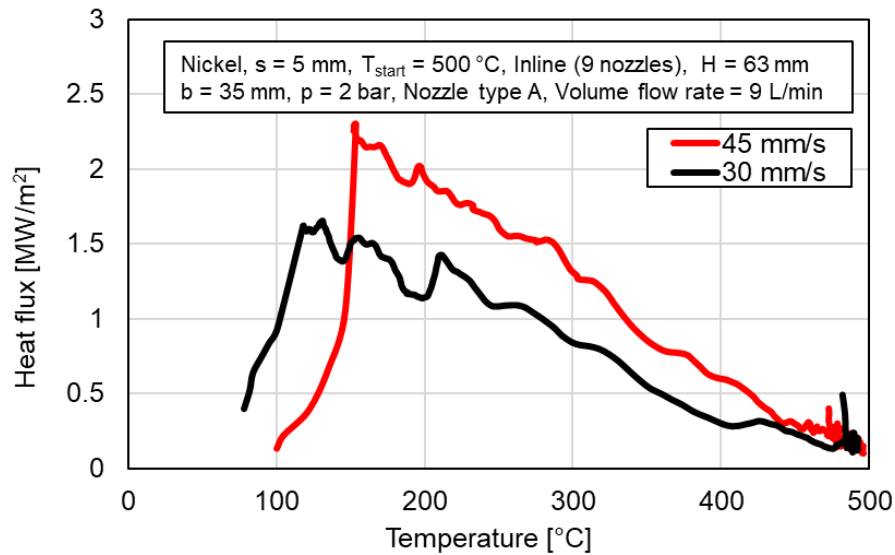


Figure 5.93: Influence of plate velocity on the boiling curve (nickel, $H = 63$ mm, $b = 35$ mm)

It can be seen that the maximum heat flux is higher for a plate velocity of 45 mm/s compared to 30 mm/s plate velocity, whereas there is no significant change in DNB temperature with an increase in plate velocity. Figure 5.94 shows IR images and temperature profiles of the cooling of aluminum alloy plates at various plate velocities.

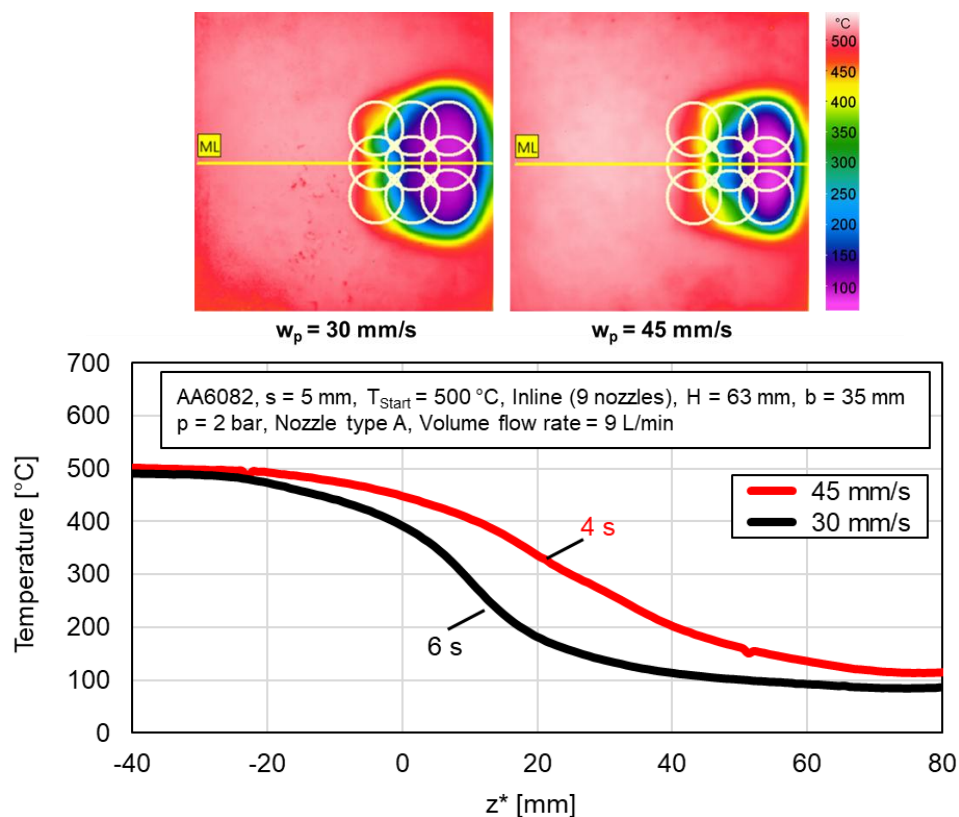


Figure 5.94: Influence of plate velocity on the cooling of AA6082 plate ($H = 63$ mm, $b = 35$ mm)

The temperature starts dropping in the upstream region due to the pre-cooling effect for both velocities. The temperature at 0 mm increases from 400 °C to 450 °C as plate velocity increases from 30 to 45 mm/s.

Figure 5.95 shows the cooling of the moving aluminum alloy plate along the plate width at various velocities.

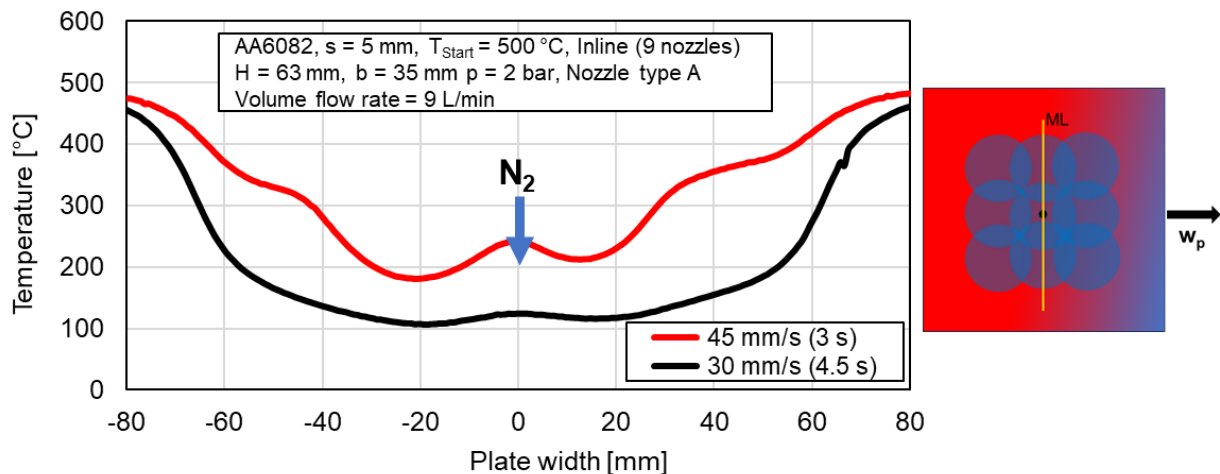


Figure 5.95: Influence of plate velocity along the width in a nozzle field (AA6082, $b = 35$ mm)

Influence of Nozzle to Plate Height

Figure 5.96 shows thermal images of the moving aluminum alloy plate with 30 mm/s velocity at various nozzle heights, and Figure 5.97 illustrates the temperature profiles for these thermal images along the measuring line.

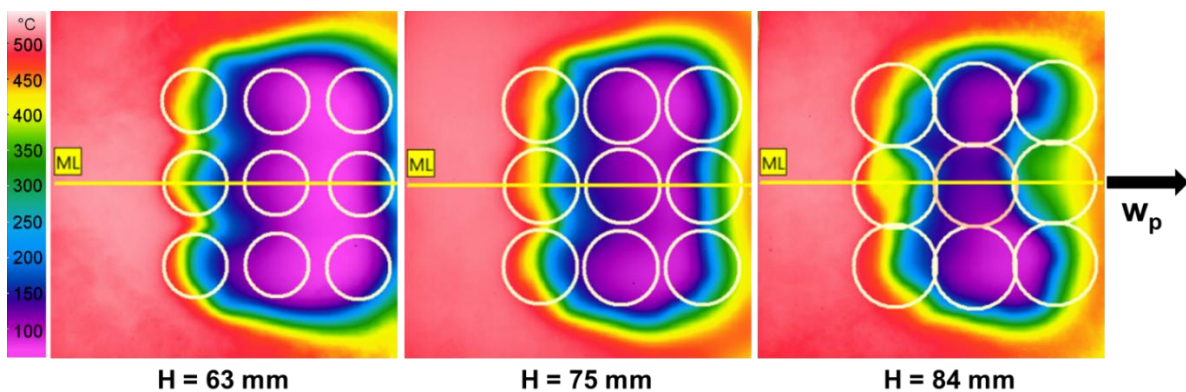


Figure 5.96: IR images of the influence of cooling of AA6082 at various nozzle heights ($b = 70$ mm)

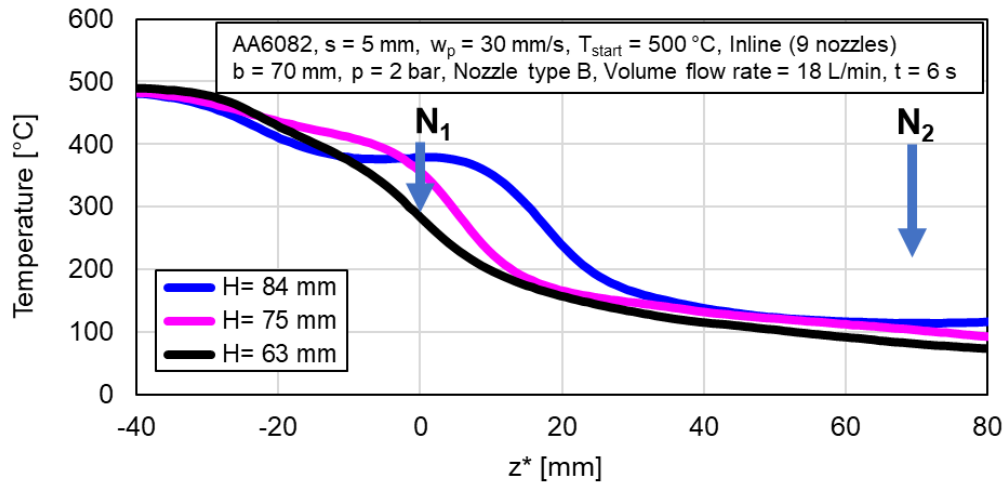


Figure 5.97: Influence of nozzle height on the cooling of AA6082 metal plates
($b = 70$ mm, $w_p = 30$ mm/s)

With the increase in nozzle height from 63 to 84 mm, the temperature at the impingement region increases from 290 °C to 390 °C.

Influence of Nozzle Configuration

The influence of nozzle configuration on the cooling of moving aluminum alloy at $H = 63 \text{ mm}$, $b = 35 \text{ mm}$, and $w_p = 30 \text{ mm/s}$ is shown in Figure 5.98.

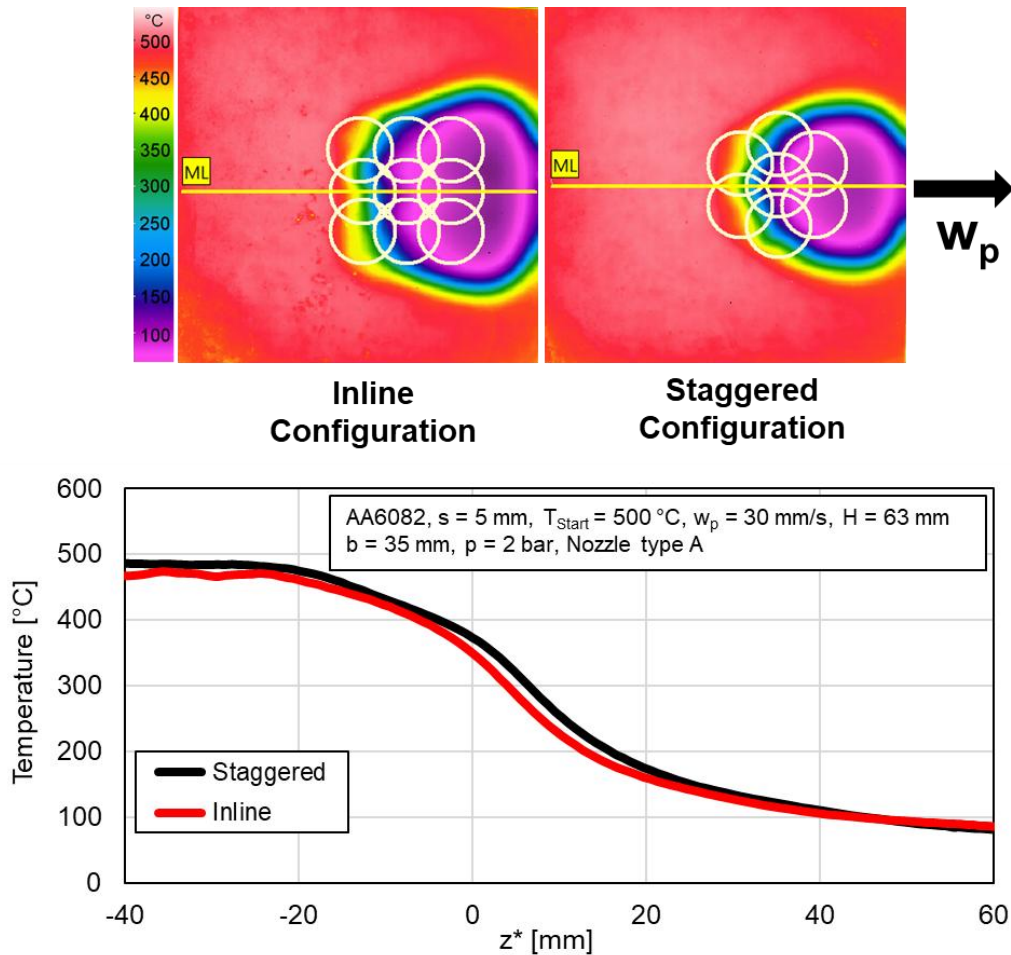


Figure 5.98: Influence of nozzle configuration on the cooling of AA6082 at a plate velocity of 30 mm/s)

Both configurations exhibit similar temperature profiles with no significant temperature difference at the impingement point.

5.5.3 Comparison of Top and Bottom Side Cooling

The cooling of moving metals of nickel and aluminum alloy are compared for top-side and bottom-side cooling and resulting temperature profiles at $H = 63 \text{ mm}$, $b = 70 \text{ mm}$, and $w_p = 30 \text{ mm/s}$ are shown below in Figure 5.99, and Figure 5.100.

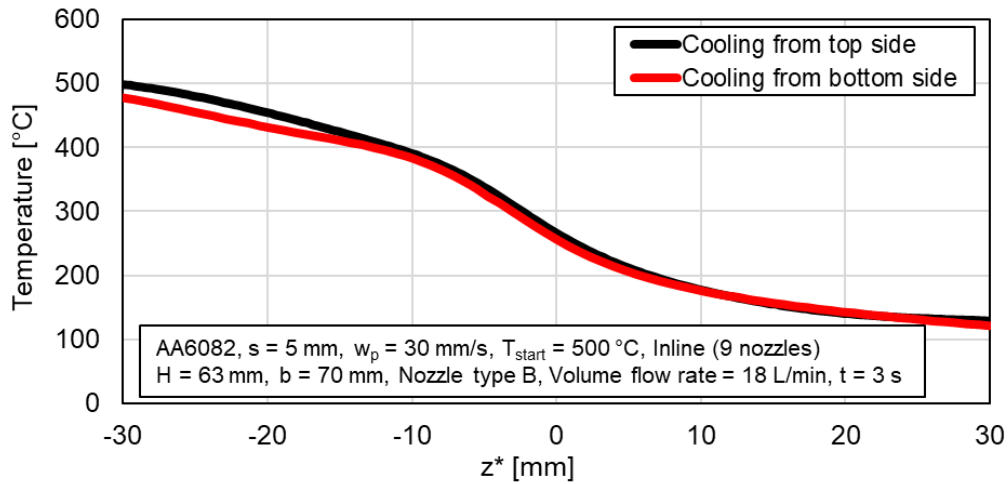


Figure 5.99: Top side vs bottom side cooling (AA6082, $H = 63$ mm, $b = 70$ mm, $w_p = 30$ mm/s)

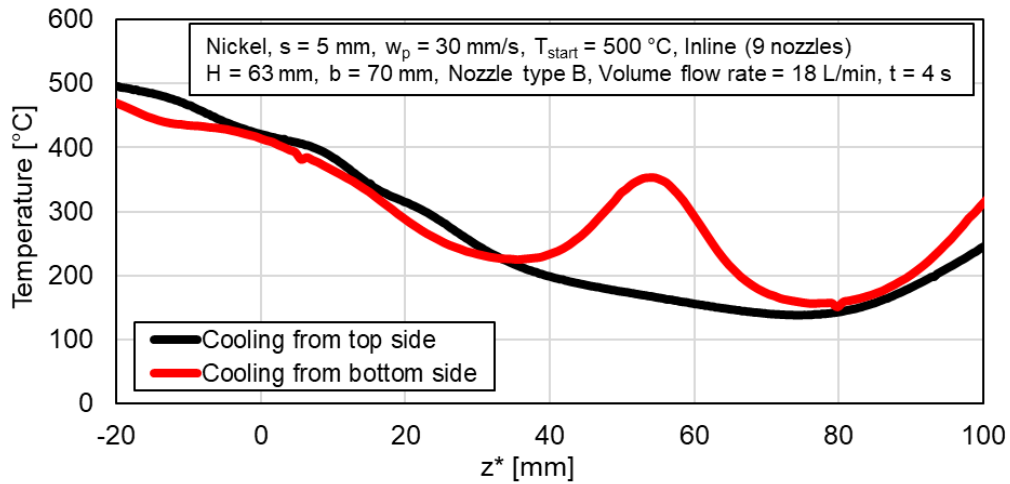


Figure 5.100: Top side vs bottom side cooling (nickel, $H = 63$ mm, $b = 70$ mm, $w_p = 30$ mm/s)

The comparison shows no significant influence of the side of cooling on the temperature profiles for both metals, however, the temperature at the impingement position for bottom-side cooling is relatively lower in contrast to top-side cooling. For nickel, there is a peak at 50 mm position, which appears between two nozzles in case of bottom side cooling.

5.6 Comparison of Single Nozzle and Nozzle Field

Figure 5.101 compares the cooling performance of a single nozzle and inline field at 4 seconds of cooling for a 5 mm nickel plate. The comparison is made at two different nozzle heights, with a nozzle-to-nozzle distance of 70 mm.

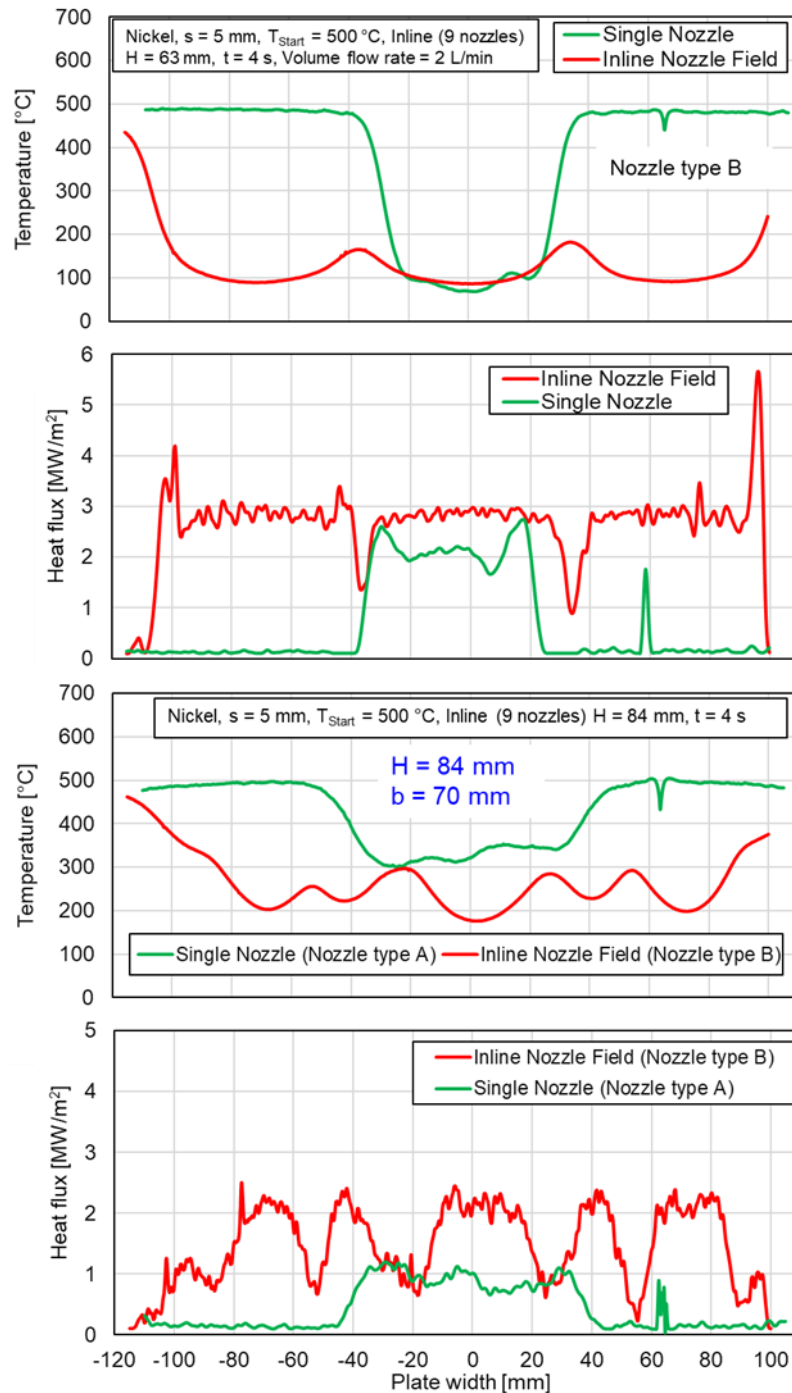


Figure 5.101: Comparison of single nozzle and inline field ($T_{\text{start}} = 500^\circ\text{C}$)

The inline field cools a wide plate more effectively than a single nozzle, achieving a higher heat flux at both nozzle heights. The temperature and heat flux distribution are relatively more uniform at a nozzle height of 63 mm compared to 84 mm, due to higher impingement density.

Figure 5.102 compares the temperature and heat flux history during the cooling of nickel using a single nozzle and an inline nozzle field.

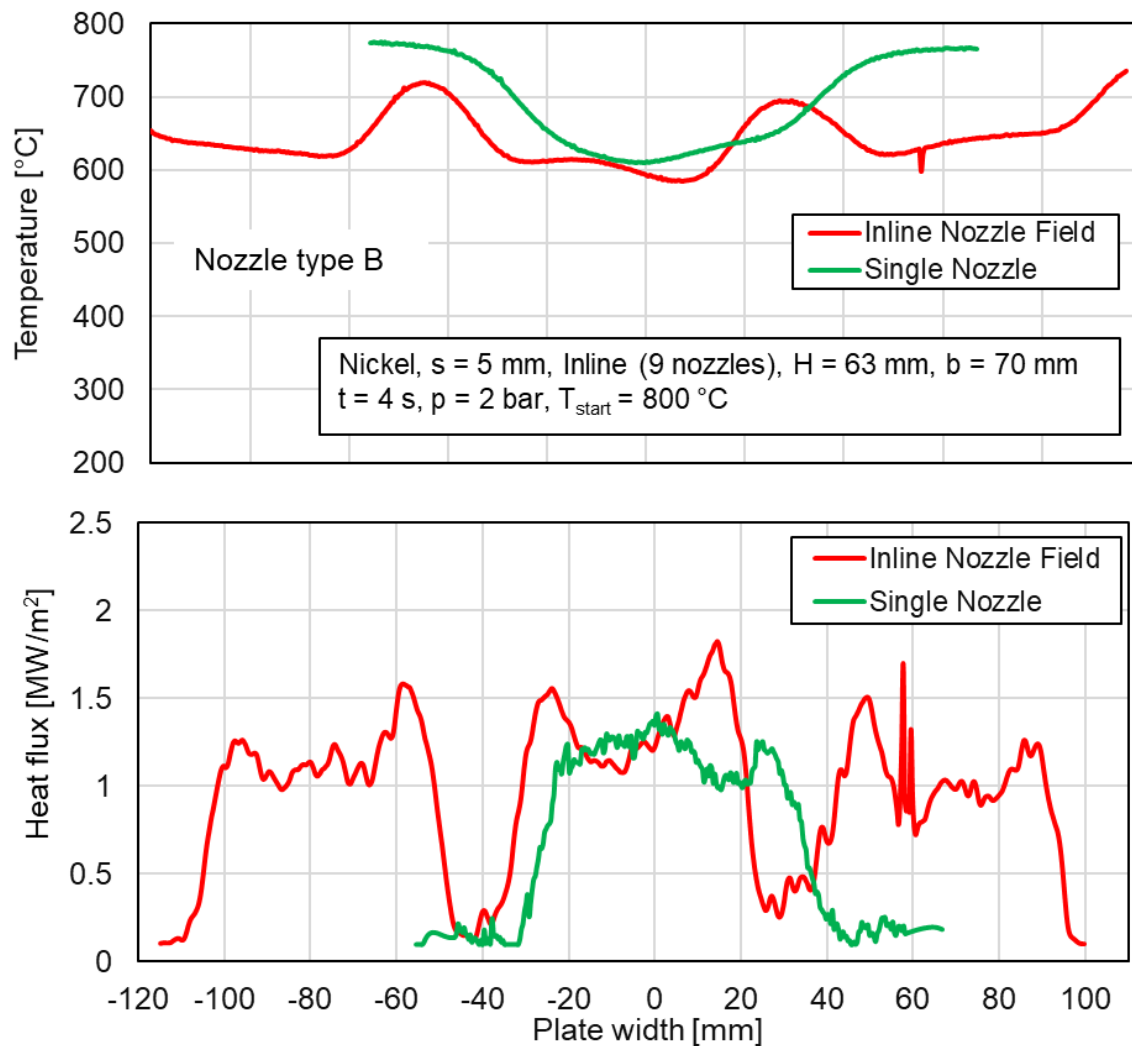


Figure 5.102: Comparison of single nozzle and inline field ($T_{\text{start}} = 800$ °C)

At the center of the middle nozzle, both the temperatures and heat fluxes are approximately the same for both configurations. The heat flux for the inline nozzle field is the overall maximum and decreases in between two nozzles.

Similarly, Figure 5.103 shows the temperature and heat flux profiles during the cooling of the 10 mm aluminum alloy plate.

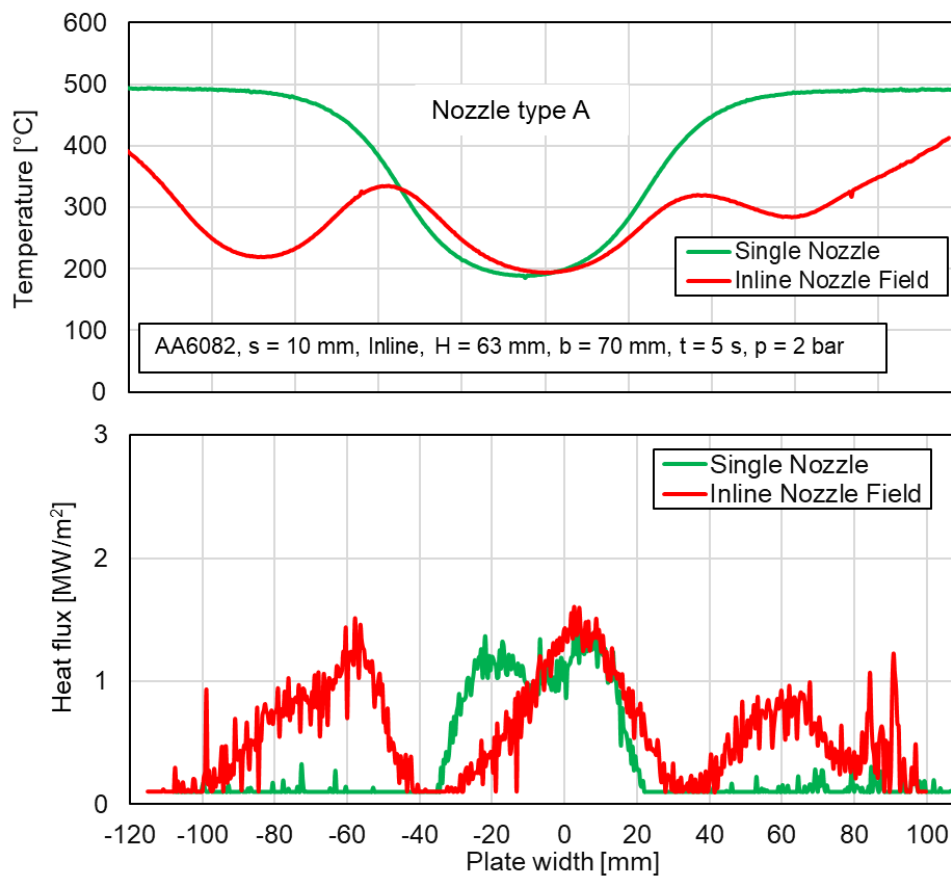


Figure 5.103: Comparison of a single nozzle and inline nozzle field (AA6082)

Figure 5.104 illustrates the temperature profiles of nickel and aluminum alloy moving plates after 5 seconds of cooling.

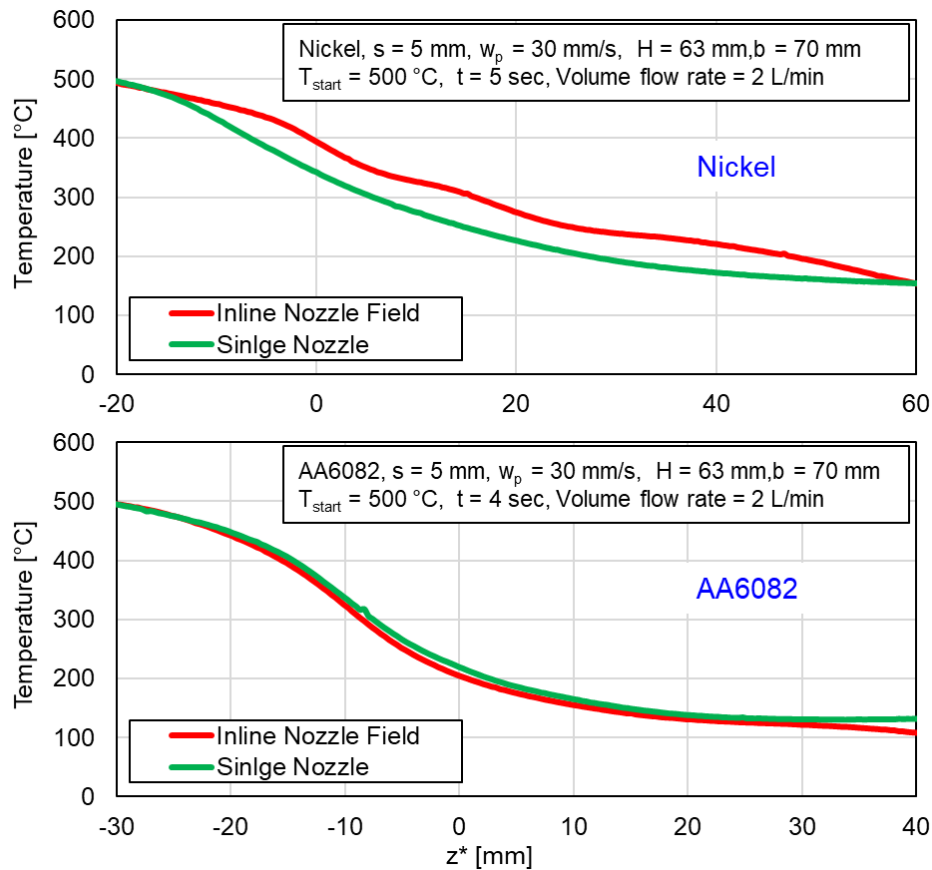


Figure 5.104: Comparison of of moving nickel and AA6082 for single nozzle and inline nozzle field

The temperature profiles are compared for a single nozzle and the inline nozzle filed at a plate velocity of 30 mm/s. The temperature in the vicinity of the nozzle for nickel at $z^* = 0$ mm is 50 °C higher in the nozzle field, compared to the single nozzle, whereas there is no difference in temperature for the aluminum alloy plate. Therefore, the nozzle configuration is more influential in the case of nickel.

5.7 Reproducibility of Experiments

To illustrate the repeatability of experiments in this study temperature measurements were repeated under identical parameters and experimental conditions.

Figure 5.105 depicts the temperature profiles obtained through the repetition of an experiment employing a single full-cone nozzle.

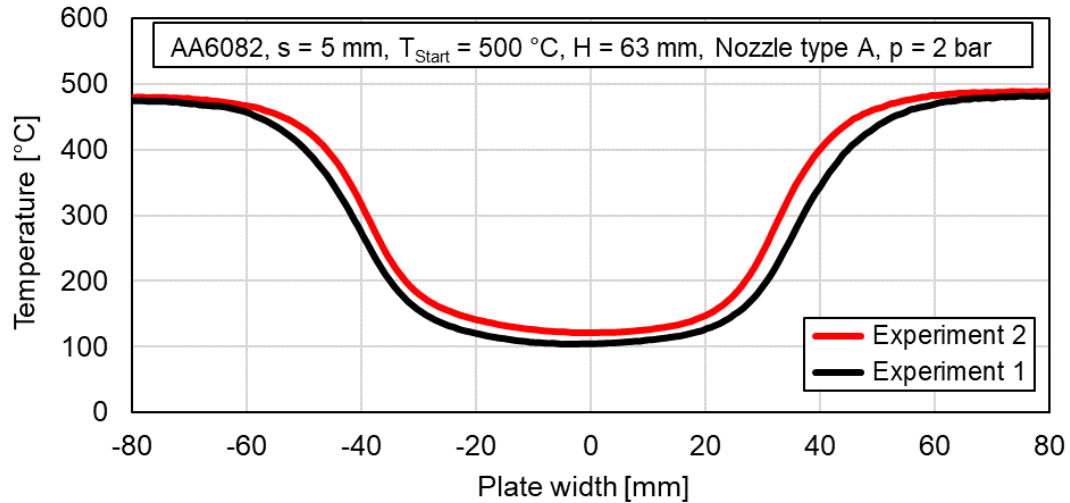


Figure 5.105: Repeatability of experiments single full cone nozzle (AA6082, H = 63 mm)

Remarkably, the observed temperature profiles for both experiments exhibit a high degree of similarity, with a minimal temperature difference of 20 °C between the two measurements. This reaffirms the accuracy and consistency of the temperature measurements and highlights the reliability of the experimental setup.

Figure 5.106 the repeatability analysis conducted in an inline nozzle field for aluminum alloy.

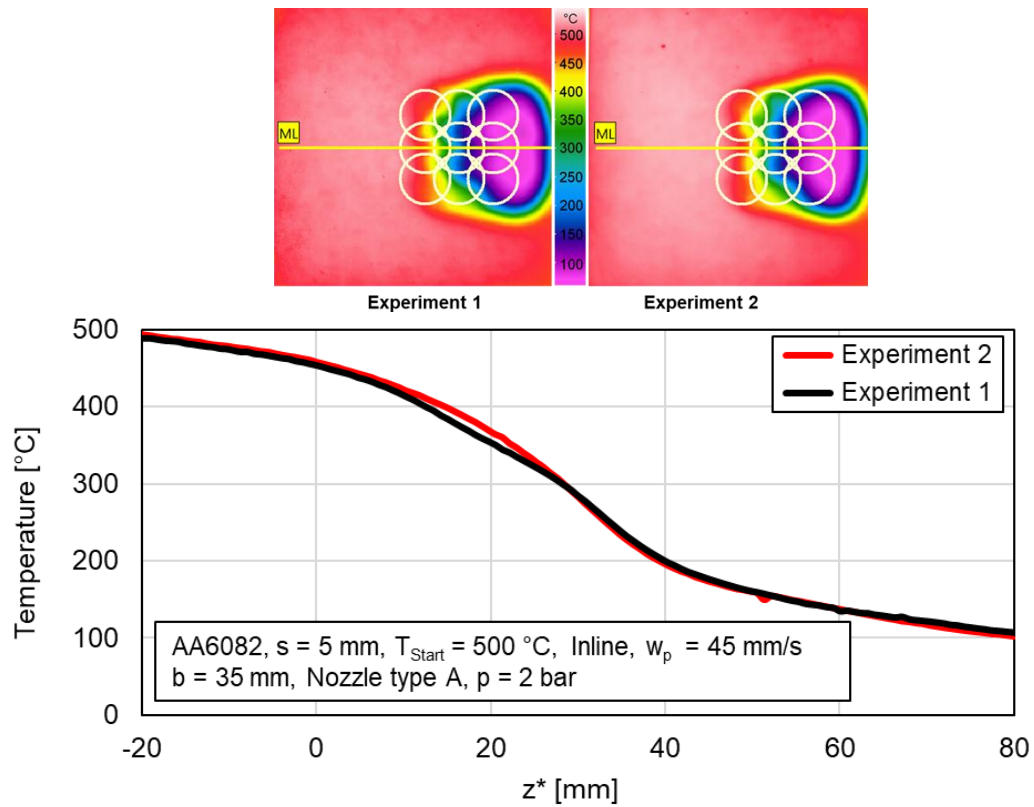


Figure 5.106: Repeatability of experiments in an inline nozzle field (AA6082)

Notably, there is a promising resemblance in the cooling curves between experiment 1 and 2. Following the same methodology, experiments were replicated for nickel plates in the inline nozzle field, and the resulting temperature profiles are depicted in Figure 5.107 with a temperature difference of 21 °C between both experiments.

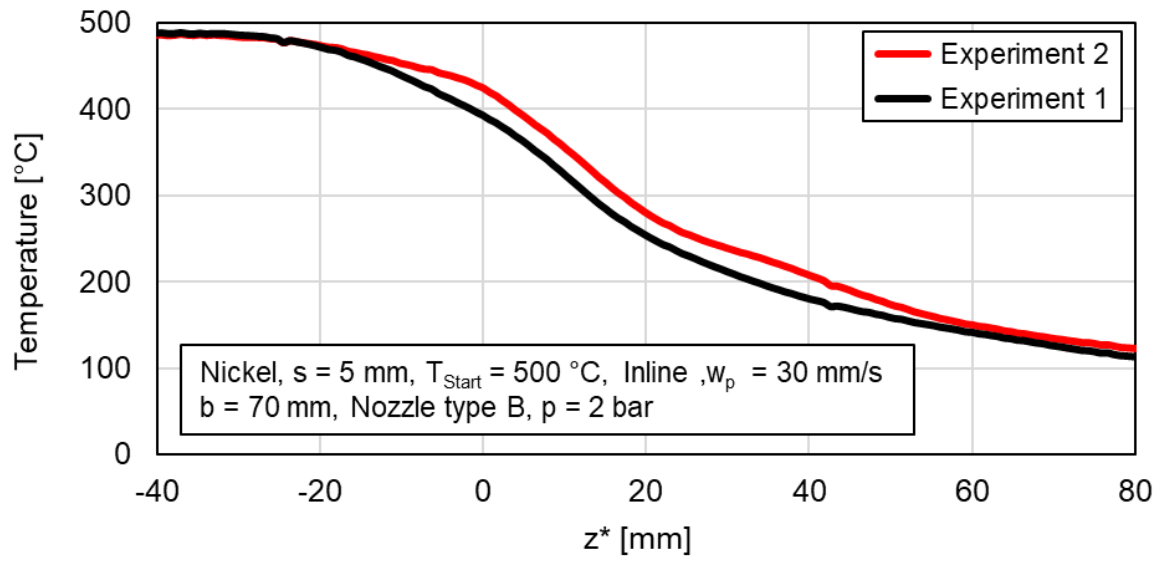


Figure 5.107: Repeatability of experiments in an inline nozzle field (nickel)

These experiments aim to establish the consistent replication of temperature profiles and ensure the accuracy of the experimental process. It is important to acknowledge that slight variations may occur, attributable to the inhomogeneity of the spray.

6 Quenching of Vertical Plates

6.1 Overview

In this chapter, the quenching of plates is investigated by employing two flat spray nozzles. Variations in process parameters, including plate velocity, metal thickness, metal type, and nozzle inclination angle, are investigated. The subsequent analysis focuses on the impact of these varied parameters on the cooling rate and the resultant heat fluxes.

As the water from the nozzle impinges on the hot, moving plate, three distinct regions form on it. The schematic depiction of these regions (A, B, C) and the corresponding temperature profile are illustrated below in Figure 6.1.

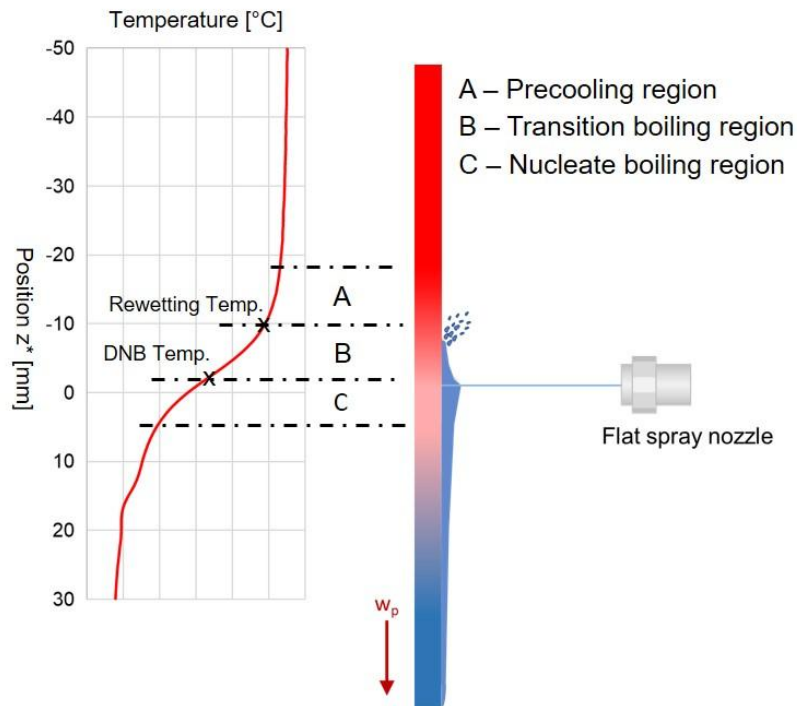


Figure 6.1: Schematics of formation of various boiling regions along the plate length during cooling

The temperature profiles are graphically represented against the plate length, where $z^* = 0$ indicates the position of the nozzle or impingement point on the plate.

The negative range of z^* shows the top hot part of the plate (upstream region). The temperature starts decreasing before the wetting front approaches, because of axial heat conduction known as the pre-cooling region. In metals with high thermal

conductivity, such as aluminum, the temperature drops more sharply in this region. The rewetting temperature is the temperature at which the sheet is wet by water and starts cooling down due to water quenching. The region between the rewetting temperature and the DNB temperature is the transition boiling region. The nucleate boiling region starts after the DNB temperature where the maximum heat flux is obtained.

6.2 Influence of Plate Velocity

The temperature profiles of a 2 mm nickel plate with a nozzle angle of 90° for different plate velocities are depicted in Figure 6.2.

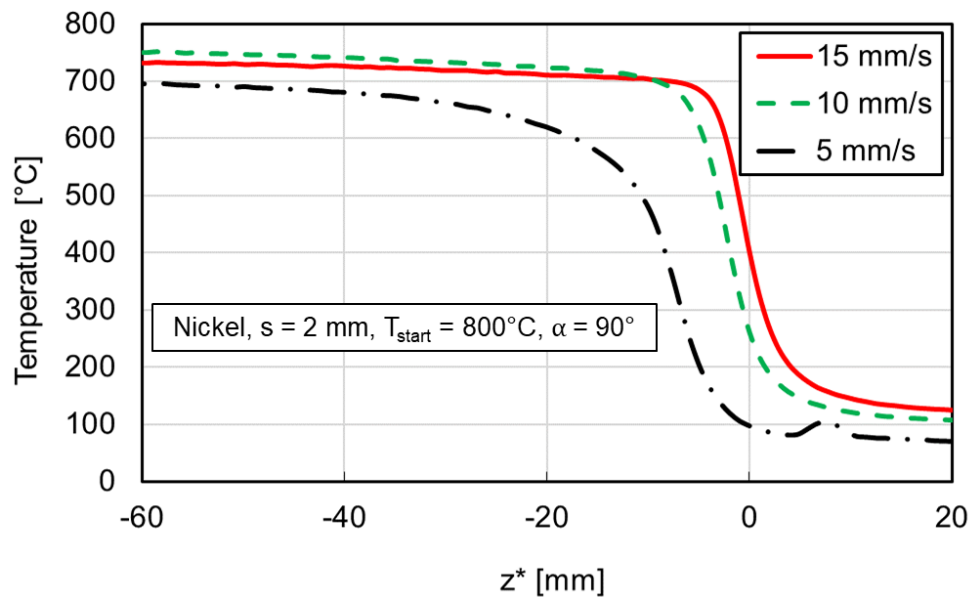


Figure 6.2: Cooling curves of 2 mm nickel plate with varying plate velocities ($\alpha = 90^\circ$)

The above cooling curves along the plate length are shown at quasi-stationary time, to avoid start-up disruptions. A negative range of z^* on the left side of the x-axis plate indicates the top unquenched part of the moving plate, where the temperature of the plate is near the start temperature of 800°C , see Figure 6.3.

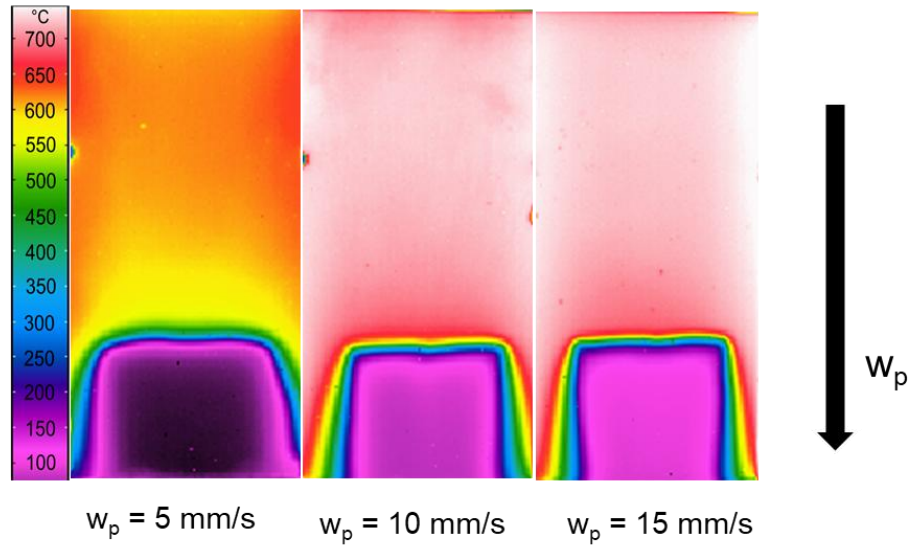


Figure 6.3: IR images of cooling 2 mm nickel at quasi-stationary time at various plate velocities

The zero on the x-axis ($z^* = 0$) shows the position of the spray impact on the moving plate. The impingement of spray cools the moving plate and water flows down due to the gravitational force from $z^* = 0$ to 20 mm.

The red curve shows the decrease in temperature for a maximum plate velocity of 15 mm/s and the black represents the minimum plate velocity of 5 mm/s. It can be seen, that all temperature curves start to drop before the impingement point. The reason is the axial heat conduction and the movement of the wetting front in the upward direction. As the plate velocity increases from 5 to 15 mm/s, the temperature in the vicinity of the impingement region increases from 100 °C to 400 °C, and as a result, the pre-cooling effect reduces.

The boiling curves estimated from the cooling curves for varying plate velocities are illustrated in Figure 6.4.

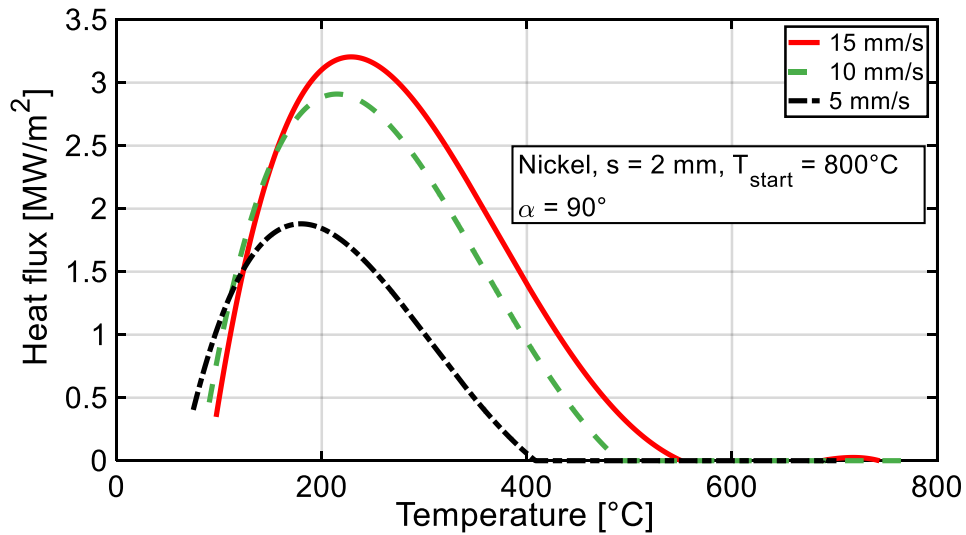


Figure 6.4: Boiling curves of 2 mm nickel plate with varying plate velocities ($\alpha = 90^\circ$)

The average heat transfer, as well as the maximum heat flux, are higher with increasing plate velocity. The DNB temperatures are in the range of 180 °C to 220 °C and the rewetting temperature increases from 400 °C to 550 °C. The higher sheet velocities cause a minor increase in the DNB temperature.

The temperature profiles for the cooling of the aluminum alloy plates are shown in Figure 6.5.

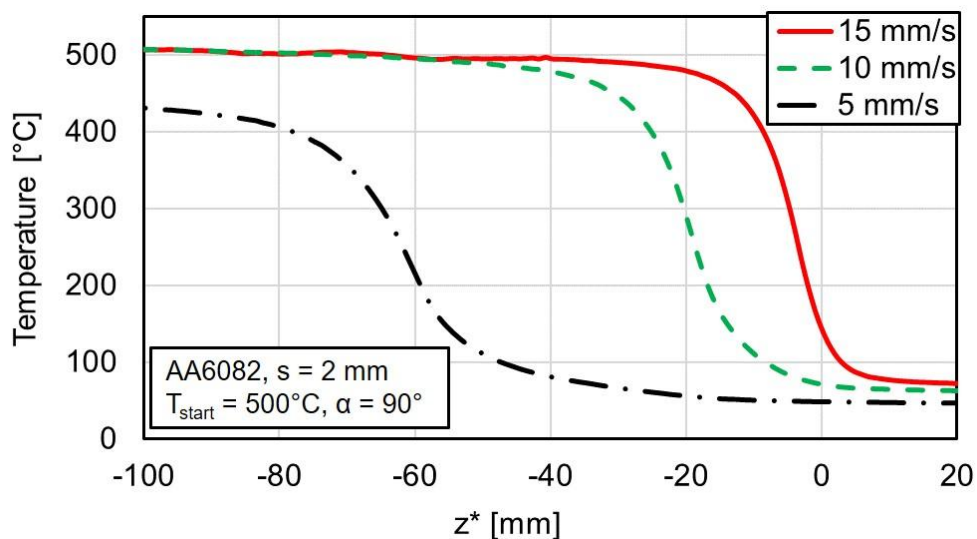


Figure 6.5: Cooling curves of AA6082 plate with varying velocities ($\alpha = 90^\circ$)

Due to the lower melting point of aluminum alloy metal, these plates are heated to a start temperature of 500 °C. It can be seen, that aluminum alloy plates show a similar trend as nickel plates with varying plate velocities. The temperature of the plate starts decreasing before the impingement point due to the precooling effect for all three plate velocities. Due to the high thermal conductivity of aluminum alloy, the temperatures are close to 100 °C at the impingement position at $z^* = 0$. Hence, higher thermal conductivity results in a large and fast precooling range.

Boiling curves of 2 mm aluminum alloy at 5, 10 and 15 mm/s plate velocities corresponding to the above cooling curves are shown in Figure 6.6.

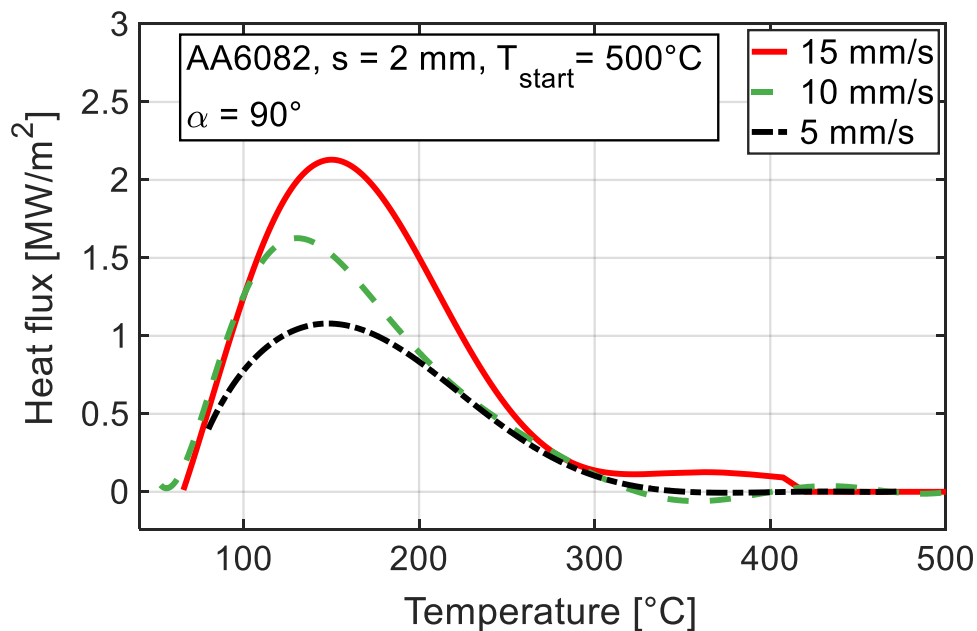


Figure 6.6: Boiling curves of 2 mm AA6082 plate with varying plate velocities ($\alpha = 90^\circ$)

The maximum heat flux increases with an increase in the plate velocity from 5 to 15 mm/s. The maximum heat fluxes for aluminum alloy are comparatively lower than of the nickel plate, as the start temperature and thermal properties of aluminum alloy are different from nickel. The rewetting temperature lies around 310 °C for all three velocities. The DNB temperature is approximately 170 °C with a minimum increase at 15 mm/s plate velocity.

The cooling curves of 2 mm microfer plates moving with 5, 10, and 15 mm/s velocities at nozzle inclination angles are shown in Figure 6.7.

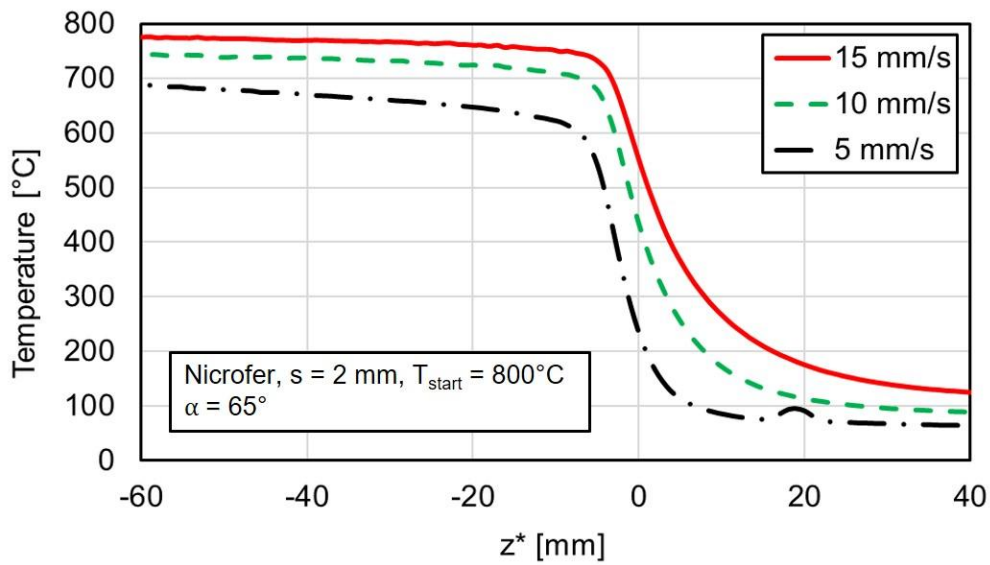


Figure 6.7: Cooling curves of 2 mm nicrofer plate with varying velocities ($\alpha = 65^\circ$)

For all three velocities, the plates cool down at quasi-stationary conditions. It can be seen that the temperatures are 230 °C, 440 °C, and 580 °C at the impingement point ($z^* = 0$) for 5, 10, and 15 mm/s moving plates, respectively. nicrofer has a three times lower thermal conductivity than a nickel. Due to the lower thermal conductivity of nicrofer, the temperatures are lower at the impingement point, compared to nickel plates. Apart from that, as the nozzle inclination angle for nicrofer is 65° , the inclination angle hinders the movement of the wetting front in the upward direction.

Figure 6.8 shows the boiling curves of 2 mm nicrofer plates for the cooling curves corresponding to Figure 6.7.

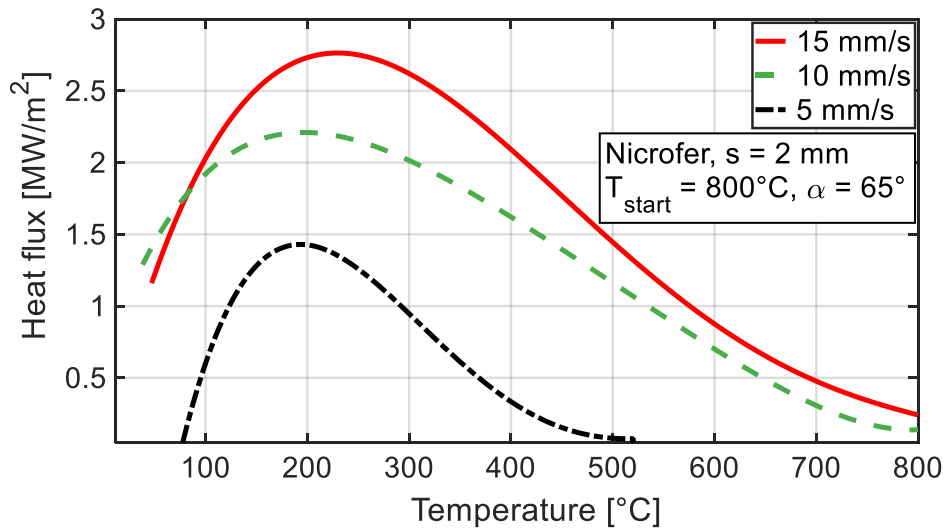


Figure 6.8: Boiling curves of 2 mm nicrofer plate with varying plate velocities ($\alpha = 65^\circ$)

The maximum heat flux, the rewetting temperature, and the DNB temperature increase by increasing the plate velocity. Compared to nickel, the maximum heat flux for nicrofer is lower whereas the DNB temperature is higher.

6.3 Influence of Metal Thickness

The metal thickness is varied and studied with two flat spray nozzles. The wetting front velocity decreases with an increase in metal thickness as reported by (Agrawal et al., 2017).

Figure 6.9 shows the influence of thickness for temperature profiles of aluminum alloy plates of 10 mm/s plate velocity.

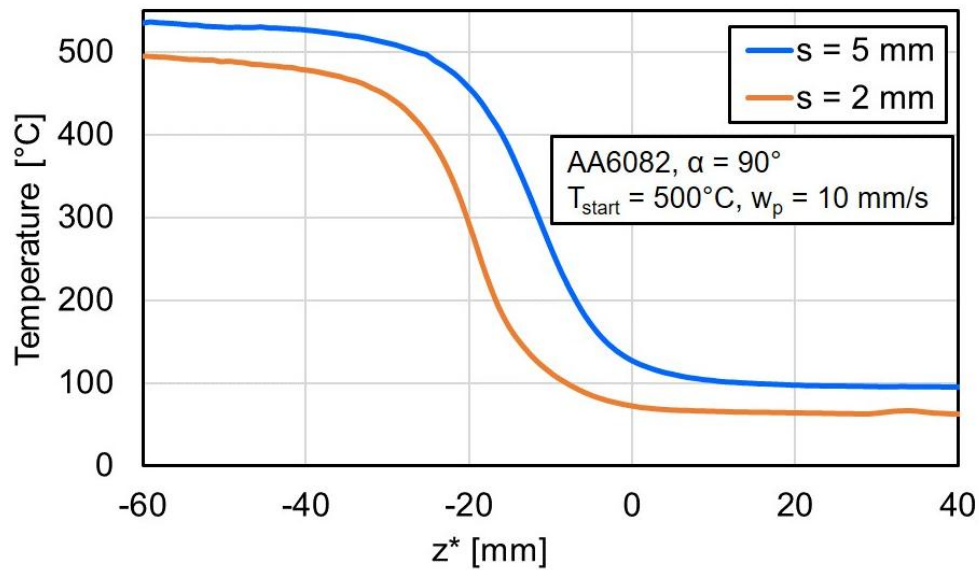


Figure 6.9: Cooling curves of AA6082 of 2 mm and 5 mm thick plates ($w_p = 10$ mm/s)

Both cooling curves follow a similar trend, where the cooling occurs from approximately 500 °C to 100 °C. The axial heat conduction is relatively lower for a 5 mm plate compared to a thin 2 mm plate. Consequently, the precooling effect decreases, and the temperature at impingement $z^* = 0$ is higher for the 5 mm plate.

Figure 6.10 shows the influence of metal thickness on the boiling curve for aluminum alloy plates at a constant plate velocity of 10 mm/s.

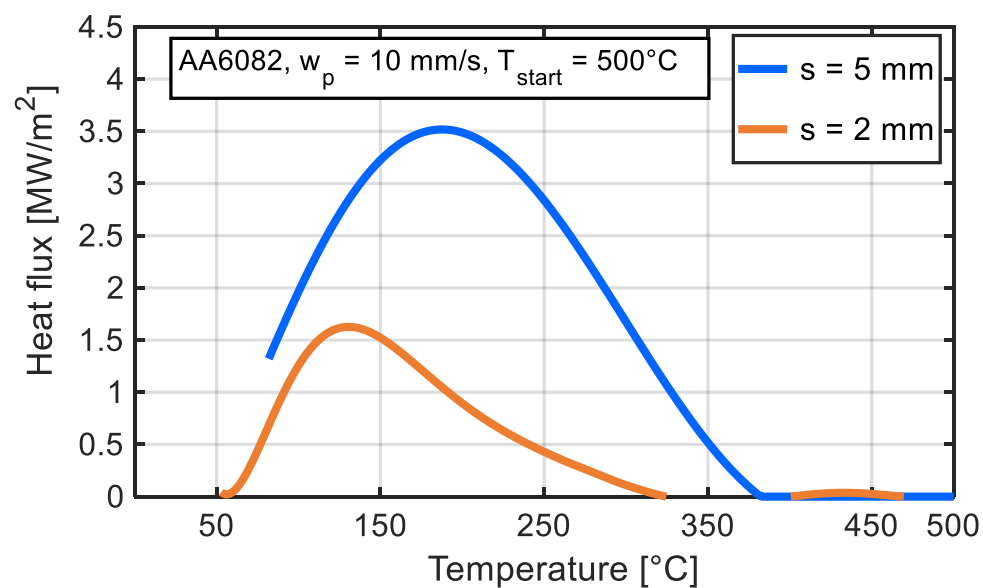


Figure 6.10: Boiling curve of 2 mm and 5 mm AA6082 plate ($w_p = 10$ mm/s)

It can be seen, that the heat transfer of a 5 mm plate is higher than the 2 mm plate. The maximum heat flux observed for the 5 mm plate is 3.5 MW/m^2 , whereas the 2 mm plate exhibits a lower value of 1.6 MW/m^2 . With increasing thickness, the rewetting temperature, as well as the DNB temperature, increases. Under constant plate velocity conditions, the heat conduction rate within the plate becomes a pivotal factor, influencing the heat transfer on the plate surface. Consequently, there is a reduction in rewetting and DNB temperatures for the 2 mm thick plate due to the influence of heat conduction within the material.

Figure 6.11 shows the influence of metal thickness on nickel plates at a constant plate velocity of 5 mm/s.

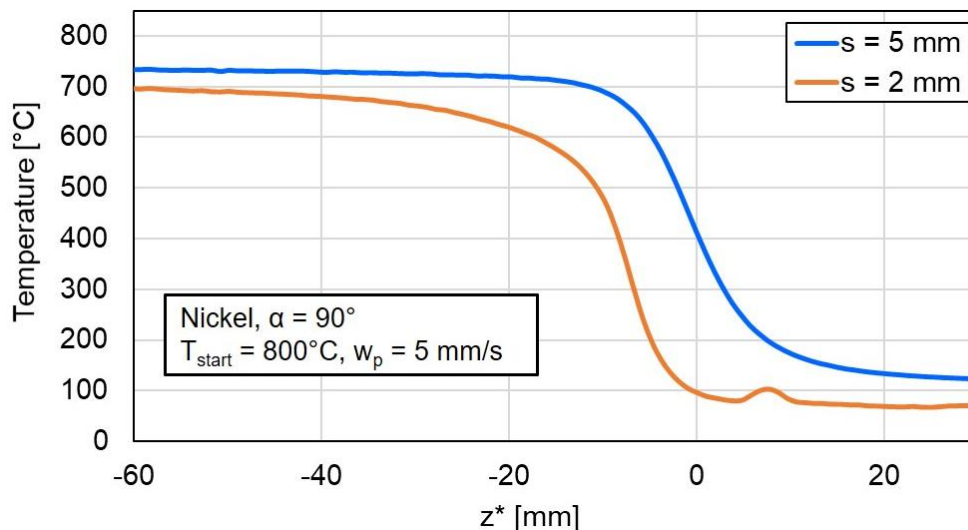


Figure 6.11: Cooling curves of nickel of 2 mm and 5 mm thick plates at 5 mm/s plate velocity

Nickel shows a similar trend as aluminum alloy with varying plate thicknesses. The temperature at the impingement point $z^* = 0$ is 400°C for a 5 mm thick plate compared to 100°C for a 2 mm plate. This observation highlights the influence of thickness on the thermal behavior of nickel, indicating a significant temperature differential between the two plate thicknesses at the impingement point.

The corresponding boiling curves of 2 mm and 5 mm nickel plates at 5 mm/s are illustrated in Figure 6.12.

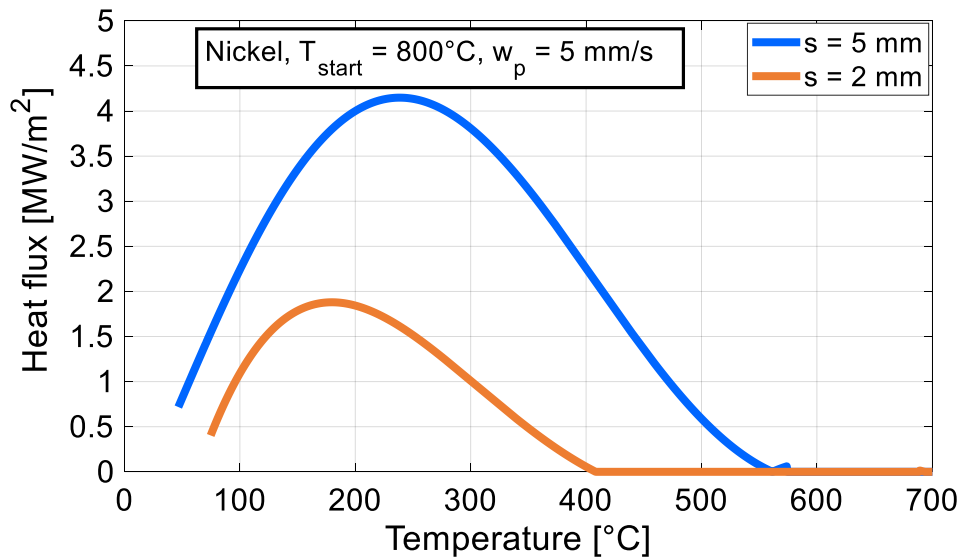


Figure 6.12: Boiling curve of 2 mm and 5 mm nickel plate at 5 mm/s plate velocity

An increase in metal thickness from 2 mm to 5 mm leads to an increase in the maximum heat flux as well as rewetting and DNB temperatures.

6.4 Influence of Metal Type

The influence of different kinds of metal, using two flat sprays is investigated. For investigation nickel, nicrofer, and aluminum alloy of 2 mm are employed. nickel and nicrofer plates are cooled from a start temperature of 800 °C and aluminum alloy plates are cooled from 500 °C. The temperature profiles of nickel, nicrofer, and aluminum alloy at the quasi-stationary time are presented in Figure 6.13.

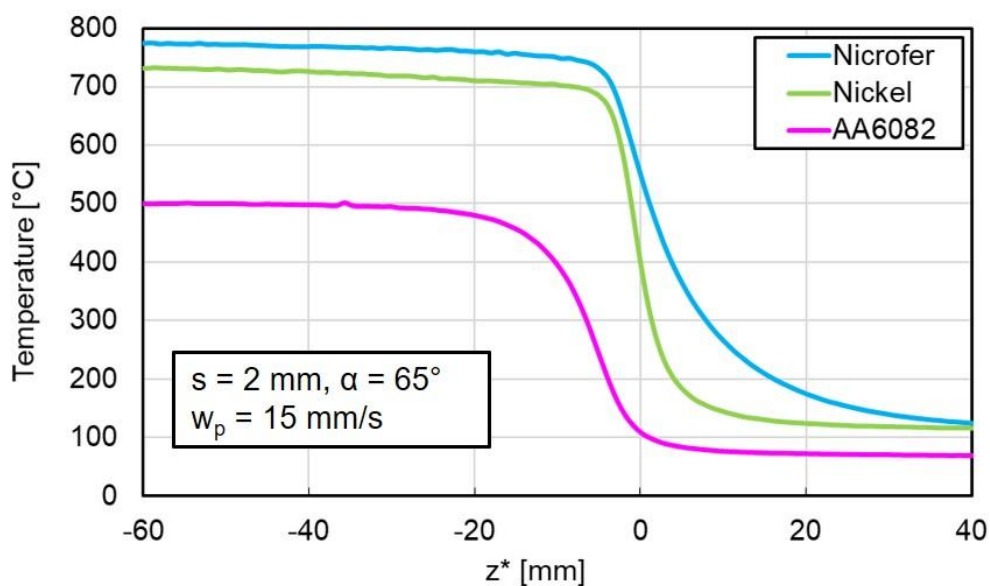


Figure 6.13: Influence of metal type on temperature profile at 15 mm/s plate velocity

It can be seen, that the metal type has a significant influence on the cooling curves. aluminum alloy has the highest thermal conductivity, compared to the other two metals. Hence, the precooling effect is higher during the cooling of the aluminum alloy metal plate. Despite higher plate velocity, the temperature at the impingement point $z^* = 0$ for aluminum alloy is at 100 °C, whereas, nickel and nicrofer are at 400 °C and 550 °C, respectively.

The boiling curves of nickel, nicrofer, and aluminum alloy are presented in Figure 6.14.

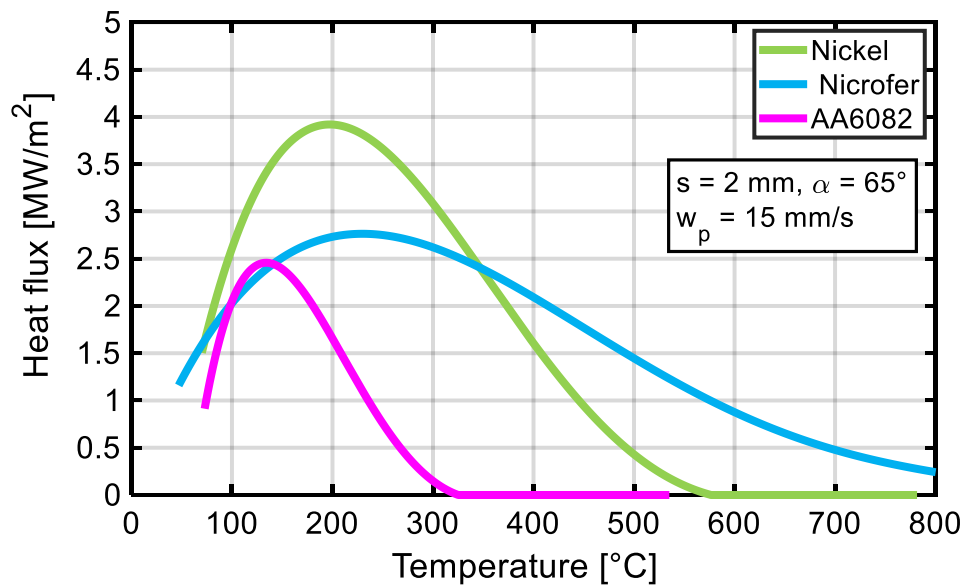


Figure 6.14: Influence of metal type on the boiling curve at 15 mm/s plate velocity

Nicrofer has the highest rewetting temperature, followed by nickel and aluminum alloy. The maximum heat flux is higher for nickel, compared to nicrofer and aluminum alloy at the DNB temperature of 200 °C. The DNB temperature of nicrofer is around 220 °C and for aluminum alloy is at 150 °C. A similar trend is reported during the study of a full jet nozzle by (Fang, 2019).

Figure 6.15 illustrates the maximum heat fluxes with varying plate velocities for nickel, nicrofer, and aluminum alloy at a nozzle inclination angle of 65°.

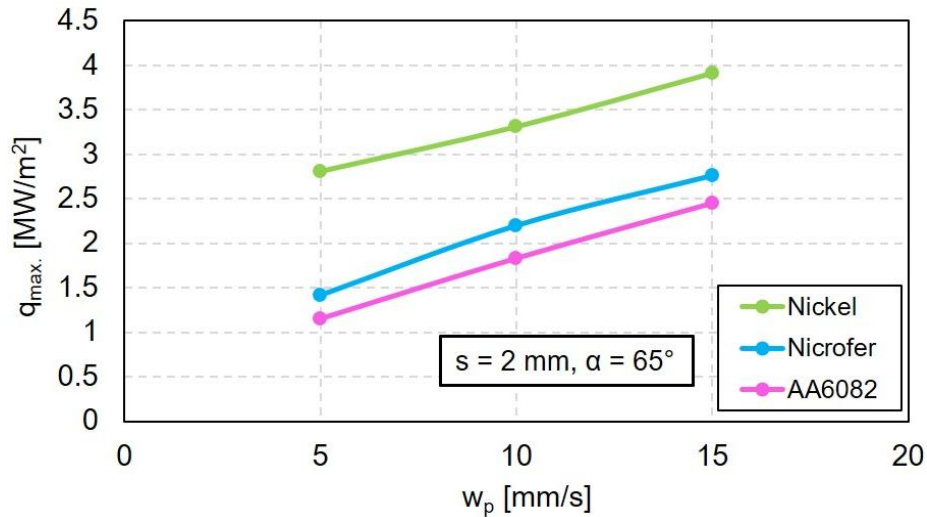


Figure 6.15: Influence of meta-type on maximum heat flux for varying plate velocities

It can be seen, that for all metals maximum heat flux increases as plate velocity increases from 5 to 15 mm/s. At higher plate velocities, the precooling effect due to conduction within the plate decreases. As a result, the temperature gradient at the impingement point is larger, compared to lower plate velocities. Higher temperature gradients lead to higher maximum heat fluxes. Compared to nicrofer and aluminum alloy plates, nickel shows higher heat flux at all velocities.

6.5 Influence of Nozzle Inclination Angle

The nozzle inclination angle has been investigated for all three metals with a thickness of 2 mm. Experiments are performed with various nozzle inclination angles of 90°, 65°, and 45°. Notably, the nozzle inclination angle plays a pivotal role in influencing the propagation of the wetting front on the surface of the moving plates. Specifically, at a nozzle angle of 45°, the wetting front exhibits comparatively less upward movement, in contrast to the more pronounced upward motion observed at a 90° angle. This observation highlights the significant impact of the nozzle inclination angle on the behavior of the wetting front during the experiments.

Figure 6.16 illustrates the effect of inclination on cooling curves of a 2 mm nickel plate moving with 15 mm/s plate velocity.

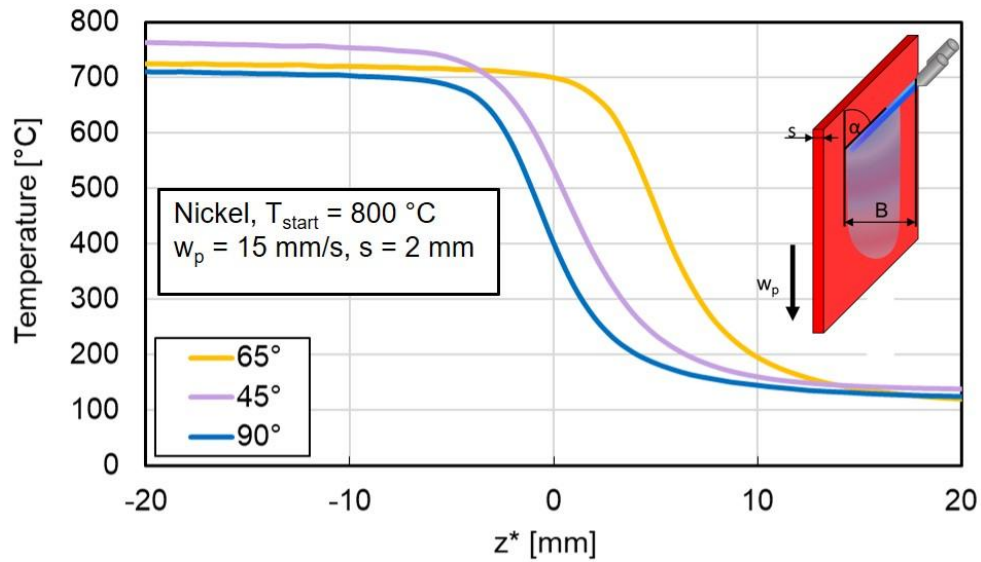


Figure 6.16: Influence of nozzle angle during cooling a nickel plate ($w_p = 15\text{ mm/s}$)

As the inclination angle decreases from 90° to 45° , there is a noticeable rise in the temperature at the impact point. This shift in inclination angle significantly influences the flow dynamics of water on the plate, giving rise to distinct temperature profiles along the length of the plate.

Figure 6.17 presents the boiling curves for the above-varied nozzle angles.

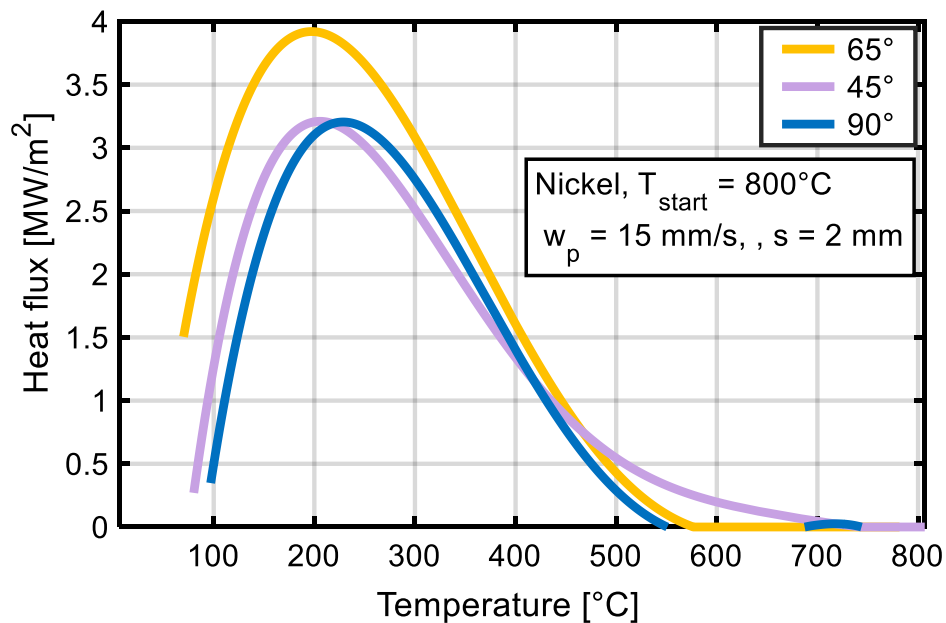


Figure 6.17: Influence of nozzle angle on boiling curve of nickel plate ($w_p = 15\text{ mm/s}$)

The maximum heat flux is notably elevated at a 65° nozzle angle in comparison to both 45° and 90° angles. Despite this variation, the DNB temperature remains approximately constant at around 200 °C for all nozzle angles. Notably, the rewetting temperature experiences a distinct change, reaching 700 °C at the 45° nozzle angle. This shift is attributed to the increased inclination, resulting in more pronounced water splashing at the impact point. The water splashing impedes the wetting front movement along the plate length. In contrast, the rewetting temperatures for 90° and 65° nozzle angles are lower.

Figure 6.18 shows the comparison of the maximum heat fluxes of the 2 mm aluminum alloy plate at three investigated nozzle angles for various plate velocities.

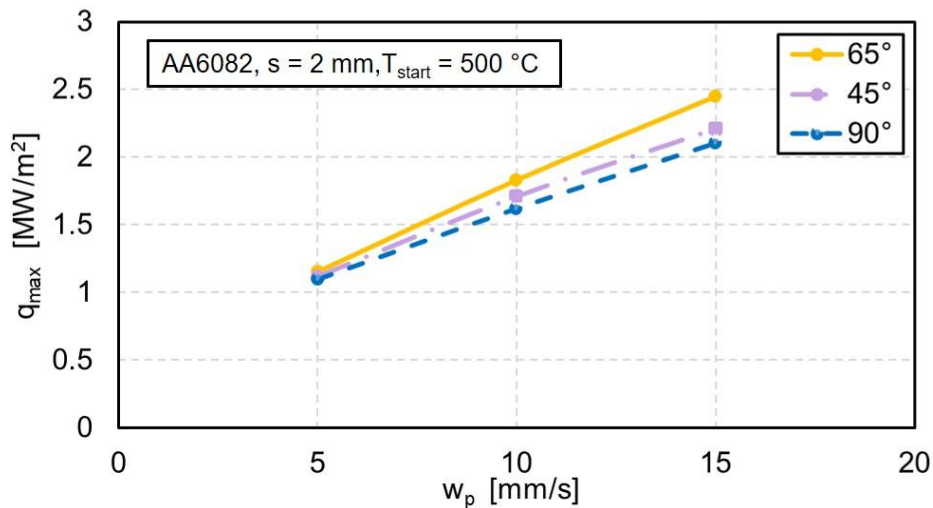


Figure 6.18: Influence of nozzle angle on maximum heat flux for varying plate velocities (AA6082)

The maximum heat flux exhibits an upward trend across all nozzle angles as the plate velocity increases. Notably, the nozzle inclination angle exerts a more pronounced influence on the maximum heat flux, particularly at higher plate velocities. At all velocities considered, the maximum heat is more substantial at a 65° inclination angle compared to 45° and 90° angles. This observation shows the impact of the nozzle inclination angle on the overall heat transfer dynamics, with a clear emphasis on the significant role played at elevated plate velocities.

6.6 Mechanism of Heat Transfer

The mechanism of heat transfer is influenced by the water flow rate and type of metal. As the water flow rate is significantly higher than the plate velocity, it becomes independent of both, plate velocity and plate thickness. Hence, the heat transfer is dependent on the local position (z^*) of the plate. It is notably higher in proximity to the impingement point and gradually decreases as it moves away from the impact point.

In all temperature profiles, a consistent observation is the attainment of the DNB temperature associated with the maximum heat flux, consistently in the downstream zone beneath the impingement point ($z^* > 0$). As the plate velocity increases, there is a notable shift of the DNB temperature towards the impingement region, resulting in an increased value of the maximum heat flux.

A similar effect is observed with an increase in plate thickness; as the thickness increases, the DNB temperature shifts closer to the impingement region, leading to the occurrence of maximum heat flux. Therefore, the following figures depict the maximum heat flux in relation to the local position (z^*), highlighting the influence of plate velocity and sheet thickness on heat transfer.

Figure 6.19 shows the dependence of maximum heat flux on the local position z^* on the surface of the plate for all three investigated metals by varying plate velocities.

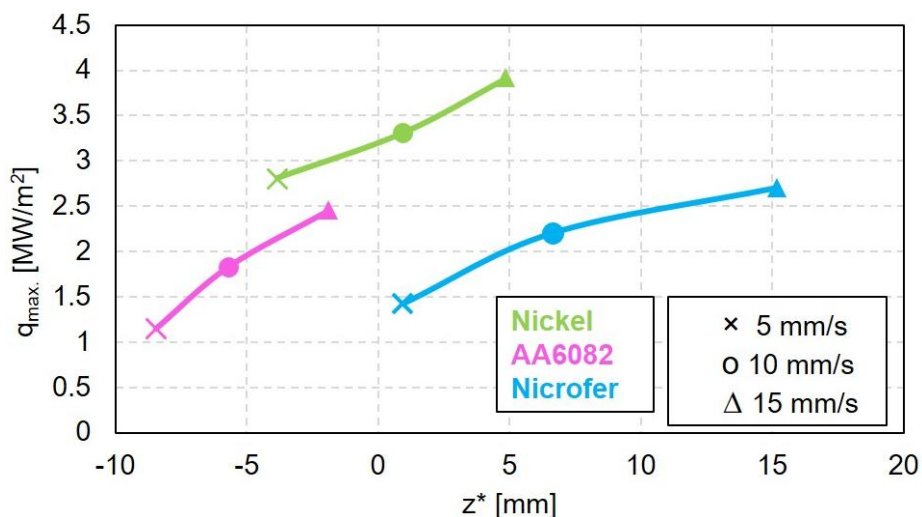


Figure 6.19: Maximum heat flux of nickel, nicrofer, and AA6082 for various plate velocities ($\alpha = 65^\circ$)

The observed trend reveals, that for all metals, there is a consistent rise in the maximum heat flux, as plate velocities increase and the local position (z^*) at which this maximum is reached, shifts downstream. Notably, AA6082, characterized by its rapid cooling attributed to high thermal conductivity and a larger precooling region, achieves maximum heat flux at positions ($z^* < 0$) for all velocities. However, at higher velocities, there is a notable shift of the maximum heat flux closer to the impact zone. In contrast, nicrofer, possessing a lower thermal conductivity, exhibits a different behavior. The maximum heat flux for nicrofer is obtained at positions ($z^* > 0$). This distinction underscores the influence of metal properties, especially thermal conductivity, on the heat transfer dynamics, resulting in diverse patterns of maximum heat flux across different metals and velocities. The nozzle inclination angle plays a crucial role in shaping the movement of the wetting front, both in the upstream and downstream zones. This, in turn, alters the extent of the pre-cooling and quenching regions, leading to variations in the maximum heat flux.

Figure 6.20 represents the influence of the nozzle angle on the position of the maximum heat flux for nickel at different plate velocities.

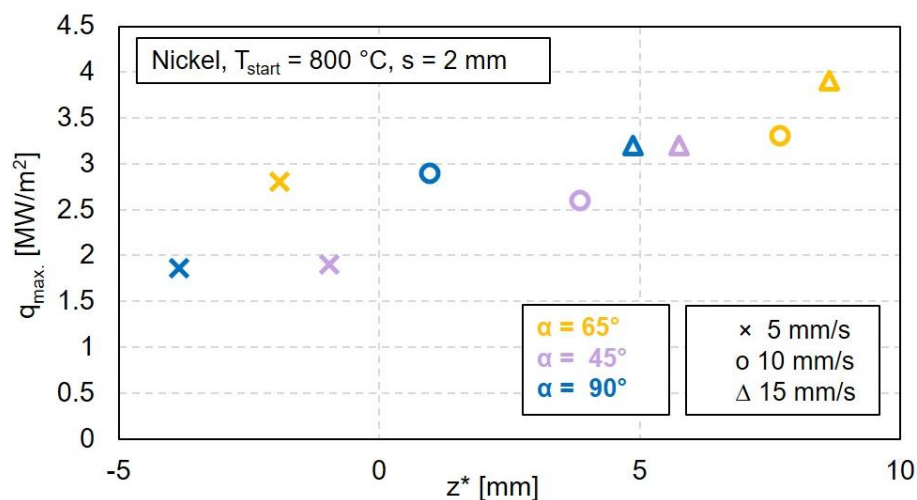


Figure 6.20: Maximum heat flux of nickel for various nozzle angles and plate velocities

As the inclination angle decreases, there is a significant shift in the position of maximum heat flux towards the downstream direction ($z^* > 0$). This observation underscores the influence of the nozzle inclination angle on the localization of heat transfer dynamics, emphasizing how alterations in the angle impact the distribution and intensity of the heat flux along the material surface.

Figure 6.21, and Figure 6.22 show the influence of the nozzle angle on the position of maximum heat flux for nicrofer and aluminum alloy, respectively with varying plate velocities.

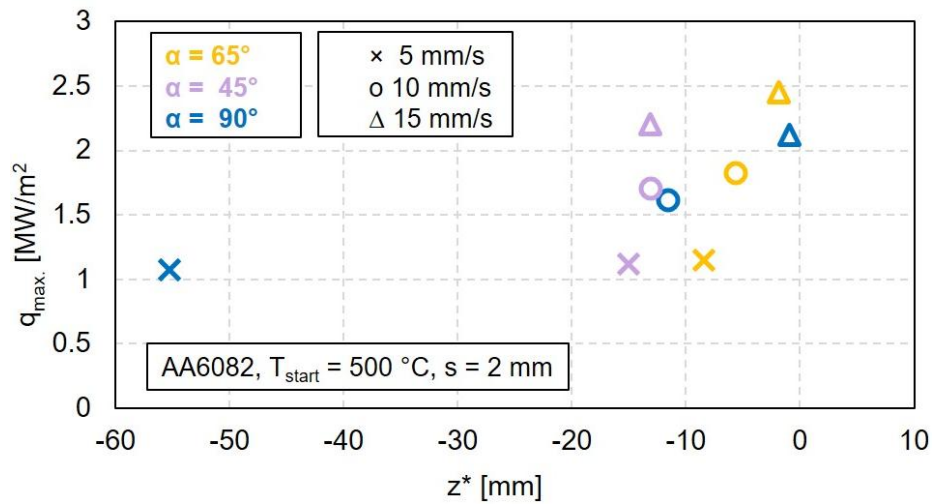


Figure 6.21: Maximum heat flux of AA6082 for various nozzle angles and plate velocities

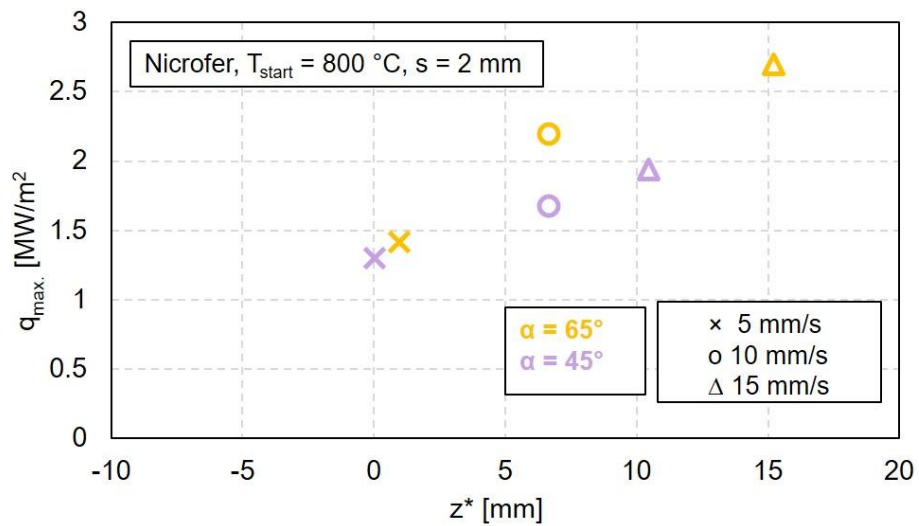


Figure 6.22: Maximum heat flux of nicrofer for various nozzle angles and plate velocities

In Figure 6.23 various cooling regions are represented on the cooling curve.

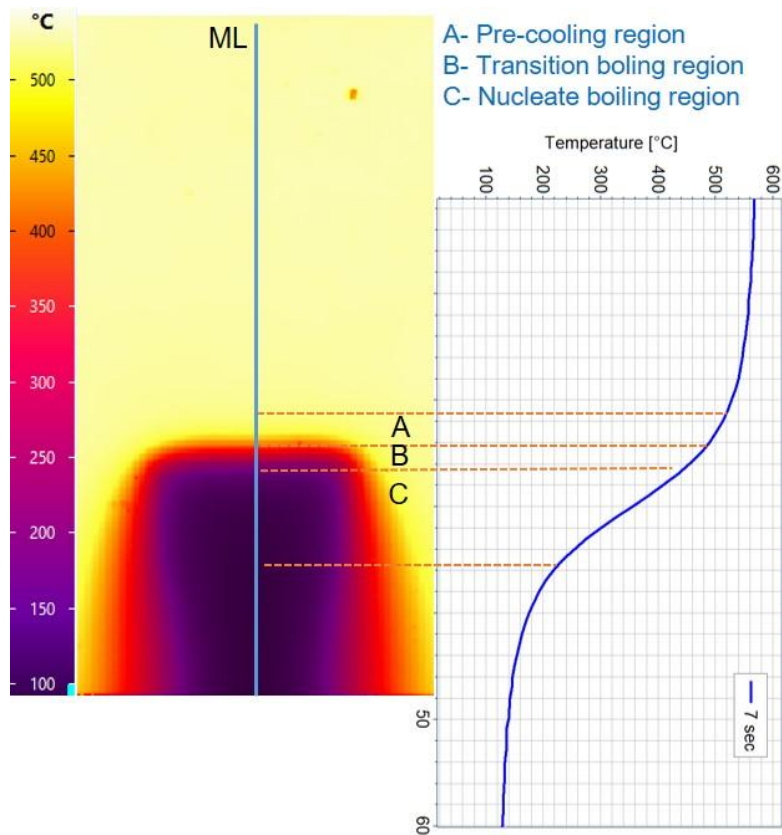


Figure 6.23: IR image with various quenching regions ($s = 5$ mm, AA6082)

The infrared camera provides a comprehensive view of temperature data, enabling the visual measurement of the widths of these regions.

Table 6 shows the widths of various boiling regions for a 2 mm nickel plate at various velocities.

Table 6: Width of various cooling regions for nickel at various plate velocities ($\alpha = 90^\circ$, $s = 2$ mm)

Plate velocity	5 mm/s	10 mm/s	15 mm/s
Precooling region	9 mm	4 mm	3 mm
Transition boiling region	6 mm	4 mm	4 mm
Nucleate boiling region	5 mm	10 mm	32 mm
Rewetting temperature	400 °C	500 °C	550 °C
DNB temperature	190 °C	210 °C	220 °C

The front width in the pre-cooling region demonstrates a decreasing trend with higher plate velocity. Specifically, at a velocity of 5 mm/s, it measures 16 mm, while at 15 mm/s, it reduces to 4 mm.

Table 7 depicts the width of different cooling regions for microfer at a nozzle inclination angle of 65° .

Table 7: Width of various cooling regions for microfer at various plate velocities ($\alpha = 65^\circ$, $s = 2$ mm)

Plate velocity	5 mm/s	10 mm/s	15 mm/s
Precooling region	5 mm	4 mm	4 mm
Transition boliling region	6 mm	9 mm	14 mm
Nucleate boiling region	5 mm	9 mm	28 mm
Rewetting temperature	480 °C	780 °C	800 °C
DNB temperature	200 °C	200 °C	220 °C

The width of the pre-cooling region experiences a reduction of 1 mm at higher velocities. In contrast, the widths of the transition and nucleate boiling regions exhibit an increase with the escalating velocities.

Table 8 shows the front widths of various regions during the cooling of aluminum alloy at a 90° nozzle angle.

Table 8: Width of various cooling regions for AA6082 at various plate velocities ($\alpha = 90^\circ$, $s = 2$ mm)

Plate velocity	5 mm/s	10 mm/s	15 mm/s
Precooling region	15 mm	9 mm	6 mm
Transition boliling region	6 mm	9 mm	4 mm
Nucleate boiling region	7 mm	5 mm	4 mm
Rewetting temperature	330 °C	332 °C	335 °C
DNB temperature	150 °C	145 °C	150 °C

It has been observed that, across all three investigated metals, the length pre-cooling region decreases with increasing plate velocities and plate thickness. Consequently, this leads to an increase in the maximum heat flux. Additionally, the local position of the DNB temperature shifts towards the impingement region as the sheet velocity rises. The DNB temperatures for nickel and nicrofer are between 190 °C and 220 °C, while for aluminum alloy, they fall within the range of 140 °C to 150 °C. These findings highlight the relationship between plate velocities, heat transfer dynamics, and the spatial distribution of boiling phenomena.

7 Conclusion

In the production of metals, heat treatment plays a crucial role in shaping the mechanical properties of the final product. Achieving a rapid cooling rate of up to 300 K/s is imperative, particularly in processes involving aluminum alloys stated by (Ostermann, 2014; Zhang et al., 2014). In industrial practices, these high cooling rates are achieved through arrays of sprays, which uniformly impinge the water on the entire width of the metal strip. The resulting heat transfer and temperature distribution are significant factors influencing the quality and hardness of the material. Non-uniform temperature distribution and higher gradients can cause thermal stresses in the metal strip, which contribute to deformation and cracks.

In the present study, the heat transfer on horizontal plates using a single full cone nozzle as well as fields consisting of full cone nozzles, was investigated. The influencing parameters such as nozzle pressure, nozzle-to-plate height, nozzle-to-nozzle distance, volume flow rate, nozzle configuration, the thickness of metal plate, type of metal, start temperature, and the velocity of plates were varied. The aforementioned parameters were investigated for top-side cooling and bottom-side cooling. Additionally, the heat transfer in the cooling of vertically moving metal plates using a field of two flat sprays was studied. The temperatures during the cooling of metal plates were measured on the back side (measuring side) using a high-frequency infrared camera, which enables the measurement of the whole surface. The measured high spatial and temporal data was further used in the developed two-dimensional inverse heat conduction method. The heat fluxes, boiling curves, and temperature distribution on the quenching side were numerically simulated using the model with the help of measured temperatures on the measurement side. The findings of this study can be divided similarly to structure the dissertation as follows:

Quenching of Horizontal plates using full cone nozzles

Single full cone nozzle

The study reveals several key findings regarding the non-homogeneous heat transfer across the impingement region, primarily due to the non-uniform impingement flux of the investigated full cone nozzle. Increasing the nozzle height from 63 to 127 mm, results in longer cooling time due to the longer film boiling period. Increasing the nozzle

height from 63 to 127 mm results in longer cooling times, attributable to an extended film boiling period. This increase in nozzle height leads to a reduction in spray flux, subsequently decreasing both, the maximum heat flux and the cooling rate.

The variation in nozzle pressure from 2 to 9 bar affects the uniformity of cooling, particularly at the nozzle center. Higher nozzle pressure reduces the cooling time and film boiling period while increasing the maximum heat flux.

When increasing the thickness of aluminum alloy plates from 2 to 10 mm, it is observed that thicker plates result in longer film boiling and cooling times. This is due to the higher stored thermal energy in thicker plates, which also contributes to higher maximum heat flux and rewetting temperatures. An increase in the initial temperature enhances the maximum heat flux and the heat flux within the film boiling region. The rewetting temperature is slightly higher at a starting temperature of 800 °C compared to 500 °C, while the DNB temperature shows no significant change

Nickel plates exhibit a higher maximum heat flux compared to aluminum alloy plates. For a 5 mm nickel plate, the rewetting temperature ranges between 350 °C and 400 °C, whereas for an aluminum alloy plate, it ranges between 250 °C and 300 °C.

The observed trends in heat transfer parameters are consistent for bottom-side cooling, where water is sprayed from the bottom and temperatures are measured from the top. Bottom-side cooling results in quicker surface rewetting, reducing the film boiling period. The wetting front propagation speed and maximum heat flux are higher for bottom-side cooling, which demonstrates more uniform heat transfer with fewer fluctuations across the plate width.

Increasing the plate velocity from 30 mm/s to 60 mm/s reduces the cooling intensity, with higher temperatures at the impingement point ($z^* = 0$) for higher velocities. The AA6082 plate cools uniformly from 500 °C to 100 °C at velocities of 30 and 45, but for 60 mm/s, it enters the film boiling region. The nickel plate shows film boiling at 45 mm/s and cools to 470 °C. The extracted heat flux along the plate length increases with higher plate velocities, except when the plate is in the film boiling region. Due to higher thermal conductivity, aluminum alloy plates exhibit higher axial heat conduction, leading to a pre-cooling effect and lower temperatures at the impingement point. For

moving plates, there is no significant difference between top-side and bottom-side cooling.

Nozzle field

Variation in nozzle height within a nozzle field influences the interaction and overlap of spraying nozzles, depending on the nozzle height and nozzle-to-nozzle distance. At a nozzle height of 63 mm and a nozzle distance of 70 mm, the plate cools relatively uniformly, with temperature peaks occurring between the nozzles. However, increasing the nozzle height to 84 mm introduces surface turbulence, resulting in inhomogeneous heat transfer. At a nozzle height of 127 mm, strong overlapping of wetting fronts from adjacent nozzles leads to water stagnation at the center of the middle nozzle, reducing the heat flux from 3 to 1.5 MW/m².

Increasing the nozzle-to-nozzle distance from 35 to 70 mm at a constant nozzle height results in hot spots between nozzles, causing fluctuations and a drop in heat flux. A higher nozzle pressure at a nozzle height of 63 mm and a nozzle distance of 35 mm reduces the water stagnation under the middle nozzle but does not significantly increase the heat flux. However, increasing the nozzle pressure from 1 to 3 bar at a nozzle distance of 70 mm reduces temperature fluctuations and increases the heat flux. Thicker plates result in greater inhomogeneities and fluctuations in heat transfer rates. Increasing the volume flow rate from 9 to 18 L/min improves the cooling uniformity but does not significantly enhance the heat flux.

Comparing the inline and staggered nozzle configurations, it is found that overall the staggered configuration promotes a more uniform and homogeneous cooling, compared to the inline configuration. However, the cooling at the center of the middle nozzle is faster for the inline configuration.

Bottom-side cooling in the nozzle field is observed to be relatively faster and more uniform, with a shorter film boiling period, consistent with findings from single nozzle studies.

As the velocity of the plate increases, inhomogeneities and non-uniformities during the cooling process rise. The rate of cooling decreases for higher plate velocities and temperatures in the vicinity of the first nozzle increase. The influence of the nozzle height on the cooling of the moving plate is investigated and it is found that the

temperature profiles show a similar trend with varying nozzle heights for a velocity of 30 mm/s. Although, the temperature at position $z^* = 0$ mm increases for higher nozzle heights. The nozzle-to-nozzle distance of 35 mm for moving plates promotes a more uniform and faster cooling compared to the 70 mm distance and maximum heat flux is higher for a 35 mm nozzle distance. The maximum heat flux is higher for a velocity of 45 mm/s at a nozzle height of 63 mm and a nozzle distance of 35 mm compared to 30 mm/s. However, the DNB temperature lies approximately at 170 °C.

Quenching of vertical plates using flat sprays

The results of the current study indicate that the cooling of hot plates by flat sprays is influenced by several parameters, including plate velocity, plate thickness, metal type, and nozzle inclination angle. Based on these findings, the following conclusions can be drawn:

It is observed, that by increasing the plate velocity, the maximum heat flux rises, while the front width of the pre-cooling region decreases. As the plate velocity increases, the water spray impinges on a higher temperature surface due to the reduced axial pre-cooling effect. Consequently, the highest heat transfer and cooling occurs near the impingement region, resulting in the maximum heat flux in that area. The results indicate that the plate velocity is a critical parameter, and selecting an appropriate velocity is essential to achieve homogenous cooling and maximize the heat flux. Although the DNB temperature also increases with higher sheet velocity, this increase is not as significant as the rise in maximum heat flux.

The variation in plate thickness exhibits a similar trend to that of the velocity. The maximum heat flux increases with thicker plates due to a reduction in the front width of the pre-cooling region. This indicates that the pre-cooling process, which involves cooling the plate before it enters the impingement region, has a smaller effect on thicker plates compared to thinner ones. Consequently, the front width of the pre-cooling region decreases for thicker plates, leading to an increase in the maximum heat flux. The pre-cooling effect in the axial direction for the aluminum alloy (a highly conductive metal) and thin plates of 2 mm thickness is more pronounced, resulting in a larger pre-cooling region. This increased pre-cooling effect leads to a decrease in the maximum heat flux. The maximum heat flux is observed to be higher for nickel,

following nicrofer and aluminum alloy plates. The local position z^* of DNB temperatures shifts towards the impingement region for higher velocities and thicker plates. The DNB temperatures range from 190 °C to 220 °C for nickel and nicrofer, and from 140 °C to 160 °C for aluminum alloy. Furthermore, varying the nozzle inclination angle shows that this parameter has minimal influence on the cooling process. However, at a 65° inclination angle, the maximum heat flux is comparatively high.

The findings summarized in this work enhance the understanding of heat transfer during the cooling of moving metals in nozzle fields. These insights can be applied to the design of new and existing industrial plants, improving efficiency and effectiveness.

8 References

- Aamir, M., Qiang, L., Xun, Z., Hong, W., Zubair, M., 2014. Ultra Fast Spray Cooling and Critical Droplet Diameter Estimation from Cooling Rate. *JPEE* 02 (04), 259–270. 10.4236/jpee.2014.24037.
- Abdalrahman, K.H., Sabariman, Specht, E., 2014. Influence of salt mixture on the heat transfer during spray cooling of hot metals. *International Journal of Heat and Mass Transfer* 78, 76–83. 10.1016/j.ijheatmasstransfer.2014.06.070.
- Abdalrahman, K.H.M., 2012. Influence of Water Quality and Kind of Metal in the Secondary Cooling Zone of Casting Process. PhD.
- Agrawal, C., Gotherwal, D., Singh, C., Singh, C., 2017. Effect of surface thickness on the wetting front velocity during jet impingement surface cooling. *Heat Mass Transfer* 53 (2), 733–741. 10.1007/s00231-016-1855-9.
- Alam, U., Krol, J., Specht, E., Schmidt, J., 2008. Enhancement and Local Regulation of Metal Quenching Using Atomized Sprays. *J. ASTM Int.* 5 (10), 1–10. 10.1520/JAI101805.
- Alifanov, O.M., 1994. *Inverse Heat Transfer Problems*. Springer Berlin Heidelberg, Berlin, Heidelberg.
- Cebo-Rudnicka, A., Malinowski, Z., Buczek, A., 2016. The influence of selected parameters of spray cooling and thermal conductivity on heat transfer coefficient. *International Journal of Thermal Sciences* 110, 52–64. 10.1016/j.ijthermalsci.2016.06.031.
- Fang, Y., 2019. Influence of nozzle type and configuration and surface roughness on heat transfer during metal quenching with water.
- Freund, S., Pautsch, A.G., Shedd, T.A., Kabelac, S., 2007. Local heat transfer coefficients in spray cooling systems measured with temperature oscillation IR thermography. *International Journal of Heat and Mass Transfer* 50 (9-10), 1953–1962. 10.1016/j.ijheatmasstransfer.2006.09.028.
- Gradeck, M., Kouachi, A., Lebouché, M., Volle, F., Maillet, D., Borean, J.L., 2009. Boiling curves in relation to quenching of a high temperature moving surface with liquid jet impingement. *International Journal of Heat and Mass Transfer* 52 (5-6), 1094–1104. 10.1016/j.ijheatmasstransfer.2008.09.015.
- Groß, S., Soemers, M., Mhamdi, A., Sibai, F.A., Reusken, A., Marquardt, W., Renz, U., 2005. Identification of boundary heat fluxes in a falling film experiment using

- high resolution temperature measurements. *International Journal of Heat and Mass Transfer* 48 (25-26), 5549–5562. 10.1016/j.ijheatmasstransfer.2005.06.030.
- Heung-Kyu Kim, Soo-Ik Oh, 2001. Evaluation of heat transfer coefficient during heat treatment by inverse analysis. *Journal of Materials Processing Technology*.
- Hof, J., 2023. Experimentelle Untersuchung der Strömungstopographie von Sprühdüsenfeldern auf horizontalen Oberflächen. Dissertation, Deutschland.
- Hu, H., Xu, C., Zhao, Y., Ziegler, K.J., Chung, J.N., 2017. Boiling and quenching heat transfer advancement by nanoscale surface modification. *Sci Rep* 7 (1), 6117. 10.1038/s41598-017-06050-0.
- Huang, C.-H., Wang, S.-P., 1999. A three-dimensional inverse heat conduction problem in estimating surface heat flux by conjugate gradient method. *International Journal of Heat and Mass Transfer* 42 (18), 3387–3403. 10.1016/S0017-9310(99)00020-4.
- J. Beck, B. Blackwell, A. Haji-sheikh, 1996. Comparison of some inverse heat conduction methods using experimental data. *International Journal of Heat and Mass Transfer*.
- Kaymak, Y., 2007. Simulation of Metal Quenching Processes or the Minimization of Distortion and Stresses. PhD, Magdeburg.
- Kotrbáček, P., Chabičovský, M., Komínek, J., Resl, O., Bellerova, H., 2022. Influence of water temperature on spray cooling at high surface temperatures. *Applied Thermal Engineering* 216, 119074. 10.1016/j.applthermaleng.2022.119074.
- Krauss, G., 2015. Steels. ASM International.
- Kulkarni, G.A., 2019. Local heat transfer and stress analysis of direct chill casting process. Dissertation. Docupoint Verlag, Barleben.
- Malinowski, Z., Cebo-Rudnicka, A., Hadała, B., Szajding, A., Telejko, T., 2018. Implementation of one and three dimensional models for heat transfer coefficient identification over the plate cooled by the circular water jets. *Heat Mass Transfer* 54 (8), 2195–2213. 10.1007/s00231-017-2195-0.
- Minamoto, S., Tsukamoto, S., Kasuya, T., Watanabe, M., Demura, M., 2022. Prediction of continuous cooling transformation diagram for weld heat affected zone by machine learning. *Science and Technology of Advanced Materials: Methods* 2 (1), 402–415. 10.1080/27660400.2022.2123262.

- Müller, H.R., Jeschar, R., 1983. Wärmeübergang bei der Spritzwasserkühlung von Nichteisenmetallen. *International Journal of Materials Research* 74 (5), 257–264. 10.1515/ijmr-1983-740501.
- Nallathambi, A.K., Specht, E., 2009. Estimation of heat flux in array of jets quenching using experimental and inverse finite element method. *Journal of Materials Processing Technology* 209 (12-13), 5325–5332. 10.1016/j.jmatprotec.2009.04.001.
- Nayak, S.K., Mishra, P.C., Ukamanal, M., Chaini, R., 2018. Experimental Result on Heat Transfer during Quenching of Hot Steel Plate by Spray Impingement. *Heat Transfer Engineering* 39 (9), 739–749. 10.1080/01457632.2017.1341193.
- Orlande, H.R.B., Özisik, M.N., 2021. *Inverse Heat Transfer: Fundamentals and applications*. CRC Press, Boca Raton, London, New York.
- Ostermann, F., 2014. *Anwendungstechnologie Aluminium*, 3rd ed. Springer Vieweg, Berlin.
- R. D. Lopez-Garcia, Israel Medina-Juárez, A. Maldonado-Reyes, 2022. Effect of Quenching Parameters on Distortion Phenomena in AISI 4340 Steel. *Metals*.
- Sabariman, 2015. Heat transfer analysis in metal quenching with sprays and jets. Zugl.: Magdeburg, Univ., Fak. für Verfahrens- und Systemtechnik, Diss., 2015. Docupoint-Verl., Barleben.
- Samuel, A., Prabhu, K.N., 2022. Residual Stress and Distortion during Quench Hardening of Steels: A Review. *J. of Materi Eng and Perform* 31 (7), 5161–5188. 10.1007/s11665-022-06667-x.
- Schweizer, N., 2010. *Multi-Scale Investigation of Nucleate Boiling Phenomena in Microgravity*, Darmstadt.
- Specht, E., 2017. *Heat and Mass Transfer in Thermoprocessing - Fundamentals - Calculations - Processes*. Vulkan Verlag, [S.l.].
- Stark, P., Schuettenberg, S., Fritsching, U., 2011. Spray quenching of specimen for ring heat treatment, 201–212. 10.2495/MPF110171.
- Umair Alam, 2011. *Experimental Study of Local Heat Transfer during Quenching of Metals by Spray and Multiple Jets*. PhD, Magdeburg.
- Wang, B., Lin, D., Xie, Q., Wang, Z., Wang, G., 2016. Heat transfer characteristics during jet impingement on a high-temperature plate surface. *Applied Thermal Engineering* 100, 902–910. 10.1016/j.applthermaleng.2016.02.054.

- Woodbury, K.A., 2002. Inverse engineering handbook. CRC Press, Boca Raton, FL, London.
- Yang, H., Cao, X., Sun, X., 2012. Effects of Spray Angle on Spray Cooling of Extruded aluminum Alloy Plate. AASRI Procedia 3, 630–635. 10.1016/j.aasri.2012.11.100.
- Zhang, Y., Milkereit, B., Kessler, O., Schick, C., Rometsch, P.A., 2014. Development of continuous cooling precipitation diagrams for aluminium alloys AA7150 and AA7020. Journal of Alloys and Compounds 584, 581–589. 10.1016/j.jallcom.2013.09.014.

9 Appendix

9.1 Quenching of Horizontal Plates

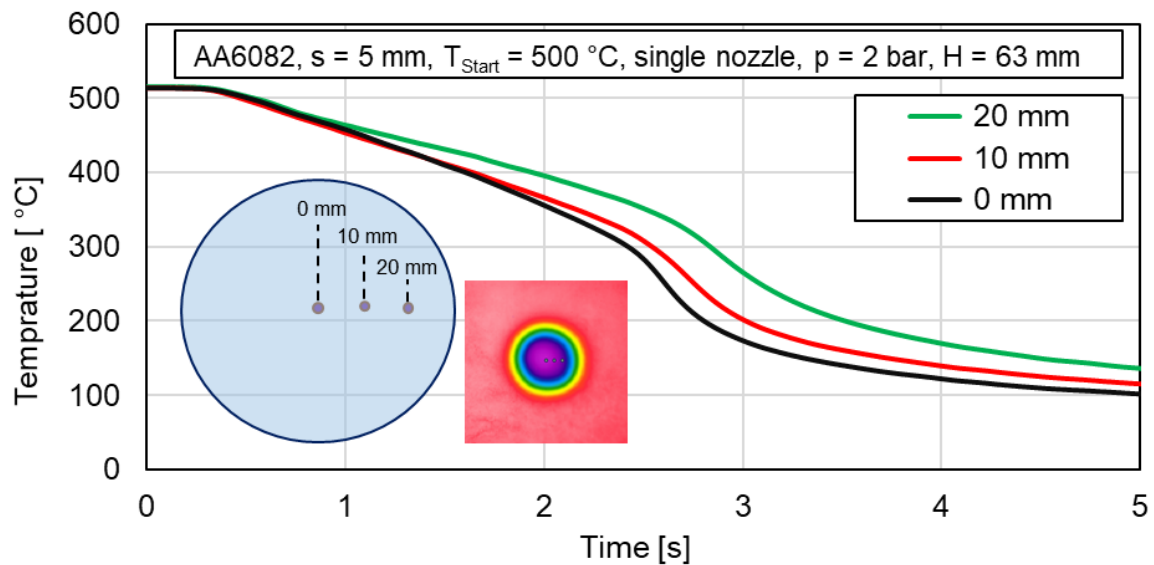


Figure 9.1: Cooling curve comparison along the radial position of the wetting front

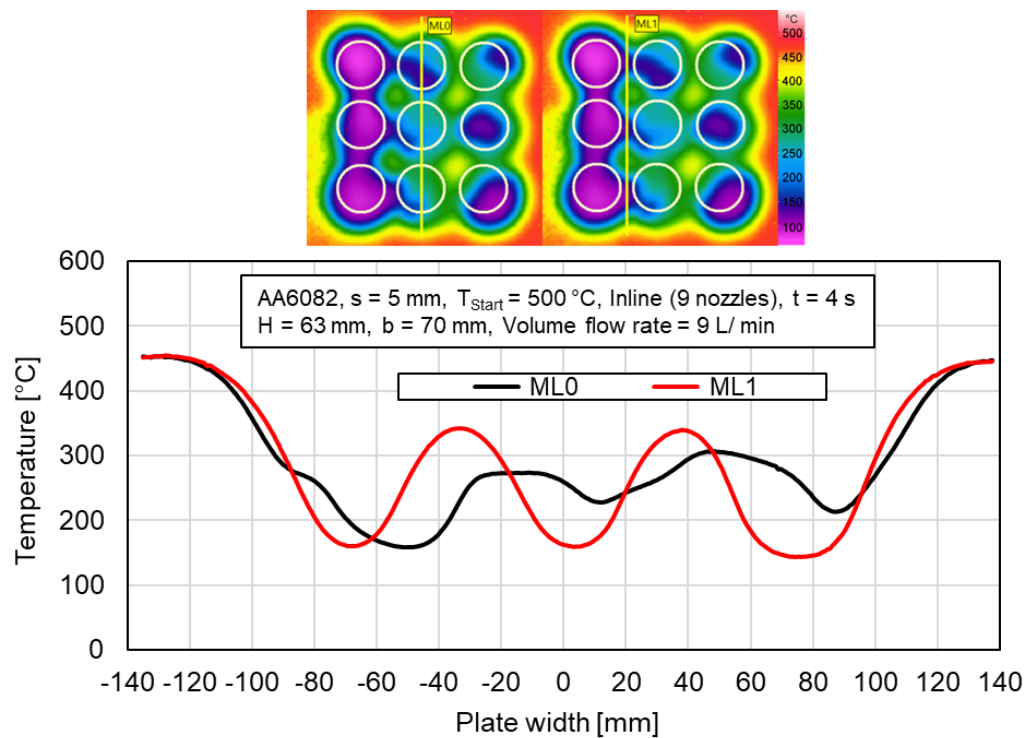


Figure 9.2: Temperature variation of AA6082 for two different ML positions at 4 s

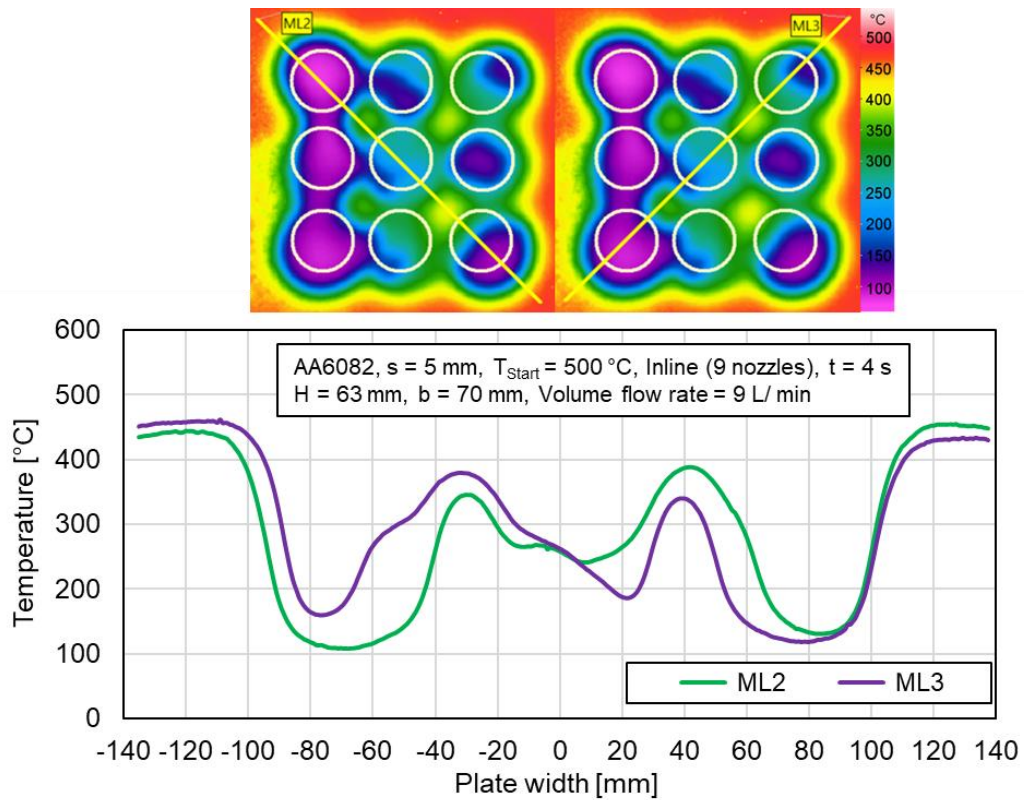


Figure 9.3: Temperature profiles of AA6082 along the plate width for ML2 and ML3

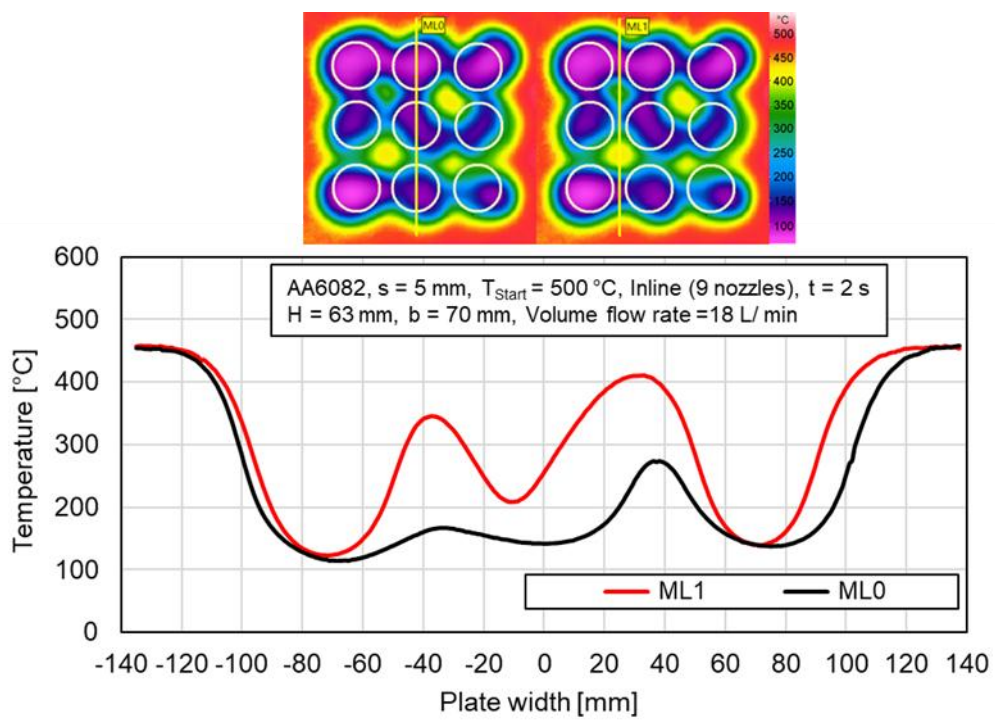


Figure 9.4: Temperature variation of AA6082 for two different ML positions at 2 s

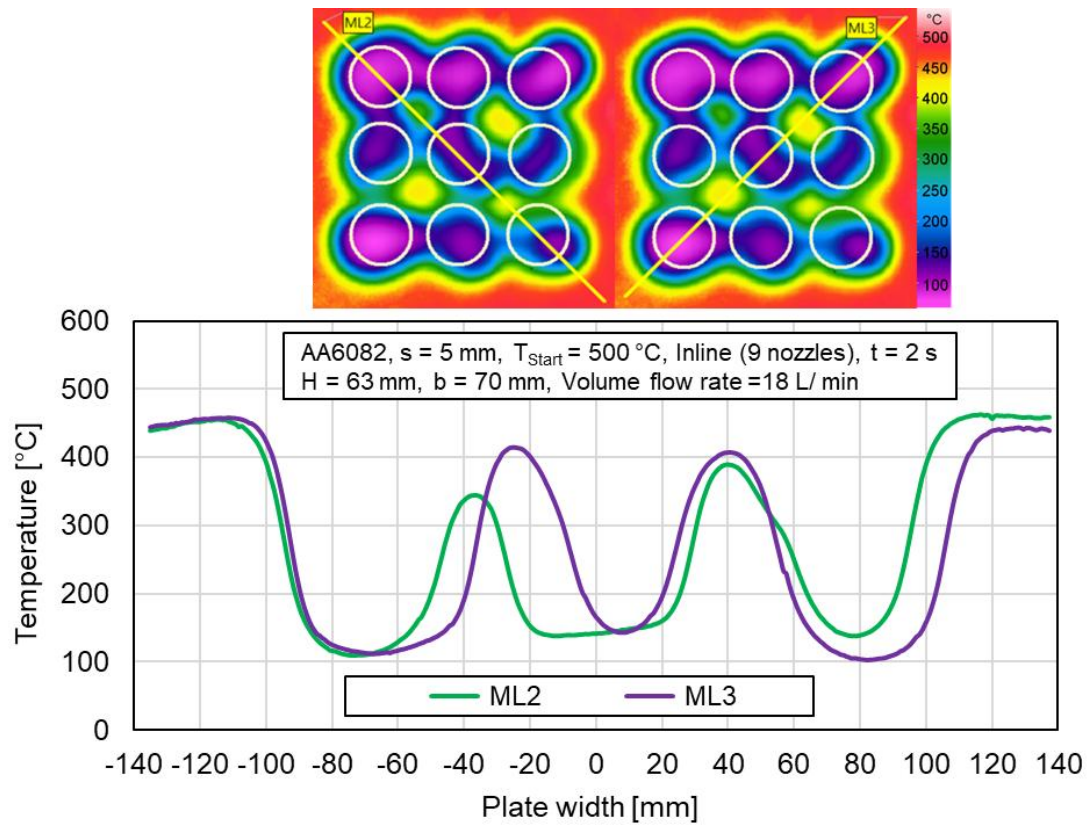


Figure 9.5: Influence of measuring line on the temperature distribution in an inline field

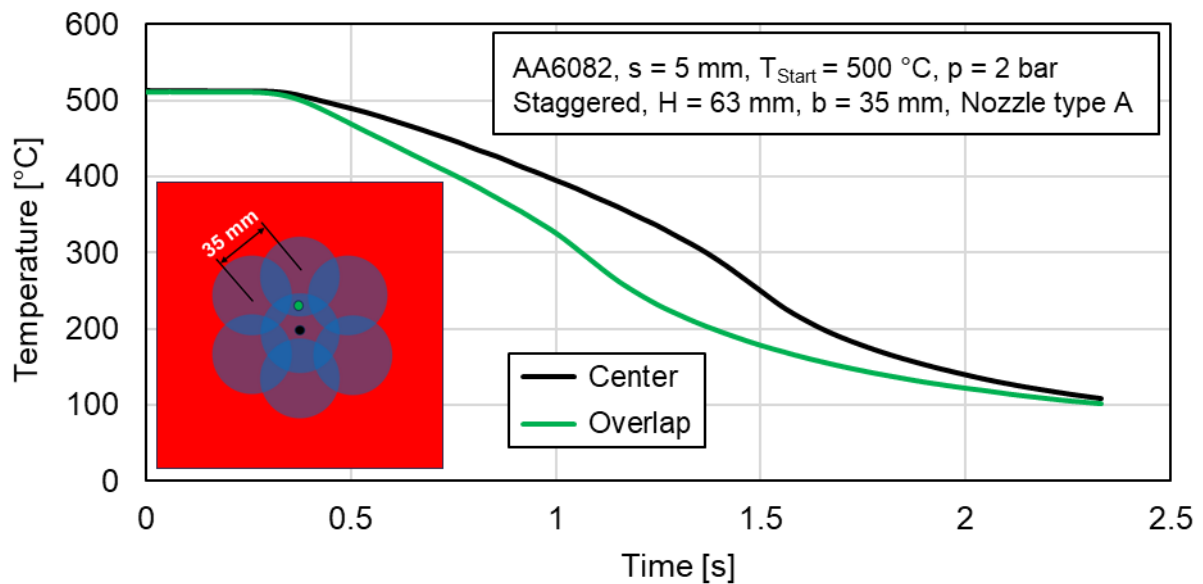


Figure 9.6: Cooling curve comparison of the center of the middle nozzle and overlap positions in nozzle field (Staggered, $H = 63$ mm, AA6082, $b = 35$ mm)

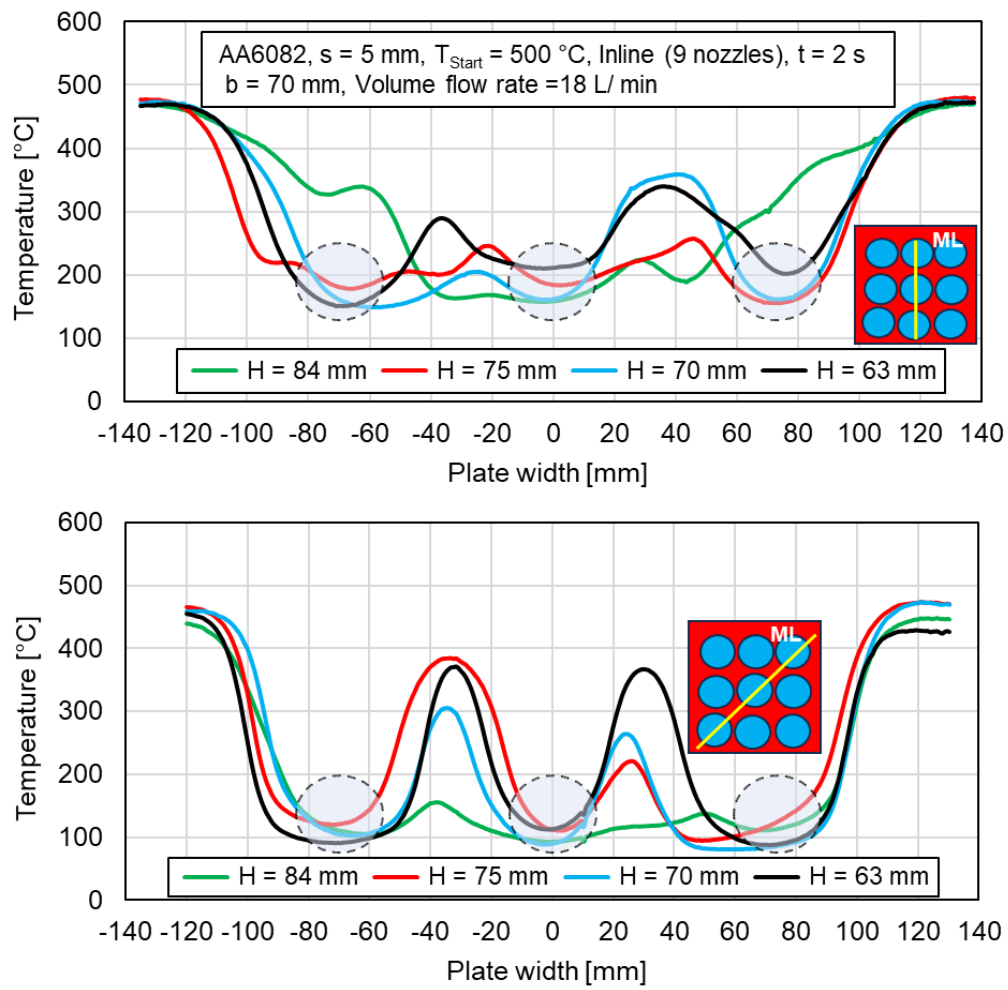


Figure 9.7: Temperature distribution of AA6082 along the plate width at various nozzle heights

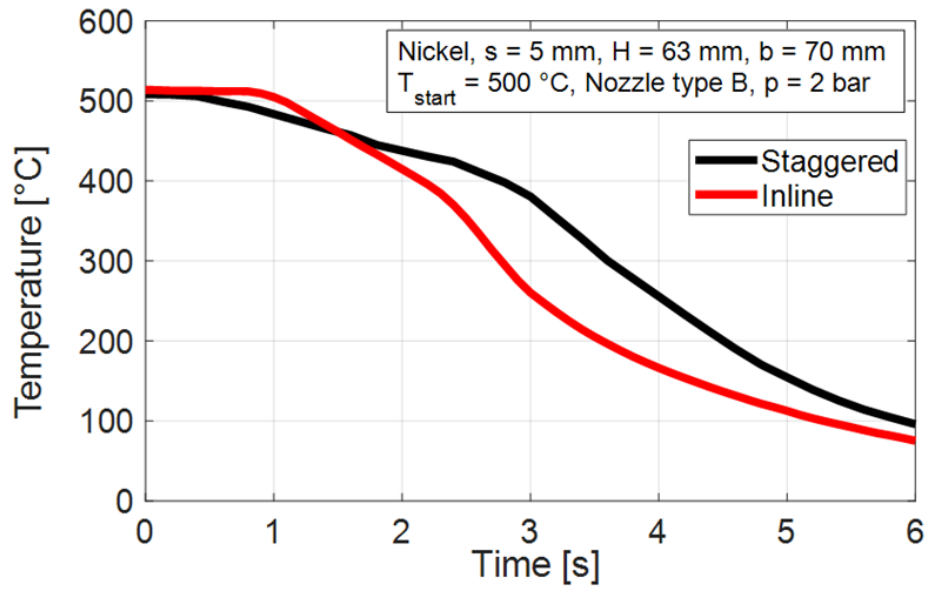


Figure 9.8: Comparison of nozzle configuration on the cooling curve at the center of the middle nozzle ($H = 63$ mm, $b = 70$ mm, bottom side cooling)

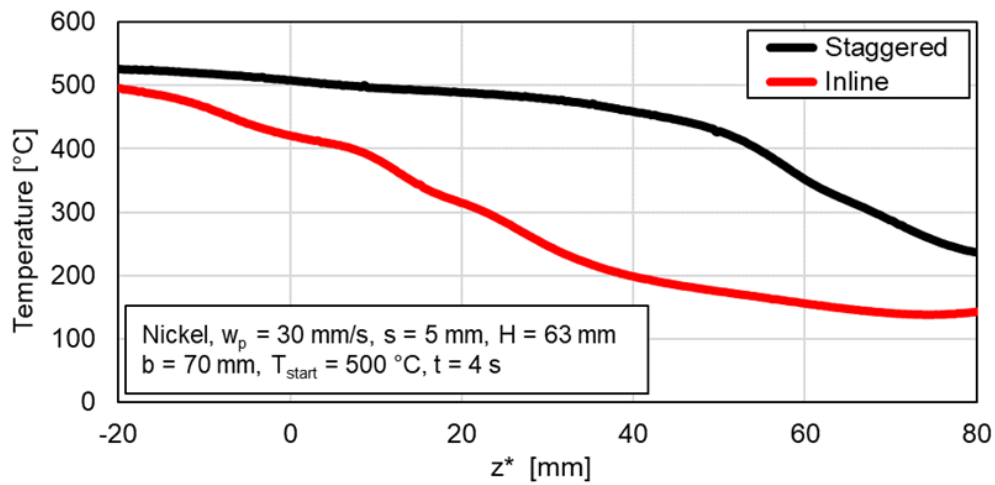


Figure 9.9: Influence of inline and staggered nozzle configuration on the cooling of nickel moving plate ($H = 63$ mm, $b = 70$ mm, $w_p = 30$ mm/s)

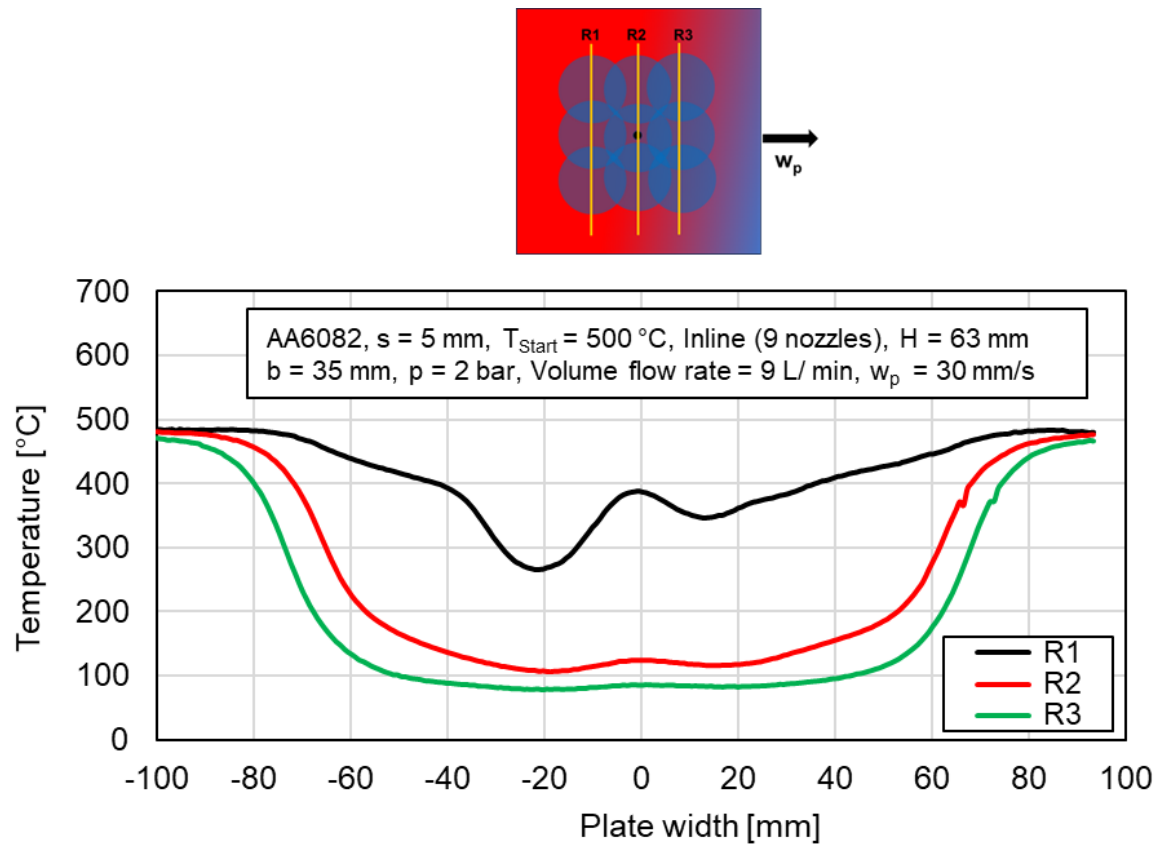


Figure 9.10: Temperature profiles along the plate width at three nozzle rows
 (AA6082, $H = 63 \text{ mm}$, $b = 35 \text{ mm}$, $w_p = 30 \text{ mm/s}$)

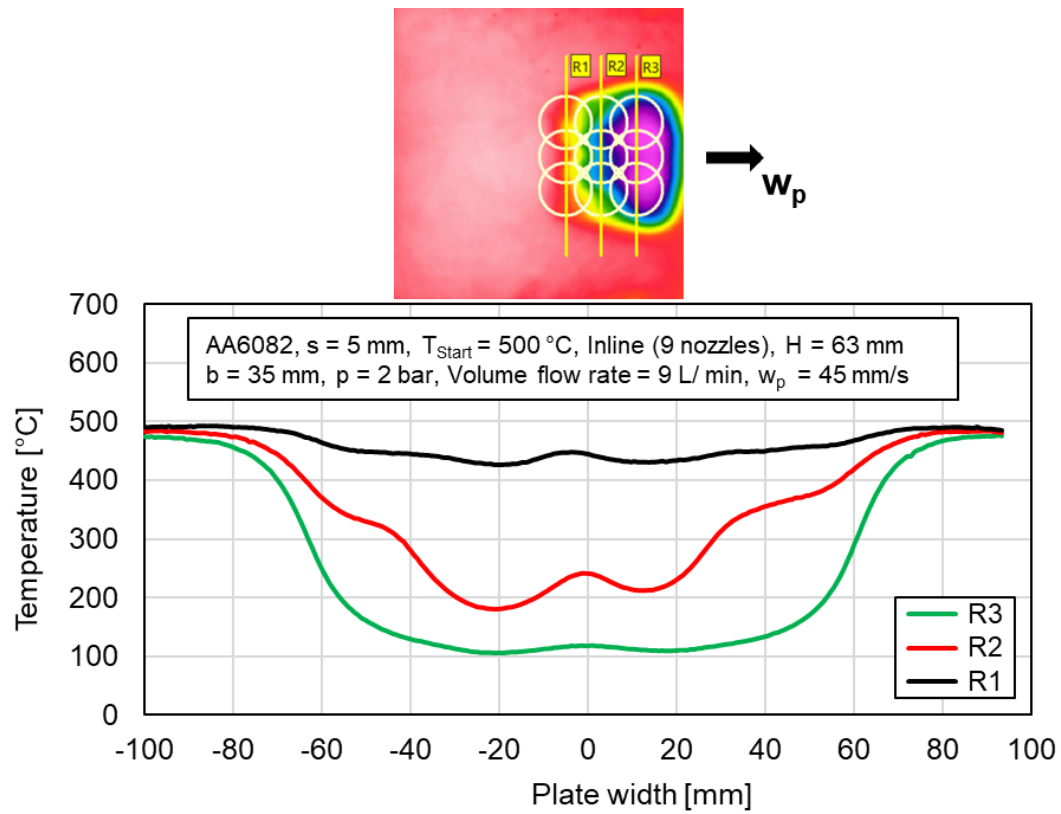


Figure 9.11: Temperature profiles along the plate width at three nozzle rows (AA6082, $H = 63$ mm, $b = 35$ mm, $w_p = 45$ mm/s)

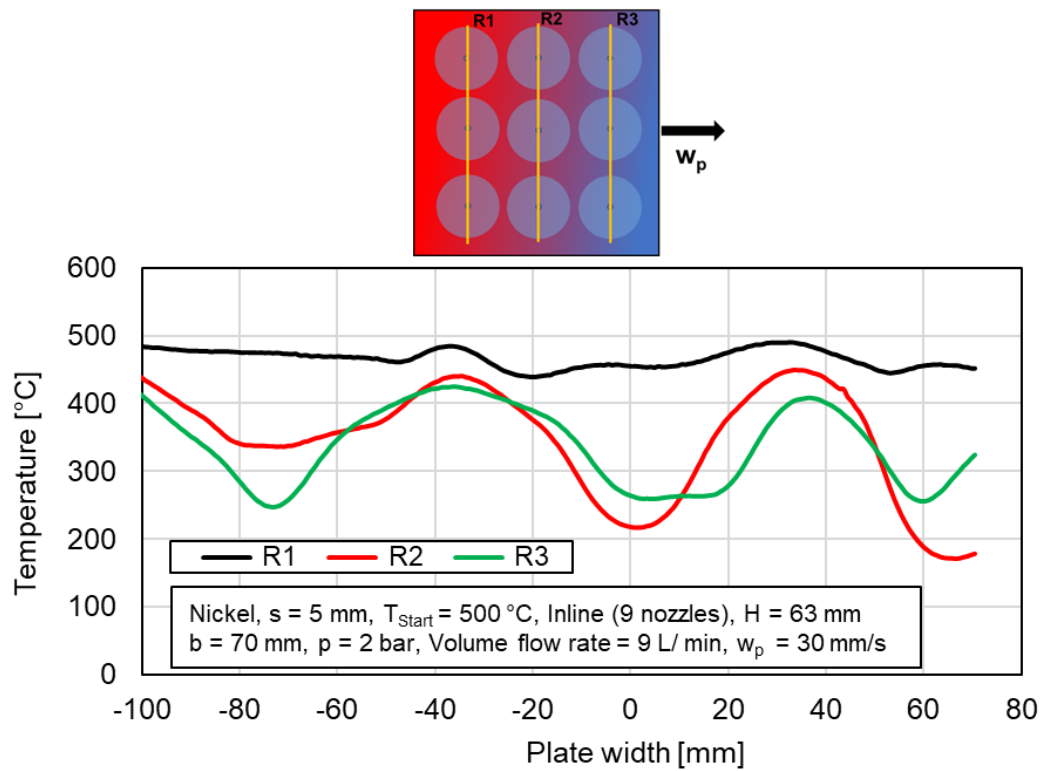


Figure 9.12: Temperature profiles along the plate width at three nozzle rows
(nickel, $H = 63$ mm, $b = 70$ mm, $w_p = 30$ mm/s)

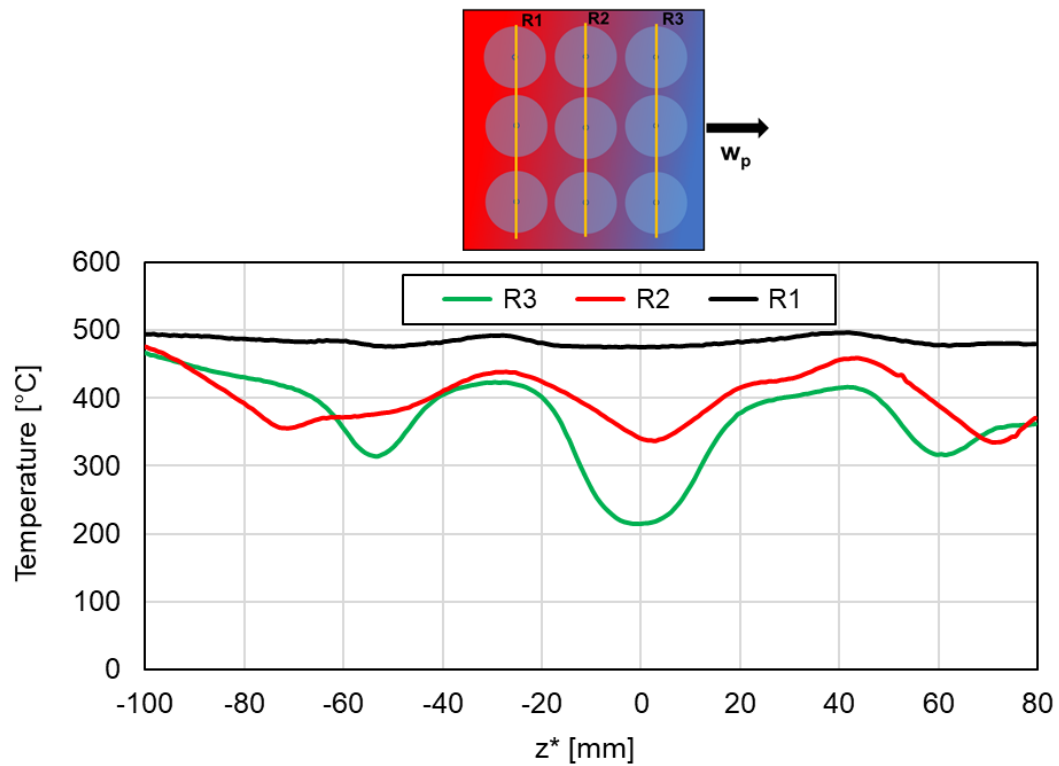


Figure 9.13: Temperature profiles along the plate width at three nozzle rows
(nickel, $H = 63$ mm, $b = 35$ mm, $w_p = 45$ mm/s)

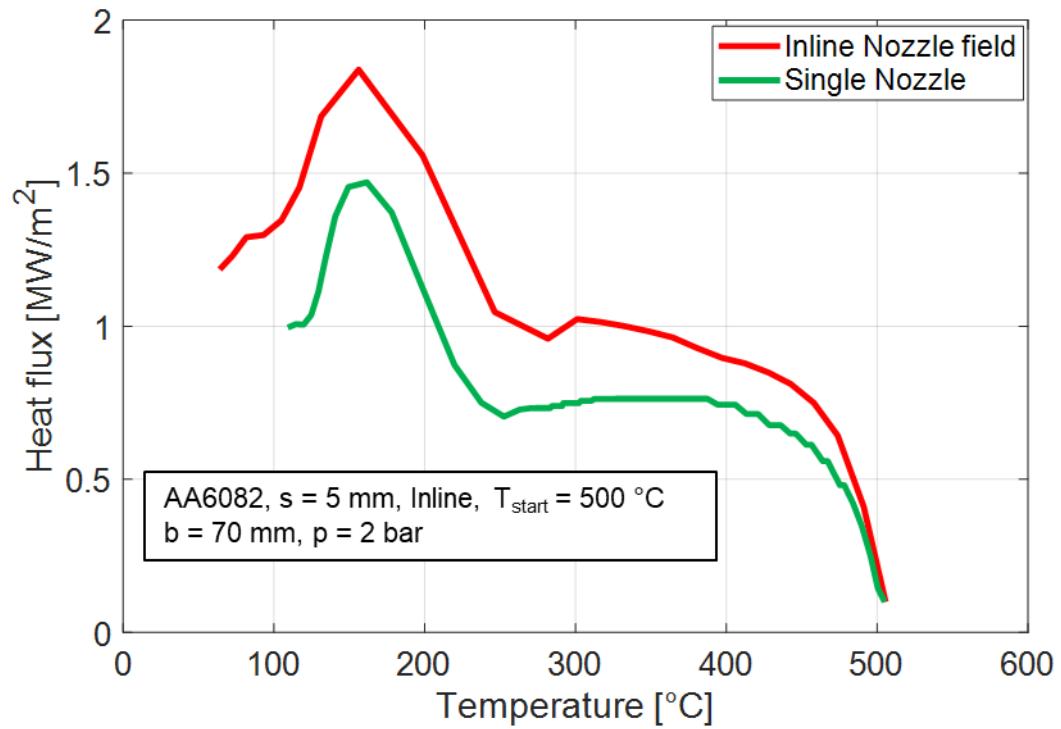


Figure 9.14: Boiling curve of Single nozzle vs Inline nozzle field (5mm, AA6082)

9.2 Quenching of Vertical Plates

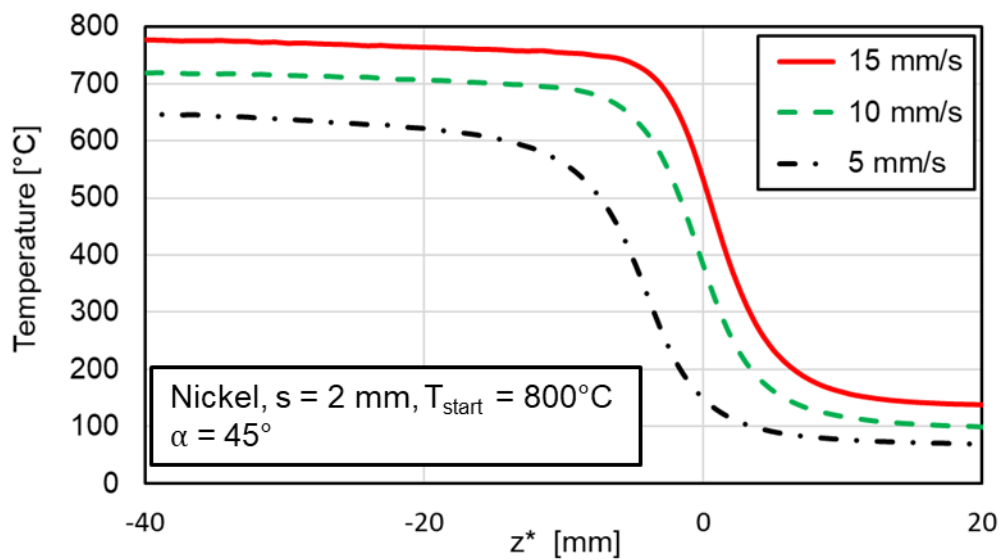


Figure 9.15: Cooling curves of 2 mm nickel plate with varying plate velocities ($\alpha = 45^\circ$)

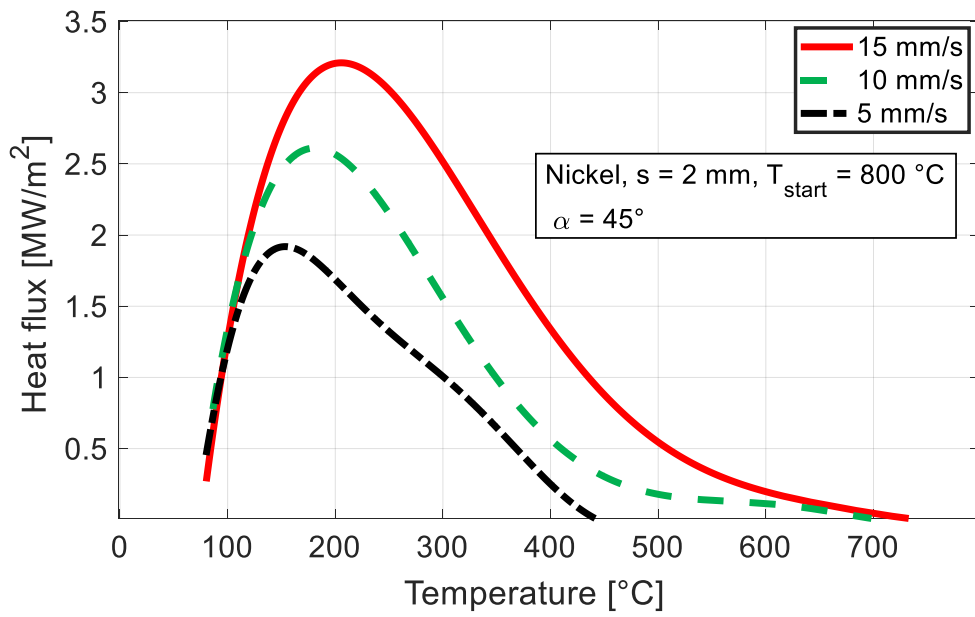


Figure 9.16: Boiling curves of 2 mm nickel plate with varying plate velocities ($\alpha = 45^\circ$)

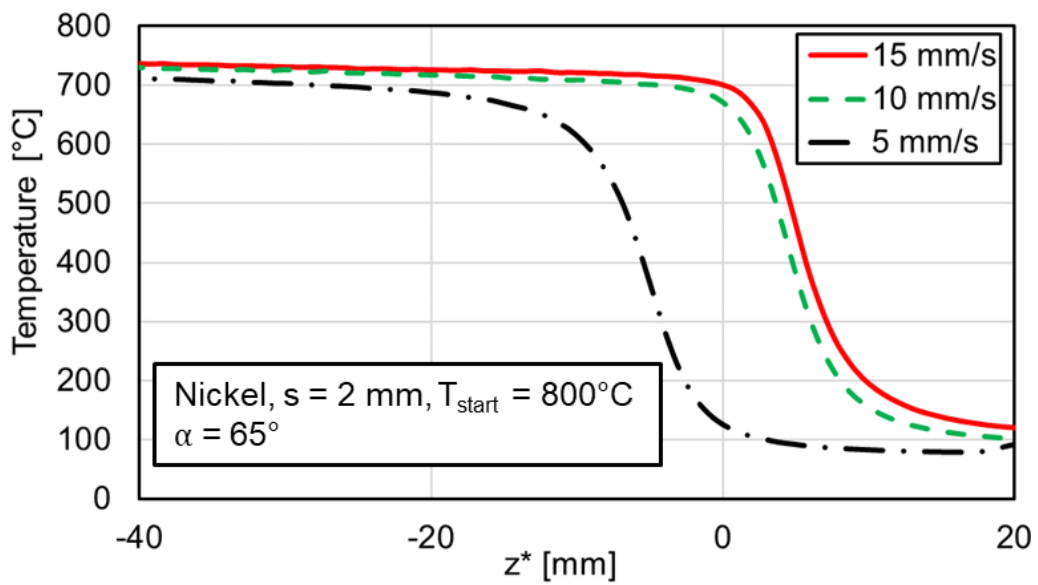


Figure 9.17: Cooling curves of 2 mm nickel plate with varying plate velocities ($\alpha = 65^\circ$)

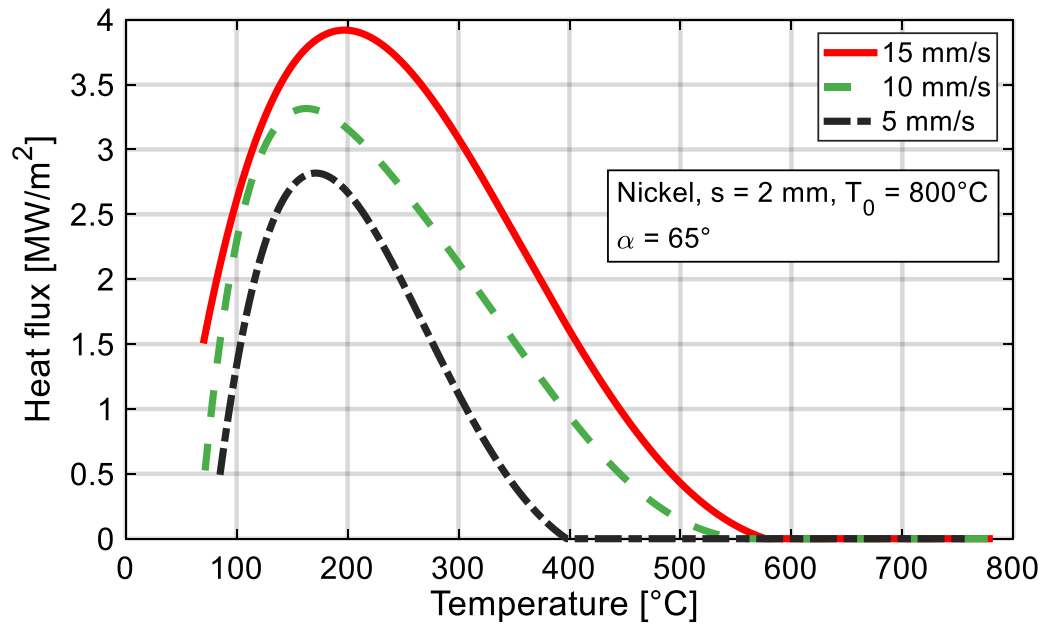


Figure 9.18: Boiling curves of 2 mm nickel plate with varying plate velocities ($\alpha = 65^\circ$)

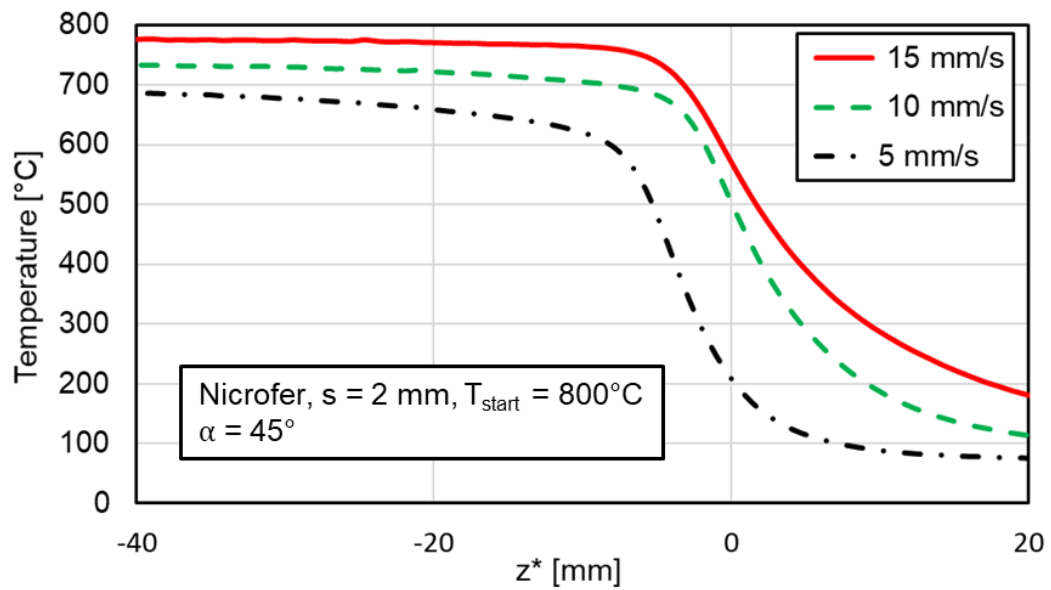


Figure 9.19: Cooling curves of 2 mm nicrofer plate with varying plate velocities ($\alpha = 45^\circ$)

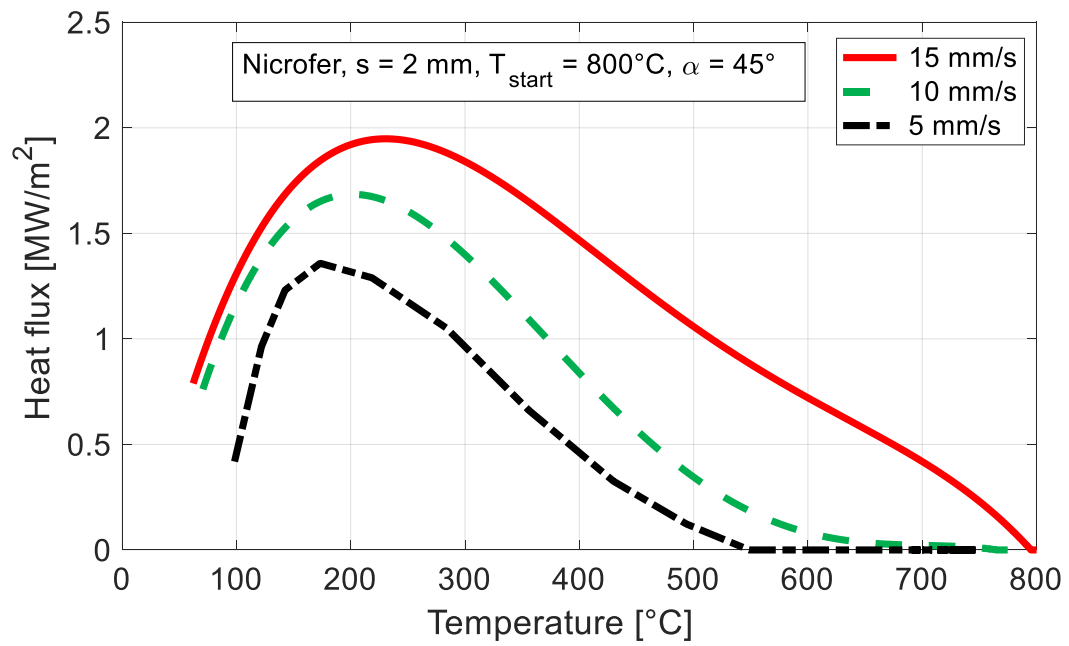


Figure 9.20: Boiling curves of 2 mm nicrofer plate with varying plate velocities ($\alpha = 45^{\circ}$)

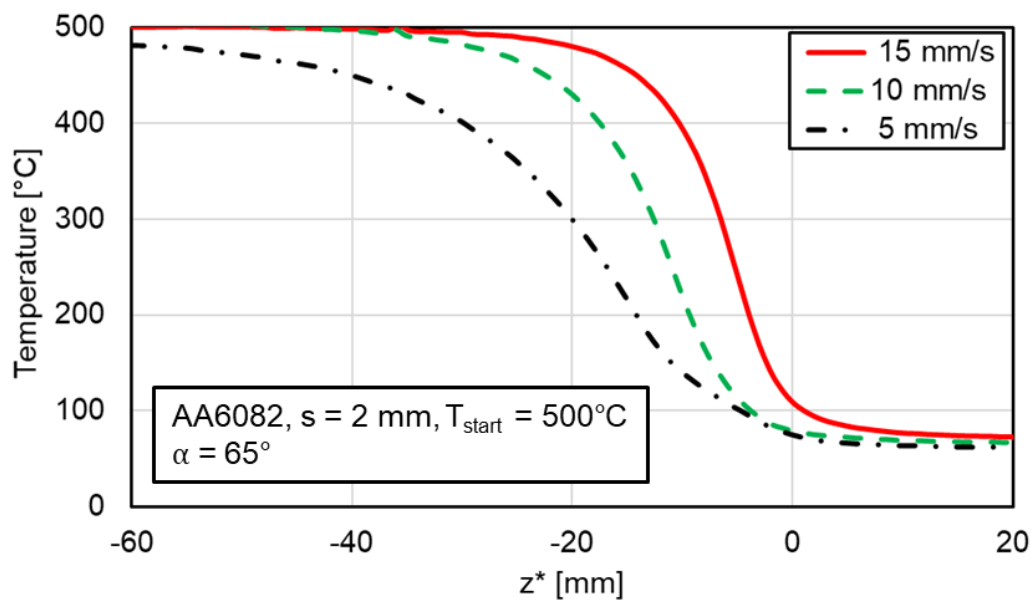


Figure 9.21: Cooling curves of 2 mm AA6082 plate with varying plate velocities ($\alpha = 65^{\circ}$)

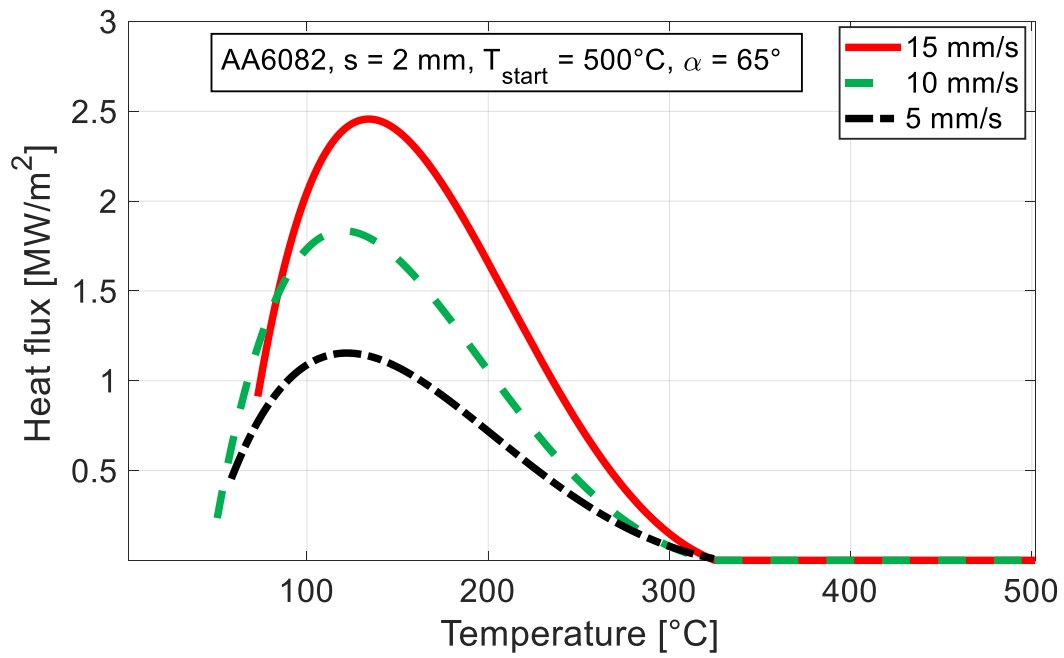


Figure 9.22: Boiling curves of 2 mm AA6082 plate with varying plate velocities ($\alpha = 65^{\circ}$)

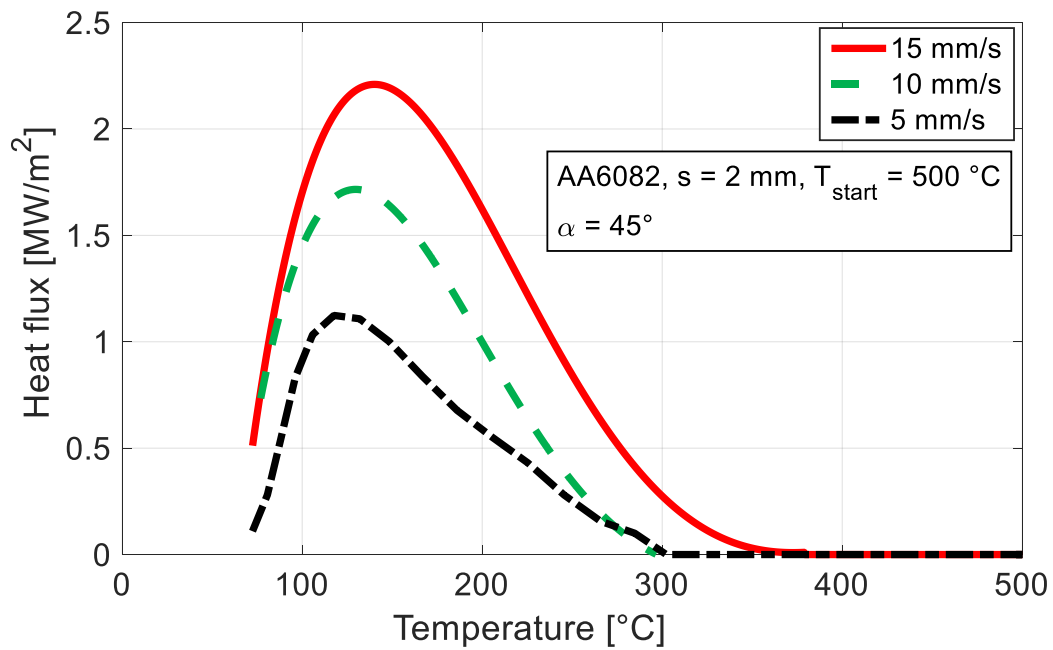


Figure 9.23: Boiling curves of 2 mm AA6082 plate with varying plate velocities ($\alpha = 45^{\circ}$)

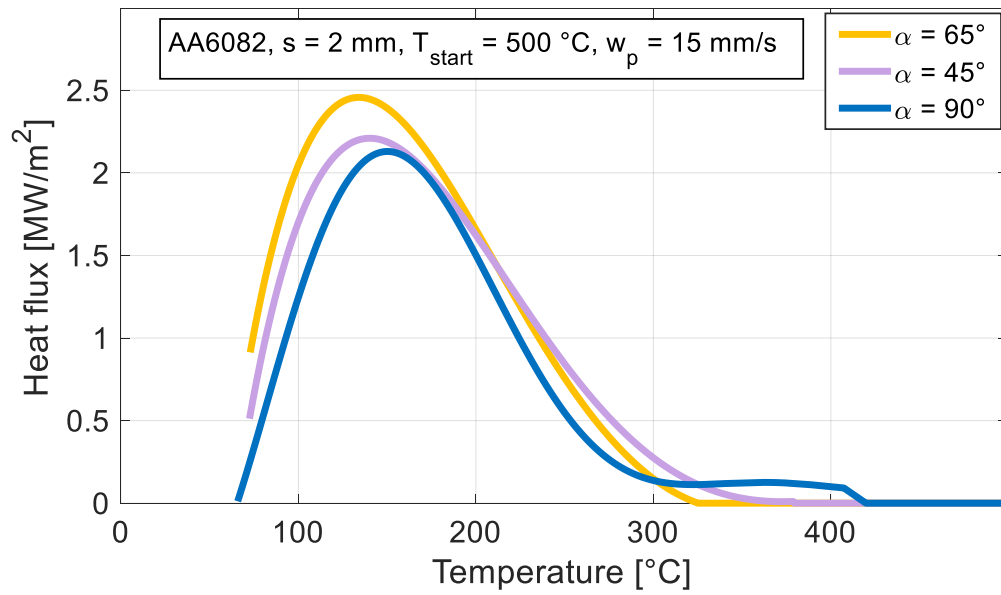


Figure 9.24: Boiling curves of 2 mm AA6082 plate with varying nozzle angle ($w_p = 15$ mm/s)

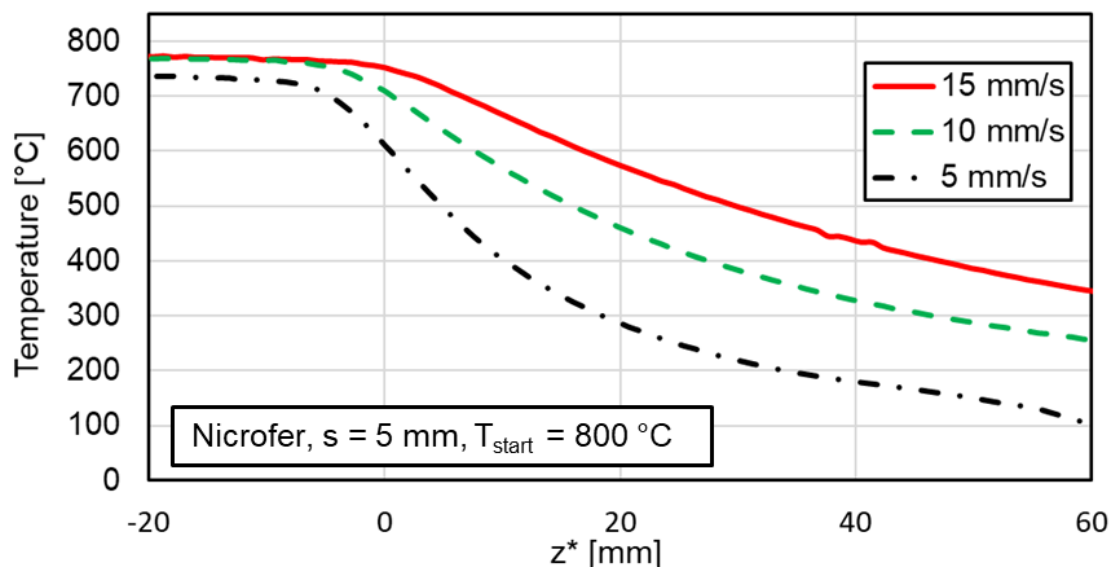


Figure 9.25: Cooling curves of 5 mm nicrofer plate with varying plate velocities

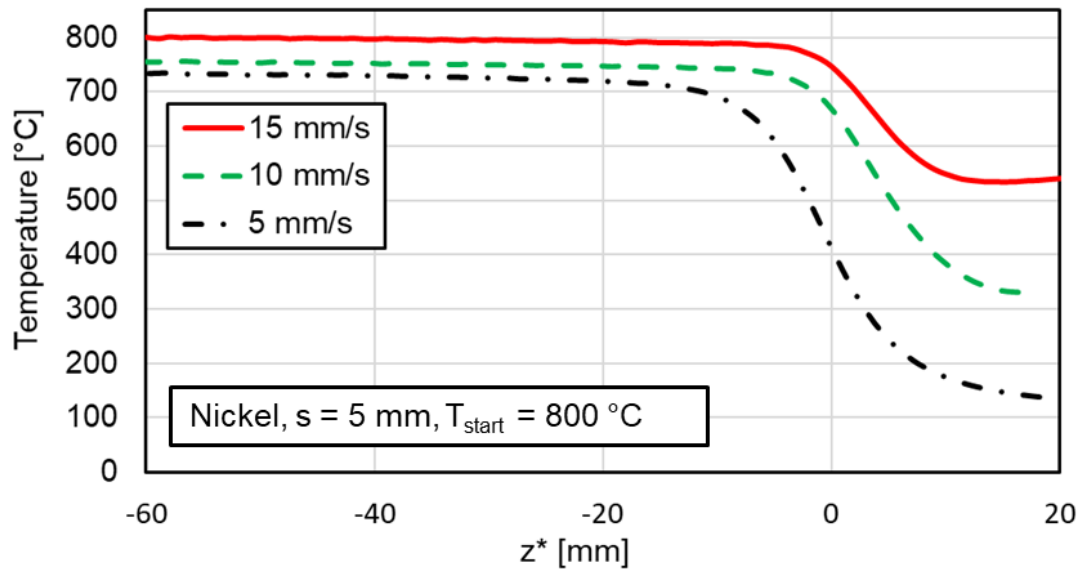


Figure 9.26: Cooling curves of 5 mm nickel plate with varying plate velocities

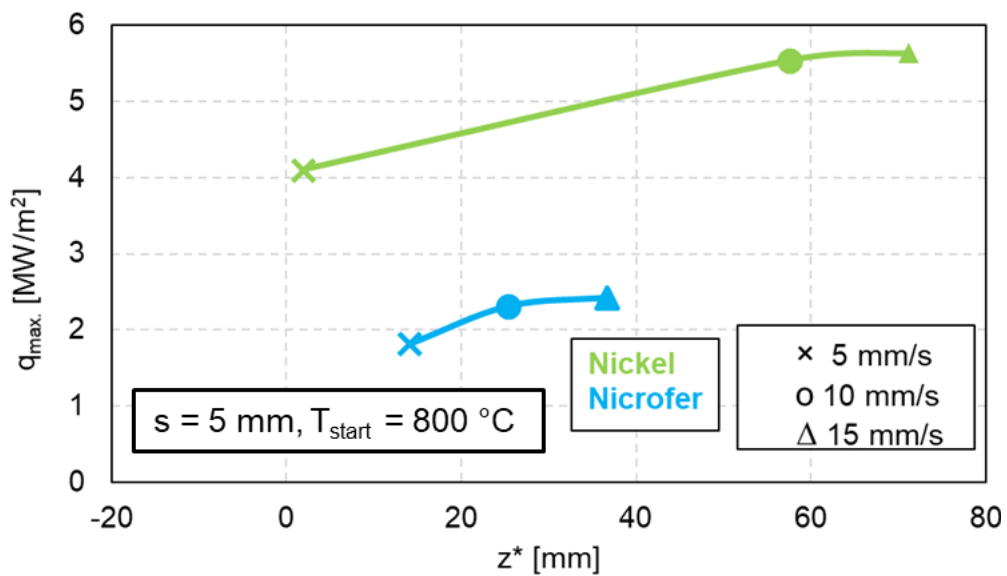


Figure 9.27: Maximum heat flux against the local position z^* with varying plate velocities (nickel, nicrofer, $s = 5$ mm)

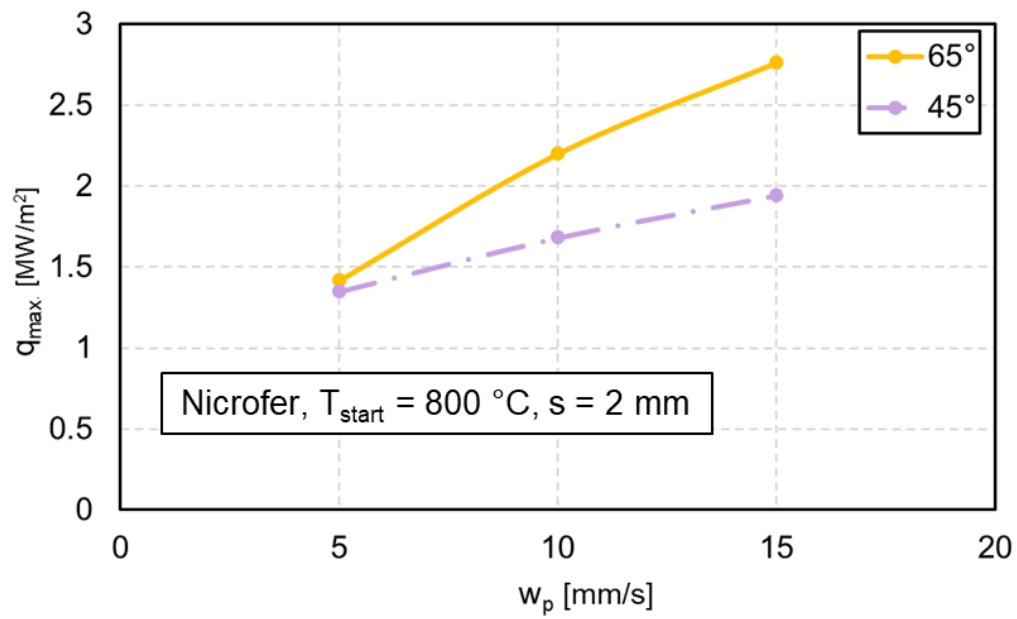


Figure 9.28: Influence of nozzle angle on maximum heat flux for varying plate velocities (nicrofer)

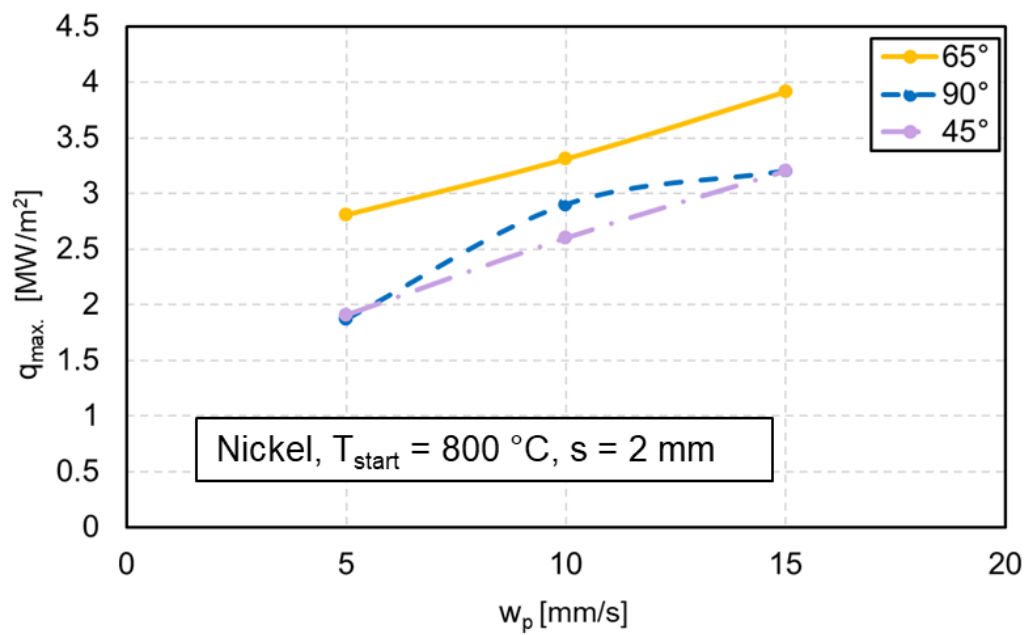


Figure 9.29: Influence of nozzle angle on maximum heat flux for varying plate velocities (nickel)

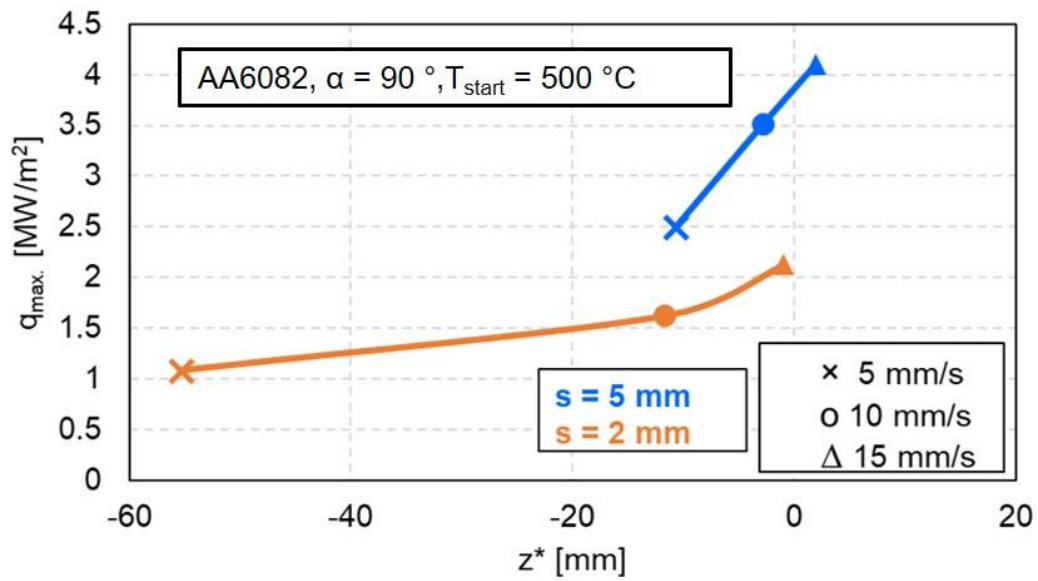


Figure 9.30: Maximum heat flux of AA6082 for various plate velocities and plate thicknesses

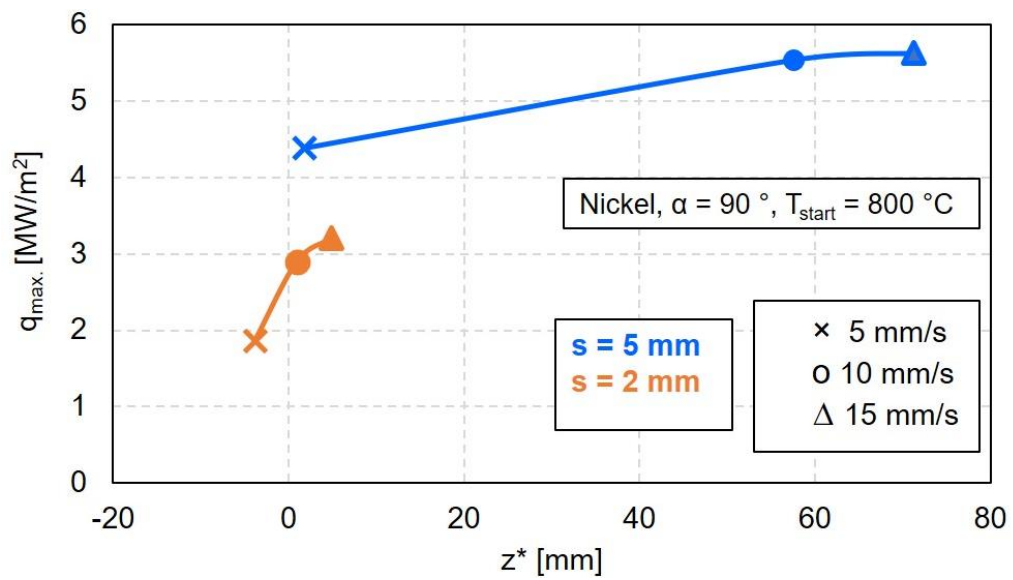


Figure 9.31: Maximum heat flux of nickel for various plate velocities and plate thicknesses